Large Eddy Simulation of Premixed Combustion Using Flamelets

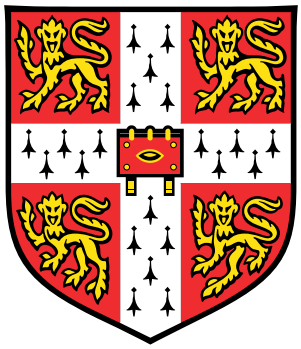

Ivan Langella

Department of Engineering

University of Cambridge

This dissertation is submitted for the degree of

Doctor of Philosophy

Robinson College October 2015

Sometimes I still look up in the sky and wonder what is that force that keeps men going beyond themselves. This thesis is dedicated to all those who still listen to this force and have never stopped to believe in their dreams. The world needs these people more than ever. I also dedicate this work to the people who loved and supported me the most since the day I was born, my mother Franca, my father Pietro, my sisters and my missing grandfather Giovanni.

Declaration

I hereby declare that except where specific reference is made to the work of others, the contents of this dissertation are original and have not been submitted in whole or in part for consideration for any other degree or qualification in this, or any other university. This dissertation is my own work and contains nothing which is the outcome of work done in collaboration with others, except as specified in the text and Acknowledgements. This dissertation contains approximately 65,000 words including appendices, bibliography, footnotes, tables and equations and has 112 figures.

Ivan Langella
October 2015

Acknowledgements

I would like to acknowledge Prof. N. Swaminathan for being a brilliant supervisor and also a great mentor. In these PhD years he has been more than supportive and always available for any kind of problem I may have had. The opportunity he has given to me with this PhD is priceless and I will be always thankful for this.

I acknowledge Prof. N. Chakraborty, for his help and advices in developing the models presented in this paper, and Y. Gao for sharing her DNS results, which have been useful for the understanding of the models presented in this work. I also want to acknowledge Prof. E. Mastorakos for his priceless help and several advices during the PhD period, and Profs. R. W. Pitz and F. A. Williams for their helps and suggestions for some of the simulations presented in this thesis.

I acknowledge Mr. P. Benie, a formidable expert in computing technologies, which helped me several times on different issues related with Unix systems and programming languages.

I would like to thank my colleagues and friends at the Hopkinson Lab in Cambridge, the professors I have been in contact with and the technicians, all of which have contributed to my personal and professional growth. A particular thought goes to the 'italian team' which have passed the lab across these years: A. Maffioli, D. Cavaliere, G. Borghesi and more recently Simone Lombardi, A. Giusti and A. Cabboi, but also to Z. Nicolau, I. Ahmed, M. Youstos, G. Ghiasi and T. Zhi Chen. I wish the best for all of them.

Finally, I would like to give a special thanks to my girlfriend Eli, for giving inspiration and support during the busy months of my PhD.

I acknowledge the funding through the EPSRC and the partnerships of Siemens and Rolls-Royce in this PhD project and also the conference grants received from the Combustion Institute

and Robinson College. This work made use of the Darwin high performance computing service at the University of Cambridge, whose access was partly funded by EPSRC and Siemens.

Publications

In chronological order, results from this work have appeared, or are currently prepared for publication in

Journals:

1. I. Langella, N. Swaminathan, Y. Gao, N. Chakraborty, *Combust. Theory Model.*, vol. 19, pp. 628-656. Assessment of dynamic closure for premixed combustion LES.

2. I. Langella, N. Swaminathan, *Combust. Theory Model.*, accepted, DOI 10.1080/13647830.2016.1140230. Unstrained and strained flamelets for LES of premixed combustion.

3. I. Langella, N. Swaminathan, Y. Gao, N. Chakraborty, *Combust. Sci. Technol.*, submitted August (2015) - accepted pending revision. LES of premixed combustion using an algebraic closure involving scalar dissipation rate.

4. I. Langella, N. Swaminathan, F. Williams, J. Furukawa, *Combust. Sci. Technol.*, submitted October (2015) - accepted pending revision. LES of premixed combustion in corrugated flamelets regime.

5. I. Langella, N. Swaminathan, R. Pitz. LES of lean premixed combustion behind a bluff-body, *Combust. Flame*, submitted January (2016) - accepted pending revision.

Conferences:

1. I. Langella, N. Swaminathan, N. Chakraborty. Large Eddy Simulation of Turbulent Premixed Combustion, *6th European Combustion Meeting (ECM)*, Lund-Sweden, July (2013).

2. I. Langella, N. Swaminathan, N. Chakraborty, Large Eddy Simulation of Premixed Combustion Using Scalar Dissipation Rate Approach, *8th Mediterranean Combustion Symposium (MCS)*, Ceşme-Turkey (2013).

3. I. Langella, N. Swaminathan, LES of Premixed Combustion Using Unstrained and Strained flamelets, *Joint combustion meeting of the Nordic-Scandinavian and British Sections of the Combustion Institute*, Cambridge-UK (2014).

4. I. Langella, N. Swaminathan, LES of Lean Premixed Combustion Using a Flamelet Approach, *Conference on Thermal Energy Systems: Production, Storage, Utilization and the Environment (ASME-ATI-UIT)*, Napoli-Italy (2015).

5. I. Langella, N. Swaminathan, R. Pitz, LES of Bluff Body turbulent premixed flame using Scalar Dissipation Rate Based Modelling, *9th Mediterranean Combustion Symposium (MCS)*, Rhodes-Greece (2015).

Abstract

Large Eddy Simulation (LES) has potential to address unsteady phenomena in turbulent premixed flames and to capture turbulence scales and their influence on combustion. Thus, this approach is gaining interest in industry to analyse turbulent reacting flows. In LES, the dynamics of large-scale turbulent eddies down to a cut-off scale are solved, with models to mimic the influences of sub-grid scales. Since the flame front is thinner than the smallest scale resolved in a typical LES, the premixed combustion is a sub-grid scale (SGS) phenomenon and involves strong interplay among small-scale turbulence, chemical reactions and molecular diffusion. Sub-grid scale combustion models must accurately represent these processes.

When the flame front is thinner than the smallest turbulent scale, the flame is corrugated by the turbulence and can be seen as an ensemble of thin, one-dimensional laminar flames (flamelets). This allows one to decouple turbulence from chemistry, with a significant reduction in computational effort. However, potentials and limitations of flamelets are not fully explored and understood. This work contributes to this understanding. Two models are identified, one based on an algebraic expression for the reaction rate of a progress variable and the assumption of fast chemistry, the other based on a database of unstrained flamelets in which reaction rates are stored and parametrised using a progress variable and its SGS variance, and their potentials are shown for a wide range of premixed combustion conditions of practical interest. The sensitivity to a number of model parameters and boundary conditions is explored to assess the robustness of these models. This work shows that the SGS variance of progress variable plays a crucial role in the SGS reaction rate modelling and cannot be obtained using a simple algebraic closure like that commonly used for a passive scalar. The use of strained flamelets to include the flame stretching effects is not required when the variance is obtained from its transport equation and the resolved turbulence contains predominant part of the turbulent kinetic energy. Thus, it seems that SGS closure using unstrained flamelets model is robust and adequate for wide range of turbulent premixed combustion conditions.

Table of contents

List of figures xvii

List of tables xxix

Nomenclature xxxi

1 Introduction 1

1.1 The role of turbulent combustion . . . 1
1.2 Modelling of turbulent premixed combustion . . . 3
1.3 Aims and objectives . . . 4
1.4 Outline . . . 4

2 Background on premixed combustion 7

2.1 Governing equations . . . 7
2.2 Essential parameters in premixed flames . . . 9
2.2.1 Progress variable . . . 9
2.2.2 Flame thickness . . . 9
2.2.3 Flame speed . . . 10
2.3 Turbulent premixed flames . . . 11
2.3.1 Turbulence-combustion interaction . . . 11
2.3.2 Combustion regimes . . . 12
2.4 Modelling for turbulent premixed combustion . . . 13
2.4.1 LES filtering . . . 15
2.4.2 Favre filtering . . . 16
2.4.3 Governing equations for LES . . . 16
2.4.4 Chemistry modelling . . . 17
2.4.5 Modelling for turbulent-flame interaction . . . 18
2.4.6 Laminar flamelets approach: range of validity and limitations . . . 24
2.5 Scalar dissipation rate modelling in turbulent premixed combustion . . . 26

2.5.1 SDR model for LES 28
2.6 Summary 29

3 Numerical modelling **31**
3.1 Residual stresses and common practices in LES 31
3.1.1 Eddy diffusivity models 31
3.1.2 One equation model for LES of premixed combustion 34
3.1.3 Relation between LES filter, grid spacing and numerical scheme . . . 34
3.1.4 Comparison with experiments 36
3.2 Discretisation 37
3.2.1 Numerical schemes 37
3.2.2 Solver 39
3.3 Filtered reaction rate modelling 39
3.3.1 Algebraic closure 40
3.3.2 Presumed PDF approaches 42
3.3.3 Estimation of sub-grid scale velocity 50
3.3.4 Dynamic formulations 52
3.3.5 Laminar flame computation 56
3.4 Mathematical model and equations summary 59

4 Validation cases **63**
4.1 Propane-air mixing 63
4.1.1 Computational model 63
4.1.2 Results 65
4.2 Piloted jet burner 68
4.2.1 Computational model 69
4.2.2 Cold flow results 71
4.3 Bluff body burner 73
4.3.1 Computational model 74
4.3.2 Cold flow results 75
4.4 Non piloted jet burner 76

5 Piloted flames - Algebraic closure **79**
5.1 Experimental Cases 79
5.2 Specific numerical detail 81
5.3 Results for static β_c 82
5.3.1 General flame features 83

5.3.2 Sensitivities to SGS velocity modelling . . . 85
5.3.3 Analysis of flame brush structure . . . 90
5.3.4 Analysis of SGS kinetic energy equation . . . 101
5.4 Assessment of dynamic procedure for β_c . . . 104
5.4.1 Flame structure . . . 104
5.4.2 The PDF of β_c . . . 111
5.5 Summary . . . 119

6 Piloted flames - Presumed PDF closures **121**
6.1 Specific numerical detail . . . 121
6.2 Filtered reaction rate . . . 122
6.3 Grid sensitivity . . . 123
6.4 Unstrained vs Strained Flamelets . . . 125
6.4.1 Major species comparison . . . 131
6.4.2 Minor species comparison . . . 134
6.5 Analysis of Da_Δ and Ka_Δ . . . 138
6.6 Comparison of static and dynamic β_c . . . 140
6.7 Summary . . . 140

7 Bluff body stabilised flame **143**
7.1 Experimental case . . . 144
7.2 Flame and recirculation region . . . 145
7.2.1 2% approach turbulence . . . 145
7.2.2 24% approach turbulence . . . 149
7.3 Post-flame region . . . 155
7.4 Implication of local Damköhler and Karlovitz numbers . . . 157
7.5 Species comparisons . . . 160
7.5.1 Sensitivity to choice of progress variable . . . 170
7.6 Analysis of β_c PDF . . . 172
7.7 Summary . . . 176

8 Non piloted jet flame **177**
8.1 Experimental case . . . 178
8.2 Numerical details . . . 179
8.3 Results . . . 181
8.3.1 Role of SGS velocity modelling . . . 181
8.3.2 Comparison of statistics . . . 184

8.3.3 Bimodal of radial velocity 187
8.3.4 Influence of numerical grid 191
8.3.5 Influence of bimodal PDF on statistics 193

9 Concluding remarks **199**
9.1 Summary and final considerations 199
9.2 Future work 203

References **205**

Appendix A Database **221**

List of figures

2.1 Typical behaviour of progress variable, θ, in freely propagating unstrained laminar premixed flame. 10

2.2 Regimes diagram for premixed turbulent combustion [180]. The subscript δ indicates that Karlovitz and Damköhler numbers are computed using the Zel'dovich thickness. 14

3.1 Comparison of different terms of Eq. (3.30) for increasing values of $u'^{+}_{\Delta} = u'_{\Delta}/s_L$, and for (a) $\Delta = 4\delta_{th}$ and (b) $\Delta = 8\delta_{th}$. 41

3.2 β-PDF of c, obtained using Eq. (3.34) for $\widetilde{c} = 0.01$ and $\sigma^2_{c,\mathrm{sgs}} = 0.0089$. Arrows indicate presence of very large values. The approximated PDF, obtained using Eq. (3.38), is shown with dashed line in the inset. 44

3.3 Isolines of $\widetilde{c}$, obtained using Eq. (3.33) (with c integrated instead of $\dot{W}$) and (3.38) (continuous lines), are shown on the plane $\widetilde{c}$-$\widetilde{g}$, where $\widetilde{g} = \sigma^2_{c,\mathrm{sgs}}/[\widetilde{c}(1-\widetilde{c})]$. Isolines obtained using Eq. (3.39) are also shown (dashed lines). 44

3.4 Scatter plot of computed $\sigma^2_{c,\mathrm{sgs}}$ and its modelled value using $\mathscr{A}\Delta^2|\nabla\widetilde{c}|^2$ with $\mathscr{A} = 1$ in the top row. The results for the revised model, $\mathscr{A}_1\left(\widetilde{c}\mathrm{Da}_\Delta + \Delta^2|\nabla\widetilde{c}|^2\right)$ with $\mathscr{A}_1 = 0.15$, are shown in the bottom row. The first and second columns are for two different grid sizes, of 1.5M and 4.2M cells, for F1 flame of [46] respectively. 49

3.5 Scatter plot of computed $\sigma^2_{c,\mathrm{sgs}}$ and its modelled value using $\mathscr{A}\Delta^2|\nabla\widetilde{c}|^2$ with $\mathscr{A} = 1$. 50

3.6 Comparisons of functions f_I and f_{II} in Eqs (3.64) and (3.65) respectively. The dashed line represents $f_I\mathscr{F}_b$, where $\mathscr{F}_b$ is the bridging function discussed in [61, 77, 79]. 55

3.7 Strained flamelet configuration. 56

3.8 Variation of consumption speed, s_c (normalised with the unstrained flamelet consumption speed, s_c^0), with characteristic strain rate for stoichiometric strained flamelets. The strain rate is estimated as $a \approx (|U_r| + |U_p|)/L$. Three particular values of strain rate are marked with circles. 57

3.9 Profiles of (a) axial velocity, U, and (b) progress variable, c, along the centreline for the three values of strain rate marked in Fig. 3.8. x_0 is the location at which $c = 0.5$. 57

3.10 Profiles of (a) reaction rate, $\dot{\omega}_c$, and (b) scalar dissipation rate, N_c, in c space for the three strain rates marked in Fig. 3.8. 58

3.11 Profiles of (a) major and (b) minor species mass fractions in c space for the three strain rates marked in Fig. 3.8. 58

3.12 Mass flux profiles in c space for the three strain rates marked in Fig. 3.8. The arrows at $c = 0$ and $c = 1$, and the corresponding labels, indicate the mass fluxes at the boundaries. 59

4.1 Sketch of the numerical domain used for the Sandia propane-air non-reacting case in [214]. 64

4.2 Mean axial velocity centreline profiles from LES, obtained using cases A (–·–), B (– –), C (——) and D (•••) of Table 4.2, are compared with experimental results [214] (symbols). 65

4.3 Radial profiles of mean (a) axial and (b) radial velocity from LES are compared with experimental results. Legend is as for Fig. 4.2. 66

4.4 Radial profiles of (a) axial and (b) radial velocity variance from LES are compared with experimental results (symbols). Legend is as for Fig. 4.2. . . . 66

4.5 Mixture-fraction half radius predictions from LES of case B (– –) and C (——) of table 4.2 are compared with experimental data [214] (symbols). 67

4.6 A schematic of (a) the experimental [46] and (b) computational setup of piloted stoichiometric methane-air Bunsen flames. 68

4.7 Numerical grid used for piloted flame case [46] for 1.5M case. An axial slice through the mid-plane ($z = 0$) is shown in (a) for a region of $0 \leq x \leq 15D$ and $0 \leq y \leq 5D$. The grid distribution in a radial slice of size $y \times z = 5D \times 5D$ is shown for axial locations of (b) $x = 0$, (c) $4.5D$ and (d) $10.5D$. 70

4.8 Centerline profiles of (a) mean normalised axial velocity, $\langle U \rangle / U_b$, and (b) turbulent kinetic energy, $\langle k \rangle / U_b^2$, computed using LES on 4.2M grid for cases B (– –), C (–·–), SM1 (+), SM2 (×) and SC (——) of Table 4.2 are compared with experimental results (circles) for the F2 cold flow configuration [46]. . . 71

4.9 Comparison of measured [46] (symbols) and computed (lines) normalised mean axial velocity and turbulent kinetic energy in cold flow of flame F2. The radial variations are shown for 5 axial locations and two numerical grids, 1.5M (solid line) and 4.2M (dotted line). 72
4.10 A sketch of (a) the experimental burner configuration and (b) its numerical model. 73
4.11 Computational mesh in the mid-plane ($z = 0$) around the bluff body for (a) 1.8M and (b) 2.2M grids. An enlargement of the 2.2M grid is also shown in (c). 74
4.12 The variation of computed (lines) and measured [176] (symbols) $\langle U \rangle / U_{\text{ref}}$ along the centreline for cold flow with (a) 2% and (b) 24% TI. The results are shown for both 1.8M (——) and 2.2M (——) grid. The sensitivity to wall functions is shown for 1.8M grid (– –). 76

5.1 Combustion regime diagram showing conditions of flames F1, F2 and F3. . . 80
5.2 The spatial variation of normalised filtered temperature, $\widetilde{T}^+$, field in $z = 0$ plane for the three flames, obtained using algebraic model for $\overline{\dot{\omega}}$ with $\beta_c = 7.5$. The result from 4.2M grid is shown only for F2 to depict the grid influence. . 83
5.3 The spatial variation of averaged and normalised temperature, $\langle \widetilde{T}^+ \rangle$, in three flames, obtained using algebraic model for $\overline{\dot{\omega}}$ with $\beta_c = 7.5$. 84
5.4 Histogram of normalised filter width, Δ^+, for (a) 1.5M and (b) 4.2M numerical grids. Different domain sizes have been used: whole computational domain (▬), $0 \leq x \leq 20D$, $0 \leq r \leq 10D$ (▬), and $0 \leq x \leq 11D$, $0 \leq r \leq 2D$ (▬). . 85
5.5 Colour map of normalised filtered reaction rate, $\overline{\dot{\omega}}^+$, for flame F2, computed for various u'_Δ models. 86
5.6 Colour map of normalised mean reaction rate, $\langle \overline{\dot{\omega}}^+ \rangle$, for flame F2, computed for various u'_Δ models. 87
5.7 Influence of SGS velocity modelling on averaged streamwise velocity, $\langle U \rangle$, and turbulent kinetic energy, $\langle k \rangle$, obtained using algebraic model for $\overline{\dot{\omega}}$ with $\beta_c = 7.5$. Symbols (○) are experimental results [46], lines are from simulations using Eq. 3.50 (–·–), Eq. 3.51 (——), Eq. 3.52 (•••) and Eq. 3.55 (– –). 88
5.8 Influence of SGS velocity modelling on averaged fuel mass fraction and normalised temperature, obtained using algebraic model for $\overline{\dot{\omega}}$ with $\beta_c = 7.5$. The legend is as in Fig. 5.7. 89
5.9 Comparison of radial variation of normalised axial velocity, $\langle U \rangle / U_b$, in experiments [46] (symbols) and simulations (——) using Eqs. (2.19), (2.22) (with $\beta_c = 7.5$) and (3.51) on 1.5M grid. Results obtained using 4.2M grid (•••) are shown only for F2. Previous RANS [122] (– –) and LES [240] (–·–) results are also shown for comparison. 91

5.10 Comparison of measured [46] (○ ○ ○) and computed (——) normalised mean TKE, $\langle k \rangle / k_0$, variation with r/D, obtained using algebraic model for $\overline{\dot{\omega}}$ with $\beta_c = 7.5$. The computational results are for the 1.5M grid. Results of the 4.2M grid (•••) are shown only for F2. Previous results [53] (△), [122] (– –) and [240] (– · –) are shown for comparison. 92

5.11 The mean fuel mass fraction computed on the 1.5M grid (——), obtained using algebraic model for $\overline{\dot{\omega}}$ with $\beta_c = 7.5$, is compared to the measurements (○ ○ ○). Previous results [53] (△), [56] (□), [122] (– –) and [240] (– · –) are shown for comparison. 93

5.12 The mean normalised temperature computed on the 1.5M grid (——), obtained using algebraic model for $\overline{\dot{\omega}}$ with $\beta_c = 7.5$, is compared to the measurements (○ ○ ○). Previous results [53] (△), [56] (□), [122] (– –) and [240] (– · –) are shown for comparison. 94

5.13 Comparison of mean mass fraction of O_2: experimental data (○ ○ ○), results obtained using algebraic model for $\overline{\dot{\omega}}$ with $\beta_c = 7.5$ (——), [53] (△), [56] (□), and [122] (– –). The dash-dotted line (– · –) for F1 at $x/D = 2.5$, 8.5 and 10.5 shows the value obtained without using Eq. (3.70). 96

5.14 Comparison of mean mass fraction of H_2O: experimental data (○ ○ ○), results obtained using algebraic model for $\overline{\dot{\omega}}$ with $\beta_c = 7.5$ (——), [53] (△), [56] (□), [122] (– –) and [240] (– · –). 97

5.15 Comparison of mean mass fraction of CO_2: experimental data (○ ○ ○), results obtained using algebraic model for $\overline{\dot{\omega}}$ with $\beta_c = 7.5$ (——), [53] (△), [56] (□), and [122] (– –). 98

5.16 Comparison of mean mass fraction of OH: experimental data (○ ○ ○), results obtained using algebraic model for $\overline{\dot{\omega}}$ with $\beta_c = 7.5$ (——), [56] (□) and [122] (– –). 99

5.17 Comparison of mean mass fraction of H_2: experimental data (○ ○ ○), results obtained using algebraic model for $\overline{\dot{\omega}}$ with $\beta_c = 7.5$ (——), and [122] (– –). . . 100

5.18 Comparison of mean mass fraction of CO_2: experimental data (○ ○ ○), results obtained using algebraic model for $\overline{\dot{\omega}}$ with $\beta_c = 7.5$ (——), [53] (△), [56] (□), and [122] (– –). 101

5.19 Flame brush thicknesses, δ_t (mm), computed here using the radial variation of averaged temperature ($\diamond$) and fuel mass fraction ($\square$) reported in [46] are compared to δ_t values reported ($\circ$) in [46] (top row). The values of δ_t obtained from LES using algebraic model for $\overline{\dot{\omega}}$ with $\beta_c = 7.5$ and SGS velocity model in Eq. (3.51) (+) and k_{sgs} transport equation ($\times$) on 1.5M grid are compared with experimental data [46] ($\diamond$) and past RANS [122] ($\bullet$) and LES [240] ($\triangle$) studies in the bottom row. 102

5.20 Radial profiles of mean normalised velocity, $\langle U \rangle / U_b$, normalised TKE, $\langle k \rangle / k_0$, methane mass fraction, $\langle CH_4 \rangle$ and normalised temperature, $\langle T^+ \rangle$, obtained using algebraic model for $\overline{\dot{\omega}}$ with $\beta_c = 7.5$ and models K1 (–·–), K2 (––) and K3 (•••) of table 5.1, are compared with LES results obtained using Eqs. (2.22) and (3.51) (——) and with experimental data [46] (symbols) for flame F2 and 1.5M grid. 103

5.21 The spatial variation of mean progress variable field for flame F1 obtained using algebraic model for $\overline{\dot{\omega}}$ with static and dynamic approaches for β_c. This comparison is shown for both 1.5M and 4.2M grids. 105

5.22 Comparison of measured [46] (symbols) and computed (lines) radial variation of normalised axial velocity, $\langle U \rangle / U_b$, obtained using algebraic model for $\overline{\dot{\omega}}$ with dynamic (——, •••) and static (——, •••) β_c models for flames F1 and F3. The results are shown for 1.5M (solid lines) and 4.2M (dotted) grids. 106

5.23 Comparison of measured [46] (symbols) and computed (lines) radial variation of normalised mean turbulent kinetic energy, $\langle k \rangle / k_0$. The legend is as in Fig. 5.22. 108

5.24 Comparison of measured [46] (symbols) and computed (lines) radial variation of mean fuel mass fraction. The legend is as in Fig. 5.22. The dash-dotted line is for the power-law based model in Eqs. (3.60) and (3.61) for 4.2M grid. . . 109

5.25 Measured [46] (symbols) and computed (lines) radial variations of normalised mean temperature are compared above. The legend is as in Fig. 5.22. 110

5.26 Comparison of measured [46] (symbols) and computed (lines) mean O_2 mass fractions. The legend is as in Fig. 5.22. 112

5.27 Comparison of measured [46] (symbols) and computed (lines) mean H_2O mass fractions. The legend is as in Fig. 5.22. 113

5.28 Comparison of measured [46] (symbols) and computed (lines) mean CO_2 mass fractions. The legend is as in Fig. 5.22. 114

5.29 Comparison of measured [46] (symbols) and computed (lines) mean OH mass fractions. The legend is as in Fig. 5.22. 115

5.30 Comparison of measured [46] (symbols) and computed (lines) mean H_2 mass fractions. The legend is as in Fig. 5.22. 116

5.31 Comparison of measured [46] (symbols) and computed (lines) mean CO mass fractions. The legend is as in Fig. 5.22. 117

5.32 The PDF of β_c obtained from LES of flames (a) F1 and (b) F3 using algebraic model for $\overline{\dot{\omega}}$ with dynamic computation of β_c with 1.5M grid. The average value and the lower limit imposed by Eq. (3.59) are also shown. 118

5.33 The recomputed (◇) and LES values of flame brush thickness, δ_t, obtained using algebraic model for $\overline{\dot{\omega}}$ with dynamic computation of β_c, are compared for various cases. 118

6.1 Typical variation of normalised filtered reaction rate in unstrained and strained flamelets. 122

6.2 Comparison of measured [46] (symbols) and computed (lines) radial variation of $\langle U \rangle / U_b$ for F1 and F3 flames. Unstrained flamelet result is shown for 1.5M (——) and 4.2M (•••) grids, and strained flamelets result is shown for 1.5M (– · –) and 4.2M (– –) grids. The results of 4.2M grid is shown only for the F1 flame. 124

6.3 Comparison of measured [46] (symbols) and computed (lines) radial variation of $\langle k \rangle / k_0$ for F1 and F3 flames. The legend is as in Fig. 6.2. 125

6.4 Comparison of measured [46] (○ ○ ○) and computed mean fuel mass fraction. The computational results are shown for the 1.5M grid using unstrained (——) and strained (– · –) flamelets. Previous results [53] (△), [56] (□), [122] (– –) and [240] (•••) are shown for comparison. 126

6.5 The normalised mean temperature computed on the 1.5M grid using unstrained (——) and strained (– · –) flamelets is compared to the measurements [46] (○ ○ ○). Previous results [53] (△), [56] (□), [122] (– –) and [240] (•••) are shown for comparison. 127

6.6 Spatial variation of $\log(100\overline{\dot{\omega}}^+)$ in flame F3 obtained at an arbitrarily chosen time, $t1$, using (a) unstrained and (b) strained flamelets with 1.5M grid. These results at 20 ms later are shown in (c) and (d). The contours are shown for $\overline{\dot{\omega}}^+ > 0.01$. 129

6.7 Spatial variation of $\log(100\overline{\dot{\omega}}^+)$ in flame F1 obtained at an arbitrarily chosen time, $t1$, using (a) unstrained and (b) strained flamelets with 1.5M grid. These results at 20 ms later are shown in (c) and (d). The contours are shown for $\overline{\dot{\omega}}^+ > 0.01$. 130

6.8 Comparison of measured [46] and computed H_2O mass fraction. The legend is as in Fig. 6.4. 131

6.9 Comparison of measured [46] and computed O_2 mass fraction. The legend is as in Fig. 6.4. 132

6.10 Comparison of measured [46] and computed CO_2 mass fraction. The legend is as in Fig. 6.4. 133

6.11 Comparison of measured [46] and computed OH mass fraction. The legend is as in Fig. 6.4. 135

6.12 Comparison of measured [46] and computed H_2 mass fraction. The legend is as in Fig. 6.4. 136

6.13 Comparison of measured [46] and computed H_2 mass fraction. The legend is as in Fig. 6.4. 137

6.14 PDFs of Da_Δ and Ka_Δ from flames F1 (top row) and F3 (bottom row). The results are shown for unstrained (——) and strained (– · –) flamelets. 138

6.15 The PDF of β_c from flame (a) F1 and (b) F3 obtained using unstrained (——) and strained (– · –) flamelets with 1.5M grid. 139

6.16 Comparison of measured [46] (○ ○ ○) and computed mean fuel mass fraction. The computational results are shown for the 1.5M grid using unstrained flamelet model with dynamic (——) and static (– –) formulation for β_c. 141

7.1 Histograms of $\Delta^+ = \Delta/\delta_{th}$ for (a) 1.8M and (b) 2.2M grids are shown for the combustor region $0 \leq x/D \leq 6$ and a fraction of it for $r/D < 0.5$. 144

7.2 Stream lines of (a) filtered and (b) averaged velocity fields along with contours of (filtered and averaged) $\log_{10}(1000\,\overline{\dot{\omega}}^+)$, where $\overline{\dot{\omega}}^+ = \overline{\dot{\omega}}\delta_{th}/(\rho_u s_L)$. The results are on the mid-plane for unstrained flamelets model and 2% TI. The contour of $\log_{10}(1000\,Da_\Delta)$ is shown in (c). The three regime regions, R1, R2 and R3, are separated in the figures using dashed lines. 146

7.3 Centreline variation of (a) $\langle U \rangle / U_{\text{ref}}$, (b) $\langle T^+ \rangle$, and (c) $\sqrt{\sigma_T^2}$ for 2% TI. The results with algebraic model on 1.8M (– –) and 2.2M (——) grids and with unstrained flamelets model on 1.8M (– –) and 2.2M (——) grids are compared with experimental data [176, 178] (symbols). 147

7.4 Radial variation of $\langle T^+ \rangle$ and $\sqrt{\sigma_T^2}$ for 2% TI case with algebraic model using 1.8M (– –) and 2.2M (——) grids and with unstrained flamelets model using 1.8M (– –) and 2.2M (——) grids are compared with experimental data [176, 178] (symbols). 149

7.5 Radial profiles of (a) rms and (b) mean velocities, obtained using the algebraic model on 1.8M grid (– –) and unstrained flamelet model on 2.2M grid (——), are compared with experimental data (symbols) for 24% TI at $x/D = 0$. . . . 150

7.6 Contours of filtered normalised reaction rate $\overline{\dot{\omega}}^{+} = \overline{\dot{\omega}}\delta_{th}/(\rho_u s_L)$ at an arbitrary chosen time. The results are on the mid-plane for unstrained flamelet and algebraic models with 24% TI. Isolines having $\overline{\dot{\omega}}^{+} = 0.1$ are also shown. . . 152

7.7 Centreline variation of (a) $\langle U \rangle / U_{\text{ref}}$ and (b) $\langle T^{+} \rangle$ obtained with algebraic model using 1.8M (——) grid, and with unstrained flamelet model using 2.2M (——) grid are compared to experimental data [176, 178] (symbols) for 24% TI case. The influence of $\langle \sigma^2_{T,\text{SGS}} \rangle$ on $\langle \overline{T}^{+} \rangle$ is shown for the unstrained flamelet (– · –) and algebraic (– · –) models. 153

7.8 Scatter plots of $\langle \widetilde{c} \rangle$ and $\langle \overline{c} \rangle$ for unstrained flamelet model with 24% TI. The Reynolds average is obtained using Eq. (3.18) (a) without and (b) with SGS variance, $\langle \sigma^2_{c,\text{sgs}} \rangle$. 154

7.9 Scatter plot of mean progress variable and total variance, $\langle \sigma^2_c \rangle$ (sum of resolved and SGS parts), for unstrained flamelet model with 24% TI. Colours represent the axial locations, x/D, for the data. The maximum possible variance, $\langle \widetilde{c} \rangle (1 - \langle \widetilde{c} \rangle)$ is also shown (– –). 155

7.10 Radial variation of $\langle U \rangle / U_{\text{ref}}$ and $\langle V_r \rangle / U_{\text{ref}}$, obtained with algebraic model using 1.8M (– –) grid and with unstrained flamelets model using 2.2M (——) grid are compared with measurements [176, 178] (symbols) for 24% TI within the recirculation region. 156

7.11 Radial variation of normalised averaged temperature and its rms, obtained using the algebraic model with 1.8M (——) grid and unstrained flamelet model with 2.2M (——) grid are compared with measurements [168, 169, 176, 178] (symbols) for 24% TI case within the recirculation region. The influence of $\langle \sigma^2_{T,\text{sgs}} \rangle$ on $\langle \overline{T}^{+} \rangle$ is shown for the unstrained flamelet (– · –) and algebraic (– · –) models. 157

7.12 Radial variation of $\langle U \rangle / U_{\text{ref}}$ and $\langle V_r \rangle / U_{\text{ref}}$ are compared with measurements [176, 178] for 24% TI in the post-flame region. The legend is as in Fig. 7.10. . . . 158

7.13 Radial variation of mean normalised temperature and its rms are compared with measurements [168, 169] for 24% TI in the post-flame region. The legend is as in Fig. 7.11. 159

7.14 PDF of (a) SGS Damköhler, Da_Δ, and (b) Karlovitz, Ka_Δ, numbers in the combusting region are shown for the unstrained flamelet model on 2.2M grid with 2% (–·–) and 24% (——) TI, and algebraic model on 1.8M grid with 24% TI (––). 160

7.15 PDFs of $\widetilde{c}$ from LES using algebraic model on 1.8M grid (——) at $x/D = 0.6$ (top) and $x/D = 2.0$ (bottom) and for three radial positions along the shear are compared with β-PDFs computed using $\langle\widetilde{c}\rangle$ and resolved variance $\langle\sigma^2_{c,\mathrm{res}}\rangle = \langle\widetilde{c}^2\rangle - \langle\widetilde{c}\rangle^2$ (––), and using $\langle\widetilde{c}\rangle$ and mean SGS variance, $\langle\sigma^2_{c,\mathrm{sgs}}\rangle$ (–·–). 161

7.16 Radial profiles of CH_4 mass fraction, obtained using the algebraic model with 1.8M grid (––) and the unstrained flamelet model on 2.2M grid using Eq. (7.2) (——), are compared with experimental data [168, 169] (symbols) for (a) six axial locations within the recirculation region and (b) three locations in the post-flame region. Results obtained using Eq. (7.4) (–·–) are also shown. . . 162

7.17 Radial profiles of O_2 mass fraction are compared with experimental data [168, 169] for six axial locations within the recirculation region (top) and three locations in the post-flame region (bottom). The legend is as in Fig. 7.16. . . 164

7.18 Radial profiles of CO_2 mass fraction are compared with experimental data [168, 169] for six axial locations within the recirculation region (top) and three locations in the post-flame region (bottom). The legend is as in Fig. 7.16. . . 165

7.19 Radial profiles of H_2O mass fraction are compared with experimental data [168, 169] for six axial locations within the recirculation region (top) and three locations in the post-flame region (bottom). The legend is as in Fig. 7.16. . . 166

7.20 Radial profiles of CO mass fraction are compared with experimental data [168, 169] for six axial locations within the recirculation region (top) and three locations in the post-flame region (bottom). The legend is as in Fig. 7.16. . . 167

7.21 Radial profiles of H_2 mass fraction are compared with experimental data [168, 169] for six axial locations within the recirculation region (top) and three locations in the post-flame region (bottom). The legend is as in Fig. 7.16. . . 168

7.22 Radial profiles of OH mass fraction are compared with experimental data [168, 169] for six axial locations within the recirculation region (top) and three locations in the post-flame region (bottom). The legend is as in Fig. 7.16. . . 169

7.23 Mass fractions variation of major and minor species using different progress variable definitions for a stoichiometric methane-air flamelet. 170

7.24 Enlargement of OH mass fraction in Fig. 7.23 on the burnt side using different definitions of c: $c = 1 - Y_{\mathrm{CH4}}/Y^u_{\mathrm{CH_4}}$ (——), $c = Y_{\mathrm{H_2O}}/Y^b_{\mathrm{H_2O}}$ (––) and $c = (Y_{\mathrm{CO_2}} + Y_{\mathrm{CO}})/(Y^b_{\mathrm{CO_2}} + Y^b_{\mathrm{CO}})$ (–·–). 171

7.25 Radial profiles of CH_4 mass fraction, obtained using the unstrained flamelets model with 2.2M grid using Eq. (7.2) for three different definition of c, $c = 1 - Y_{CH4}/Y^u_{CH_4}$ (——), $c = Y_{H_2O}/Y^b_{H_2O}$ (– –) and $c = (Y_{CO_2} + Y_{CO})/(Y^b_{CO_2} + Y^b_{CO})$ (– · –), are compared with experimental data [168, 169] (symbols) for six axial locations. 172
7.26 Radial profiles of O_2 mass fraction from LES, obtained using three different definitions of the progress variable, are compared with experimental data [168, 169] for six axial locations. The legend is as for Fig. 7.25. 173
7.27 Radial profiles of CO_2 mass fraction from LES, obtained using three different definitions of the progress variable, are compared with experimental data [168, 169] for six axial locations. The legend is as for Fig. 7.25. 173
7.28 Radial profiles of H_2O mass fraction from LES, obtained using three different definitions of the progress variable, are compared with experimental data [168, 169] for six axial locations. The legend is as for Fig. 7.25. 174
7.29 Radial profiles of CO mass fraction from LES, obtained using three different definitions of the progress variable, are compared with experimental data [168, 169] for six axial locations. The legend is as for Fig. 7.25. 174
7.30 Radial profiles of H_2 mass fraction from LES, obtained using three different definitions of the progress variable, are compared with experimental data [168, 169] for six axial locations. The legend is as for Fig. 7.25. 175
7.31 Radial profiles of OH mass fraction from LES, obtained using three different definitions of the progress variable, are compared with experimental data [168, 169] for six axial locations. The legend is as for Fig. 7.25. 175
7.32 PDF of β_c for algebraic (– –) and unstrained flamelet (——) models and 24% TI. The realisability limit, $2/(2C_m - 1)$, is also marked. 176

8.1 A direct photograph (a) and a schematic (b) of the lean propane-air flame of [76]. 178
8.2 Numerical domain for the preliminary RANS. 181
8.3 Profiles of (a) mean axial velocity and (b) mean temperature at the jet exit, computed using RANS. 181
8.4 Variation of $\widetilde{\varepsilon}^+ = \widetilde{\varepsilon}\delta_{th}/s_L$, with $u'^+_\Delta = u'_\Delta/s_L$, for $\Delta/\delta_{th} = 1.4$. 182
8.5 Comparison of measured (symbols) and computed axial velocity along the centreline; Eq. 3.50 (dashed line), Eq. 3.51 (continuos line) and Eq. 3.56 (dash-dotted line). 184
8.6 Scatter plot of normalised sub-grid SDR versus progress variable, obtained using models of Eq. (3.50) (Lilly), Eq. (3.51) (Pope) and Eq. (3.56) (Colin *et al.*) for u'_Δ. 185

8.7 Contours of $\langle u'^*_\Delta \rangle / \langle u'^*_\Delta \rangle_{\max}$ in the mid-plane. The values of $\langle u'^*_\Delta \rangle_{\max}$ are 0.15, 0.80 and 2.03 m/s respectively for Lilly, Pope and Colin *et al.* models. 185

8.8 Contours of (a) filtered, $\widetilde{U}$, and (b) mean, $\langle U \rangle$, axial velocity, obtained using Eq. (3.51) for SGS velocity. The mean progress variable isoline $\langle c \rangle = 0.5$, is also shown (black line). 186

8.9 Comparison of measured and computed centreline variation of radial rms velocity. The legend is as in Fig. 8.5. 187

8.10 Radial variations of mean and rms velocities in axial and radial directions. The rms of tangential velocity is also shown. The legend is as in Fig. 8.5. 188

8.11 Comparison of measured and computed Reynolds- and Favre-averaged progress variable variation. The legend is as in Fig. 8.5. Error bars are also shown. . . 189

8.12 Resolved and SGS variance of the progress variable. The legend is as in Fig. 8.5 and the dotted line is for 23M grid. 190

8.13 The computed isolines of $\langle \widetilde{c} \rangle = 0.5$ are compared to the experimental result in (a) along with the uncertainty for the measurements. A comparison of flame brush thickness is shown in (b). The legend is as in Fig. 8.5. The dotted line is for 23M grid. 191

8.14 Normalised histograms of [76] for three velocity components at $x = 50$ mm for various radial locations. 192

8.15 Normalised histograms from LES for the three components of velocity at $x = 50$ mm and $r = 10.2$ mm for various values of δ_{samp}. The legend is as in Fig. 8.5. The result for 23M grid (•••) is also shown for v_r for comparison. . . 193

8.16 RMS and SGS velocity profiles for 5.4M (continuous line) and 23M (dotted line) grids are compared to the experimental data (symbols) at $x = 50$ mm. . . 194

8.17 The PDF of (a) measured and (b) computed radial velocity component v_r at $x = 50$ mm. The modelled values using two Gaussians are shown in (b) for the mean and variance of unburnt ($\widetilde{c} \leq 0.05$) and burnt ($\widetilde{c} \geq 0.95$) mixtures in LES data. 195

8.18 The PDF (continuous line) obtained with samples collected from a single numerical cell ($\delta_{\text{samp}} < \Delta$) at $x = 50$ mm and $r = 10.2$ mm is compared to a Gaussian model with the same mean and standard deviation of $\sigma_L + \sigma_R$ (dashed line). 195

8.19 Radial variation of measured (open circle) and computed (lines) rms of radial velocity at $x = 50$ mm. Results are shown for 5.4M (left) and 23M (right) grids. The effect of δ_{samp} is shown for $\delta_{\text{samp}} < \Delta$ (continuous line), $\delta_{\text{samp}} = 3$ mm for 5.4M or 2.4 mm for 23M grids (continuous line with squares); $\delta_{\text{samp}} = 6$ mm for 5.4M or 5 mm for 23M grids (continuous line with triangles). The dashed lines represent the corresponding curves when the $v'_{r,\Delta}$ is included. 196

List of tables

4.1 Geometrical and physical parameters for the Sandia propane-air non-reacting case in [214]. 64
4.2 List of simulations for the Sandia propane-air non-reacting case in [214]. . . . 65
4.3 Geometrical and physical parameters for the F2 cold case in [46]. 69
4.4 Simulation parameters for the LES of F2 cold flow configuration in [46]. C_s is the Smagorinsky constant appearing in Eq. (3.3). 71
4.5 Geometrical and physical parameters for the bluff-body configuration [176–178]. 75

5.1 SGS kinetic energy models used for testing. 103

8.1 Values of β_c' obtained using the SGS velocity models in Eqs. (3.50), (3.51) and (3.56). 183

A.1 Simulations list for the piloted flames case from Chen *et al.* [46] - algebraic model (AM). 222
A.2 Simulations list for the piloted flames case from Chen *et al.* [46] - unstrained flamelets model (UFM). 223
A.3 Simulations list for the piloted flames case from Chen *et al.* [46] - strained flamelets model (SFM). 224
A.4 Simulations list for the bluff body case [168, 169]. 225
A.5 Simulations list for the low-turbulence flame case from Furukawa *et al.* [76]. . 226

Nomenclature

Roman Symbols

c	Progress or regress variable
C_m	Bray-model constant
C_p	Heat capacity at constant pressure
C_s	Smagorinsky constant
D	Diameter, total derivative
$\mathscr{D}$	Diffusivity
h	Total enthalpy (sensible + chemical)
Δh_f^0	Enthalpy of formation
k	Turbulent kinetic energy
k_r	Residual kinetic energy
k_{sgs}	Sub-grid scale kinetic energy
L_r	Length of recirculation zone
N_c	Scalar dissipation rate of c
p	Pressure
r	Radial coordinate
R_0	Universal constant of ideal gases
s_L	Laminar flame speed

s_T	Turbulent flame speed
S_{ij}	Strain tensor
t	Time
U	Axial velocity
$\mathbf{u}$	Velocity vector
u'	Root mean square axial velocity
u'_Δ	Sub-grid scale velocity
$\mathcal{V}$	Volume
v'_r	Root mean square radial velocity
v'_t	Root mean square tangential velocity
V_r	Radial velocity
V_t	Tangential velocity
$\dot{W}$	Reaction rate in $[\mathrm{s}^{-1}]$
W	Molecular weight
x, y, z	Spatial coordinates
Y_k	Mass fraction of species k
Z	Passive marker or normalised mixture fraction

Non-dimensional Parameters

Da	Damköhler number
Ka	Karlovitz number
Le	Lewis number
Re	Reynolds number
Re_T	Turbulent Reynolds number
Sc_T	Turbulent Schmidt number

Greek Symbols

α	Fractal model exponent
Δ	Filter width
δ	Zel'dovich flame thickness
δ_L^0	Laminar flame thickness
δ_t	Flame brush
δ_{samp}	Sampling width
δ_{th}	Thermal flame thickness
$\dot{\omega}$	Reaction rate in $[\text{Kg}\,\text{m}^{-3}\,\text{s}^{-1}]$
η_k	Kolmogorov's scale
Λ	Integral length scale
λ	Thermal diffusivity
μ	Dynamic viscosity
μ_T	Dynamic residual eddy-viscosity
ν_T	Kinematic residual eddy-viscosity
ϕ	Equivalence ratio
Π	Pressure dilatation term in k_{sgs} transport equation
ρ	Density
σ	Standard deviation
σ_c^2	Total variance of c
$\sigma_{c,\text{res}}^2$	Resolved variance of c
$\sigma_{c,\text{sgs}}^2$	Sub-grid variance of c
τ	Heat release parameter
τ_{ij}^R	Residual stress tensor

τ_{ij}^{r} Anisotropic part of residual-stress tensor

τ_{ij} Stress tensor

ε Dissipation

$\widetilde{\varepsilon}_c$ Sub-grid scale scalar dissipation rate of c

ξ Mixture fraction

Superscripts

Φ' Reynolds residual of Φ

Φ'' Favre residual of Φ

Φ^{+} Normalised Φ

Subscripts

Δ Sub-grid scale

b Fully burnt condition

f Fuel

L Laminar

u Fully unburnt condition

sgs Sub-grid scale

mix Mixture

Other Symbols

$\langle\Phi\rangle$ Reynolds average or Favre average of Φ

$\overline{\Phi}$ Filtered Φ

$\widehat{\Phi}$ Test-filtered Φ

$\widetilde{\Phi}$ Favre-filtered Φ

Acronyms / Abbreviations

CFD Computational fluid dynamics

CFL Courant-Friedrichs-Lewy number

DNS Direct numerical simulation

LES Large eddy simulation

LHS Left hand side

PDF Probability density function

RANS Reynolds averaged Navier-Stokes

RHS Right hand side

SDR Scalar dissipation rate

SGS Sub-grid scale

TI Turbulent intensity

TKE Turbulent kinetic energy

URANS Unsteady-RANS

Chapter 1

Introduction

1.1 The role of turbulent combustion

The world's energy demand is increasing at a rate of about 2% p.a., and this demand is estimated to have increased to 37% by 2040 [14]. An investment of around 900 billion dollars per year in the energy sector is needed by 2030 to meet this projected energy demand. The BP 2014 annual report shows that 87% of the total energy demand is met by fossil fuels and that this percentage has remained almost unaltered in the last decade, while renewable energies are growing in place of nuclear energy, which faces an uncertain future. For this reason one can expect that combustion will remain as the main source of energy for several decades. Reserves of fossil fuels, specifically coal, oil and gas, amount in fact to 892 billion tonnes, 1688 million barrels and 186 trillion cubic meters respectively, and are estimated to run out in 113, 53 and 55 years respectively, using the current rates of supply. The recent growth in the North American oil supply also helps to maintain a stability. The total fossil fuel energy supply is divided almost equivalently between the fossil sources above, with low-carbon sources to take the place of coal by 2040 [14]. The choice of a particular fuel depends on the particular requirement in terms of total energy, power, emissions etc., with applications ranging from power generation for stationary and mobile power plants to the transportation sector. However, among the fossil fuels, the use of natural gas is seeing the fastest growth, also encouraged by increasing flexibility in the global trade of liquefied natural gas. In contrast to oil, gas production is increasing almost everywhere, and is expected to become the largest fuel source by 2030. This is also because future coal use is constrained by measures to reduce emissions, despite it is having the biggest reserves [14].

Due to the continuing dominance of combustion in meeting the world's energy demand, concern over emissions has recently been heightened. Emissions can be categorised in 'greenhouse' gases and air pollution gases. The first category involves mainly CO_2, and to a lesser extent

N_2O and CH_4, and takes this name because these gases contribute to the so called 'greenhouse' effect. The following paragraphs report data from the 2014 BP annual report and world energy investment outlook [14]. On the current energy path, CO_2 emissions are expected to contribute to the predicted long-term global increase in temperature of 3.6°, and the global objectives are to restrict this rise to 2°. Since CO_2 is a main combustion product, it is proportional to the amount of fuel used; thus its emissions can be reduced only with fuel economy improvements. In Europe, average emission targets exist of 130 g/Km for new passengers cars, and 175 g/Km for light commercial vehicles, to be reduced to 95 g/Km and 147 g/Km respectively by 2020. In the US, greenhouse gas reduction target is of 30%, fixed for 2016. Other countries are also active in producing emission reduction policies, including Japan and South Korea. The development of technologically advanced and more efficient combustion devices assumes a fundamental role in this picture. As CO_2 emissions are proportional to the amount of fuel used, increased efficiency will allow to energy demands to be met with less fuel, and thus less emissions.

Different considerations exist for air pollution. Air pollution involves emissions of toxic, intermediate combustion species, mainly NO_x and CO, but also particulate matter, HCHO and other hydrocarbons. Regulations exist for both the energy production and transportation sector, and depend on the weight of the machine. The current European standard is the Euro 6, while in the US emissions standards are controlled by the EPA, which has adopted the California emissions standards. Other standards exist in Japan and South Korea. The production of intermediate species is intrinsically related to the completeness, and thus the efficiency, of the the combustion process. In this scenario increasingly efficient, environmental-friendly combustion devices are needed to meet both energy demand and pollution regulations. Modern engines can operate in two main different modes: non-premixed combustion, in which fuel and oxidiser enter the combustion chamber separately, and premixed combustion, in which reactants are homogeneously mixed before being burned. The combustion in both cases is generally turbulent, as turbulence enhances the mixing between fuel and oxidiser, resulting in higher efficiencies.

Due to concern for the environment, of these two combustion modes premixed combustion has recently captured industry interest, as high efficiency and low emissions can be achieved simultaneously. In fact, in homogenous mixtures, the nature of the reactants controls the thermo-chemistry of the process and hence the maximum temperature attainable. Since emissions of CO and NO_x can be seen proportional to the maximum temperature attainable [233], premixed combustion can effectively control the level of emissions. The maximum temperature of the system can be reduced by making the reactants composition lean, i.e. with an excess of oxidiser. However, lean premixed combustion is prone to instabilities, thus additional effort is required

to make a system operate in this condition. Moreover, in practical combustors the reactants are never fully premixed because the time scales of the mixing are usually larger than reactants resident time, and by measures taken to avoid potential flashbacks. The combustion systems operate in between turbulent premixed and non-premixed modes, a condition which is referred to as partially premixed combustion, posing additional challenges.

For all of these reasons, the development of modern, advanced lean premixed combustion devices plays a key role in the whole energy sector, and its research is a priority for short and long term goals.

1.2 Modelling of turbulent premixed combustion

Computational Fluid Dynamics (CFD) is quickly assuming the role of a complementary tool for the design of modern, efficient and environmentally-friendly combustion devices. Direct Numerical Simulation (DNS) for combustion is still unaffordable for complex geometries involving practical flows and is used as an investigation tool to gather insight for development of closures for Reynolds Averaged Navier-Stokes (RANS) and Large Eddy Simulation (LES) methodologies. These methodologies will be discussed in detail in later chapters. RANS and unsteady-RANS (URANS) techniques are limited in capturing highly unsteady phenomena such as extinctions and blow-off, which are of high interest to industry. With the advent of high-performing computers, LES is becoming attractive as it can capture transient phenomena, but the computational cost can be quite high if the closures involved with this methodology are not robust in mimicking the relevant physics. The LES methodology and the associated modelling are described in a number of earlier studies for non-reacting (for example [196]) and reacting (for example [191]) flows, and it is seen here as a higher fidelity approach compared to URANS as expressed in classical views for LES [54, 139, 140, 216, 217] rather than as a degenerate from DNS. The LES studies on turbulent combustion have been reviewed in [85, 185].

In LES, the larger scales obtained using a low-pass filter are solved down to a cut-off scale, Δ, and the remaining sub-grid scales (SGS) are modelled. This operation is done through the use of a spatial filter of a certain shape and width. Large and small scales influence each other depending on filter size and SGS modelling, which are closely related [196]. Thus, estimating the validity of SGS closure can become a difficult task. Furthermore, the LES solutions are sensitive to grid anisotropies and boundary conditions used.

In LES of premixed combustion, the flame thickness is usually thinner than the smallest scale solved [226], hence combustion typically occurs at SGS level and must be entirely modelled. The relative importance of the SGS modelling is expected to diminish as the filter size approaches zero, which typically dictates very fine grids leading to formidably

expensive calculations. This is unattractive for industry applications. The importance of the SGS modelling is thus fundamental when relatively coarser grids are employed, and robust, accurate and computationally efficient models are required to bring LES to a design step.

The modelling used in this study relies on the assumption that the flame is thin and turbulence does not modify its inner structure, thus the flame can be seen as an ensemble of laminar one-dimensional structures (flamelets). Turbulence can be separated from thermochemistry in this case, and the latter can be modelled using one equation for a progress variable. This flamelets assumption, which will be discussed in next chapter, reduces the computational time substantially, allowing the LES as a practical tool to use in the design cycle of 'green' combustion equipments.

1.3 Aims and objectives

Many flamelet-based approaches have been proposed in the past, and are discussed in the next chapter. The aim of this study is to analyse and assess the strengths and weaknesses of flamelets modelling based on presumed probability density function (PDF) for turbulent premixed combustion, and propose sensible modifications to it if required. The presumed PDF requires variance, which in turn requires modelling for its dissipation rate, which is explored for LES by extending its modelling for RANS. Thus, the specific objectives of this study are

1. To implement, test and validate presumed PDF based flamelets for LES of premixed combustion.

2. To study their applicability to various combustion regimes.

3. To identify and develop further improvement, if required. Specifically, the need to include the stretch effects for sub-grid scale reaction rate closure for LES.

4. To derive and study a transport equation for the SGS variance of reaction progress variable, to be defined in the next chapter, for premixed combustion.

5. To identify ways to minimise arbitrary tuneable parameters and thereby evaluate various sub-models and their physical consistencies.

1.4 Outline

The outline of the thesis is as follows. Chapter 2 provides an overview of turbulent premixed combustion. The main characteristics of this mode of combustion are briefly introduced, and

various existing modelling approaches are discussed. Particular emphasis will be given to flamelet models. The scalar dissipation rate and its role for modelling in RANS and LES is also discussed. Chapter 3 presents the numerical procedures and techniques used for this study. General sub-grid modelling and discretisation techniques used for this study are discussed in the first part of this chapter, and the numerical procedures associated with the flamelets modelling are discussed in the second part. Chapter 4 details validations of the numerical procedures and sensitivity analyses. Cold flow simulations in various flame configurations considered are performed to assess the validity of model setup. The results obtained with different models and different configurations are presented in Chapters 5 to 8. Piloted jet flames belonging to the thin reaction zones regime of turbulent combustion are used as benchmark test cases (Chapters 5 and 6) to analyse the various characteristics and limitations of models and sub-models used in this work. A confined bluff-body stabilised flame lying between thin and distributed reaction zones regimes is analysed in Chapter 7, with a particular focus on the importance of the SGS variance. Chapter 8 focuses on low-Reynolds number flames. An overall discussion of these three flame configurations is given in Chapter 9, which is followed by conclusions and future work.

Chapter 2

Background on premixed combustion

Premixed combustion is a situation where fuel and oxidiser are mixed at molecular level before the chemical reactions occur. This is a physico-chemically complex phenomenon and introduces several challenges. The flame structure in premixed combustion is maintained by a dynamic balance between reaction and diffusion of heat and mass [34]. Chemical reactions occur within the reaction zone at a rate determined by the supply of reactants. The interaction of diffusion and reaction with straining affects the rate of mixing and enhances the scalar gradients, and these effects become particularly relevant in LES [107]. The reaction-diffusion coupling may lead to instabilities [152] and the strong heat release may produce other effects such as buoyancy [197], posing additional challenges to the modelling. A brief review of the progresses on the topic from literature is provided in this chapter.

2.1 Governing equations

Combustion gives additional complexity in the treatment of the governing equation in respect to non-reacting problems. Species react and their rate of reaction must be modelled; species and heat coefficients vary within the solution; transport coefficients depend on the species [191]. Because of this complexity, a number of assumptions is required. The fluid mixture is considered to be Newtonian and obeys perfect gas law. Neither Soret effects (species diffusion coefficients do not depend on temperature gradients), nor Dufour effects (heat diffusivity does not depend on gradients of species mass fraction) are considered, and Lewis number is taken to be constant.

In premixed combustion the flame front advances into the reactants field at speed s_L. The interest in this study is for deflagration flames, in which this speed is much smaller than the speed of sound and the pressure is almost constant across the flame [242]. Thus, effects of pressure changes can be neglected in the energy equation. Despite the Mach number is low,

the density, ρ, is not constant, as there is strong heat release across the flame. Neglecting volume forces and viscous heating, and in absence of external heat sources, the resulting set of instantaneous equations, using Einstein notation, is as follows (see for example [191]):

- conservation of mass

$$\frac{\partial \rho}{\partial t} + \frac{\partial \rho u_i}{\partial x_i} = 0 \tag{2.1}$$

  where u_i is the velocity component in spacial direction x_i;

- conservation of momentum

$$\frac{\partial \rho u_j}{\partial t} + \frac{\partial \rho u_i u_j}{\partial x_i} = -\frac{\partial p}{\partial x_j} + \frac{\partial \tau_{ij}}{\partial x_i} \tag{2.2}$$

  where p is the pressure and

$$\tau_{ij} = \mu \left(\frac{\partial u_i}{\partial x_j} + \frac{\partial u_j}{\partial x_i} \right) - \frac{2}{3} \mu \frac{\partial u_k}{\partial x_k} \delta_{ij} \tag{2.3}$$

  is the viscous tensor, μ and δ_{ij} being the kinematic viscosity and the Kronecker delta respectively;

- conservation of species

$$\frac{\partial \rho Y_k}{\partial t} + \frac{\partial}{\partial x_i}[\rho(u_i + V_{k,i})Y_k] = \dot{\omega}_k \qquad k = 1, ..., N \tag{2.4}$$

  where Y_k is the mass fraction of the k-th species, N is the number of species and $V_{k,i}$ is the diffusion velocity in direction x_i. The chemical source term of the k-th species, $\dot{\omega}_k$, is usually expressed in terms of forward and backward rate coefficients, which in turn are expressed as function of temperature using Arrhenius equation, see for example [242] for more details. The diffusion velocity can be modelled using the Hirschfelder *et al.* approximation [97]. Thus, one can write $V_k X_k = -\mathscr{D}_k \nabla X_k$, where X_k is the mole fraction of species k, $\mathscr{D}_k$ is the diffusion coefficient of species k, which is related to the thermal diffusivity, $\mathscr{D}_{th}$, and the Lewis number of species k, Le_k, as $\mathrm{Le}_k \mathscr{D}_k = \mathscr{D}_{th}$;

- conservation of total enthalpy (sum of sensible enthalpy, h_s, and enthalpy of formation, Δh_f^0)

$$\frac{\partial \rho h}{\partial t} + \frac{\partial \rho u_i h}{\partial x_i} = -\frac{\partial q_i}{\partial x_i} \tag{2.5}$$

where the heat flux in direction x_i is modelled using Fourier's law as

$$q_i = -\lambda \frac{\partial T}{\partial x_i} \tag{2.6}$$

and λ and T are the thermal conductivity and temperature respectively. The molecular diffusion term has been neglected in the above equation as it would cancel with other terms in the full expression of the enthalpy equation when $\mathrm{Le}_k = 1$. This full expression can be found for example in [191];

- state equation

$$p = \rho R_0 T \sum_{k=1}^{N} \frac{Y_k}{W_k} \tag{2.7}$$

where R_0 is the universal gas constant and W_k is the molecular mass of the k-th species.

Additional information on these instantaneous equations and their modelling in laminar premixed combustion can be found in [191]. The parameters of laminar premixed flames which are relevant for this study are discussed instead in the next section.

2.2 Essential parameters in premixed flames

2.2.1 Progress variable

Species and temperature fields are not independent [191] in premixed combustion. One can express fuel reaction rate, temperature, density and species, as function of a progress variable, which takes a value of zero and one in fresh reactants and burnt products respectively. This progress variable can be defined either in terms of temperature, $\theta = (T - T_u)/(T_b - T_u)$, or in terms of a suitable mass fraction, $c = (Y_k - Y_{k,u})/(Y_{k,b} - Y_{k,u})$, where subscripts u and b refer to fully unburnt and burnt conditions respectively. These two definitions are equivalent if the Lewis number is unitary [191]. Choice of species k depends on the problem [66] and typically fuel or product mass fractions, or a linear combination of them, are used. A typical variation of this parameter in freely propagating laminar premixed flame is shown in Fig. 2.1.

2.2.2 Flame thickness

The flame thickness can be used as a reference value for the choice of the numerical mesh size, and in this work the typical cell size in the region of the flame is chosen to be one to three times the laminar thermal thickness, δ_{th}. This quantity can be estimated either from

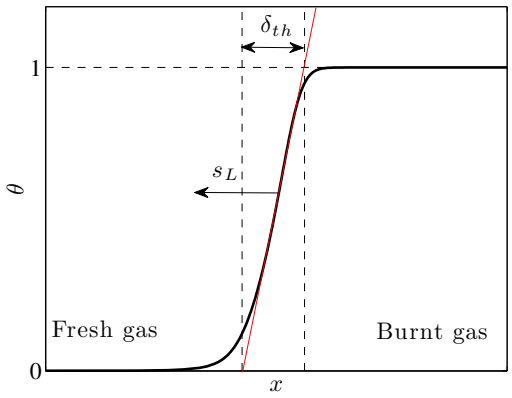

Fig. 2.1 Typical behaviour of progress variable, θ, in freely propagating unstrained laminar premixed flame.

scaling laws, as $\delta = \lambda_u/(\rho_u C_p s_L) = \mathscr{D}_{th,u}/s_L$, also known as Zel'dovich thickness, or from the solution, as $\delta_L^0 = (T_b - T_u)\,|\partial T/\partial x|_{\max}^{-1}$; or as the length in which θ varies from 0.01 to 0.99. The first definition is commonly known to underestimate the flame thickness, and the third gives an overestimation. The second definition is thus the most accurate and is used in this study to compute δ_{th} when needed. However, it requires the knowledge of the solution, which is not known, for example, at the first iteration of a Newton-like algorithm commonly used in laminar flames computations. An estimation was proposed in [15] in terms of δ for constant heat capacity and Prandtl number. This estimation is $\delta_L^0 \approx 2\delta(1+\tau)^{0.7}$, where $\tau = T_{ad}/T_u - 1$ is the heat release parameter and T_{ad} the adiabatic flame temperature.

2.2.3 Flame speed

In premixed flames the flame speed, s_L, is the velocity at which the flame propagates toward the reactants in the direction normal to the flame itself. It controls the fuel consumption rate and thus the heat release rate. When the flame is unstretched, three different flame speeds can be defined [193] absolute speed, $s_a = (\partial\theta/\partial t)/|\nabla\theta|$, which is the speed of the flame front in respect to a fixed reference frame. It remains constant across the flame front if the flame thickness also remains constant; displacement speed, $s_d = (D\theta/Dt)/|\nabla\theta|$, which is the speed of the flame front in respect to the flow; and consumption speed, s_c, which is the speed at which reactants are consumed. Differently form the previous two, which are local, s_c is global, and can be expressed as $s_c = -(\int_{-\infty}^{\infty} \dot{\omega}_f \,\mathrm{d}n)/(Y_{f,u}\rho_u)$, where $\dot{\omega}_f$ is the fuel reaction rate, ρ the density, $\mathbf{n}$ is the local normal, and subscript u refers to unburnt conditions.

When the flame is stretched, the flame speed depends on stretch and a number of other parameters, and becomes complex to compute [191]. Estimations of this quantity have been provided in the limit of small stretch, and can be found for example in [242].

2.3 Turbulent premixed flames

2.3.1 Turbulence-combustion interaction

Turbulence and flame interaction involves a large range of flow and chemical scales. The heat release affects the mixture viscosity and hence the Reynolds number, which influences the flame by enhancing or quenching the reaction term [191]. Assuming the flow in statistical steady state and fuel entirely combusted across the flame (fairly true in lean mixtures), a turbulent flame speed, s_T, can be defined and related to the fuel reaction rate, $\dot{\omega}_f$, as

$$A\rho_u Y_{f,u} s_T = -\int_{\mathscr{V}} \dot{\omega}_f \, \mathrm{d}\mathscr{V}$$

where A is the cross section of the integration domain and $\mathscr{V}$ its volume. Premixed flame analyses [1, 89] show that s_T first increases linearly with the root mean square velocity, u', as $s_T \approx s_L(1+u'/s_L)$, then becomes independent of the laminar flame speed, s_L, and scales as $s_T \sim u'$ for high levels of u', before local extinctions leading to blow-off can occur for further increase of turbulence. The increase of s_T in the linear region is also proportional to the flame surface, A_T, as $s_T = s_L(A_T/A)$, where $\Xi = A_T/A$ is the wrinkling factor and it increases with the Reynolds number [191]. Recent DNS studies [133] show that s_T dependency on stretch is valid only in case of thin flamelets, and s_T rather depends on diffusivity and scalar gradients. Another DNS study [62] has shown that s_T is also strongly geometry dependent because of the different evolution of the flame brush thickness in different configurations. One dimensional turbulent studies of methane-air with forced equivalence ratio show instead that the burning velocity decreases with increasing equivalence ratio oscillations because of the induced damping of turbulent fluctuations [215]. Heat losses also affect the turbulent flame speed [158].

Combustion also modifies turbulence. Kinematic viscosity increases in burnt gases of a factor $T_b/T_u \approx 8$. Consequently, the Reynolds number decreases of a factor $\mathrm{Re}_u/\mathrm{Re}_b \approx 40$, which can lead to a re-laminarisation of the flow. On the other hand, the flow is accelerated by a factor of $s_L(T_b/T_u - 1)$ across the flame, leading to an increase in the vorticity (flame generated turbulence). These two effects contrast each other. Experiments [165] have shown that depending on the initial magnitude of the turbulence, a vortex can be enhanced (weak

turbulence), damped (intermediate magnitudes), or remain unmodified (strong turbulence). The strain induced by the flame-turbulence interaction in premixed combustion alters the instantaneous and statistical behaviour of the scalar gradients. In non-reactive flows, the scalar gradients tend to align with the most compressive principal strain-rate of the turbulent strain tensor [12, 174, 207]. Such alignment was found to increase the scalar gradients by reducing the distance between scalar isosurfaces. For reactive flows, the most extensive principal strain rate aligns with the flame surface normal [90, 227]. Steinberg *et al.* [221] found that this behaviour is due to the superposition of dilatation and turbulence effects. This preferential alignment was found to increase with the flame burning speed and decrease with increasing values of the progress variable. The phenomenon was observed to be due to a rotation of strain-rate structures as they approach the flame. Moreover, the maximum rotation was found to decrease with the strength of the turbulent structure, increase with the strength of the flame, but be invariant to the Karlovitz number. Finally, the dilatation does not generate scalar gradients when turbulence is weak [39], since dilatational and turbulence terms balance each other in this case. However, the two terms result with the same sign when turbulence is strong, and both contribute to the generation of scalar gradients, altering the gradients alignment in respect to non-reactive cases. These are leading order effects [225] and must be considered carefully for premixed combustion modelling.

2.3.2 Combustion regimes

Because of its complexity, the phenomenology in turbulent premixed combustion is usually divided in regimes [180]. Assuming homogenous isotropic turbulence and one-step irreversible chemistry, the reduced number $\mathrm{Da}(r) = \tau(r)/\tau_c$, where $\tau(r)$ is the turbulent characteristic time at scale r and τ_c is a chemical time scale, can be used to identify different scenarios of flame-vortex interaction. When $\mathrm{Da}(r) \gg 1$, turbulence does not affect the flame inner structure. When $\mathrm{Da}(r) \ll 1$, turbulence is much faster than reaction and strongly modifies the flame. The Damköhler number,

$$\mathrm{Da} = \mathrm{Da}(\Lambda) = \frac{\Lambda s_L}{u'\delta},$$

and the Karlovitz number,

$$\mathrm{Ka} = \frac{1}{\mathrm{Da}(\eta_k)} = \frac{u'_k \delta}{\eta_k s_L} = \left(\frac{u'}{s_L}\right)^{3/2} \left(\frac{\Lambda}{\delta}\right)^{-1/2}$$

are representative of this time scale ratio respectively at integral scale, Λ, and Kolmogorov scale, η_k, and are used to identify different regimes in premixed combustion. The Kolmogorov

velocity scale in the above expression is indicated with u'_k. A possible classifications of combustion regimes is [180]

- Flamelet regime, where the chemical time scale is smaller than any turbulent time scale (Da $>$ 1) and the flame thickness is smaller than any turbulent scale (Ka $<$ 1). The flame front is thin and with a quasi-laminar structure. This regime is further divided into wrinkled flamelet regime, in which $u' < s_L$ and turbulence is too weak to alter the flame structure, and corrugated flamelet regime, in which $u' > s_L$ and the smallest turbulent eddies enter the preheat zone, forming pockets of fresh and burnt gases;

- Thickened flame regime, where Kolmogorov scales are smaller than the flame thickness and can modify the inner structure of the flame (Ka > 1). It can be further divided in thin reaction zones regime, in which turbulent eddies enter and modify the preheat zone but not the reaction zone of the flame, which keeps a quasi-laminar structure; and broken (or distributed) reaction zones regime, in which both diffusion and reaction zone of the flame are affected by turbulence. No laminar structure is likely to be present in the distributed reaction zones regime and the effect of strain can cause local extinctions.

A sketch of the various regimes is shown in Fig. 2.2. These regimes are only indicative as they are based on order of magnitude analysis and frozen turbulence, but serve as good guidance. For example, even when Ka $>$ 1, Kolmogorov scale eddies may be too small or too short in time to affect the flame structure, or may induce curvature which counteracts the influence of strain [191]. Moreover, the vortex-flame interaction depends on time. Recent studies on methane-air flames show that flame quench occur at Ka $>$ 1000 rather than Ka $\approx$ 100 [213, 220], which can be due to high rate of dissipation in small eddies [191] and high burning rates [213]. A pilot effect through eddies carrying hot products was observed in [220], which may also explain the high Ka for the flame quenching in respect of what expected form the regime diagram.

2.4 Modelling for turbulent premixed combustion

Turbulence modelling can be divided in three main categories, Direct Numerical Simulation (DNS), Reynolds Averaged Navier Stokes (RANS) and Large Eddy Simulation (LES).

DNS is the simplest approach, for no closure models are required, but also the computationally most expensive. The grid must be fine enough to resolve the Kolmogorov scale and/or the flame thickness. Consequently, the grid size depends on the Reynolds number, and large meshes are required even for simple computational domains with high turbulence level. In turbulent combustion, since the flame moves quickly and exhibits a considerable wrinkling,

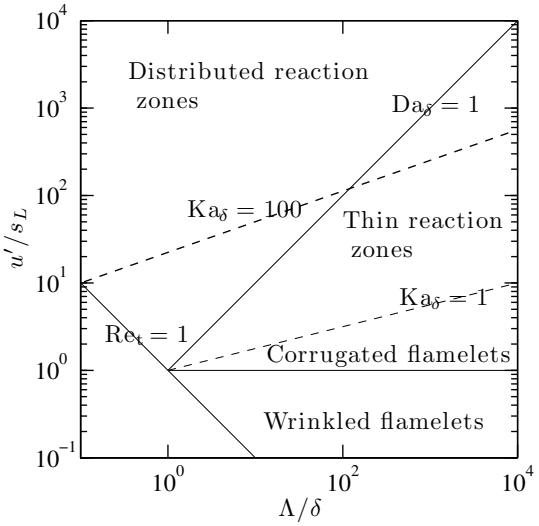

Fig. 2.2 Regimes diagram for premixed turbulent combustion [180]. The subscript δ indicates that Karlovitz and Damköhler numbers are computed using the Zel'dovich thickness.

self-adaptive meshing techniques cannot be easily exploited [191]. Besides, detailed chemistry would involve time scales of different orders which make the solution stiff. For these reasons, DNS requires very large computational resources and simple estimates are given in [187]. Thus, it is rather used as a tool to gather insights required for development of closures for RANS and LES.

In RANS, the probabilistic mean is applied to the govering equations, and the theorem of ergodicity [69] is used to substitute this probabilistic mean with temporal average. In this way the temporal derivative disappears from Eqs. (2.1)-(2.4). The application of the probabilistic mean on the non-linear terms leads to additional unresolved terms which need modelling. An extension to unsteady problems is possible by keeping the temporal term in the governing equations (Unsteady-RANS or URANS)[1]. Even with URANS, only the time varying mean characteristics of the flow can be captured.

In LES, only the large-scale motion of the flow field is solved, with models to mimic the unresolved scales. This is obtained by filtering the governing equations with a spatial filter. If the filter is homogenous in space and time, it commutes with the differential operators, and the resulting equations are formally identical to those for URANS, but with different meaning. The unresolved term represents in fact the contribution of the residual motion, i.e. the motion at scales smaller than the filter width. LES has a computational cost which is between RANS and DNS. It is accepted generally that at least the 80% of the turbulent kinetic energy should be

[1] In this case the ergodicity does not apply and this approach has been largely argued in the literature.

resolved in a good LES because of the energy cascade from large to small scales [196], and this can be used as a general thumb rule for the choice of the numerical grid in a LES.

2.4.1 LES filtering

A filtered variable $\overline{\phi}(x,t)$ is obtained through a spatial convolution with a filter function [196]:

$$\overline{\phi}(x,t) = \int_{-\infty}^{\infty} \phi(x',t) G(x-x';\Delta)\,\mathrm{d}x' \tag{2.8}$$

where the filter function, G, depends on space and on the filter width, Δ. Equation (2.8) is written for simplicity for the one-dimensional case, and extension to three dimensions is straightforward. Formally, the integration domain is unbounded. However, filters used in practice approach zero very quickly, and the integral is truncated. Thus, filtering can be seen as a weighted spatial average, where the weight distribution is determined by the filter shape, and their magnitude by the filter width. The filter width also controls the accuracy in LES, as it determines which scales are solved and which are modelled. Several filters exist and their description can be found in the literature (see for example [196]). It is worth noting that:

- the filter commutes with the differential operator only if it is uniform;
- the filter is not chosen explicitly. It is defined by SGS modelling, and by grid and numerical scheme if it is linked to the mesh spacing (see §3.1.3). In this case non-uniform grids would imply non-uniform filter, and this effect can be partly compensated using dynamic approaches [65];
- in general, for a variable ϕ, $\overline{\overline{\phi}} \neq \overline{\phi}$ and $\overline{\phi'} \neq 0$, where $\phi' = \phi - \overline{\phi}$ is the Reynolds residual of ϕ.
- establishing the actual filter shape is difficult because the effects of grid, numerical schemes and SGS models are difficult to separate from one another in most practical cases.

A common filter is the Gaussian filter, whose normalised expression for one dimension is

$$G(x) = \left(\frac{6}{\pi\Delta^2}\right)^{1/2} \exp\left(-6\frac{x^2}{\Delta^2}\right) \tag{2.9}$$

and extension to a three-dimensional case is straightforward [196].

2.4.2 Favre filtering

Because of heat release, the density varies in combustion. This variation is fundamentally different form that of compressible flows, e.g. in presence of shock waves. In deflagration problems density changes do not depend on pressure, which is almost constant across the flame [180]. Because of variable density, the filtering operation leads to coupling terms involving density and transported variables. To avoid this, a Favre filtering is defined as [191] $\widetilde{\phi} = \overline{\rho\phi}/\overline{\rho}$. The Favre-residual of ϕ is defined, in analogy with ϕ', as $\phi'' = \phi - \widetilde{\phi}$, and in general $\widetilde{\widetilde{\phi}} \neq \widetilde{\phi}$ and $\widetilde{\phi}' \neq 0$.

2.4.3 Governing equations for LES

The LES governing equations are obtained by filtering Eqs. (2.1)-(2.4) with a uniform filter, yielding (see for example [191])

$$
\begin{aligned}
\frac{\partial \overline{\rho}}{\partial t} + \frac{\partial \overline{\rho}\widetilde{u}_i}{\partial x_i} &= 0 \\
\frac{\partial \overline{\rho}\widetilde{u}_i}{\partial t} + \frac{\partial \overline{\rho}\widetilde{u}_i\widetilde{u}_j}{\partial x_j} &= \frac{\partial \overline{p}}{\partial x_i} + \frac{\partial}{\partial x_j}\left(\overline{\rho\mu\frac{\partial u_i}{\partial x_j}}\right) - \frac{\partial}{\partial x_j}\widetilde{\tau}^R_{ij} \\
\frac{\partial \overline{\rho}\widetilde{h}}{\partial t} + \frac{\partial \overline{\rho}\widetilde{u}_j\widetilde{h}}{\partial x_j} &= \frac{\partial}{\partial x_j}\left(\overline{\rho\frac{\mu}{\mathrm{Pr}}\frac{\partial h}{\partial x_j}}\right) - \frac{\partial}{\partial x_j}\widetilde{\tau}^R_{hj} \\
\frac{\partial \overline{\rho}\widetilde{c}}{\partial t} + \frac{\partial \overline{\rho}\widetilde{u}_j\widetilde{c}}{\partial x_j} &= \overline{\dot{\omega}} + \frac{\partial}{\partial x_j}\left(\overline{\rho\frac{\mu}{\mathrm{Sc}_c}\frac{\partial c}{\partial x_j}}\right) - \frac{\partial}{\partial x_j}\widetilde{\tau}^R_{cj} \\
\overline{p} &= \frac{\overline{\rho}R_0\widetilde{T}}{\widetilde{W}}
\end{aligned}
\tag{2.10}
$$

where the species equation is substituted with the equation for a Favre-filtered progress variable, $\widetilde{c}$. Additional equations may be required depending on the particular closure model, which will be discussed in Chapter 3. Also, terms due to radiation and pressure changes have been neglected in the total enthalpy equation.

The filtered molecular diffusion and turbulent transport, appearing inside momentum, enthalpy and progress variable equations, need modelling. The filtered diffusion is approximated as

$$
\overline{\rho\mathscr{D}_\phi\frac{\partial\phi}{\partial x_i}} \approx \overline{\rho}\widetilde{\mathscr{D}}_\phi\frac{\partial\widetilde{\phi}}{\partial x_i} \tag{2.11}
$$

where ϕ is the generic transported variable. The residual stress tensor $\widetilde{\tau}_{ij}^R = (\overline{\rho}\widetilde{u_i u_j} - \overline{\rho}\widetilde{u}_i\widetilde{u}_j)$ in the momentum equation can be written as the sum of its trace and an anisotropic part [196]:

$$\widetilde{\tau}_{ij}^R = \frac{1}{3}\widetilde{\tau}_{kk}^R + \widetilde{\tau}_{ij}^r \tag{2.12}$$

The trace is added to the pressure term, in analogy with what is done for the stress tensor in Eq. (2.1), and computed implicitly in a pressure-correction algorithm. The anisotropic residual term, τ_{ij}^r, is modelled in this work using either a Smagorinsky model or a residual-kinetic energy model (see §3.1.1). The turbulent fluxes in scalar equations are instead modelled with a gradient hypothesis, i.e.

$$\widetilde{\tau}_j^R \equiv \overline{\rho}\widetilde{\phi u_j} - \overline{\rho}\widetilde{\phi}\widetilde{u}_j = -\frac{\nu_T}{\mathrm{Sc}_T}\frac{\partial \phi}{\partial x_j} \tag{2.13}$$

where $\widetilde{\tau}_j^R$ is the turbulent transport of the generic scalar ϕ, ν_T is the kinematic residual viscosity to be discussed in §3.1.1 and Sc_T is the turbulent Schmidt number. Gradient models do not account for counter-gradient effect due to dilatation in combustion problems [24, 181]. A model for RANS which captures this effect is for example [236]

$$\widetilde{u_i c} - \widetilde{u}_i\widetilde{c} = \widetilde{c}(1-\widetilde{c})\left(\tau s_L - 2\alpha u'\right) \tag{2.14}$$

where τ, s_L and u' are computed ahead of the flame, and $\alpha = 0.5$. Gradient behaviour was also seen to increase with the turbulence level in past studies, see for example [45, 68, 131, 145]. More information on gradient and counter-gradient transport in premixed combustion can be found in [25, 144]. However, due to partial resolution of the turbulent scales, gradient hypothesis in LES is effective in most cases [66] as most of the transport is solved at the large scales and only a part is to be modelled [17]. Thus, using a gradient hypothesis is acceptable [131].

Further modelling of the Eqs. (2.10) is discussed in Chapter 3. The modelling approaches for chemical kinetics and SGS reaction rates are reviewed briefly below.

2.4.4 Chemistry modelling

Infinitely fast chemistry has been shown to be appropriate in capturing flame length and flame speed in many cases, but chemical kinetics must be considered for problems involving soot formation, ignition delay, stabilisation in combustion devices and intermediate species predictions [66]. The large range of turbulent and chemical scales, and the many species involved in a combustion process, make the problem intractable in its details. Moreover, small scale processes like the coupling of reaction and diffusion are non-linear. First approaches

were based on global schemes reduction, in which some species are considered to be in a quasi-steady state or be a part of reaction in partial equilibrium. However, such approaches give a computational work reduction that is less than expected [191]. Moreover, these assumptions give poor predictions in 'colder' region of the flame, where transport processes are also important [234]. To overcome these issues the literature moved towards automatic chemistry reduction and tabulated chemistry. The first approach consists in expressing the species which have a short time scale as a function of a small number of species. Of this class of methods is the Intrinsic Low Dimensional Manifold (ILDM) [148]. Tabulated chemistry consists instead in tabulating complex chemistry for 1D laminar premixed combustion in function of a limited set of variables (mixture fraction, progress variable, etc.). The choice of the variables must capture the impact of kinetics, diffusion and heat losses on flame structure [66]. The first models to use tabulated chemistry were the flame prolongation of ILDM (FPI) [86] and the flamelet generated manifold (FGM) [234]. In the two models above the tabulation is done *a priori*. An alternative approach is the in situ adaptive tabulation (ISAT) [195], in which the tabulation is done on the fly as this was shown to be advantageous in terms of computational effort when the number of tabulation coordinates is larger than two or three. Tabulated chemistry were observed to yields better predictions than ILDM at low temperatures, but their mathematical assumption is weaker than for ILDM.

The tabulated values must be pre-integrated with the joint probability density function (PDF) of the related quantities in order to take into account the statistical properties of small scales of the simulated field in a LES. Alternatively, one can avoid tabulation and use transported PDF [7, 31, 94, 103, 204, 238]. As will be described in next paragraph, a modelled equation for a joint-PDF of composition variables must be solved in this case.

2.4.5 Modelling for turbulent-flame interaction

The LES methodology and its modelling are described in a number of earlier studies for non-reacting and reacting flows, see for example the books by [196] and [191]. The LES studies on turbulent combustion are reviewed by [185] and [85]. The combustion is usually a sub-grid scale (SGS) phenomenon requiring modelling and various modelling approaches used for premixed combustion are reviewed and summarised in earlier studies [33, 85, 191, 226]. These approaches can be broadly categorised into two classes, namely, flamelets and non-flamelets or geometrical and statistical [85]. The *geometrical* category of flamelets includes thickened flame [47, 53], flame surface density or flame-wrinkling, see for example, [17, 36, 38, 88, 92, 115, 241], level-set or G equation [164, 184]. The *statistical* category of flamelets includes approaches such as algebraic closure involving scalar dissipation rate [32, 61, 77, 130, 147] and presumed probability density function (PDF) methodology with laminar flamelets. The

EBU (eddy-break-up) model also can be included in this category if the variance is assumed to be bimodal (see next paragraph). The non-flamelets category includes transported PDF [6, 104] and conditional moment closure (CMC) [13, 113] methodologies. Each of these methods has its merits and drawbacks, and a brief summary is given below.

EBU model

The Eddy Break Up (EBU) model was first conceived for RANS. The idea is that the chemical source term is proportional [149, 219] to a chemical, τ_c, and a turbulent mixing, τ_t, time scales, i.e. $\overline{\dot{\omega}} \sim \tau_c^{-1} + \tau_t^{-1}$. The model was then extended to LES [70, 84, 162] by replacing the turbulent mixing time scale with a SGS time scale, $\tau_{t,\text{sgs}} \approx k_{\text{sgs}}/\varepsilon_{\text{sgs}}$, yielding

$$\overline{\dot{\omega}} = C_{\text{ebu}} \frac{\overline{\rho}\,\sigma_c^2}{\tau_{t,\text{sgs}}}$$

where C_{ebu} is the model constant, k_{sgs} is the subgrid turbulent kinetic energy and ε_{sgs} is the subgrid dissipation. The latter can be estimated in LES as $\varepsilon_{\text{sgs}} = c_\varepsilon k_{\text{sgs}}^{3/2}\Delta$, where c_ε is a model constant. This model is valid for high Reynolds and Damköhler numbers and in the hypothesis of infinitely fast chemistry. The variance of $\widetilde{c}$, σ_c^2, can be assumed to be bimodal, $\sigma_c^2 = \widetilde{c}(1-\widetilde{c})$ in the hypothesis of infinitely thin flame. This model is computationally cheap and simple to implement. Moreover, differently to RANS, the model constant can incorporate effects of wrinkling. However, this model tends to overestimate the reaction rate in regions of strong shear and does not take into account the thickness of the flame [191].

FSD models

The main idea of Flame Surface Density (FSD) models is to express the filtered reaction rate as $\overline{\dot{\omega}} = \rho_u s_L^0 \overline{\Sigma}$, where $\overline{\Sigma} = \overline{|\nabla c|}$ is the FSD per volume unit in a computational cell. An algebraic model for $\overline{\Sigma}$ is [17]

$$\overline{\Sigma} = 4\Xi_\Delta \sqrt{\frac{6}{\pi}} \frac{\overline{c}(1-\overline{c})}{\Delta} \tag{2.15}$$

where $\Xi_\Delta = \overline{|\nabla c|}/|\nabla \overline{c}|$ is the SGS wrinkling factor and can be a constant [17] or modelled using fractal analysis [43, 114]. This approach was observed to underestimate the pressure peaks in engine simulation when Eq. (2.15) is used [111]. An alternative approach is to use a dynamic procedure for $\overline{\Sigma}$. The latter is decomposed in a solved contribution $|\nabla\overline{\theta}|$, modelled with Eq. (2.15) with $\Xi_\Delta = 1$, and an unresolved part, $\overline{|\nabla\theta|} - |\nabla\overline{\theta}|$, which can be modelled

as [114]

$$\overline{|\nabla c|} - |\nabla \overline{c}| \approx c_s \left[\frac{\overline{c}(\widehat{1-\overline{c}})}{\Delta} - \frac{\widehat{\overline{\theta}}(1-\widehat{\overline{c}})}{\widehat{\Delta}} \right]$$

where c_s is a model constant and the hat indicates a test-filter operation. Another approach consists in solving a transport equation for $\overline{\Sigma}$ [17, 47]. Hawkes and Cant [92] showed that FSD models can capture the net flame propagation rate independently of the filter size, and that wrinkling becomes more and more relevant at sub-grid scale as the turbulence increases. In a following work Hawkes and Cant [93] noted that the realisability condition, $\overline{\Sigma} \geq 0$, may not be always satisfied, and extra care is needed in this approach.

Thickened Flame Models

The approach in thickened flame model (TFM) is to artificially thicken the flame front [47]. The flame thickness scales as $\delta \sim (\lambda/A)^{1/2}$, where A is the Arrhenius pre-exponential constant. If A is scaled by a factor F, δ increases. Since the thermal diffusivity scales as $\lambda \sim s_L \delta$, this quantity is also multiplied by F in order to keep the value of s_L unchanged. Thus, the reaction layer thickness can be increased and resolved on the computational mesh in a LES. However, the Damköhler number is decreased of a factor F [191], thus an *efficiency function* is introduced to compensate for the resulting decrease of flame SGS wrinkling [47]. Thickened flame models can also be used in conjunction with FGM [170] and presumed sub-grid PDF models [57]. A model based on thickened flame, in which flamelets are simply filtered instead of being pre-integrated, was proposed by Wang *et al.* [240], in which the effect of the wrinkling is recovered by estimating a wrinkling factor using asymptotic analyses [184]. In [17, 63, 157], a filter larger than the mesh size is used to resolve the filtered flame structure, which is observed to be necessary when the cell size is larger than the flame thickness to avoid mis-prediction of flame speed due to the broadening of the flame front. Nevertheless, additional DNS and LES investigations using filtered one-dimensional flamelets and FGM to model the sub-grid combustion show that diffusion and heat release are well represented when the grid size is of order of flame thickness, and deviations from DNS results are seen only in the unresolved convection term in this case [166].

Level set approaches

These models treat the flame as a very thin interface, which is tracked using a transport equation (G-equation) and assuming that this interface corresponds to a level of a progress

variable [100, 109, 218]. A model for the conditionally filtered velocity is required in this model as explained in [184]. The approach models the turbulent burning speed as $s_T/s_L = 1 + A(u'_\Delta/s_L)^n$, where A and n are model constants and u'_Δ is a SGS velocity scale. Effects of finite chemistry and non-unitary Lewis numbers may be included in the modelling through s_L [226]. However, this model introduces flame cusps and artificial viscosity is needed to smooth the G-field [101].

LEM-LES

The idea behind this approach is to include effects of SGS reaction, diffusion and convection by looking at 1D unsteady transport equation [110]:

$$\frac{\partial Y_k}{\partial t} = -\frac{1}{\rho}\frac{\partial \tau_i}{\partial s} + \frac{\dot{\omega}_k}{\rho} + F_{\text{mix}}$$

where s is the local normal specified by the gradient of Y_k. A similar equation is used for the temperature field. A stochastic term, F_{mix}, is introduced into the equation to represent the mixing at subgrid scales [41, 211, 232]. full 3D LES equations are used for larger scales. Thus, reaction kinetics and molecular diffusion are modelled exactly without additional SGS modelling. However, in addition to the high computational cost, the stochastic term in this model, F_{mix}, needs a mapping procedure [110] and a PDF [211] which may be difficult to model.

PDF models

Filtered reaction rate are function, in general, of temperature, T, and composition space, $\mathbf{Y}$. A closure for the generic reaction rate of species k, $\overline{\dot{\omega}}_k$, can be expressed as [84, 162]

$$\overline{\dot{\omega}}_k = \int P(\mathbf{Y},T)\dot{\omega}_k(\mathbf{Y},T)\ \mathrm{d}\mathbf{Y}\ \mathrm{d}T \tag{2.16}$$

where $\dot{\omega}_k$ is the laminar reaction rate and P is the multi-dimensional sub-grid PDF, which accounts for the SGS statistical properties of the turbulent flame. This PDF can be presumed or transported.

In presumed PDF approaches, the sub-grid PDF is usually described as function of a small number of composition variables. In the more specific case of flamelets assumption, it is described as function only of a progress variable and its moments. A transport equation for a Favre-filtered progress variable of the form of that in Eqs. (2.10) is used to compute the first moment in the turbulent domain, while other moments, if required, are either transported or modelled. The reaction rate of the filtered progress variable, along with other quantities needed

in the turbulent computation, are thus computed as

$$\overline{\phi} = \int P(c;\overline{c},\dots)\phi(c)\ \mathrm{d}c$$

where ϕ is a generic quantity which needs closure. The simplest model of this type is the Bray-Moss-Libby (BML) model [30, 137]. Similarly to RANS, the sub-grid PDF in LES is modelled as

$$P(c) = \alpha\delta(c) + \beta\delta(1-c) + \gamma f(c) \tag{2.17}$$

where δ is the Dirac function and $f(c)$ is a function of c which integrates to one in the c space. The constants α, β and γ represent respectively the probability of having only reactants ($c = 0$), only products ($c = 1$) or intermediate species in the mixture. In the hypothesis of very large Damköhler number the flame becomes a very thin interface separating products and reactants, thus $\gamma \ll 1$, and α and β can be expressed as functions of only the first moment of c, $\widetilde{c}$, and the heat release parameter, τ, with an error of $\mathscr{O}(1/\mathrm{Da})$. Also, the integral of Eq. (2.17) can be computed analytically for any quantity ϕ. The BML model has the advantage of being simple and computationally cheap. Moreover, the density can be treated as constant respectively for reactants and products sides, and no closure is needed for the interface flux. However, the assumption of high Da limits its application. An improvement of this approach uses a joint PDF of progress variable and velocity field [136], and in this case the reaction rate of progress variable was shown to be proportional to the scalar dissipation rate. Additional details will be discussed in §2.5.

To account for finite chemistry effects, the sub-grid PDF can be modelled using a β-function. This PDF, which will be discussed in more details in next chapter, is parametrised using $\widetilde{c}$ and its SGS variance, $\sigma^2_{c,\mathrm{sgs}}$. The latter can be either modelled or transported, and it will be shown in §3.3.2 that simple models based only on turbulence can be a very inaccurate representation of $\sigma^2_{c,\mathrm{sgs}}$. Integrations based on β-PDF in LES have been shown to overestimate the flame speed in laminar regions when the filter size is larger than the laminar flame thickness [67]. Alternative PDF integrations have been investigated recently in [210, 231] using modified laminar flamelets PDF and LEM-formulated PDF, showing improved performances compared to β-PDF in change of additional complexity.

In transported PDF models [192], also known as filtered density function (FDF) models [194] in case of LES, a transport equation for the sub-grid PDF in Eq. (2.16) is computed, and chemical mechanisms can in principle be applied without further simplifications. Transport equations for the sub-grid PDF of a scalar variable or the sub-grid joint-PDF of a scalar variable and the velocity field are commonly used, but extension to joint-PDFs to any other variable is possible. Thus, this method can incorporate detailed and accurate chemical kinetics and is for

this reason very attractive for the turbulence-chemistry interaction modelling. However, the molecular transport term in the PDF equation becomes an issue for Da $\gg 1$, as it is strongly affected by the chemical reaction in this case and needs to be modelled. One approach is to solve for a set of coupled stochastic differential equations using Lagrangian particle method and Monte Carlo simulations [6], as done for example in [48, 204]. Another approach is to solve a set of Eulerian stochastic fields [104], in which the stochastic fields correspond to an equivalent stochastic system with same one-point PDFs rather than a particular realisation of the flow [80], and a number of works have appeared recently for premixed combustion [31, 56, 102], showing very good potentiality of this approach. A review of PDF methods for LES is for example in [87].

CMC model

In conditional moment closure (CMC) transport equation for conditional mean of species mass fractions and temperature are solved [13, 113]. These variables are conditional on chosen scalars, usually a progress variable in premixed combustion. The key assumption is that the fluctuations of the conditional mean are small and can be ignored at least for first order CMC, and the conditional reaction rate can be expressed as $\langle \dot{\omega} | c \rangle = \dot{\omega}(Q)$, where Q is the conditional species or temperature (or a combination of them). These models need a closure for the conditional SDR, which is not straightforward to provide. The CMC method was tested for RANS simulations of premixed flames [4, 5, 151] but yet to be fully assessed for premixed combustion LES. An application for compressible flows is described in [230]. More information on this method can be found for example in [126].

More recently, scale similarity assumptions for modelling parameters such as flame wrinkling and flame surface density have been proposed and investigated using DNS [91, 244] and LES [43, 88, 114, 115, 117, 127, 185, 241] for most of the above models. Dynamic models based on the scalar dissipation rate have been investigated for non-premixed combustion [105], and recently for premixed combustion [79, 129]. Although the assumption of scale similarity is arguable for reacting quantities, these modelling approaches seem promising [66], and are observed to work on different regimes [158].

The focus in this thesis will be on presumed PDF approaches. These methods are simple and can account for finite rate chemistry with an enormous advantage in terms of computational time in respect to other models. Thus, they have potential to meet the aims presented in §1.3.

This will be rigorously tested in this study on different configurations and regimes. Since flamelets are usually assumed in these methods, this hypothesis is briefly discussed next.

2.4.6 Laminar flamelets approach: range of validity and limitations

Premixed flames are usually thin and quite robust to turbulent perturbations and variations in thermochemistry [34]. Thus, if Ka < 1, turbulence can merely corrugate the flame, which can be seen as an ensemble of thin, locally one-dimensional laminar structures (flamelets). A laminar flamelet consists of a thin and highly wrinkled interface propagating like a strained and curved laminar flame. In flamelets hypothesis, turbulence can be decoupled from the chemistry; laminar properties can be used to evaluate the local rates of reaction and transport, while the turbulent modelling is used to evaluate the main features of the flow. The coupling between molecular diffusion and reaction is confined to a low-dimensional manifold: the detailed chemistry from laminar computation is tabulated and parametrized by a small number of variables [197].

One of the earliest models for turbulent premixed combustion is the Bray-Moss model [30]. This model was extended by Libby *et al.* [137] to include effects of molecular transport and finite chemical reaction rates. They demonstrated theoretically that laminar premixed flames can naturally parametrise the turbulent flames. In a following work, Libby and Bray [136] raised doubts in the application in premixed combustion of models for turbulent transport taken from non-reactive turbulence. In fact, the mean scalar dissipation rate (SDR), controlled by the chemical term, influences directly turbulent mixing and dissipation. Hence, models derived from non-reacting flows must be revised in flamelet context. Statistics of the turbulent motion must be taken into account in flamelet approaches, e.g. by defining a joint PDF of the progress variable and the velocity field. Under the assumption of high Reynolds number, Bray *et al.* [28] showed that since reactions happen in some points within the flamelets, they are proportional to the crossing frequency at which flamelets cross that point. A study on the limits of flamelet assumption was carried out by Meneveau and Poinsot [155], using a model for intermittent turbulence and taking into account all possible turbulence scales acting on the flame front. By investigating on the effect of stretch and quenching in the thickened reaction zones of the premixed combustion diagram, they found that the flamelets assumption in premixed turbulent flames is valid in a domain larger than expected and that quenching occurs depending on the level of sub-adiabaticity of the flame. This extended domain of applicability was also observed in experiments [59, 60, 202]. Knudsen and Pitsch [118] have shown that flamelets applicability on multi-regime flames is possible, and possible inaccuracies are due finite chemistry effects rather than inappropriate regime predictions. More recently, flamelets assumption in LES modelling have been observed to hold up to Ka ≈ 1000 [220].

Moreover, the flamelet assumption was shown to be reasonably valid for stratified flames also [51, 95, 179, 190, 201, 203, 229].

Strain effects on flamelets have also been investigated in past studies. Poinsot *et al.* [188] observed that the strain has no effect on the consumption speed, s_c, at unity Lewis numbers in premixed laminar flames. The displacement speed, s_d, increases instead by almost an order of magnitude due to hydrodynamic and diffusive mechanisms. The first effect is due to the modification of the flame surface by lateral flow divergence and the second is due to the misalignment of diffusive and hydrodynamic mechanisms. Moreover, curvature induces different propagation speeds at different locations. Flamelets which are strongly curved toward the fresh gases have higher displacement speed and come rapidly back to planar shapes. These highly curved flamelets have a short life time, but might have strong effects on the flame surface variation, raising questions on the choice of flamelets canonical configuration to choose for modelling. Thermo-diffusive instability effects at non-unity Lewis number have been investigated recently for turbulent premixed combustion [108]. It was observed that instability arises after a critical level of strain, and this effect can be taken into account in a flamelet model if the laminar flame speed is scaled appropriately. The fluid dynamic straining effects were shown [122] to be important in RANS calculations of piloted stoichiometric methane-air Bunsen flames of [46] using presumed PDF involving unstrained and strained flamelets. When the straining effects were excluded, the computed flame length was observed to be very much shorter than the measured length in [46] suggesting that the fuel is consumed quickly. There is only one turbulence length and time scales involved in the RANS and the affects of the spectrum of turbulence scales on the flame need to be included in the combustion modelling. Various approaches such as *efficiency function* were introduced in the past [155] to include flame stretching caused by the turbulent eddies which are lost in the averaging involved in the RANS method. A similar approach is also used to include the effects of unresolved eddies on the filtered flame in LES using thickened flame model [47, 53]. Alternatively, one could also use strained flamelets to model filtered reaction in LES as has been attempted in [116]. The past RANS study [122] used averaged scalar dissipation rate of a reaction progress variable to parameterise strained flamelets whereas atomic hydrogen mass fraction was used in [116] for LES. The SGS variance of progress variable, $\sigma^2_{c,\mathrm{sgs}}$, required in presumed PDF methods, is modelled in earlier studies typically using an expression developed for passive scalars. The relevance of such modelling for turbulent premixed combustion is an open question on physical grounds because chemical reactions ought to influence this variance as was remarked in [182] and an algebraic model for $\sigma^2_{c,\mathrm{sgs}}$ including this effect is yet to be developed. These points are of specifically high importance for the presumed sub-grid PDF approach because this PDF has a direct dependence on $\sigma^2_{c,\mathrm{sgs}}$ and influences the filtered reaction rate value. Moreover,

this variance may assume a different importance on different configurations and combustion regimes. Thus, a large scope of investigation is left with this methods. The aim of this study is to contribute to reduce this gap and provide a deeper understanding of strengths and weaknesees of flamelets modelling for LES of premixed combustion. The particular SGS modelling used in this study, to be explained in detail in the next chapter, needs a model for the SDR of a progress variable. This modelling and the role of SDR in premixed combustion are discussed in the next section.

2.5 Scalar dissipation rate modelling in turbulent premixed combustion

The instantaneous SDR of a reaction progress variable, c, with diffusivity $\mathscr{D}_c$, is defined as $N_c = \mathscr{D}_c(\nabla c \cdot \nabla c)$. Closures for mean and filtered reaction rates based on the SDR have been proposed in the past (see for example [226] for a review) and can be categorised into algebraic and transport equation models. The algebraic model assumes that the molecular dissipation of the SDR balances its generation by turbulent straining, dilatation and chemical reaction rate terms. In RANS, this equilibrium between production and destruction of SDR gradients is strictly valid in the corrugated flamelets regime and the PDF of the progress variable can be well approximated by a bimodal function in this case. Furthermore, in the thin reaction zones regime, reaction rate and SDR contributions are of leading order in the scalar variance equation even at high Karlovitz numbers. Since in premixed combustion the rate of heat from the reaction to the preheat zone determines the flame propagation rate, the mean reaction rate is directly proportional to the SDR, at least in the context of flamelets assumption [23]. If the Damköhler number is high, the PDF of c is well approximated by a double delta function, and it can be shown that [23]

$$\sigma_c^2 = \widetilde{c}(1-\widetilde{c}) \tag{2.18}$$

and

$$\overline{\dot{\omega}} = \frac{2}{2C_m - 1}\overline{\rho}\widetilde{N}_c \tag{2.19}$$

where σ_c^2 is the variance of $\widetilde{c}$ and C_m is a constant. The model constant C_m in this relation is defined as

$$C_m = \frac{\int_0^1 [\dot{\omega}\, c]_L f(c) \;\; \mathrm{d}c}{\int_0^1 \dot{\omega}_L f(c) \;\; \mathrm{d}c}, \tag{2.20}$$

where $f(c)$ is the burning mode probability density function (PDF) of c and the subscript 'L' refers to planar laminar flame [22, 23]. The integrals in Eq. (2.20) can be evaluated using

the laminar flame data and thus C_m is a thermo-chemical parameter. This relation has been verified for RANS [37, 40] and LES [61, 77, 129] paradigms in past DNS studies through *a priori* testing. The use of this closure for RANS calculation overestimates the turbulent burning rate [121]. However, a variant of this model, known as eddy-break-up model, involving a time scale for SGS turbulent mixing rate gave reasonable results [70, 162, 173]. Also, it has been shown that the scalar dissipation rate based closure can yield improved results compared to other combustion modelling approaches for LES [32, 129, 147]. An algebraic model for RANS for the SDR was first proposed by Borghi [18]. Nevertheless, he did not account for the dilatation effects. Swaminathan and Bray [225] analysed the order of magnitude of the various terms in the transport equation for the instantaneous SDR. In particular, they showed that the dilatation is affected by two contributions, one representing a direct effect of density changes, and the other an indirect effect due to dilatation on turbulence-scalar interaction. The original model was then modified via *a priori* analyses and comparison with the turbulent flame speed from experiments, based on new findings of the physics of turbulence-scalar interaction [120]. In particular, while neglecting the indirect term alters the true flame speed only when turbulence is weak, neglecting the direct term always gives poor predictions [123]. Using *a-priori* DNS analysis, Kolla and Swaminathan [122] improved the model of [167] by developing a closure for corrugated flamelets regime, based on equilibrium at the leading order.

If $\mathrm{Da} \gg 1$, the progress variable variance can be modelled with equation (2.18). If the flame is not thin, turbulent eddies can enter the reaction zone, inducing tangential strain-rate. Flamelet-like structures can still be found under strain effect and at high Da, as described in §2.4.6. Thus, flamelet models are still possible. Kolla and Swaminathan [123], using the SDR as parameter, showed that the effect of the dynamic strain of reducing the burning rate could be captured in the thin reaction zones regime. This approach is more advantageous than using the strain as parameter in the flamelet formulation [20] since the SDR is defined at each location on the flamelet and is naturally related to the reaction-convection-diffusion coupling of premixed combustion, as noted earlier. Besides, asymptotic studies have shown that N_c is closely related to the flamelet structure at both high and low strain values [138].

An extension to LES of the above model was proposed by Dunstan *et al.* [61] and analysed through DNS [61] and LES [32, 129, 147]. Since the SDR features in the transport equation for the progress variable variance and is directly proportional to the square of the scalar gradient magnitude, this equation is also controlled by the SDR. Analyses were done by Bray *et al.* [26], which proposed a transport model for the scalar variance by accounting for effects of dilatation and proposing a model in case of high, but not infinite Da. Kolla and Swaminathan [122] showed that unstrained flamelets model over-predict the mean reaction rate in RANS, and the SDR was in that case added as third controlling variable in a strained flamelets formulation. The

importance of the scalar variance was shown for the mixture fraction in LES of non-premixed combustion [105] and stratified flames [10]. Contrary to RANS, it will be shown in this thesis that, because of the partial resolution of the strain at larger scales, strained flamelets models are not essential in LES even at relatively high Karlovitz numbers, as long as the progress variable variance is appropriately estimated. On the other hand, results from [116] show that strain modelling cannot be neglected in LES. However, a simple algebraic model for the progress variable variance was used in [116].

2.5.1 SDR model for LES

For RANS methodology, Bray [22, 23] showed that the averaged reaction rate of progress variable is directly related to averaged scalar dissipation rate when the Damköhler number is large, see Eq. (2.19). The validity of this relation for low Damköhler number flames was also demonstrated in [37, 40] for RANS approach and its applicability to model filtered reaction rate for LES was shown in [61, 77]. Dunstan *et al.* [61] performed an *a priori* analysis with DNS, using single-step chemistry and filtering explicitly the data with different filter sizes. They showed that the qualitative behaviours of $\overline{\dot{\omega}}$ and $\overline{\rho}\widetilde{N}_c/(2C_m-1)$ are significantly different when the filter width, Δ, is smaller than the laminar thermal thickness, δ_{th}. This is because the Bray model of Eq. (2.19) assumes a PDF which is bimodal, which does not hold when $\Delta < \delta_{th}$ because of the partial resolution of the flame in LES. The model is expected to hold when $\Delta \gg \delta_{th}$, since in this case the filter includes relatively large amounts of both burnt and unburnt gases. Following this study [61], the Favre filtered scalar dissipation rate is expressed as a sum of resolved and unresolved contributions as

$$\overline{\rho}\widetilde{N}_c = \overline{\rho\,\mathscr{D}_c}(\nabla\widetilde{c}\cdot\nabla\widetilde{c}) + \overline{\rho}\widetilde{\varepsilon}_c. \tag{2.21}$$

The unresolved SDR of c, $\widetilde{\varepsilon}_c$, is related to SGS phenomena. Simple models for $\widetilde{\varepsilon}_c$ based only on turbulence scale such as $\widetilde{\varepsilon}_c \approx \mathscr{K}\,\widetilde{\mathscr{D}}_c\sigma^2_{c,\mathrm{sgs}}/\Delta^2$, where $\mathscr{K}$ is usually a constant of order one, would give an inaccurate representation of the sub-grid SDR because of the missing effects of dilatation, reaction and flame-turbulence interaction terms which may be at leading order in combustion [225], as also supported by DNS results [150, 175, 225]. Thus, such models are unphysical and would require *ad hoc* tuning of the modelling constant. Dunstan *et al.* [61] proposed a model which involves all these relevant effects. The sub-grid SDR is modelled in this case as

$$\widetilde{\varepsilon}_c = \mathscr{F}\left[2K_c\frac{s_L}{\delta_{th}} + (C_3 - \tau C_4 \mathrm{Da}_\Delta)\left(\frac{2u'_\Delta}{3\Delta}\right)\right]\frac{\widetilde{c}(1-\widetilde{c})}{\beta_c}, \tag{2.22}$$

where $\mathscr{F} = 1 - \exp(-\theta_5 \Delta^+)$ with $\theta_5 = 0.75$ and $\Delta^+ = \Delta/\delta_{th}$ is the normalised filter width. The factor $\mathscr{F}$ ensures that $\widetilde{N}_c \to N_c$ when $\Delta^+ \to 0$ [61]. The planar laminar flame speed is denoted as s_L. The SGS velocity scale is u'_Δ which is to be modelled and the sub-grid scale Damköhler number is $\mathrm{Da}_\Delta = \left(\Delta^+/u'^+_\Delta\right)$ with $u'^+_\Delta = u'_\Delta/s_L$. The heat release parameter, τ, can be a constant or can also be defined using mixture density as $\tau = \rho_u/\overline{\rho} - 1$ and it is observed that the numerical results to be reported in §5.3 are not unduly influenced by this choice. If the reactant mixture is stratified then the later definition is more suited as it can capture spatial variation in τ.

The thermo-chemical parameter, K_c, in Eq. (2.22) is given as [120]:

$$K_c = \frac{\delta_{th}}{s_L} \frac{\int_0^1 [\rho N_c \nabla \cdot \mathbf{u}]_L \, f(c) \;\; \mathrm{d}c}{\int_0^1 [\rho N_c]_L \, f(c) \;\; \mathrm{d}c} \tag{2.23}$$

where $\mathbf{u}$ is the velocity vector. This parameter is taken to be $K_c = 0.79\,\tau$ for the flames studied here. The other parameters C_3 and C_4 in Eq. (2.22) are not free parameters and they are related to SGS Karlovitz number defined as $\mathrm{Ka}_\Delta = \sqrt{u'^{+3}_\Delta/\Delta^+}$. These parameters are given by $C_3 = 1.5\sqrt{\mathrm{Ka}_\Delta}/(1+\sqrt{\mathrm{Ka}_\Delta})$ and $C_4 = 1.1/(1+\mathrm{Ka}_\Delta)^{0.4}$ [61].

The only one parameter which needs a close attention is β_c in Eq. (2.22) and this parameter is related to strong interaction among flamelet curvature, spatial variation of molecular diffusivity and the spatial gradient of reaction rate resulting from the former two effects [39, 78]. This effect is important in premixed combustion because of inherently strong coupling between reaction rate and molecular diffusion in premixed flamelets. Both steady and unsteady RANS calculations of a variety of turbulent premixed flames in various configurations using the RANS counterpart of Eq. (2.22) suggested a reasonably robust value of 6.7 for β_c [2–5, 120, 206, 228]. However, this value cannot be simply adopted for LES because of the difference in scales involved for combustion modelling between RANS and LES. For example, Dunstan *et al.* [61] showed that $\beta_c = 2.4$ worked well for their *a priori* testing of Eq. (2.22). Furthermore, this parameter was observed to vary with τ [77] and possibly with turbulence Reynolds number also. Hence, specifying β_c value for this study is postponed until the discussion in Chapter 5. The implementation of this model and related sub-models will be discussed in Chapter 3.

2.6 Summary

The present work focuses on flamelet modelling for LES of turbulent premixed combustion. As shown in this chapter, flamelet models have been largely used in the literature; however their strengths and weaknesses are not fully understood. Previous models have been based on linear relaxation model for the SDR and/or algebraic models for the SGS-variance of the key

scalars. These models, as will be shown in the next chapter, can be physically inconsistent and lead to inaccurate results. In this work the SDR and the SGS-variance of progress variable are modelled in a more physically meaningful way, respectively using Eq. (2.22) and a transport equation for these two quantities. The potentials of flamelet modelling is revised in this light by simulating premixed combustion in corrugated-flamelets, thin reaction zones and distributed reaction zones regimes of premixed combustion. Two models are used for this purpose, one based on fast chemistry assumption, Eq. (2.19), and another based on presumed PDF approach. Their relative ability to predict the premixed flame structure is assessed. It will be shown in particular that when the variance equation is carried in the simulation and the various SGS closures related to combustion involve the physical aspects of premixed combustion, strain effect is not needed in the LES modelling. This is an unexpected result for common views in the literature and opens new avenues to investigate flamelets models.

Chapter 3

Numerical modelling

The governing equation are presented in Chapter 2 and as noted there, SGS processes need to be modelled. Common models for residual stresses are used and the particular ones relevant for this thesis are discussed first. The particular numerical scheme and discretization technique are then introduced, before presenting reaction rate closures used in this study.

3.1 Residual stresses and common practices in LES

3.1.1 Eddy diffusivity models

Eddy viscosity models for LES are based on the assumption that the anisotropic residual tensor is aligned to the filtered strain. For variable density flows this can be expressed as

$$\widetilde{\tau}_{ij}^{r} = -2\nu_T \left(\widetilde{S}_{ij} - \frac{1}{3}\widetilde{S}_{kk}\delta_{ij} \right) \tag{3.1}$$

where

$$\widetilde{S}_{ij} = \frac{1}{2}\left(\frac{\partial \widetilde{u}_i}{\partial x_j} + \frac{\partial \widetilde{u}_j}{\partial x_i} \right) \tag{3.2}$$

is the Favre-filtered strain and δ_{ij} is the Kronecker delta. This assumption was shown to be incorrect [154], since the principal directions of residual tensor and filtered strain are not aligned. For this reason, eddy-viscosity models tend to overestimate the residual stress and consequently are more dissipative than required. Different models for the residual viscosity exist in the literature and a summary can be found for example in [196]. These models were originally developed for incompressible flows and then adapted to variable density flows such as combustion. A brief overview of those relevant for this work is given below in the framework of variable density flows.

Zero-equation models

Of this class are the classical Smagorinsky model [217] and the localised dynamic Smagorinsky model [141] used in this work. The classical Smagorinsky model assumes a mixing length hypothesis and is expressed as

$$\nu_T = (C_s\Delta)^2|\widetilde{S}| \tag{3.3}$$

where $|\widetilde{S}| = (2\widetilde{S}_{ij}\widetilde{S}_{ij})^{1/2}$ is the characteristic strain. The Smagorinsky constant, C_s, is found assuming a Kolmogorov energy spectrum in the inertial range, and that the mean rate of energy transfer from filtered to residual scales equals the viscous dissipation. It can be found that the filtered strain is dominant around the cut-off scale Δ and that the characteristic strain scales as $|\widetilde{S}| \sim \Delta^{2/3}$ [196].

The dynamic Smagorinsky model assumes scale invariance and exploits the resolved scales to compute the model coefficient C_s. The original model by Germano *et al.* [81] computes one global averaged value for the whole flow field and assumes that the model constant is filter-invariant. A localised formulation was proposed first by Goshal *et al.* [83]. In this work the localised mixed formulation by Lilly [141] is used, which computes C_s locally and also does not rely on the assumption of filter-invariance. Dynamic procedures can capture the physics in shear flows and near walls by automatically lowering the magnitude of C_s. This constant may assume negative values (backscatter) leading to numerical instabilities [212], thus it must be spatially averaged [154, 183]. Dynamic models can also compensate the effect of errors in the length scale due to non-uniform filters [65], thus they are useful when non-uniform grids are employed.

One-equation models

Models described previously relate the residual stress tensor to the filtered strain at the same time and in the neighbourhood of a point. A better approach would be to incorporate history and non-local effects, by adding one equation for the residual kinetic energy, k_r, defined as [196]:

$$k_r = \frac{1}{2}\left(\widetilde{u_i u_i} - \widetilde{u}_i\widetilde{u}_i\right),$$

Let's notice that by definition this is kinetic energy and not turbulent kinetic energy. In LES, the filter width, Δ, can be assumed as characteristic length for k_r, thus an additional equation, i.e. for the energy dissipation, is not needed [52]. The residual viscosity is modelled in this case as [55]

$$\nu_T = C_\nu k_r^{1/2}\Delta \tag{3.4}$$

where $C_v \approx 0.1$ and a dynamic evaluation for C_v is described in [83]. Assuming uniform filter, the transport equation for k_r can be written as [35]

$$\begin{aligned}\frac{\partial \overline{\rho} k_r}{\partial t} =& -\frac{\partial \overline{\rho} k_r \widetilde{u}_j}{\partial x_j} - \frac{R}{C_p}\frac{\partial \widetilde{q''_j}}{\partial x_j} + \frac{\partial \widetilde{\tau}^R_{ij}\widetilde{u}_i}{\partial x_j} - \tau_{ij}\widetilde{S}_{ij} + \frac{\partial}{\partial x_j}\left[\widetilde{\mu}\frac{\partial k_r}{\partial x_j}\right] \\ &+ \frac{\partial f_j}{\partial x_j} - \varepsilon_k - \varepsilon_c + \Pi + K_\mu + K_d\end{aligned} \tag{3.5}$$

where $R = R_0/W$ is the specific gas constant and $\widetilde{q''_j}$ is the residual heat flux, defined as

$$\widetilde{q''_j} = C_p\left(\widetilde{\overline{\rho} T u_j} - \overline{\rho}\widetilde{T}\widetilde{u}_j\right) \tag{3.6}$$

The terms f_j, ε_k, ε_c and Π are respectively turbulent transport, residual dissipation, dilatational dissipation and pressure dilatation term, and they are defined as

$$f_j = \frac{1}{2}\overline{\rho}\left(\widetilde{u_i u_i}\widetilde{u}_j - \widetilde{u_i u_i u_j}\right) + \frac{1}{3}\left(\overline{\mu u_j \frac{\partial u_k}{\partial x_k}} - \widetilde{\mu}\widetilde{u}_j\frac{\partial \widetilde{u}_k}{\partial x_k}\right) \tag{3.7}$$

$$\varepsilon_k = \overline{\mu \frac{\partial u_i}{\partial x_j}\frac{\partial u_i}{\partial x_j}} - \widetilde{\mu}\frac{\partial \widetilde{u}_i}{\partial x_j}\frac{\partial \widetilde{u}_i}{\partial x_j} \tag{3.8}$$

$$\varepsilon_c = \frac{1}{3}\left[\overline{\mu\left(\frac{\partial u_k}{\partial x_k}\right)^2} - \widetilde{\mu}\left(\frac{\partial \widetilde{u}_k}{\partial x_k}\right)^2\right] \tag{3.9}$$

$$\Pi = \overline{p\frac{\partial u_k}{\partial x_k}} - \overline{p}\frac{\partial \widetilde{u}_k}{\partial x_k} \tag{3.10}$$

The remaining terms are

$$K_\mu = \frac{\partial}{\partial x_j}\left[\overline{\mu\frac{\partial(\frac{1}{2}u_i u_i)}{\partial x_j}} - \widetilde{\mu}\frac{\partial \frac{1}{2}\widetilde{u_i u_i}}{\partial x_j}\right] \tag{3.11}$$

$$K_d = \left[\overline{\left(u_i\frac{\partial u_j}{\partial x_i} - u_j\frac{\partial u_k}{\partial x_k}\right)\frac{\partial \mu}{\partial x_j}} - \left(\widetilde{u}_i\frac{\partial \widetilde{u}_j}{\partial x_i} - \widetilde{u}_j\frac{\partial \widetilde{u}_k}{\partial x_k}\right)\frac{\partial \widetilde{\mu}}{\partial x_j}\right] \tag{3.12}$$

Models proposed in the literature for k_r are mostly based on incompressible flows [83, 124], in which terms ε_c, Π, K_μ and K_d are usually negligible. Models for $\widetilde{q''_j}$, f_j and ε_k can be computed either statically or dynamically and their description is reminded to the literature (see for example [35, 54, 83, 124, 196]). A number of authors [71, 98, 156, 171] has shown that one equation models improve accuracy even in variable density flows. One equations models are also beneficial in case an estimation for the sub-grid velocity is needed (see §3.3.3), and

because they allow for further investigations on statistical sub-grid properties, which can be exploited for example in PDF approaches.

3.1.2 One equation model for LES of premixed combustion

An attempt to model the pressure dilatation has been recently presented by Chai and Mahesh [35] for LES of compressible non-reacting flows. However, in the case of combustion, the dilatation term is strongly influenced by the reaction rate and this influence must be taken into account while modelling. In the assumption of low Mach number, Eq. (3.5) can be re-arranged as

$$\overline{\rho}\frac{Dk_r}{Dt} = \frac{\partial}{\partial x_j}\left(\widetilde{\mu}\frac{\partial k_r}{\partial x_j}\right) + \widetilde{u}_i\frac{\partial \tau_{ij}^R}{\partial x_j} - \frac{\partial f_j}{\partial x_j} - \varepsilon_k + \Pi, \tag{3.13}$$

This modelled equation is similar to that in [35] for compressible flow except for the dilatational dissipation resulting from compressibility and that the residual heat flux in Eq. (3.6) is written using state equation as $\widetilde{q_j''} = C_p(\overline{pu_j} - \overline{p}\widetilde{u}_j)/R$ and its divergence in Eq. (3.5) is subtracted from Eq. (3.10). The pressure dilatation term is thus written as

$$\Pi \equiv \widetilde{u}_i\frac{\partial \overline{p}}{\partial x_i} - \overline{u_i\frac{\partial p}{\partial x_i}} = \left[\overline{p\frac{\partial u_i}{\partial x_i}} - \overline{p}\frac{\partial \widetilde{u}_i}{\partial x_i}\right] - \left[\overline{\frac{\partial pu_i}{\partial x_i}} - \frac{\partial \overline{p}\widetilde{u}_i}{\partial x_i}\right] \tag{3.14}$$

By using an analogy to turbulent kinetic energy (TKE) equation for RANS [142], this term is modelled as

$$\Pi \approx 0.5\,\overline{\dot{\omega}}\widetilde{c}\,\tau^2 s_L^2 + \frac{\widetilde{\mu}_T}{\overline{\rho}\,\widetilde{T}\,\mathrm{Pr}_T}\frac{\partial \widetilde{T}}{\partial x_k}\frac{\partial \overline{p}}{\partial x_k} \tag{3.15}$$

where $\mathrm{Pr}_T \approx 1$ is the turbulent Prandtl number and $\mu_T = \overline{\rho}\nu_T$ is the dynamic residual viscosity.

3.1.3 Relation between LES filter, grid spacing and numerical scheme

Let's distinguish between residual motion, which is the motion occurring below the filter-width scale, and sub-grid scale motion, which is the motion occurring below the grid size. The LES momentum equation in Eqs. (2.10) becomes formally identical to the laminar one, Eq. (2.2), if one excludes the residual stress term. Thus, this term hides information about the LES filter. Pope [196] showed that in homogenous and isotropic turbulence, the Smagorinsky model has a unique implied filter, the Smagorinsky filter, obtained on the basis of *a priori* DNS analysis. In particular, he noticed that the shape of the filter depends on the form assumed for the dissipation spectrum. Further analyses showed that the Smagorinsky model implies a filter which is close to a Gaussian one. These analyses used a filter size, imposed through the Smagorinsky term, larger than the grid size to exclude possible effects of the numerical grid.

When the filter size is linked to the grid spacing, numerical grid and discretization schemes affect the LES filter [125, 161]. This link appears explicitly in case of Smagorinsky-like models (see for example Eq. (3.3)). Pope [196] showed that in this case the grid must be refined enough and at least second order spatial schemes are required in order to avoid that numerical-diffusion effects compromise the solution. More recently some authors have tried to unlink residual model and grid spacing by using explicitly filtered LES (EFLES) models in non-reacting flows (see for example [19, 153, 199, 235]). Although these methods are yet to be applied for reacting flows, the focus of the present study is not on this kind of LES. In Smagorinsky-like models one can reduce this dependence on grid spacing by choosing Δ much larger than the grid size. However, this would imply a significant increase of computational effort, as will be shown in the next paragraph. This approach is unpractical for the purposes of this work, and the filter size required in Eqs. (3.3) and (3.4) is set to the cubic root of the cell volume, following common practice. Additional analyses to evaluate effects of grid spacing and numerical scheme on the solution are left to future work. The final shape of the filter will be supposed to be Gaussian for simplicity, following the DNS analysis in [196]. Because of this choice, residual motion and SGS motion will be referred to indiscriminately from here onwards.

Choice of grid size

The choice of the grid size in a proper LES is usually associated with the resolution of at least the 80% of TKE [196], which corresponds usually to 4 to 5 cells at least within the integral length scale, Λ. However, if the filter size is bigger than the cell size, the amount of turbulent kinetic energy at the residual level must depend on the filter size rather than the grid size as noted in the previous paragraph. An estimation of the amount of residual kinetic energy in terms of the integral length scale is as follows. Since the residual kinetic energy in this analysis must represent the amount of energy 'lost' at residual scales, k_r must be related to the residual model. The residual kinetic energy can be expressed as $k_r = 3u'^2_\Delta/2$, where u'_Δ is the residual velocity scale, which can be related directly to the eddy viscosity model as [196] $u'_\Delta = C_q \nu_T/\Delta$, where C_q is a constant. Modelling ν_T with Eq. (3.3) for the purpose of this analysis, one can write

$$k_r = \frac{3}{2}u'^2_\Delta = \frac{3}{2}C'_q\Delta^2\widetilde{S}_{ij}\widetilde{S}_{ij}.$$

where $C'_q = 2C_q^2C_s^4$. Assuming a Kolmogorov cascade of the kinetic energy in the inertial range, the mean strain could be approximated using rms velocity, u', and integral length scale, Λ. Thus, taking the statistical mean of above equation one obtains

$$\langle k_r\rangle \approx \frac{3}{2}\langle C'_q\rangle\Delta^2\frac{u'^2}{\Lambda^2} = \langle C'_q\rangle k\left(\frac{\Delta}{\Lambda}\right)^2$$

where k is the mean TKE, and the mean of the products was approximated with the product of the means just to obtain an order of magnitude scale. Following this, the SGS kinetic energy scales as

$$\langle k_r \rangle \sim k \left(\frac{\Delta}{\Lambda} \right)^2 \tag{3.16}$$

This equation does not account for grid effects and indicates that the amount of residual kinetic energy increases with the filter size, at least when Smagorinsky-like models are used. This result must be taken into account when using a filter size larger than the grid size.

3.1.4 Comparison with experiments

Strictly, statistics should be collected for each time and spatial location performing an ensemble average over hundreds of experiments. This approach is impractical in both experiments and simulations and, unless particular properties must be studied, ergodicity theorem is used to apply time average in place of ensemble average [69]. In experiments, data are sampled with a certain frequency and spatial accuracy. Non-intrusive, laser diagnostic techniques (i.e. LDA, Raman and Raylegh scattering, CARS, PLIF, PIV) are capable to reach very high frequencies in time, therefore the signal in time is usually directly comparable with that of a typical LES. The accuracy in space is of order of millimetres, i.e. the signal is filtered in space. For this reason results from LES should be processed appropriately before being compared with experiments. Another issue comes for variable density flows. An averaged quantity is usually obtained by simply time-averaging a filtered LES quantity, i.e. assuming $\langle \phi \rangle \approx \langle \overline{\phi} \rangle$. Favre-averaged quantities are instead obtained from Favre-filtered ones, as [191]

$$\frac{\langle \rho \phi \rangle}{\langle \rho \rangle} \approx \frac{\langle \overline{\rho \phi} \rangle}{\langle \overline{\rho} \rangle} \tag{3.17}$$

If the signal in the experimental technique is proportional to density, than Eq. (3.17) can be used to compare LES and experimental results. However, the signals in techniques like Raman and Rayleigh scattering do not depend on density, thus LES results and experiments are not directly comparable. A relation between Reynolds- and Favre-averaged first order moments was derived by Kolla and Swaminathan [121] in the hypothesis of a β-distribution for a normalised variable ϕ bounded in the interval $[0,1]$. This relation is

$$\langle \overline{\phi} \rangle \;=\; \langle \widetilde{\phi} \rangle + \frac{\tau}{(1+\tau\langle \widetilde{\phi} \rangle)} \langle \sigma_\phi^2 \rangle \tag{3.18}$$

where $\langle \sigma_\phi^2 \rangle = \langle \sigma_{\phi,\mathrm{sgs}}^2 \rangle + \langle \sigma_{\phi,\mathrm{res}}^2 \rangle$ is the total variance, sum of SGS and resolved contribution. The resolved variance is obtained as $\langle \sigma_{\phi,\mathrm{res}}^2 \rangle = \langle (\widetilde{\phi} - \langle \widetilde{\phi} \rangle)^2 \rangle$, while the SGS variance, $\sigma_{\phi,\mathrm{sgs}}^2$,

must be modelled or computed using a transport equation. The symbol $\langle\ \rangle$ is used here to indicate either simple or mass-weighted time average respectively for $\overline{\phi}$ and $\widetilde{\phi}$, and in general one can infer which one is appropriate from the nature of the LES variable, e.g. $\langle\rho\rangle$ indicates simple average of $\overline{\rho}$ in time and $\langle c\rangle$ indicates mass weighted average of $\widetilde{c}$. The explicit symbolism, like $\langle\widetilde{\phi}\rangle$ and $\langle\overline{\phi}\rangle$ in Eq. (3.18), is used rather than simply $\langle\phi\rangle$ to distinguish these quantities when $\langle\overline{\phi}\rangle$ is computed using Eq. (3.18).

It is worth noting that the SGS variance contribution should always be included when comparing second order moments to experimental results [191]. This is not always possible as the SGS variance of a generic quantity is missing in the LES framework unless a model is provided or a transport equation is computed. The only SGS variance which is always computed in the LES framework used in this thesis is the SGS kinetic energy, which will always be included in the comparison of TKE to be shown in the next chapters. For other second order statistics the inclusion of the SGS variance will be discussed from case to case.

3.2 Discretisation

The numerical discretization used in this work is explained next before discussing the filtered reaction rate closures, so that the implementation of these closures can also be described unambiguously.

3.2.1 Numerical schemes

The LES equations (2.10) are solved using a commercial code, Precise-MB [8], which uses a finite volume approach. This approach is summarised below. The generic transport equation for a Favre-filtered variable $\widetilde{\phi}$ with source term $\overline{\dot{\omega}}$ is written in its integral form as

$$\frac{d}{\mathrm{d}t}\int_{\mathscr{V}}\overline{\rho}\widetilde{\phi}\,\mathrm{d}\mathscr{V}+\int_{\partial\mathscr{V}}\overline{\rho}(\widetilde{u}_i\cdot n_i)\widetilde{\phi}\,\mathrm{d}S=\int_{\partial\mathscr{V}}\left(\widetilde{\mu}+\frac{\mu_T}{\mathrm{Sc}_T}\right)\frac{\partial\widetilde{\phi}}{\partial x_i}\cdot n_i\,\mathrm{d}S+\int_{\mathscr{V}}\overline{\dot{\omega}}\,\mathrm{d}\mathscr{V} \tag{3.19}$$

and is solved at each cell of the domain. The convective fluxes are approximated at each face of the cell as

$$\int_{S_f}\overline{\rho}(\widetilde{u}_i\cdot n_i)\widetilde{\phi}\,\mathrm{d}S\approx(\overline{\rho}\widetilde{u}_i\cdot n_i)S_f\widetilde{\phi}_f \tag{3.20}$$

where S_f is the f-th boundary face of the cell, n_i is the component of the unity normal to this surface in direction i and $\widetilde{\phi}_f$ is the value of $\widetilde{\phi}$ at the center of the face. The latter can be expressed in function of the values $\widetilde{\phi}_P$ and $\widetilde{\phi}_{P+1}$ at the center of the contiguous cells using a

second order interpolation. Numerical instability can arise when using high order schemes in regions of strong gradients produced by the flame. This instability can be treated either ensuring a minimum number of cells within the flame thickness, or using a filter size bigger than the cell size as proposed in [17], or using flux limiters (see for example [135]). In the first case one reduces the relative strength of the convection in respect to the diffusion, which would be small if the cell size is bigger than the flame thickness. This approach leads to large grid size and is thus unpractical for the LES considered here. The other two approaches consist in increasing the diffusion term instead. When the filter size is bigger than the cell size, the additional diffusion comes from the SGS model, which is usually proportional to Δ. This approach is also unpractical because Δ must remain small to have a residual kinetic energy smaller than 20% of the TKE, as discussed in §3.1.3. When a limiter is used, the additional diffusion comes from the numerical scheme. Since the amount of this numerical diffusion can be directly controlled, this approach is preferred. In Precise a blending factor can be used and $\widetilde{\phi}_f$ is evaluated as

$$\widetilde{\phi}_f = \widetilde{\phi}_f^{(I)} + \beta\left(\widetilde{\phi}_f^{(II)} - \widetilde{\phi}_f^{(I)}\right) \tag{3.21}$$

where $\widetilde{\phi}_f^{(I)}$ and $\widetilde{\phi}_f^{(II)}$ are the values obtained using first and second order approximation respectively.

Diffusive fluxes are approximated as

$$\int_{S_f} \widetilde{\mathscr{D}}_\phi \frac{\partial \widetilde{\phi}}{\partial x_i} \cdot n_i \, \mathrm{d}S \approx \left(\widetilde{\mathscr{D}}_\phi \frac{\partial \widetilde{\phi}}{\partial x_i} \cdot n_i\right)_f S_f \tag{3.22}$$

where $\widetilde{\mathscr{D}}_\phi = (\widetilde{\mu} + \mu_T/\mathrm{Sc}_T)$. The gradients at the face centre are computed with a second order scheme and then interpolated at the cell centre as for the convective flux.

The source term $\overline{\dot{\omega}}$ cannot be put in conservative form and is approximated on the cell i of volume $\mathscr{V}_i$ as

$$\int_{\mathscr{V}_i} \overline{\dot{\omega}} \, \mathrm{d}\mathscr{V} \approx \mathscr{V}_i \langle \overline{\dot{\omega}} \rangle_{\mathscr{V}_i} \tag{3.23}$$

where $\langle \, \rangle_{\mathscr{V}_i}$ refers to volume average on cell i. The volume average is then approximated to the value at the cell centre (second order approximation), $\langle \overline{\dot{\omega}} \rangle_{\mathscr{V}} \approx \overline{\dot{\omega}}_i$.

Finally, time discretisation is performed using a second order Euler scheme in order to have a good correlation in time. A relaxation factor can be used for reacting cases to avoid numerical instabilities if the time step is small enough and sub-loops are used. Five sub-iterations are used at each time step for all variables and all simulations in this thesis. Additional details on the finite volume approach can be found for example in [65, 135].

3.2.2 Solver

The final set of discretised equations in Precise-MB [8] is in the form

$$C\underline{\phi} = \underline{S} \tag{3.24}$$

where C is the coefficients matrix coming from the discretisation, $\underline{\phi}$ is the vector of the unknowns and $\underline{S}$ is the vector of the known terms (boundary conditions and source terms). The linear system in Eq. (3.24) is solved using the TDMA algorithm [65], which needs a tridiagonal matrix. Matrix C is thus first split as $C = A - B$, where A is its diagonal. The new system is

$$A\underline{\phi} = B\underline{\phi} + \underline{S} \tag{3.25}$$

and it is solved iteratively until a prefixed tolerance is reached. Additional details can be found in [65].

All simulations discussed in later chapters have been run using 2.60GHz eight-core Sandy Bridge E5-2670 processors of the Darwin cluster at the University of Cambridge. The time step in each simulation is constant and is specified to have a maximum CFL number of 0.3 everywhere in the numerical domain. The LES results for each simulation are averaged first over the sampling period and in azimuthal direction in case of comparison with radial variation of mean quantities. The reacting cases to be presented in later chapters have been performed after validating cold flow. These cold flow validations are presented in Chapter 4.

3.3 Filtered reaction rate modelling

Using Eqs. (2.11) and (2.13), the progress variable equation in the set of Eqs. (2.10) becomes

$$\frac{\partial \overline{\rho}\widetilde{c}}{\partial t} + \frac{\partial \overline{\rho}\widetilde{u}_j\widetilde{c}}{\partial x_i} = \frac{\partial}{\partial x_i}\left[\left(\widetilde{\mu} + \frac{\mu_T}{\mathrm{Sc}_T}\right)\frac{\partial \widetilde{c}}{\partial x_i}\right] + \overline{\dot{\omega}} \tag{3.26}$$

Since in premixed combustion diffusion and turbulent mixing are strongly coupled with the reaction rate, this coupling must be retained in the modelling. Equations (2.11) and (2.13) come from incompressible models, thus this coupling has to be considered in the reaction rate model. In this work three closures for the filtered reaction rate are employed, one based on algebraic expression and two on presumed PDF approach. These closures are discussed below. A fourth closure, based on power-law, is also discussed in this section.

3.3.1 Algebraic closure

The filtered reaction rate of the progress variable is related directly to its scalar dissipation rate using Eq. (2.19), in which the SDR is modelled with Eqs. (2.21)-(2.22). This model is derived from a transport equation for $\widetilde{N}_c$, which involves reaction, diffusion and turbulent transport [61, 77]. Thus, the algebraic closure accounts for the coupling between these three terms. This model is derived under the assumption of high Reynolds number and filter width larger than the laminar flame thickness. Because of this, the turbulent flame speed does not converge to the laminar flame speed when the flow becomes laminar. Nevertheless, similar models used for RANS have shown that the turbulent flame speed is well predicted in this modelling framework [147].

This model is implemented as follows. Equation (3.23) is used to approximate the volume integral of $\overline{\dot{\omega}}$. If a regress variable is used, then $\overline{\dot{\omega}}$ is negative, and its value at the centre of cell i can be written as

$$\overline{\dot{\omega}}_{c_i} = -\left[C_1\widetilde{D}\left(\frac{\partial\widetilde{c}}{\partial x_j}\frac{\partial\widetilde{c}}{\partial x_j}\right) + \mathscr{F}C_1C_2\widetilde{c}(1-\widetilde{c})/\beta_c\right]_i \tag{3.27}$$

where

$$\begin{aligned} C_1 &= \frac{2}{2C_m - 1}\overline{\rho} \qquad \text{and} \\ C_2 &= 2K_c\frac{s_L}{\delta_{th}} + (C_3 - \tau C_4 \mathrm{Da}_\Delta)\left(\frac{2}{3}\frac{u'_\Delta}{\Delta}\right) \end{aligned}$$

Equation (3.27) is non-linear in $\widetilde{c}$ and involves its gradient. The source term is written as

$$\overline{\dot{\omega}} \approx S_p\widetilde{c} + S_u \tag{3.28}$$

Where S_p and S_u contribute to the LHS and RHS of Eq. (3.24), respectively. To ensure diagonal dominance and stability in the linear system of Eq. (3.24), the conditions

$$\begin{aligned} S_u &\geq 0 \qquad \text{and} \\ S_p &\leq 0 \end{aligned} \tag{3.29}$$

must be fulfilled. The only term which can be negative in Eq. (3.27) is

$$C_{34} = (C_3 - \tau C_4 \mathrm{Da}_\Delta)$$

where C_3 and C_4 are defined in §2.5.1. In figure 3.1, terms in C_2 are compared to each other for different values of u'^{+}_{Δ} and two values of Δ^{+}. Values of s_L, δ_{th} and τ are taken from laminar 1D computation of a premixed stoichiometric methane-air flame. To avoid the infinity for $u'^{+}_{\Delta} \to 0$, C_2 is written as

$$C_2 = \frac{2}{3}\frac{s_L}{\delta_{th}}\left[3K_c + (C_3^* - \tau C_4^* \mathrm{Da}_\Delta)\right] \tag{3.30}$$

where $C_3^* = C_3 u'^{+}_{\Delta}/\Delta^{+}$ and $C_4^* = C_4 u'^{+}_{\Delta}/\Delta^{+}$. C_{34} becomes negative for a certain value of $u'_\Delta = u^*_\Delta$ which increases with Δ^{+}. Since C_3^* and $\tau C_4^* Da_\Delta$ vary monotonically with u'^{+}_{Δ}, the largest negative value is for $u'_\Delta = 0$. Since $3K_c$ is always larger than $(C_3^* - \tau C_4^* \mathrm{Da}_\Delta)$ when $u'^{+}_{\Delta} = 0$, C_2 is always positive. Same considerations apply for different fuels and equivalence

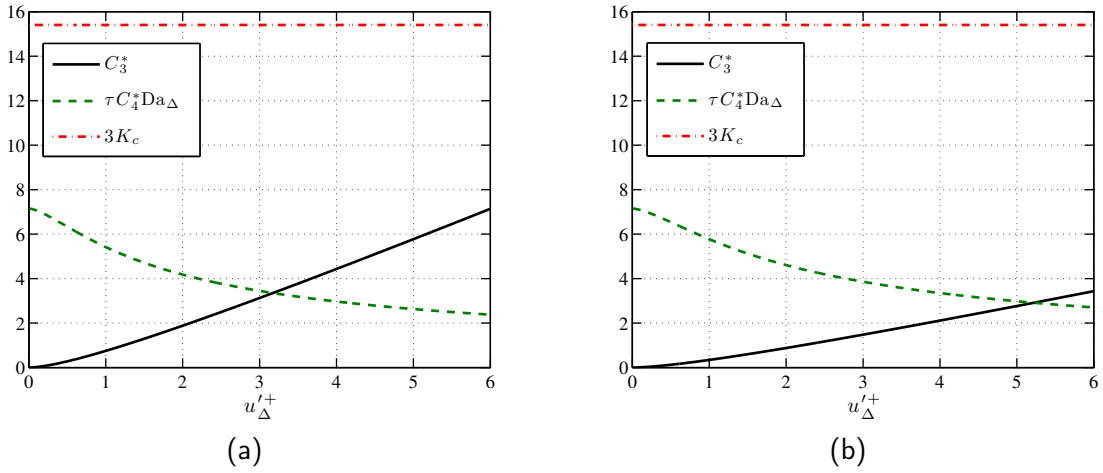

Fig. 3.1 Comparison of different terms of Eq. (3.30) for increasing values of $u'^{+}_{\Delta} = u'_\Delta/s_L$, and for (a) $\Delta = 4\delta_{th}$ and (b) $\Delta = 8\delta_{th}$.

ratios. Thus, an expression which fulfils the conditions in Eq. (3.29) is

$$S_u = -C_0 \widetilde{\mathscr{D}}_c \left(\frac{\partial \widetilde{c}}{\partial x_i}\frac{\partial \widetilde{c}}{\partial x_i}\right)_n + \mathscr{F} C_0 C_2 \widetilde{c}_n^2/\beta_c \tag{3.31}$$

$$S_p = -\mathscr{F} C_0 C_2/\beta_c \tag{3.32}$$

Subscript n refers to the current time step, as terms in Eq. (3.31) are updated each sub-iteration. The negative term in equation (3.31) does not affect the stability of system in in Eq. (3.24), since its magnitude is generally small. It is worth noting that although many constant are involved in Eq. (2.22), only u'_Δ and β_c are tuneable while all other parameters were found *a priori* using DNS [61].

3.3.2 Presumed PDF approaches

A. Unstrained flamelet model

A closure for the filtered reaction rate using the unstrained flamelet is well known and this closure is written as

$$\overline{\dot{\omega}} = \int_0^1 \dot{\omega}(\zeta)\, P(\zeta;\widetilde{c},\sigma^2_{c,\mathrm{sgs}})\ \mathrm{d}\zeta \ = \overline{\rho}\int_0^1 \dot{W}(\zeta)\, \widetilde{P}(\zeta;\widetilde{c},\sigma^2_{c,\mathrm{sgs}})\ \mathrm{d}\zeta, \tag{3.33}$$

where $\widetilde{P}(\zeta;\widetilde{c},\sigma^2_{c,\mathrm{sgs}})$ is the density weighted sub-grid PDF of c and $\dot{\omega} = \rho\dot{W}$ is the flamelet reaction rate obtained from a freely propagating unstrained planar laminar flame for a given thermo-chemical condition. The symbol ζ is the sample space variable for reaction progress variable c. This closure is analogous to the RANS counterpart and was originally proposed for RANS by Bradley *et al.* [21] and then used by Cook and Riley [50] for LES, and it has been used in many past LES of premixed combustion. The sub-grid PDF is obtained using a presumed shape such as β-function, which has been used for reacting scalars in many past works, see for example [57, 128, 132, 163, 239]. This presumed shape is given by

$$\widetilde{P}(\zeta) = \frac{\zeta^{a-1}(1-\zeta)^{b-1}}{\Psi(a,b)} \quad \text{with} \quad \Psi(a,b) = \int_0^1 \zeta^{a-1}(1-\zeta)^{b-1}\ \mathrm{d}\zeta \tag{3.34}$$

where the parameters a and b are related to $\widetilde{c}$ and $\sigma^2_{c,\mathrm{sgs}}$ through

$$a = \widetilde{c}\left[\frac{\widetilde{c}(1-\widetilde{c})}{\sigma^2_{c,\mathrm{sgs}}} - 1\right], \quad b = \frac{(1-\widetilde{c})\,a}{\widetilde{c}} \tag{3.35}$$

This density weighted sub-grid PDF is related to its unweighted counterpart through $\overline{\rho}\,\widetilde{P} = \rho\, P$. The Favre-filtered progress variable, $\widetilde{c}$, is obtained using Eq. (3.26). The sub-grid variance is obtained using its transport equation written as

$$\begin{aligned}\overline{\rho}\frac{D\sigma^2_{c,\mathrm{sgs}}}{Dt} \approx \nabla\cdot\left[\left(\overline{\rho\mathscr{D}} + \overline{\rho}\frac{\nu_T}{\mathrm{Sc}_T}\right)\nabla\sigma^2_{c,\mathrm{sgs}}\right] + 2\overline{\rho}\left(\widetilde{\dot{W}c} - \widetilde{\dot{W}}\widetilde{c}\right) \\ -2\overline{\rho}\,\widetilde{\varepsilon}_c + 2\overline{\rho}\,\frac{\nu_T}{\mathrm{Sc}_T}\left(\nabla\widetilde{c}\cdot\nabla\widetilde{c}\right)\end{aligned} \tag{3.36}$$

It is quite straightforward to derive the above equation using the transport equations for $\widetilde{c^2}$ and $\widetilde{c}^2$ because $\sigma^2_{c,\mathrm{sgs}} = \widetilde{c^2} - \widetilde{c}^2$. The third and fourth terms of Eq. (3.36) need closures and the

reaction related term is closed using

$$\widetilde{\dot{W}c} = \int_0^1 \dot{W}\,\zeta\,\widetilde{P}(\zeta)\;\mathrm{d}\zeta, \tag{3.37}$$

which is consistent with the closure in Eq. (3.33). The algebraic closure from Dunstan et al. [61] of Eq. (2.22) is used to model the SGS SDR, $\widetilde{\varepsilon}_c$, in which the SGS variance, $\sigma^2_{c,\mathrm{sgs}}$, is used in place of $\widetilde{c}(1-\widetilde{c})$ for consistency with the transported equation. Let's notice that the last three terms in Eq. (3.36) behave like a source term and are treated similarly to Eq. (3.28), as

$$-2\overline{\rho}\widetilde{\varepsilon}_c + 2\overline{\rho}\left(\widetilde{\dot{W}c} - \widetilde{\dot{W}}\widetilde{c}\right) + 2\frac{\mu_T}{Sc_T}\frac{\partial\widetilde{c}}{\partial x_j}\frac{\partial\widetilde{c}}{\partial x_j} \approx S_p\sigma^2_{c,\mathrm{sgs}} + S_u.$$

The SGS SDR, $\widetilde{\varepsilon}_c$, is always positive and $\sigma^2_{c,\mathrm{sgs}}$ appears explicitly in its expression, thus the dissipation term is modelled implicitly. The last two terms in Eq. (3.36) are always positive and are then treated explicitly. The condition (3.29) is thus satisfied by imposing

$$\begin{aligned} S_u &= 2(\overline{\dot{\omega}c} - \overline{\dot{\omega}}\widetilde{c}) + 2\frac{\mu_T}{Sc_T}\frac{\partial\widetilde{c}}{\partial x_j}\frac{\partial\widetilde{c}}{\partial x_j} \\ S_p &= -2\overline{\rho}\frac{\widetilde{\varepsilon}_c}{\sigma^2_{c,\mathrm{sgs}}} \end{aligned}$$

where the division by $\sigma^2_{c,\mathrm{sgs}}$ only appears because of formalism and it is not actually performed in the computation. Finally, the precomputed filtered values of $\widetilde{\dot{W}}$ obtained using the unstrained flamelet model are stored in a look-up table with $\widetilde{c}$ and $\sigma^2_{c,\mathrm{sgs}}$ as controlling parameters.

It is worth noting that the integral in Eq. (3.33) can become an issue when the PDF becomes bimodal for large values of the SGS variance, as the β-function has a very sharp variation near the boundaries $\widetilde{c} = 0$ and 1, and it approaches infinity at $c = 0$ and $c = 1$ in these regions. This very sharp variation of the PDF near the boundaries can make the integration inaccurate. A common approach is to exclude points $c = 0$ and $c = 1$, find the new bounds ε and $1-\varepsilon$ by imposing

$$\int_{\varepsilon}^{1-\varepsilon} \widetilde{P}(c)\mathrm{d}c = 1 \tag{3.38}$$

and using a Newton-like algorithm, in which $\varepsilon > 0$ is the iteration parameter. In Fig. 3.2 a β-PDF is shown for $\widetilde{c} = 0.01$ and $\sigma^2_{c,\mathrm{sgs}} = 0.0089$. Using 1000 points to discretise c, a value $\varepsilon \approx 6.6 \times 10^{-7}$ is found to satisfy Eq. (3.38). The difference between the real PDF and the approximated PDF is shown in the inset for region near $c = 1$. Unless the variable

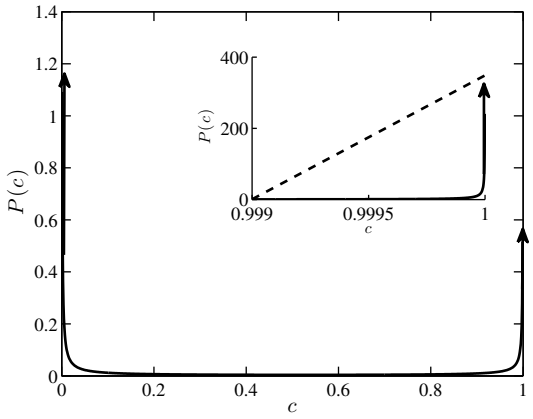

Fig. 3.2 β-PDF of c, obtained using Eq. (3.34) for $\widetilde{c} = 0.01$ and $\sigma^2_{c,\mathrm{sgs}} = 0.0089$. Arrows indicate presence of very large values. The approximated PDF, obtained using Eq. (3.38), is shown with dashed line in the inset.

to be integrated approaches zero in this region, a standard numerical integration such as the trapezoidal rule for Eq. (3.33) would yield a very poor estimate. For example, using c instead of $\dot{W}$, the analytical integral of Eq. (3.33) is $\widetilde{c}$ independently of the value of $\sigma^2_{c,\mathrm{sgs}}$. However, numerical integration with trapezoidal rule gives $\widetilde{c} \approx 0.18$, which largely over-estimates the imposed value $\widetilde{c} = 0.01$. In Fig. 3.3, isolines of $\widetilde{c}$, obtained using Eq. (3.33) (with c integrated instead of $\dot{W}$) and (3.38), are shown. These isolines are not parallel, despite 10,000 points are used to discretise c. This numerical issue is relevant whenever a quantity which does

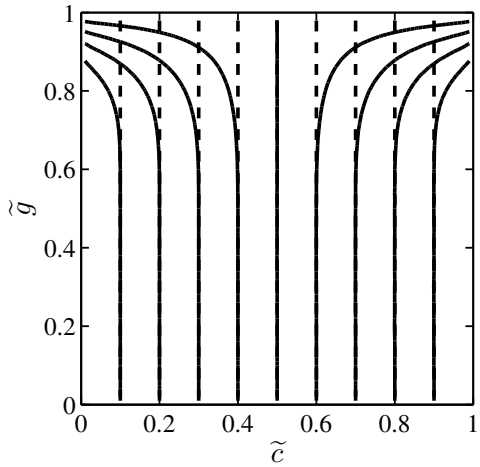

Fig. 3.3 Isolines of $\widetilde{c}$, obtained using Eq. (3.33) (with c integrated instead of $\dot{W}$) and (3.38) (continuous lines), are shown on the plane $\widetilde{c}$-$\widetilde{g}$, where $\widetilde{g} = \sigma^2_{c,\mathrm{sgs}}/[\widetilde{c}(1-\widetilde{c})]$. Isolines obtained using Eq. (3.39) are also shown (dashed lines).

not approach zero at $c = 0$ and $c = 1$ has to be integrated, such as heat capacity, enthalpy of formation and molecular weight used in the numerical procedure to be described in §3.4, and would lead to large numerical problems and eventually divergence of the solution. It is worth noting that this issue cannot be solved by simply increasing the number of discretisation points because of the presence of the steep variation. The issue can be avoided very easily if one uses integration by part to include CDF (cumulative distribution function), $\mathscr{C}$, of P since the CDF does not have such sharp variations. This is outlined below using a generic variable Q,

$$\overline{Q} = \int_0^1 Q(\zeta)P(\zeta)\ \mathrm{d}\zeta = \int_0^1 Q\ \mathrm{d}(\mathscr{C}) = Q(\zeta=1) - \int_0^1 \mathscr{C}\,Q'\ \mathrm{d}\zeta, \tag{3.39}$$

where the derivative $Q' = \partial Q/\partial\zeta$ is usually well behaved in the domain $0 \le \zeta \le 1$. Thus, the integral in Eq. (3.39) can be evaluated accurately, as can be inferred in Fig. 3.3. This approach implies that $\mathscr{C}$ is known or computed accurately, and it is computed using Matlab implicit routines in this work.

B. Strained flamelet model

The strained flamelets approach used in this study is an extension of that proposed in [121] for RANS methodology and the filtered reaction rate is modelled as

$$\overline{\dot{\omega}} = \int_0^1 \int_{\psi_{\min}}^{\psi_{\max}} \dot{\omega}\, P(c,\psi;\widetilde{c},\sigma^2_{c,\mathrm{sgs}},\widetilde{N}_c)\ \mathrm{d}\psi\,\mathrm{d}c \tag{3.40}$$

where ψ is the sample space variable for N_c, which is the SDR representing the effect of turbulent strain on the flamelets. The sub-grid joint PDF is written as $P(c,\psi) = P(c)P(\psi|c)$ using Bayes theorem. The marginal PDF of c is modelled using a β-function, Eq. (3.34), discussed in §3.3.2, and the $\sigma^2_{c,\mathrm{sgs}}$ required is obtained through Eq. (3.36). The reaction term in the variance equation is closed in a manner similar to Eq. (3.40) for consistency. The conditional PDF $P(\psi|c)$ is modelled as a log-normal PDF following [121], where it is written as

$$P(\psi|c) = \frac{1}{(\psi|c)\sigma\sqrt{2\pi}} \exp\left\{-\frac{1}{2\sigma^2}[\ln(\psi|c) - \mu]^2\right\} \tag{3.41}$$

where μ and σ^2 denote respectively mean and variance of $\ln(\psi|c)$ and are related to the conditional mean $\langle\psi|c\rangle$ and conditional variance G_N^2 as

$$\langle\psi|c\rangle = \exp(\mu + \sigma^2/2), \quad G_N^2 = \langle\psi|c\rangle^2[\exp(\sigma^2) - 1] \tag{3.42}$$

A nominal value of $\sigma = 0.3$ is taken in this thesis on the basis of previous works [121], and results to be presented in next chapters are not unduly sensitive to this parameter when it is increased to 0.5. The Favre filtered SDR required for the conditional PDF is approximated as $\widetilde{N}_c \approx \widetilde{\varepsilon}_c$ because the premixed flame front is unlikely to be resolved in a typical LES and thus $\widetilde{D}(\nabla\widetilde{c}\cdot\widetilde{c}) \ll \widetilde{\varepsilon}_c$. The SGS dissipation rate is estimated using Eq. (2.22), in which the SGS variance, $\sigma^2_{c,\mathrm{sgs}}$, is used in place of $\widetilde{c}(1-\widetilde{c})$ as in the unstrained flamelets closure. The conditional mean can be expressed as

$$\langle\psi|c\rangle = \int_{\varepsilon}^{N_{\max}} \psi(c,N)P(\psi|c;\widetilde{N})\,\mathrm{d}\psi \approx \int_{0}^{a_{\max}} \psi(c,a)P(a)\,\mathrm{d}a \tag{3.43}$$

where $\psi(c,a)$ is the SDR in a flamelet subject to strain rate a. Following Kolla et al. [121], $\psi(c,a)$ is approximated as $\psi(c,a) \approx \psi(c^*,a)f(c)$, where c^* corresponds to the location of peak heat release rate. Using Eq. (3.40) with $\widetilde{N}_c$ instead of $\overline{\dot{\omega}}$ one then obtains

$$\widetilde{\varepsilon}_c \approx \widetilde{N}_c \approx \int_0^1 \langle\psi|c^*\rangle f(c)\widetilde{P}(c)\,\mathrm{d}c \tag{3.44}$$

and thus

$$\langle\psi|c\rangle \approx \frac{\widetilde{\varepsilon}_c f(c)}{\int_0^1 f(c)\widetilde{P}(c)\,\mathrm{d}c} \tag{3.45}$$

It may be possible to use another flamelet attribute or variable, for example peak value of atomic hydrogen mass fraction [116], to represent the straining effect. A quantity related to scalar gradient is a natural first choice to represent turbulent strain and so the dissipation rate is adopted for this study as suggested by Libby and Williams in their asymptotic analysis [138]. Furthermore, atomic hydrogen is produced through chemical reactions and thus its value would depend on the progress of the reaction. Hence, using it as an independent variable to represent the fluid dynamic straining is questionable.

The precomputed filtered values of $\widetilde{\dot{W}}$ obtained using the strained flamelets model are stored in a look-up table with $\widetilde{c}$ and $\sigma^2_{c,\mathrm{sgs}}$ as controlling parameters as for the unstrained flamelet model, and $\widetilde{\varepsilon}_c$ is used as a third parameter for the strained flamelets.

C. Role of SGS variance

The SGS variance of progress variable, $\sigma^2_{c,\mathrm{sgs}}$, is modelled in earlier studies typically using an expression developed for passive scalars, i.e. $\sigma^2_{c,\mathrm{sgs}} \simeq \mathscr{A}\Delta^2(\nabla\widetilde{c}\cdot\nabla\widetilde{c})$, where the model parameter $\mathscr{A}$ is usually obtained through dynamic evaluation and typically takes a value of

about 0.5. The relevance of such modelling for turbulent premixed combustion is an open question on physical grounds because chemical reactions ought to influence this variance as was remarked in [182] and an algebraic model for $\sigma^2_{c,\mathrm{sgs}}$ including this effect is yet to be developed. Pitsch [185] also noted that this model, as well as linear relaxation model for the scalar dissipation rate, can lead to under-prediction of the SGS variance in reacting flows. These points are of specifically high importance for the presumed sub-grid PDF approach because this PDF has a direct dependence on $\sigma^2_{c,\mathrm{sgs}}$ and influences the filtered reaction rate value.

The SGS progress variable equation written earlier as Eq. (3.36) is rewritten below for convenience as

$$\underbrace{\frac{\partial \overline{\rho}\,\sigma^2_{c,\mathrm{sgs}}}{\partial t}}_{T_1} + \underbrace{\nabla\cdot\left(\overline{\rho}\,\widetilde{\mathbf{u}}\,\sigma^2_{c,\mathrm{sgs}}\right)}_{T_2} \approx \underbrace{\nabla\cdot\left[\left(\overline{\rho\mathscr{D}_c} + \overline{\rho}\,\frac{\nu_T}{\mathrm{Sc}_T}\right)\nabla\sigma^2_{c,\mathrm{sgs}}\right]}_{T_{31}+T_{32}} + \underbrace{2\overline{\rho}\left(\widetilde{\dot{W}c} - \widetilde{\dot{W}}\widetilde{c}\right)}_{T_4} - \underbrace{2\overline{\rho}\,\widetilde{\varepsilon}_c}_{T_5} + \underbrace{2\overline{\rho}\,\frac{\nu_T}{\mathrm{Sc}_T}\left(\nabla\widetilde{c}\cdot\nabla\widetilde{c}\right)}_{T_6} \tag{3.46}$$

The terms T_1 and T_2 are the unsteady and advective terms respectively. The molecular and turbulent fluxes of the SGS variance are respectively denoted using T_{31} and T_{32}. The other three terms, T_4, T_5 and T_6, signify the source and sink contributions from SGS chemical processes, dissipation of the variance, and its production through interaction of SGS scalar flux and gradient of $\widetilde{c}$. It is important to recognise these physical processes in order to evaluate the validity of the commonly used model for $\sigma^2_{c,\mathrm{sgs}}$, which results by equating T_5 and T_6 after approximating the dissipation rate as $\widetilde{\varepsilon}_c \simeq \nu_T\sigma^2_{c,\mathrm{sgs}}/(\mathscr{A}\,\mathrm{Sc}_T\,\Delta^2)$. As one shall see below, this model cannot be employed for LES of premixed flames.

The above equation is studied using an order of magnitude analysis as follows. The spatial derivatives of filtered quantities, time derivative, and density are scaled using Δ, Δ/U_{ref}, and ρ_u respectively. The filtered velocity is scaled using a reference velocity U_{ref}. The molecular diffusivity is scaled using the laminar flame scales, s_L and δ_{th}, and the SGS viscosity is scaled as $u'_\Delta\Delta$. The progress variable gradient is produced predominantly by the chemical reaction and thus the appropriate scaling for $\widetilde{\varepsilon}_c$ is s_L/δ_{th}. However one can also scale this term using u'_Δ/Δ if the combustion effects are ignored and the SGS turbulence is presumed to be responsible for the progress variable gradient which can occur through mixing of unbunt and burnt mixtures. The above scalings yield

$$T_1 \sim \mathscr{O}\left(\frac{\rho_u s_L}{\delta_{th}}; \frac{U_{\mathrm{ref}}}{u'_\Delta}\frac{1}{\mathrm{Da}_\Delta}\right) \quad T_2 \sim \mathscr{O}\left(\frac{\rho_u s_L}{\delta_{th}}; \frac{U_{\mathrm{ref}}}{u'_\Delta}\frac{1}{\mathrm{Da}_\Delta}\right) \tag{3.47}$$

$$T_{31} \sim \mathscr{O}\left(\frac{\rho_u s_L}{\delta_{th}}; \frac{1}{\mathrm{Da}_\Delta \mathrm{Re}_\Delta}\right) \quad T_{32} \sim \mathscr{O}\left(\frac{\rho_u s_L}{\delta_{th}}; \frac{1}{\mathrm{Da}_\Delta}\right) \tag{3.48}$$

$$T_4 \sim \mathscr{O}\left(\frac{\rho_u s_L}{\delta_{th}}; 1\right) \quad T_5 \sim \mathscr{O}\left(\frac{\rho_u s_L}{\delta_{th}}; 1\right) \quad T_6 \sim \mathscr{O}\left(\frac{\rho_u s_L}{\delta_{th}}; \frac{1}{\mathrm{Da}_\Delta}\right) \tag{3.49}$$

where $\mathrm{Re}_\Delta = u'_\Delta \Delta/(s_L \delta_{th})$ is the SGS Reynolds number. If the local SGS Damköhler number is large then the leading order balance is between T_4 and T_5 which implies that $\widetilde{c}\,\overline{\rho}\, s_L/\delta_{th} \simeq \overline{\rho}\, \nu_T \sigma^2_{c,\mathrm{sgs}}/\Delta^2$, suggesting that the SGS variance is proportional to Da_Δ. However, the Damköhler number is finite for most practical simulations (see for example §6.5) and thus the other terms in the balance equation cannot be neglected. If one takes a balance among sources and sinks as it is typically done in non-reacting flows then $T_5 \simeq T_4 + T_6$, which would give $\sigma^2_{c,\mathrm{sgs}} \simeq \mathscr{A}_1 \left(\widetilde{c}\mathrm{Da}_\Delta + \Delta^2 |\nabla \widetilde{c}|^2\right)$, where $\mathscr{A}_1$ is a model parameter. This balance is unacceptable because other terms in Eq. (3.46) will be of similar magnitude since they have same dependence on Da_Δ.

As noted earlier, the commonly used model for $\sigma^2_{c,\mathrm{sgs}} \simeq \mathscr{A}\Delta^2(\nabla\widetilde{c}\cdot\nabla\widetilde{c})$ is obtained through $T_5 \simeq T_6$ which can be justified only if $\left(u'_\Delta/\Delta\right)$ is used to scale $\widetilde{\varepsilon}_c$. This specific scaling gives

$$T_5 \sim \mathscr{O}\left(\frac{\rho_u s_L}{\delta_{th}}; \frac{1}{\mathrm{Da}_\Delta}\right)$$

and ignores the important aspect of premixed combustion, i.e., the progress variable gradient is produced predominantly by combustion, which is also recognised in an earlier study investigating SGS variance and dissipation rate of a conserved scalar [182]. This implies that the commonly used model will underestimate $\sigma^2_{c,\mathrm{sgs}}$, which is verified in Fig. 3.4 for unstrained flamelet modelling of F1 flame of [46], to be investigated in Chapter 6, belonging to the thin reaction zone of the premixed combustion diagram [180]. This figure is shown for two different grid sizes at an arbitrarily chosen time, and it is obtained by plotting the modelled values against $\sigma^2_{c,\mathrm{sgs}}$ computed using its transport equation. The data points are coloured using $\widetilde{c}$ value. If the modelled values agree with $\sigma^2_{c,\mathrm{sgs}}$ then the data point must cluster around the diagonal line ($\mathscr{A} = 1$). The data seems to cluster predominantly around the dash-dotted line which has a slope of about 0.125 which suggests that $\mathscr{A} \approx 8$. The scatter is reduced and thus this clustering is more apparent when the larger of the two grids is used. It is clear that the model for the SGS variance underestimates $\sigma^2_{c,\mathrm{sgs}}$ as suggested by the above scaling analysis. This reduced modelled variance, compared to $\sigma^2_{c,\mathrm{sgs}}$ from its transport equation, will give larger values of $\overline{\dot{\omega}}$ for $0.6 \leq \widetilde{c} \leq 0.8$ when the unstrained flamelet model is used (see Fig. 6.1). This issue will become even more critical in low-turbulence flame configurations, to be analysed in Chapter 8. The difference between modelled and transported equation can be of different

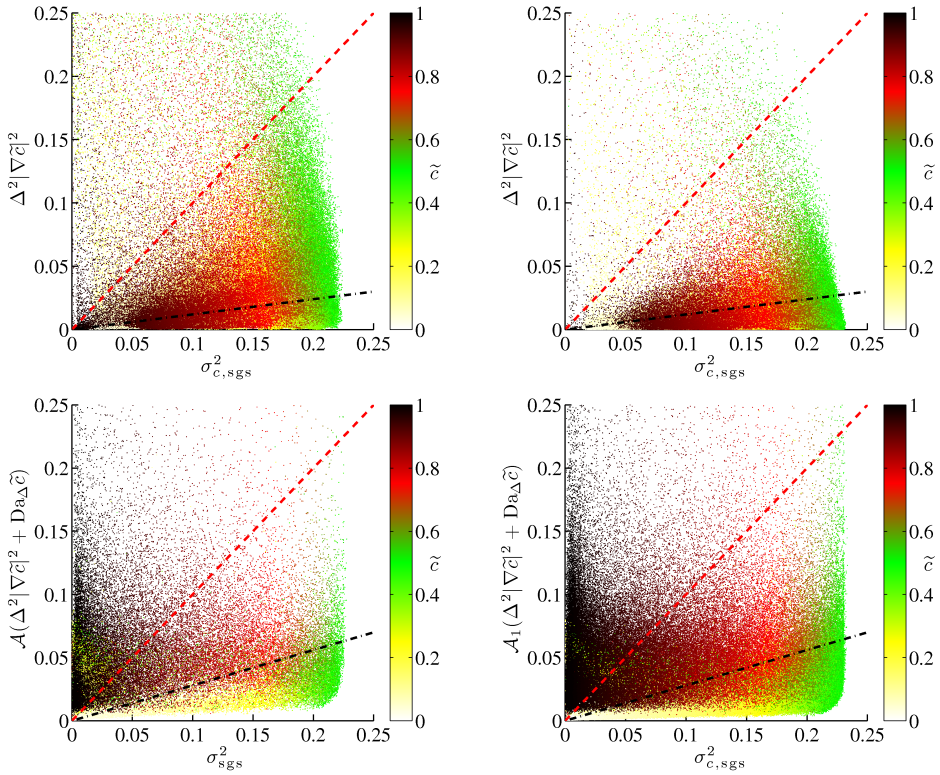

Fig. 3.4 Scatter plot of computed $\sigma^2_{c,\mathrm{sgs}}$ and its modelled value using $\mathscr{A}\Delta^2|\nabla\widetilde{c}|^2$ with $\mathscr{A}=1$ in the top row. The results for the revised model, $\mathscr{A}_1\left(\widetilde{c}\,\mathrm{Da}_\Delta+\Delta^2|\nabla\widetilde{c}|^2\right)$ with $\mathscr{A}_1=0.15$, are shown in the bottom row. The first and second columns are for two different grid sizes, of 1.5M and 4.2M cells, for F1 flame of [46] respectively.

orders of magnitude, as shown in Fig. 3.5 for a flame, to be investigated in Chapter 8, belonging to the corrugated flamelet regime, which would result in a very inaccurate filtered reaction rate. This overestimate of the filtered reaction rate resulting from the incorrect (modelled) SGS variance suggests that one may need strained flamelets model for LES of premixed combustion. If one uses the strained flamelets model with $\sigma^2_{c,\mathrm{sgs}}$ obtained from its transport equation then the filtered burning rate is underestimated leading to substantial underestimates of various reactive scalar mass fractions as will be observed in §6.4.

If one were to use the revised algebraic model given above, as shown in the bottom row of Fig. 3.4, then the SGS variance would be severely overestimated because Da_Δ varies from $\mathscr{O}(0.1)$ to $\mathscr{O}(1)$ (see §6.5) yielding the modelled SGS variance substantially larger than its maximum limit of 0.25. Indeed this overestimate can be seen in the bottom row of Fig. 3.4 for both the grids if one were to use $\mathscr{A}_1=1$ instead of 0.15 used for this figure. This substantial overestimate also suggests that the transport terms in Eq. (3.46) cannot be neglected to get meaningful values for the SGS variance and this equation need to be included for LES of

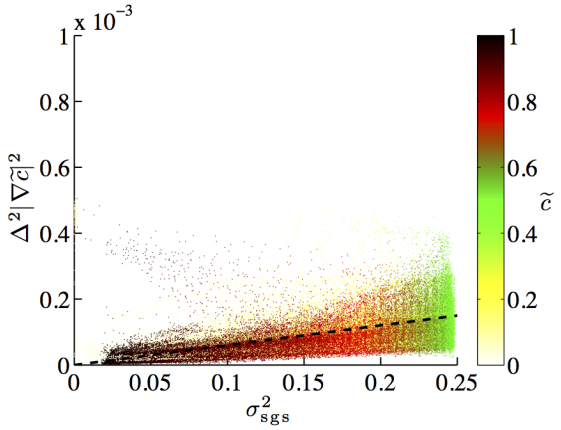

Fig. 3.5 Scatter plot of computed $\sigma^2_{c,\mathrm{sgs}}$ and its modelled value using $\mathscr{A}\Delta^2|\nabla\widetilde{c}|^2$ with $\mathscr{A}=1$.

premixed combustion using the unstrained flamelet model. The additional computational cost incurred by including this transport equation is small which is fully justified through correct representation of turbulent premixed combustion physics as discussed above.

3.3.3 Estimation of sub-grid scale velocity

The velocity scale u'_Δ influences $\widetilde{\varepsilon}_c$ in Eq. (2.22) in two ways. The direct influence is felt through the linear dependence appearing in Eq. (2.22) and additional effects come indirectly in a non-linear manner through Ka_Δ dependence of C_3 and C_4. Thus, the modelling of u'_Δ needs to be considered carefully. In this work, four different algebraic models are used to estimate u'_Δ and these models are presented below.

1. Considering that $(-\tau_{ij}\widetilde{S}_{ij})$ represents a production of small-scale kinetic energy [134, 140], the SGS-velocity can be estimated directly form the residual model implemented. Dimensionally, the quantity $\Delta|\widetilde{S}|$, is a velocity, thus u'_Δ can be considered proportional to this value. A model based on a shear stress related closure was proposed by Lilly [140] and it is given by

$$u'_\Delta = \frac{\nu_T}{\sqrt{3/2}C_L\Delta}, \tag{3.50}$$

where $\nu_T = (C_s\Delta)^2\sqrt{2\widetilde{S}_{ij}\widetilde{S}_{ij}}$ is the turbulent viscosity modelled using Smagorinsky model. The model constant is $C_L = 0.094$.

2. A second model based on scale-similarity for velocity is written as [196]

$$u'_\Delta = C_q\left|\widetilde{u}_i - \widehat{\widetilde{u}}_i\right| \tag{3.51}$$

where $\widehat{\widetilde{u}_i}$ is the velocity field obtained using a test filter. Different estimations of C_q have been given in the literature [11, 48, 159]. A dynamic evaluation of the model constant was proposed by Cook [49], but the constant requires an estimation of the integral length scale which may be difficult to provide. If a a Gaussian test filter is used, under the assumption that the implicit filter is also Gaussian (see §3.1.3), then $C_q = 1$ gives the best approximation for u'_Δ [196]. This value is thus used in this thesis.

3. A third model, based on scale-similarity for kinetic energy proposed by Bardina *et al.* [11], is written in its Galilean invariant form [64] as

$$u'_\Delta = C'_q \left| \widehat{\widetilde{u}_i \widetilde{u}_i} - \widehat{\widetilde{u}}_i \widehat{\widetilde{u}}_i \right|^{1/2}, \tag{3.52}$$

with $C'_q = 0.126$.

4. A fourth model is based on a hypothesis of constant energy transfer down to Δ scale. In this hypothesis one can write [196]

$$\frac{u'^3(\ell)}{\ell} = \frac{u'^3_\Delta}{\Delta} = \varepsilon$$

Also, if one takes $\varepsilon \approx \varepsilon_\Delta$ and supposing that $\nu_T \gg \nu$ (true for $\Delta \gg \eta_k$), then

$$u'^3_\Delta = \Delta \varepsilon_\Delta \approx 2\Delta \nu_t \widetilde{S}_{ij} \widetilde{S}_{ij} \tag{3.53}$$

The Smagorinsky model for ν_T in Eq. (3.3) gives

$$\widetilde{S}_{ij} \widetilde{S}_{ij} = \frac{\nu_T^2}{2 C_s^2 \Delta^4} \tag{3.54}$$

Substituting Eq. (3.54) into Eq. (3.53) yields

$$u'_\Delta = \frac{\nu_T}{C_s^{2/3} \Delta} \tag{3.55}$$

This model allows one to relate SGS velocity fluctuation directly to the Smagorinsky model constant, and is strictly valid only when Eq. (3.53) holds. Although the assumption of $\varepsilon \approx \varepsilon_\Delta$ seems too restrictive, the Smagorinsky model typically overestimates ν_T [99, 160] and thus the above assumption is expected to be reasonable.

5. Colin *et al.* [47] derived another model by expanding Eq. (3.51) using Taylor series truncated to second order and then applying the curl operator to exclude dilatation effects.

This expression is

$$u'_{\Delta} = c_2 \Delta^3 \left| \nabla^2 \left(\nabla \times \widetilde{\mathbf{u}} \right) \right| \tag{3.56}$$

where $c_2 = 2$ is typical value suggested by [47]. The above expression was modified by multiplying it by $(0.1\,\Delta/\Delta_x)^{1/3}$, where Δ_x is the mesh size estimated from local numerical cell volume, to accommodate cases with the filter width larger than the numerical cell size [240].

One can also obtain this velocity scale using a transport equation for the residual kinetic energy, k_r, through $u'_{\Delta} = \sqrt{2k_r/3}$. This is also explored in this work by solving an ad hoc modelled transport equation for k_r, and its modelling was discussed in §3.1.2.

The assumption that the sub-grid scale velocity and strain are proportional is arguable [196]. Moreover, the strain in combustion is subjected to dilatation due to heat release. Since models (3.50) and (3.55) are based on strain, the effect of dilatation is included in these modelling. Nevertheless, the SGS velocity still would go to zero in a laminar flame if the SGS model constant is computed dynamically, as this constant goes to zero in laminar regions. Even though it is argued that dilatation effect must be excluded from the modelling of u'_{Δ} [47], it is not completely clear, as dilatational terms appear in the k_r equation, which, by its definition, is a residual kinetic energy and not a residual turbulent kinetic energy. Thus, models (3.51) and (3.52), which are based on definition similar to k_r and also capture dilatational effects, are also related to the kinetic energy at smallest resolved scale, following scale similarity. Effects of dilatation on the SGS velocity modelling are investigated in Chapter 8.

3.3.4 Dynamic formulations

In general, dynamic modelling is based on the assumption that an unresolved quantity of interest is similar in neighbouring scales [196]. This scale similarity assumption for flame wrinkling and flame surface density have been proposed and used in past studies [43, 88, 114, 115, 117, 185, 241]. Many earlier studies [18, 194, 237] have recognised that these quantities are closely related to $|\nabla c|$ and thus N_c. Hence, the scale similarity concepts can be equally applied to the scalar dissipation rate field also.

A. Dynamic modelling for β_c

The following description is based on the algebraic model of §3.3.1. The same description is applied to unstrained and strained flamelets models by using $\sigma^2_{c,\mathrm{sgs}}$ in place of $\widetilde{c}(1-\widetilde{c})$ in all equations below. Equation (2.22) can be written as $\widetilde{\varepsilon}_c = f_1\,\widetilde{c}(1-\widetilde{c})/\beta_c$ for conciseness and a comparison of this expression to Eq. (2.22) defines f_1. The dynamic evaluation of β_c is as

follows. Firstly, one writes

$$\widehat{\overline{\rho}\widetilde{N}_c} = \widehat{\psi_1} + \widehat{\psi_2/\beta_c} \qquad \text{and} \tag{3.57a}$$

$$\widehat{\widehat{\overline{\rho}}\widehat{\widetilde{N}}_c} = \widehat{\overline{\rho}}\widehat{\widetilde{D}}(\nabla\widehat{\widetilde{c}}\cdot\nabla\widehat{\widetilde{c}}) + \widehat{\overline{\rho}}\,\widehat{f_1}\widehat{\widetilde{c}}(1-\widehat{\widetilde{c}})/\beta_c \tag{3.57b}$$

with $\psi_1 \equiv \overline{\rho}\widetilde{D}(\nabla\widetilde{c}\cdot\nabla\widetilde{c})$ and $\psi_2 \equiv \overline{\rho}\,f_1\widetilde{c}(1-\widetilde{c})$, by using a test filter of size $\widehat{\Delta} = 2\Delta$. Here, the notations $\widehat{\widetilde{N}_c}$ and $\widehat{f_1}$ imply that they must involve quantities obtained using the test filter. A Gaussian filter having $\widehat{\Delta}$ as its width is used. Subtracting Eq. (3.57b) from Eq. (3.57a) and recognising that $\widehat{\overline{\rho}\widetilde{N}_c} \approx \widehat{\overline{\rho}}\,\widehat{\widetilde{N}_c}$ one can obtain an expression for β_c. Using both parts of Eq. (3.57) one obtains

$$\beta_c = \frac{\widehat{\overline{\rho}}\,\widehat{f_1}\widehat{\widetilde{c}}(1-\widehat{\widetilde{c}})}{\widehat{\psi_1} - \widehat{\overline{\rho}}\widehat{\widetilde{D}}(\nabla\widehat{\widetilde{c}}\cdot\nabla\widehat{\widetilde{c}}) + \widehat{\psi_2/\beta_c}} \tag{3.58}$$

where the value of β_c on the RHS can be evaluated using information from previous time step. An additional averaging with the neighbouring cells is performed for numerical stability [212]. 3 to 5 neighbouring numerical grid cells in each spatial direction were used for the test-filtering and results were found to be insensitive to this choice in this range. To satisfy the realisability conditions of $\widetilde{N}_c \geq 0$ and $0 \leq \widetilde{c} \leq 1$ this parameter must satisfy $\beta_c \geq 2/(2C_m - 1)$ [39] in case of algebraic model. Thus, one gets

$$\beta_c = \max\left(\frac{2}{2C_m - 1},\ \text{Eq. 3.58}\right). \tag{3.59}$$

It is worth noting that the frequency at which this condition is applied is low in the simulations to be presented in next chapters, which is verified by looking *a posteriori* at the PDF of β_c (see Figs. 5.32 and 7.32). The condition $\beta_c > \varepsilon$, with $\varepsilon > 0$ being a small number, is used for the other closures, where ε is chosen appropriately to avoid numerical issues or singularity.

B. Dynamic power-law model

Another dynamic model explored for $\widetilde{N}_c$ is based on a power-law. The static version of this model is studied in [61, 77]. This choice was motivated by many earlier studies [17, 38, 42–44, 114] attempting to model the flame wrinkling factor or the generalised flame surface density using the power-law and these quantities are closely related to $\widetilde{N}_c$ as noted earlier in this section. This model for $\widetilde{N}_c$ is written as [61, 77]

$$\overline{\rho}\widetilde{N}_c = \overline{\rho}\widetilde{D}(\nabla\widetilde{c}\cdot\nabla\widetilde{c})\left(\frac{\Delta}{\eta_i}\right)^{\alpha} = \psi_1\left(\frac{\Delta}{\eta_i}\right)^{\alpha} \tag{3.60}$$

where α is the exponent and η_i is the inner cut-off scale, which scales as δ_{th} [38, 61, 115, 202]. Using a constant and non-zero value for α in Eq. (3.60) does not readily satisfy the expected asymptotic behaviour of $\overline{\rho}\widetilde{N}_c \to \rho D(\nabla c \cdot \nabla c)$ in the limit of $\Delta \to 0$. To overcome this, a dynamic evaluation can be followed. Following a method similar to that described for β_c, one gets

$$\alpha = \frac{\ln[\widehat{\psi_1}/\widehat{\overline{\rho}}\widehat{\widetilde{D}}(\nabla\widehat{\widetilde{c}}\cdot\nabla\widehat{\widetilde{c}})]}{\ln(\widehat{\Delta}/\Delta)}. \tag{3.61}$$

in which the assumption that α does not change during test filtering operation has been made. One can also write Eq. (3.60) as

$$\overline{\rho}\widetilde{N}_c = \psi_1 \left(1 + \frac{\Delta}{\eta_i}\right)^{\alpha_1} \tag{3.62}$$

using a different exponent α_1 to satisfy the condition that $\widetilde{N}_c \to N_c$ as $\Delta \to 0$. The dynamic procedure with Eq. (3.62) gives

$$\alpha_1 = \frac{\ln[\widehat{\psi_1}/\widehat{\overline{\rho}}\widehat{\widetilde{D}}(\nabla\widehat{\widetilde{c}}\cdot\nabla\widehat{\widetilde{c}})]}{\ln\left[(1+\widehat{\Delta}/\eta_i)/(1+\Delta/\eta_i)\right]}. \tag{3.63}$$

If one were to have the filtered dissipation rates from Eqs. (3.60) and (3.62) equal then $\alpha_1 \approx \alpha$ for $\Delta/\eta_i \gg 1$. This can be shown as follows. The relation between α and α_1 can be found by comparing Eqs. (3.60) and (3.62):

$$\alpha = \frac{\ln(\Delta/\eta_i)}{\ln(1+\Delta/\eta_i)}\alpha_1 = f_I(\Delta/\eta_i)\alpha_1 \tag{3.64}$$

which is the relation α and α_1 must satisfy in order to obtain the same $\widetilde{N}_c$. The actual relation is instead implied by the dynamic approach. Comparing Eqs. (3.61) and (3.63), and assuming $\widehat{\Delta} = k\Delta$, with $k > 1$ being a constant, one gets

$$\alpha = \frac{\ln k}{\ln\left[\left(1+k\Delta/\eta_i\right)/\left(1+\Delta/\eta_i\right)\right]}\alpha_1 = f_{II}(\Delta/\eta_i)\alpha_1 \tag{3.65}$$

The variations of functions f_I and f_{II} with Δ/η_i are compared in Fig. 3.6. The negative brunch in f_I is due to the fact that Eq. (3.60) does not converge to $\overline{\rho}\widetilde{D}(\nabla\widetilde{c}\cdot\nabla\widetilde{c})$ for $\Delta \to 0$. This behaviour can be corrected using a bridging function [61, 77, 79], as shown in the picture. This bridging function is used for small values of Δ/η_i which are not relevant for the LES analyses in this thesis, and thus will not be further discussed here.

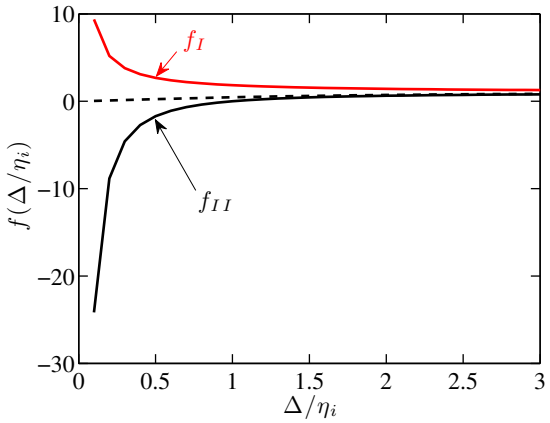

Fig. 3.6 Comparisons of functions f_I and f_{II} in Eqs (3.64) and (3.65) respectively. The dashed line represents $f_I\mathscr{F}_b$, where $\mathscr{F}_b$ is the bridging function discussed in [61, 77, 79].

Functions f_I and f_{II} do not match for small values of Δ/η_i. For a fixed value of Δ/η_i and a given value of α_1, taken for example from DNS data, in order to obtain the same $\widetilde{N}_c$ in Eq. (3.60), one should use $\alpha = f_I\alpha_1$. However, the value implied by the dynamic procedure is $\alpha = f_{II}\alpha_1 > f_I\alpha_1$. For this reason one can expect over-predictions of $\widetilde{N}_c$ in LES in respect to the value from DNS, when Δ/η_i is small. Curves f_I and f_{II} converge to each other as Δ/η_i increases, so differences between LES and DNS are expected to be small in this case. These differences are also expected to be smaller in real cases, because the volume average in Eq. (3.61), not taken into account in Fig. 3.6, is expected to smooth down f_{II}. This analysis must be considered when assessing power-law modelling for LES with *a priori* DNS analyses. In conclusion, it is immaterial if one uses Eq. (3.60) or (3.62) in LES with sufficiently large filter widths. It is worth noting that the exponential constant is always positive in the dynamic computation either using Eq. (3.61) or (3.63).

The validity of dynamic models in Eqs. (3.58) and (3.61) strongly depends on validity of scale-similarity for quantities at Δ and $\widehat{\Delta}$. Specifically the scale-similarity must hold for $\nabla\widetilde{c}$ for Eq. (3.61) and for u'_Δ and $\widetilde{c}$ for Eq. (3.58) (the term $\widehat{\psi}_1$ involving gradients in Eq. (3.58) is small compared to the other terms in the sum and thus does not affect this observation on scale similarity). As noted earlier, the above dynamic procedure is similar to that studied in [78], however, the modelling of SGS dissipation rate, $\widetilde{\varepsilon}_c$, in Eq. (2.22) is not the same as that used in [78].

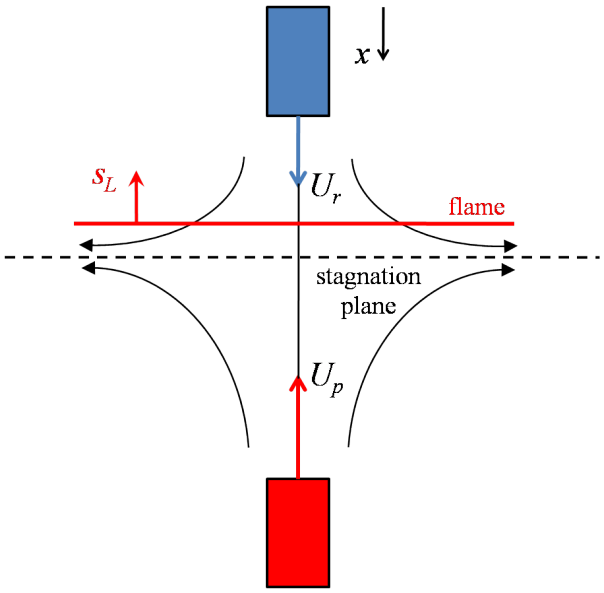

Fig. 3.7 Strained flamelet configuration.

3.3.5 Laminar flame computation

The unstrained and strained laminar one-dimensional flames are computed using PREMIX [106] and OPPDIFF [146] codes respectively, which solve the reacting incompressible one-dimensional Navier-Stokes equations using finite differences technique and adaptive grid. The GRI 3.0 chemical kinetic mechanism is used for methane-air combustion and a mechanism described by [224] is used instead in case of propane-air mixtures. In the unstrained flamelet configuration reactants enter from one side and propagate in the opposite direction. The velocity in the direction tangential to the flame is zero and the flame freely propagates toward the reactants, as was shown schematically in Fig. 2.1. The flow is accelerated by the flame and thus reactants and products move in the same direction. In the strained flamelet configuration reactants and products enter from opposite sides at velocities U_r and U_p respectively, as shown schematically in Fig. 3.7. The flame is stretched because the tangential velocity increases rapidly moving away from the centreline and thus the strain rate is $a = \nabla_t \cdot \mathbf{u} \neq 0$, where ∇_t indicates that the divergence involves only the tangential component of $\mathbf{u}$. This strain rate is directly proportional to the inlet velocities and inversely proportional to the distance L between the jet inlets in this configuration [191], $a \sim (|U_r| + |U_p|)/L$. In Figure 3.8 the variation of the consumption speed, s_c, with a is shown along the centreline for methane-air flame at stoichiometric condition. The different rate of strain are obtained by varying U_r and U_p in OPPDIFF. The consumption speed is a useful indicator of the overall burning rate and shows that this rate does not change significantly for low rates of strain as one would expect, than decreases almost linearly to suddenly drop for higher strain rates. Typical strained flamelets structures obtained using

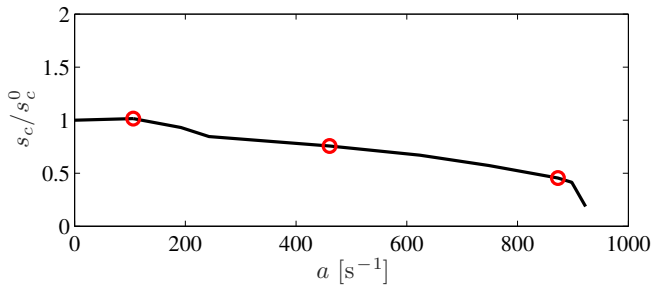

Fig. 3.8 Variation of consumption speed, s_c (normalised with the unstrained flamelet consumption speed, s_c^0), with characteristic strain rate for stoichiometric strained flamelets. The strain rate is estimated as $a \approx (|U_r| + |U_p|)/L$. Three particular values of strain rate are marked with circles.

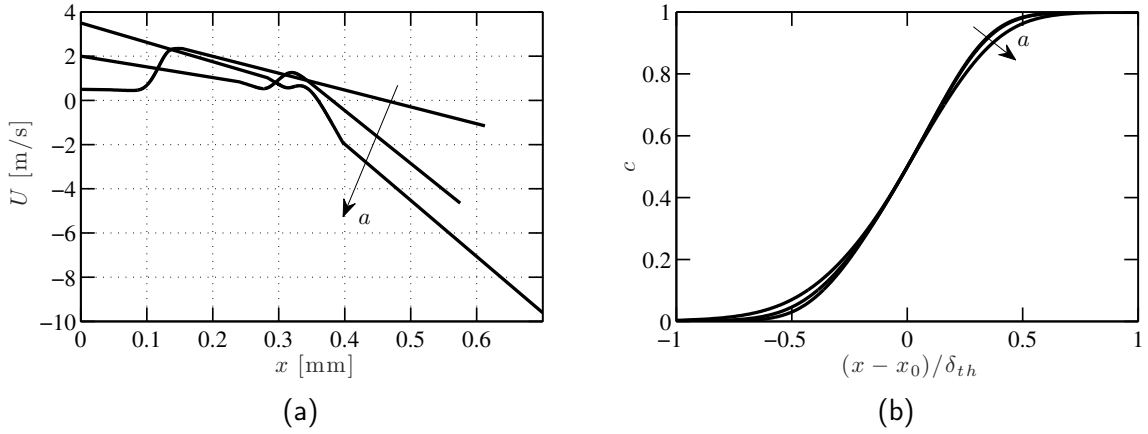

Fig. 3.9 Profiles of (a) axial velocity, U, and (b) progress variable, c, along the centreline for the three values of strain rate marked in Fig. 3.8. x_0 is the location at which $c = 0.5$.

OPPDIFF are shown in Fig. 3.9 for the three strain rates marked with circles in Fig. 3.8 . These different velocities imply increasing values of strain on the flame. The flame distance from the stagnation plane decreases with increasing strain rate as observed in Fig. 3.9a. Although the velocity distributions across the three strained flamelets are significantly different from each other, their respective progress variable profiles are similar. The main effect of the increased strain is to decrease the reaction rate as shown in Fig. 3.10a. This corresponds to decreasing values of scalar dissipation rates as shown in Fig. 3.10b. Thus, for each value of c the scalar dissipation rate varies monotonically and thus this variable is very suitable to parametrise the rate of strain in the procedure explained in §3.3.2, as already noted in [121]. Species mass fractions are also affected by the strain. In Fig. 3.11 some major and minor species mass fraction profiles across the flamelets are shown for different values of a. As one can expect, minor species are more affected by strain than major species because of the significant variation of reaction rate with the strain. The local behaviour of a species k with strain depends on the

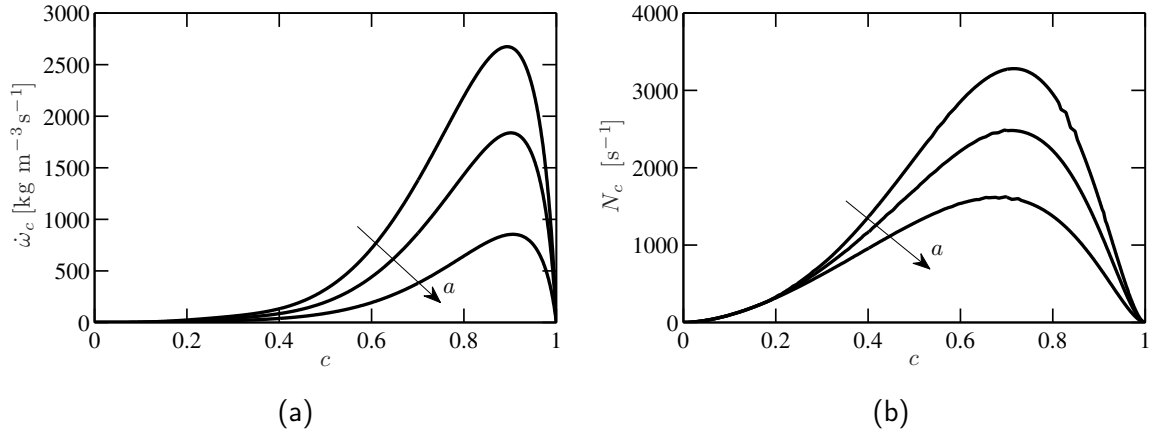

(a) (b)

Fig. 3.10 Profiles of (a) reaction rate, $\dot{\omega}_c$, and (b) scalar dissipation rate, N_c, in c space for the three strain rates marked in Fig. 3.8.

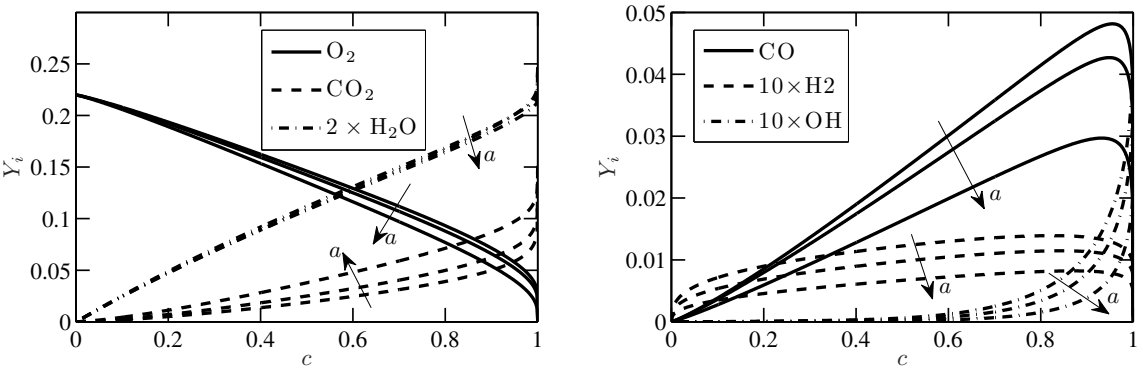

(a) (b)

Fig. 3.11 Profiles of (a) major and (b) minor species mass fractions in c space for the three strain rates marked in Fig. 3.8.

local balance between diffusion, reaction and convection. The balance equation of species k for the one-dimensional laminar steady flamelet can be written as

$$\frac{\mathrm{d}\rho U Y_k}{\mathrm{d}x} = \frac{\mathrm{d}}{\mathrm{d}x}\left(\rho \mathscr{D}_k \frac{\mathrm{d}Y_k}{\mathrm{d}x}\right) + \dot{\omega}_k \tag{3.66}$$

Integrating this equation from $-\infty$ to x and supposing that the derivatives in x are zero at $-\infty$ one obtains

$$Y_k(x) = \frac{\rho_u U_r Y_{k,u}}{\rho U} + \frac{\mathscr{D}_k}{U}\frac{\mathrm{d}Y_k}{\mathrm{d}x} + \frac{1}{\rho U}\int_{-\infty}^{x} \dot{\omega}_k(x')\,\mathrm{d}x' \tag{3.67}$$

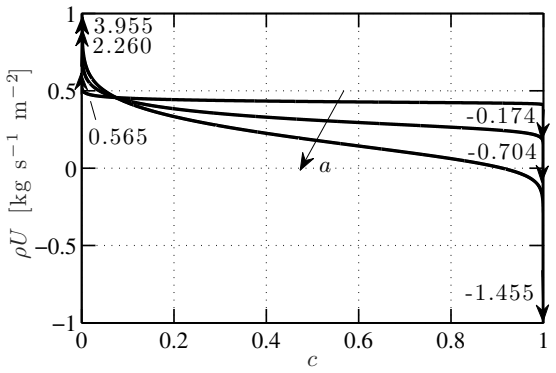

Fig. 3.12 Mass flux profiles in c space for the three strain rates marked in Fig. 3.8. The arrows at $c = 0$ and $c = 1$, and the corresponding labels, indicate the mass fluxes at the boundaries.

The terms at the RHS in Eq. (3.67) represent from left to right the ratios of initial conditions, diffusion and reaction with the mass flux, ρU. It is important to note that while the reaction rate can decrease with the strain rate as observed in Fig. 3.10a, this decrease does not necessarily correspond to a decrease of the reaction term in Eq. (3.67). The flow rate across the flame can in fact be locally smaller for higher strain rate. This is observed in Fig. 3.12, where the flow rate in the flame with highest strain becomes smaller than for lower strains after a certain value of c. Thus, depending on the local balance between reaction and mass flux, the third term at the RHS in Eq. (3.67) can increase with the strain. This can lead to unexpected behaviour in c space, as for oxygen observed in Fig. 3.11a, depending on the local balance between the above two terms and the diffusion term.

Although a significant variation of species with the strain is observed, one must consider that flamelets in turbulent configurations are free to escape from regions of high strain [188], and thus levels of strain in turbulent flames may be smaller than those observed for this laminar configuration. Moreover, unsteady strain on the turbulent flame front may not be well captured, and the use of steady flamelets must be considered here as a first step while more accurate configurations will be considered in future studies. It is also worth noting that the laminar flamelet may be harder to extinguish in this configuration [191]. Additional information for this particular configuration can be found in [119, 121].

3.4 Mathematical model and equations summary

The numerical procedure which is followed in one LES time step is as follows. The Favre filtered momentum equation in Eqs. (2.10) is solved first and the continuity equation is then used to correct pressure using SIMPLEC algorithm [58]. The sub-grid stresses are modelled

using the localised dynamic Smagorinsky model, Eq. (3.3), unless otherwise specified. The one equation closure of Eqs. (3.4) and (3.13) is used for some of the simulation to be presented in next chapter for comparison purposes. The transport equations for $\widetilde{c}$, Eq. (3.26), and SGS variance in case of PDF closures, Eq. (3.36), are used to represent the thermochemistry using flamelets hypothesis. For all combustion closures used in this study, a transport equation for the Favre filtered total enthalpy, $\widetilde{h}$, is included to account for possible sub-adiabaticity of the mixture, and takes the form specified in Eqs. (2.10). The reaction rate in the progress variable equation is modelled using Eqs. (3.27), (3.33) and (3.33) respectively for algebraic, unstrained and strained flamelets models. Equations (2.19) and (3.60) are used instead in case of the power-law closure. The temperature is computed from the computed total enthalpy $\widetilde{h}$ through

$$\widetilde{T} = T_0 + \frac{\widetilde{h} - \widetilde{\Delta h}_f^0}{\widetilde{C}_p} \tag{3.68}$$

where T_0 is the unburnt gas temperature, and $\widetilde{\Delta h}_f^0$ and $\widetilde{C}_p$ are the enthalpy of formation and specific heat capacity at constant pressure of the gas mixture respectively. This specific heat capacity is temperature dependent as described in [206]. The filtered density field is computed using the state equation in Eqs. (2.10), in which $\widetilde{W}$ is the molecular weight of the mixture. The values for $\Delta\widetilde{h}_f^0$, $\widetilde{C}_p$ and $\widetilde{W}$ are obtained in case of presumed PDF model using equations similar to Eq. (3.33) or (3.40), and stored in a look-up table along with $\widetilde{\dot{W}}$ and $\widetilde{\dot{W}c}$. In case of algebraic and power-law models, a lookup table is constructed by filtering unstrained laminar one-dimensional data with a Gaussian filter of width Δ_r, where Δ_r is the typical value of Δ in the expected flame region in LES. These values are parametrised with $\widetilde{c}$ and accessed in run-time.

For cases involving mixing with entrained air, a transport equation for a filtered fluid marker, $\widetilde{Z}$, is also included and this equation is

$$\frac{\partial \overline{\rho}\widetilde{Z}}{\partial t} + \frac{\partial \overline{\rho}\widetilde{u}_j\widetilde{Z}}{\partial x_j} = \frac{\partial}{\partial x_j}\left(\overline{\rho\frac{\mu}{\mathrm{Sc}}\frac{\partial h}{\partial x_j}}\right) - \frac{\partial}{\partial x_j}\widetilde{\tau}_{Z_j}^R \tag{3.69}$$

where Sc is the Schmidt number and $\widetilde{\tau}_{Z_j}^R$ is the turbulent transport of $\widetilde{Z}$. This dilution is included using a mixing rule [122]

$$\widetilde{\phi} = \widetilde{Z}\widetilde{\phi}_\mathrm{reac} + (1-\widetilde{Z})\phi_\mathrm{air} \tag{3.70}$$

where $\widetilde{\phi}$ is a generic variable representing $\widetilde{C}_p$ or $\widetilde{\Delta h}_f^0$ or $\widetilde{W}$ or species. The subscript 'reac' denotes that these values are taken from the lookup table for the local $\widetilde{c}$ value, while the subscript 'air' denotes their values in the air stream. The values obtained using Eq. (3.70) are used in Eqs. (3.68) and in the state equation. It is worth noting that Eq. (3.70) is used to

account for dilution rather then partial premixing effects, and that the filtered reaction rate in Eq. (3.26) does not include contributions that could arise from mixture fraction gradient in partially premixed combustion [27, 205]. Finally, the diffusion and turbulent transport terms in all scalar equations are closed using Eqs. (2.11) and (2.13) respectively. All the equations are discretised as explained in §3.2 and the solution procedure is iterated five times within the SIMPLEC algorithm.

The boundary and initial conditions to be used while solving the LES equations with the closures discussed in this chapter depend on the validation cases. Thus, these conditions are discussed along with the respective test flames in the following chapters.

Chapter 4

Validation cases

Four cases in total are used for validation of numerical methods, codes and combustion models. One of them is only a pure mixing case and the other three cases are reacting flows. These four cases and their cold flow results are discussed in this chapter. These configurations are chosen specifically to have a wide range of fluid mechanical features and conditions, and turbulence-chemistry interaction leading to a range of combustion conditions so that the robustness of the combustion closure can be tested.

4.1 Propane-air mixing

The SANDIA non-reacting propane round jet [214] is chosen as first case to validate turbulence modelling and procedure. The purpose here is to correctly capture turbulence and mixing properties as baseline for more complex reacting cases.

The main geometrical and physical parameters are shown in table 4.1 and a schematic of the computational domain is given in figure 4.1.

4.1.1 Computational model

A slip flow condition is assigned on the outer surfaces of the cylindrical three-dimensional domain, and a constant-pressure condition is assigned to the outlet. The domain boundaries extend $13D$ in the radial direction and $70D$ from the nozzle exit in the axial direction. These values are set by extracting positions at which gradients go to zero in the experimental results. A pipe extending $11D$ upstream the nozzle exit is also included into the domain in order to have fully developed turbulence at the exit. The sensitivity to grid size and wall boundary conditions, as well as the effect of the pipe in the geometry, is investigated performing four simulations, which are summarised in table 4.2. A dynamic Smagorinsky model is used for the

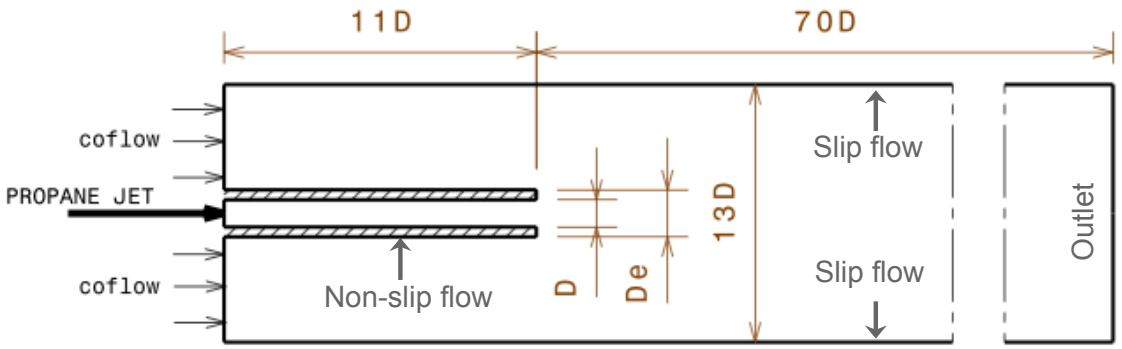

Fig. 4.1 Sketch of the numerical domain used for the Sandia propane-air non-reacting case in [214].

sub-grid stresses in all simulations, and the WALE model [172] is used for the wall boundary conditions when required. A flat velocity profile based on the mass-flow rate is assigned at the inlet for cases A to C, as velocity and turbulence are expected to evolve within the pipe. A smoothed top-hat velocity profile is used for case D, which does not include the pipe. This velocity profile is given by [200]

$$\langle U \rangle = \frac{U_0}{2}\left(1 + \frac{r}{2\theta}\right), \tag{4.1}$$

where U_0 is the centreline velocity, r is the radial distance, and θ is the momentum thickness assumed to be $\theta = D/20$. Finally, a uniform velocity of $U_{air} = 9.2\,\mathrm{m/s}$ is assigned for the coflow in all cases listed in table 4.2.

Table 4.1 Geometrical and physical parameters for the Sandia propane-air non-reacting case in [214].

Quantity	Value	Description
D	$5.3\,\mathrm{mm}$	Internal diameter
D_e	$9.0\,\mathrm{mm}$	External diameter
U_b	$53\,\mathrm{m/s}$	Bulk mean velocity of propane at the inlet
U_{air}	$9.2\,\mathrm{m/s}$	Air coflow velocity at inlet
U_0	$69\,\mathrm{m/s}$	Centreline velocity at the inlet
$\dot{m}_f$	$2.3\,\mathrm{g/s}$	Propane mass flow rate
T	$294\,\mathrm{K}$	Operating temperature
p	$1013.3\,\mathrm{kPa}$	Operating pressure
ρ_u	$1.881\,\mathrm{kg/m^3}$	Density of propane at the inlet
ρ_{air}	$1.205\,\mathrm{kg/m^3}$	Density of air at the inlet

Table 4.2 List of simulations for the Sandia propane-air non-reacting case in [214].

CASE	Grid size	Pipe	Wall Functions
A	800 k	Yes	No
B	800 k	Yes	Yes
C	3.5 M	Yes	Yes
D	2.5 M	No	N/A

Two structured grids of 800k and 3.5M cells are used and these grids have 27 and 52 cells are along the diameter respectively. The numerical cells uniformly increase in size moving in the axial and radial directions. A grid of 2.5M is also used, which differs from the 3.5M grid only for the exclusion of the pipe from the computational geometry.

4.1.2 Results

Each simulation is run in parallel using 128 processors. Statistcs are collected for a period of about 4 flow-through times, where the flow-through time is computed as the time a particle spends from the inlet to reach $x/D = 50$ moving along the centreline. Additional 3 flow-through times are used for transients to leave the numerical domain before statistics are collected. Mean centreline axial velocity profiles are shown in Fig. 4.2 for the four cases of Table 4.2. Some under-prediction is seen for all cases, probably because of the dissipative nature of eddy diffusivity models (see §3.1.1). The largest under-prediction is for case D. Cases involving the pipe produce an uncertainty on the mean axial velocity at the jet exit of 7% ($\pm 3\,\mathrm{m/s}$ in respect to U_0), which is related to the different turbulence evolution inside the pipe. Nonetheless,

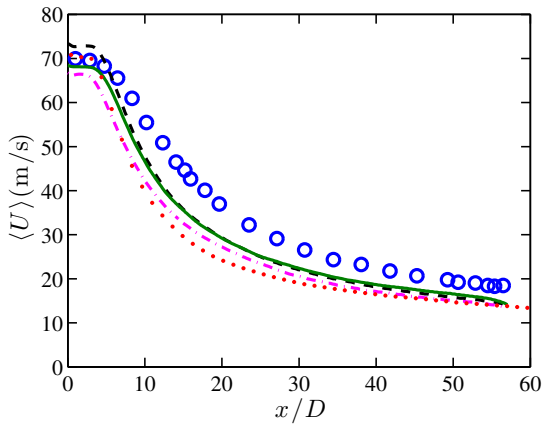

Fig. 4.2 Mean axial velocity centreline profiles from LES, obtained using cases A (–·–), B (– –), C (——) and D (•••) of Table 4.2, are compared with experimental results [214] (symbols).

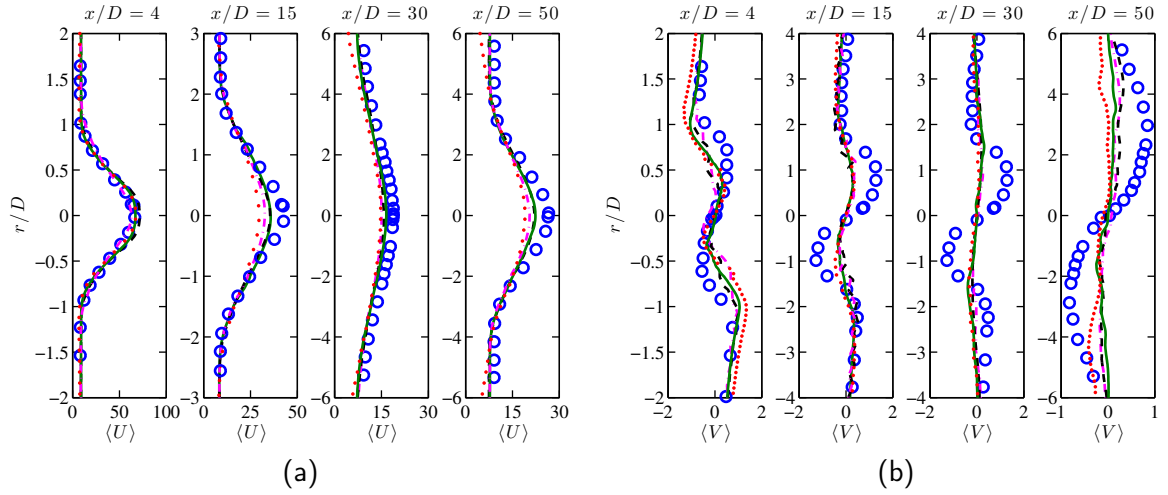

Fig. 4.3 Radial profiles of mean (a) axial and (b) radial velocity from LES are compared with experimental results. Legend is as for Fig. 4.2.

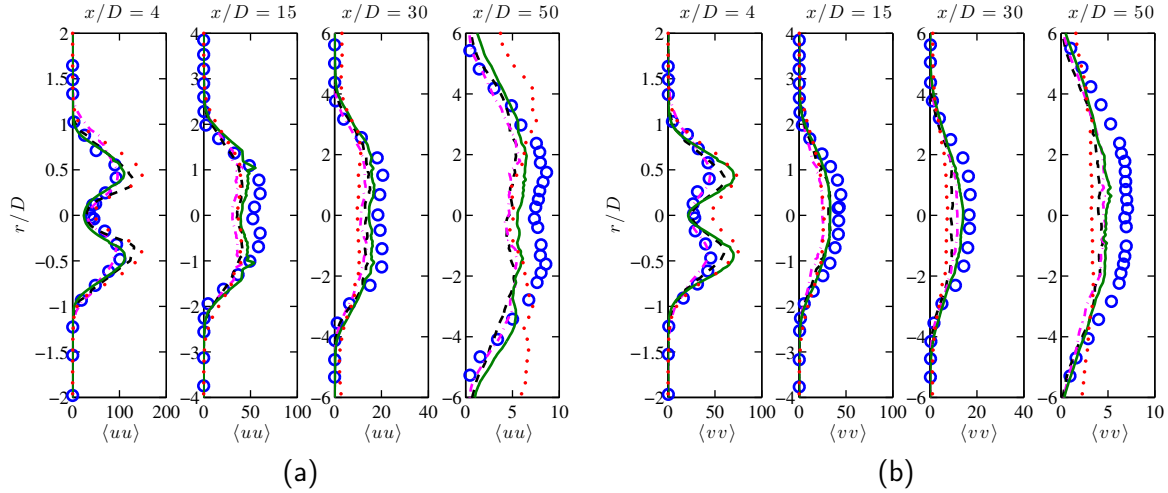

Fig. 4.4 Radial profiles of (a) axial and (b) radial velocity variance from LES are compared with experimental results (symbols). Legend is as for Fig. 4.2.

the evolution of mean axial velocity in radial and axial direction downstream of the jet exit is similar for the four cases of Table 4.2, as shown in Fig. 4.3a, suggesting that these differences at the inlet do not affect significantly the evolution downstream. Radial profiles of mean radial velocity, $\langle V \rangle$, obtained with models A to D of Table 4.2, are compared to the experimental data in Fig. 4.3b. The computed profiles are similar to each other, and they are under-predicted in downstream locations. An additional simulation has been performed with lateral boundaries extended to $\pm 26D$ to avoid possible reflection of numerical waves, which may affect the solution in case the cells close to the lateral boundary are not big enough to dissipate them [82].

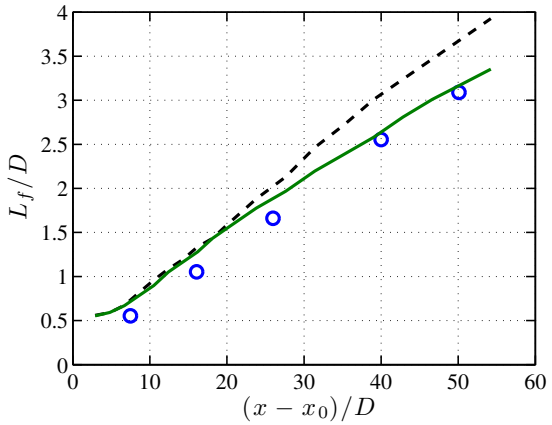

Fig. 4.5 Mixture-fraction half radius predictions from LES of case B (– –) and C (——) of table 4.2 are compared with experimental data [214] (symbols).

However, no effect on the radial velocity has been observed. A better approach may be to assign velocity or pressure conditions [16] on the lateral boundaries. It is worth noting that the velocity field is strongly dependent on turbulence and entrainment conditions at the jet exit, which are not fully described within the experimental dataset.

Axial and radial velocity variance profiles are shown in Fig. 4.4, and these second order moments show sensitivity to both grid size and turbulent conditions. Case B gives overall better predictions than case D when compared with experimental data, and this becomes evident at $x/D = 50$. Some under-prediction is seen downstream, which may be partially due to the fact that SGS variances are not included in these profiles and partially to numerical diffusion. It is worth noting that turbulence at the pipe exit is observed not to be fully developed in all cases of Table 4.2 including the pipe in the geometry. A much longer pipe is likely to be needed to reach this condition, which is unpractical. This suggests that synthetic turbulence may be a better choice for cases where inlet turbulence is relevant. Overall, predictions obtained using case B and C of Table 4.2 are reasonable, with some improved performance seen for case C. These two cases are used for further analysis below.

As noted earlier, the effect of grid size becomes relevant for second order statistics. Computed mixture-fraction half radius L_f, defined as the radial location at which the mixture fraction is equal to half its value at the centreline, are compared with experimental results in Fig 4.5. A very good prediction is observed for case C, while the smaller grid used in case B results to be inappropriate to represent the flow dynamics in downstream regions, probably because of the numerical diffusion due to the numerical cell size increase in the axial direction. On the other hand, the grid sensitivity observed for first order moments shown earlier suggests that coarser grids may be adequate to estimate first order quantities.

As result of the above analysis, a pipe will not be included in configurations where inlet conditions are well specified at the jet exit. Synthetic turbulence will be used when required for reacting flow calculations.

4.2 Piloted jet burner

The Bunsen piloted flame configuration described in [46] is chosen to assess the validity of the combustion models described in §3.3. This case involves a jet of stoichiometric methane-air

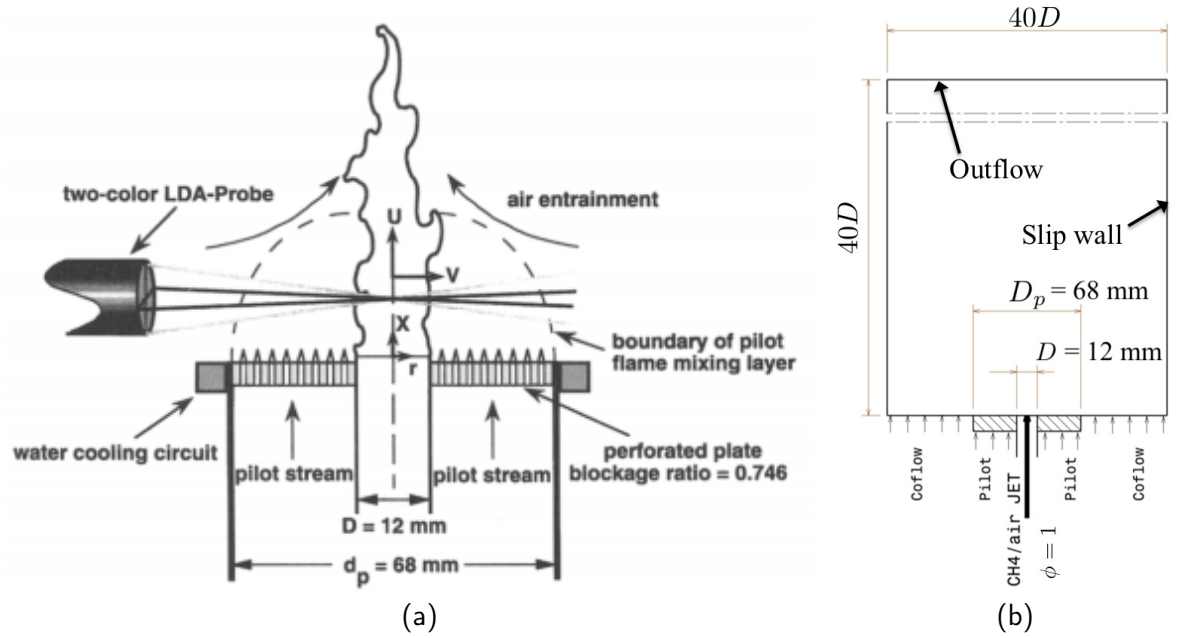

Fig. 4.6 A schematic of (a) the experimental [46] and (b) computational setup of piloted stoichiometric methane-air Bunsen flames.

mixture issuing from a pipe of diameter of $D = 12$ mm into quiescent air as shown schematically in Fig. 4.6a. This jet is surrounded by a pilot with diameter of $D_p = 68$ mm having 1175 holds of 1 mm diameter each, which inject a secondary non-reacting stoichiometric methane-air mixture into the flow at 84 cm/s per hold. This pilot has a cooling water jacket and thus its burnt mixture is sub-adiabatic for reacting flow. There are no turbulence generating devices in the reactant flow path and thus the turbulence is shear generated. Three flames F1, F2 and F3 having a bulk mean velocity of $U_b = 65$, 50 and 35 m/s respectively were investigated in [46]. These flames have Reynolds number, based on jet exit diameter and U_b, of 52,000, 40,000 and 24,000 respectively and this Reynolds number is changed by varying only U_b in the experiment. The boundary conditions, grid resolution, SGS stress closure, numerical schemes

and methods used in this study are assessed here first by comparing computational results with experimental measurements of velocity and turbulent kinetic energy (TKE) reported in [46] for the F2 non-reacting flow. The main geometrical and physical properties for this case are summarised in table 4.3.

Table 4.3 Geometrical and physical parameters for the F2 cold case in [46].

Quantity	Value	Description
D	12 mm	Internal diameter
D_p	63 mm	Diameter of the pilot
U_b	50 m/s	Bulk velocity of the jet
U_{air}	0.22 m/s	Velocity of coflow at inlet
k_0	10.8 m^2/s^2	Turbulent kinetic energy at inlet on the centeline
T	298 K	Temperature of the reactants
p	1013.3 kPa	Operating pressure
ρ_{mix}	1.15 kg/m^3	Density of jet and pilot mixture
ρ_{air}	1.205 kg/m^3	Density of the air
Λ_y	2.4 mm	Integral length scale at the inlet in the radial direction
Λ_x	4.8 mm	Integral length scale at the inlet in the axial direction
τ_t	0.65 ms	Integral time scale at the inlet

4.2.1 Computational model

A three-dimensional computational domain spanning $40D$ in all three directions as shown in Fig. 4.6b is considered in this analysis, which is discretised using structured multi-block grid having non-uniform numerical cells. These cells are fine near the burner exit and grows slowly in the downstream and radial directions. A typical grid is shown in Fig. 4.7 and two grids are considered for this study. A coarse grid having 22 cells inside the jet diameter, D, and about 4 cells within the turbulence integral length scale, measured to be about $\Lambda_y = 2.4$ mm [46] near the exit, gives a total of about 1.5 million cells for the computational volume of $\pi(40D)^3/4$ considered. This grid has 404 cells in the streamwise direction along the centreline. Increasing the cell count to 32 for D and 6 for Λ_y, keeping other grid parameters to be almost the same, yields about 4.2 million cells in total. These two grids are used to assess the grid sensitivity of the LES results reported in this study.

The jet exit velocity is specified using the radial profile reported in the experimental study [46]. There is no velocity fluctuation at the jet exit for the simulations as the turbulence

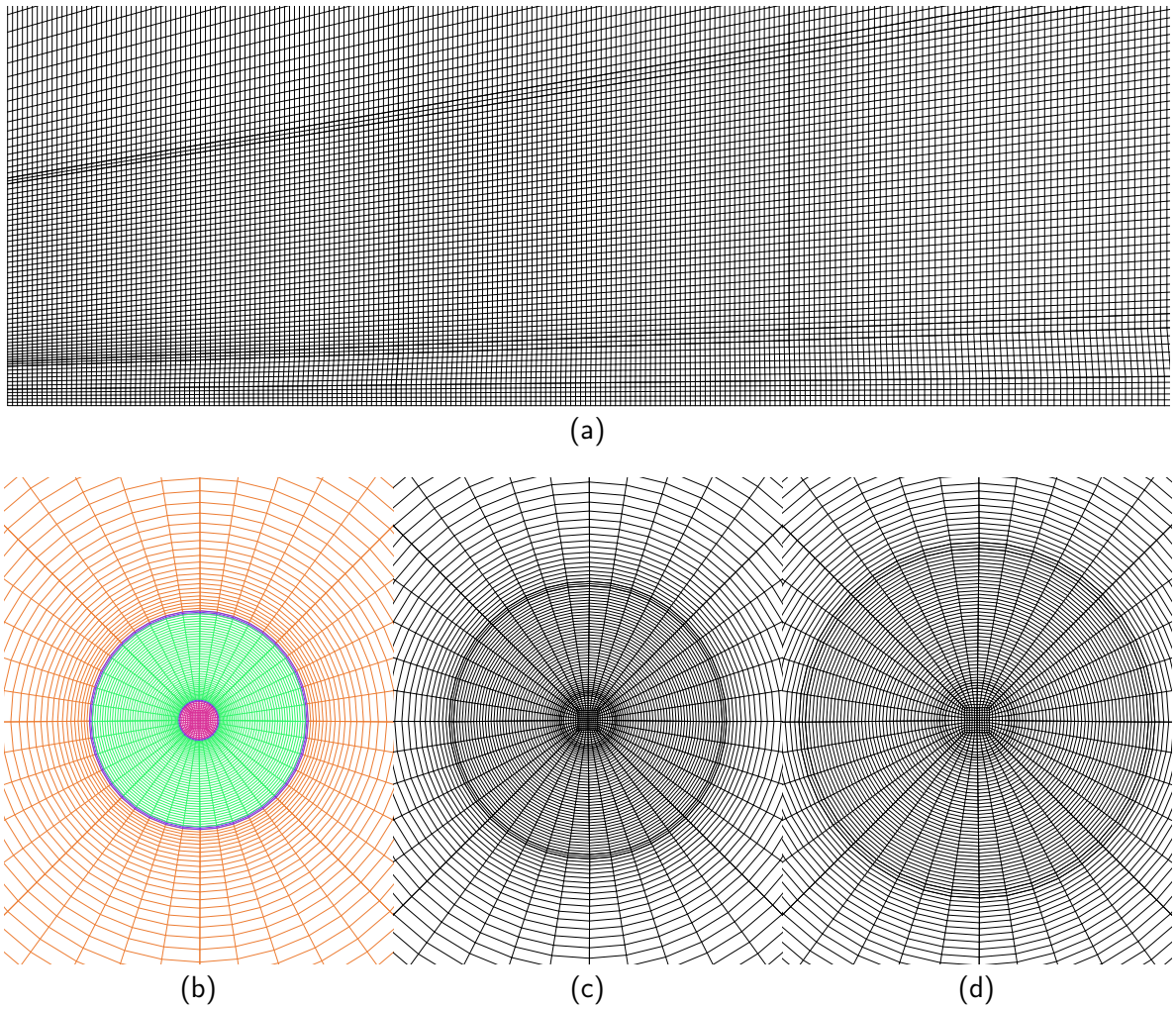

Fig. 4.7 Numerical grid used for piloted flame case [46] for 1.5M case. An axial slice through the mid-plane ($z = 0$) is shown in (a) for a region of $0 \leq x \leq 15D$ and $0 \leq y \leq 5D$. The grid distribution in a radial slice of size $y \times z = 5D \times 5D$ is shown for axial locations of (b) $x = 0$, (c) $4.5D$ and (d) $10.5D$.

in reacting region is predominantly shear generated. A uniform velocity is specified for the pilot stream on the basis of total volumetric flow rate obtained from the experimental data. A small velocity of 0.2 m/s is assigned to the coflowing air to mimic the air entrainment. The lateral boundaries are specified to be slip walls and the outlet is set to have zero gradient in the streamwise direction for all the variables. The temperature of jet, pilot stream and entrained air are taken to be 298 K for the isothermal flow analysis.

The large eddy simulations are run using 96 cores for about 0.15 to 0.25 second of real flow time. Out of these total durations, the period of data collection for averaging and analysis corresponds to about 26 flow-through times, where the flow-through time is defined using the computational domain length and the bulk-mean velocity, U_b, at the jet exit.

4.2.2 Cold flow results

The sensitivity to coflow velocity, SGS stress model and Schmidt number is assessed first using the 4.2M grid. These cases are summarised in Table 4.4. Mean axial velocity and

Table 4.4 Simulation parameters for the LES of F2 cold flow configuration in [46]. C_s is the Smagorinsky constant appearing in Eq. (3.3).

CASE	$U_{\text{air}}\,[\text{m/s}]$	$\rho_{\text{mix}}\,[\text{kg/m}^3]$	Sc_T	C_s^2
B	0.22	1.15	0.7	Dynamic
C	0.10	1.15	0.7	Dynamic
SC	0.22	1.15	Dynamic	Dynamic
SM1	0.22	1.15	0.7	0.030
SM2	0.22	1.15	0.7	0.025

TKE centreline profiles, obtained for the cases of Table 4.4, are compared with experimental results in Fig. 4.8. These quantities are normalised respectively with the jet bulk velocity

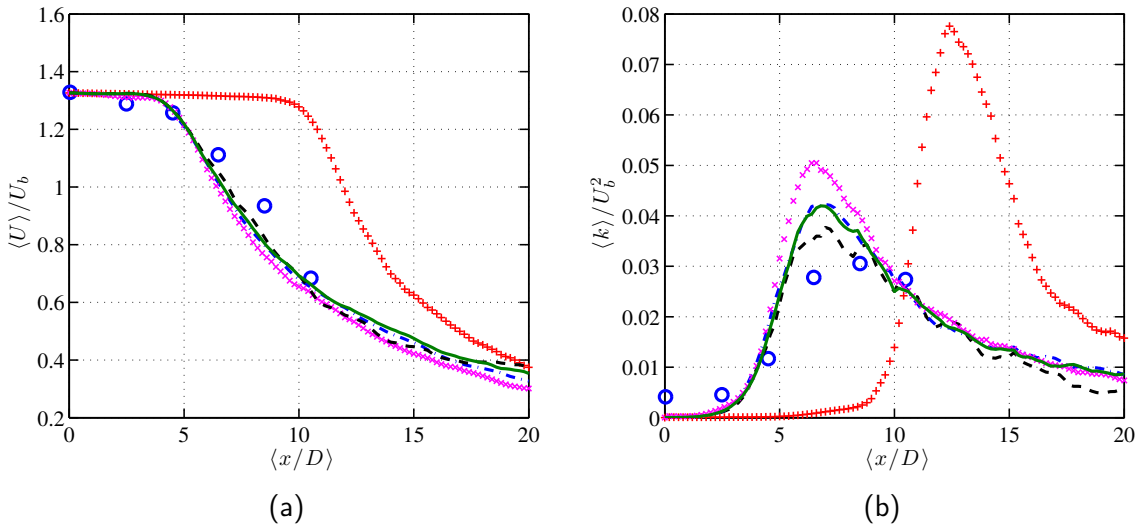

Fig. 4.8 Centerline profiles of (a) mean normalised axial velocity, $\langle U\rangle/U_b$, and (b) turbulent kinetic energy, $\langle k\rangle/U_b^2$, computed using LES on 4.2M grid for cases B (−−), C (−·−), SM1 (+), SM2 (×) and SC (——) of Table 4.2 are compared with experimental results (circles) for the F2 cold flow configuration [46].

$U_b = 50\,\text{m/s}$ and its square, U_b^2. The TKE, $\langle k\rangle$, is obtained as $\langle k\rangle = 0.5\sum\langle u_i u_i\rangle + 1.5\langle u_\Delta'^2\rangle$, where $u_i = \widetilde{U}_i - \langle U_i\rangle$. The values of u_Δ' are obtained using the Lilly's model in Eq. (3.50) for the cold flow analysed here. The energy transfer rate based model in Eq. (3.55) was also used in the analysis but no significant difference was observed for the cold flows. Small over-prediction

of mean axial velocity in the first few jet diameters are due to the absence of inlet turbulence. This over-prediction corresponds to under-prediction of TKE in the same region, as can be seen in Fig. 4.8b. After about $3D$, the TKE increases because of the shear, suggesting that the absence of inlet turbulence affects only the first few diameters. Cases B, C give similar predictions, indicating that the effect of coflow velocity is weak. The effect of using a dynamic Schmidt number, case SC, on the scalar equations (only the passive marker used to track of the air entrainment in this case) is also small as one would expect. Case SM1 suggests that a Smagorinsky constant $C_s^2 = 0.03$ is too large. Decreasing this constant to a value of $C_s^2 = 0.025$, case SM2, produces a mean axial velocity similar to case B, with a higher level of TKE in the region between $4D$ and $10D$, indicating that the choice of a dynamic formulation is more appropriate as one would expect. Because of the analysis above, case SC is kept for further analysis below and for reacting cases in the later chapters.

Figure 4.9 compares the computed and measured radial variations of averaged streamwise velocity and TKE for five axial positions. These quantities are normalised using $U_b = 50$ m/s

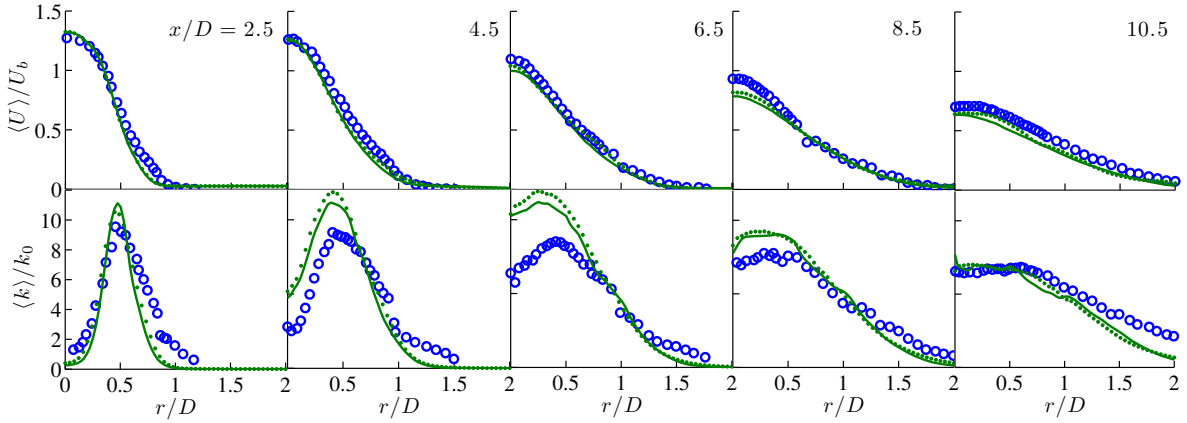

Fig. 4.9 Comparison of measured [46] (symbols) and computed (lines) normalised mean axial velocity and turbulent kinetic energy in cold flow of flame F2. The radial variations are shown for 5 axial locations and two numerical grids, 1.5M (solid line) and 4.2M (dotted line).

and $k_0 = 10.8$ m^2/s^2. Results obtained using 4.2M and 1.5M grids are compared to each other to assess the sensitivity to the grid size. The averaged streamwise velocity computed in this study agrees very well with measured values as one observes in Fig. 4.9 and the differences between 1.5M and 4.2M grid results are negligibly small not only for $\langle U \rangle / U_b$ but also for normalised $\langle k \rangle$. There are some differences between the computed and measured values of $\langle k \rangle$ for $r \leq 0.55D$. This difference decreases as one moves in the downstream direction. As seen in Fig. 4.9, the turbulence levels represented by $\langle k \rangle$ in regions of turbulent combustion (as one shall see in Chapter 5 this would be $r > 0.6D$) are captured quite well. Thus, no turbulence is specified for the jet fluid. However, feeding some inlet turbulence in commensurate with

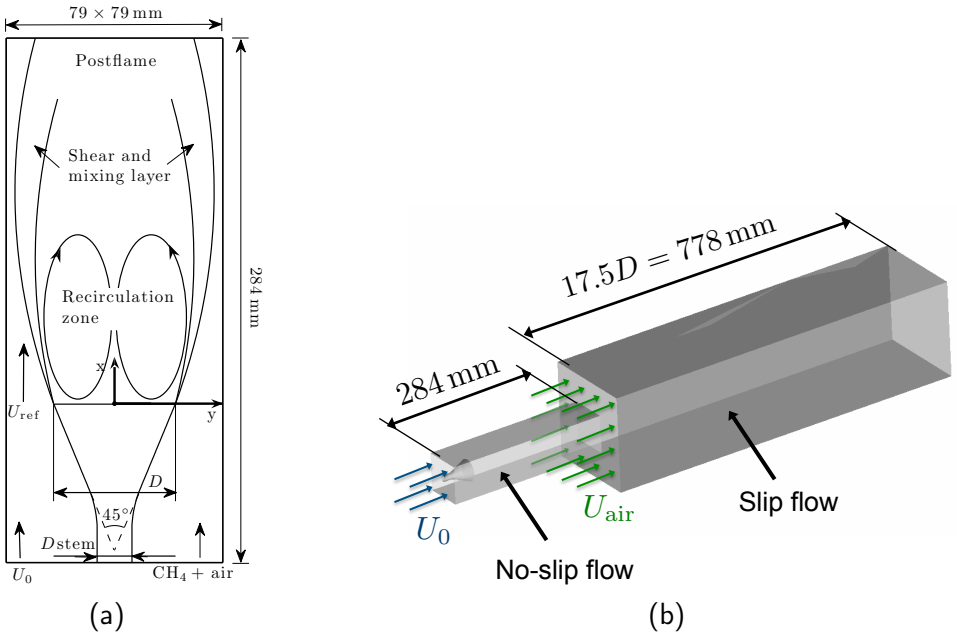

Fig. 4.10 A sketch of (a) the experimental burner configuration and (b) its numerical model.

experimental values did improve the comparison of $\langle k \rangle$ for $x = 2.5D$ but no significant changes were observed for other downstream locations because the turbulence is dominated by the shear generation mechanism in this flow configuration. Thus, ignoring a small level of inlet turbulence is acceptable. The 1.5M grid chosen here satisfies the 80% criterion of Pope [196] for TKE. Thus, it is clear that this 1.5M grid is adequate to capture the flow dynamics in the jets simulated here and hence this grid is used for flame calculations to be discussed in Chapter 5 as this choice is consistent with the views discussed earlier in the Introduction. Nevertheless, 4.2M grid will be also used for further testing and verification for reacting cases, when required.

4.3 Bluff body burner

The configuration of this burner investigated in [176–178] is shown in Fig. 4.10 along with its computational model. The flow enters a combustion chamber of dimension of $79 \times 79 \times 284$ (in mm) at 294 K. The bluff-body has a base-diameter of $D = 44.45$ mm, stem-diameter of $D_{\text{stem}} = 12.7$ mm and an apex angle of $\theta = 45^\circ$. It is placed at the centre of a square duct which also forms the combustion chamber in the downstream of the bluff-body as shown in Fig. 4.10. A turbulence generator having 3.46 mm diameter holes is placed at about 58 mm upstream of the bluff-body base. The flow entering the combustor section has a bulk-mean velocity of $U_{\text{ref}} = 15$ m/s and turbulence intensity of 2% or 24% [176–178].

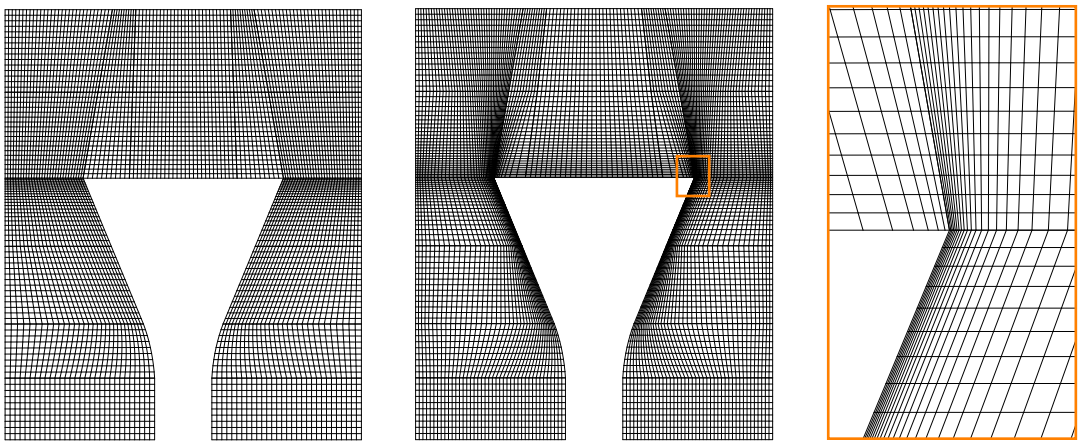

Fig. 4.11 Computational mesh in the mid-plane ($z = 0$) around the bluff body for (a) 1.8M and (b) 2.2M grids. An enlargement of the 2.2M grid is also shown in (c).

4.3.1 Computational model

The computational domain begins at 58 mm upstream of the base of conical bluff-body as shown in Fig. 4.10b and this computational boundary is specified as inflowing boundary using measured mass flow rate. The intricate geometry of the turbulence generating device used in the experiments is excluded. An additional region of $4.5D \times 4.5D \times 17.5D$ is added downstream as shown in Fig. 4.10b for numerical stability by avoiding the effects of numerical wave reflection on the combustion region if this additional domain was not present. The combustor walls are specified to be adiabatic and no-slip whereas the walls of the additional section are treated to be slip walls. The outlet at the end of the whole computational domain is specified to have zero gradients for all the variables. A flat velocity profile having $U_0 = 11.5$ m/s is specified at the inlet boundary based on the measured mass flow rate giving $U_{\text{ref}} = 15$ m/s at the entrance of the combustion chamber. A small velocity of $U_{\text{air}} = 0.2$ m/s is specified as illustrated in Fig. 4.10b for the additional computational domain to mimic the air entrainment at this location. Turbulence at the inlet of the computational domain is specified using the digital filter technique [112] and its level at the inlet is empirically adjusted so that the turbulence intensity is about 2% or 24% at the combustor entry.

The domain is discretised using two block structured meshes having 1.8M and 2.2M numerical cells and these two meshes have about 47 cells for D. Both of these grids satisfy the 80% criterion of Pope [196] for the turbulent kinetic energy. The larger grid has refined cells near the bluff-body to capture the boundary layer development along the body as shown in Fig. 4.11b. The wall refinement can be characterised in terms of the dimensionless wall distance, $y^+ = yu_*/\nu$, where y is the local normal to the wall, ν is the kinematic viscosity

Table 4.5 Geometrical and physical parameters for the bluff-body configuration [176–178].

Quantity	Value	Description
D	44.45 mm	Diameter of the bluff-body
D_{stem}	12.7 mm	Diameter of the stem
h	79 mm	height of the combustor section
L	284 mm	Length of the combustor chamber
θ	45°	Apex angle
U_{ref}	15 m/s	Reference velocity
U_0	11.5 m/s	Domain inlet velocity
U_{air}	0.2 m/s	Velocity of coflow
T	294 K	Inlet temperature

and u_* is the friction velocity, defined as $u_* = \sqrt{\tau_w/\rho}$, with τ_w being the wall shear stress. This quantity was estimated *a priori* using experimental data [168, 169] and re-computed *a posteriori* using LES data. Roughly 2 cells are encompassed in the viscous sublayer in the case of 2.2M grid, where the viscous sublayer was considered to be the region $y^+ \leq 5$. In case of 1.8M grid, the cell size near the wall is $y^+ \approx 9$ at the side of the bluff body and $y^+ \approx 90$ at the base, where the velocity gradients are small because of the effect of the recirculation zone. Since these values are outside the viscous sublayer, wall functions are employed when the 1.8M grid is used. All parameters are summarised in Table 4.5. The simulations have been run using 80 processors for a period of ten flow-through times, where the flow-through time is computed as twice the length of the combustor divided by the reference velocity, U_{ref}. The first half of this period allows the transient from the initialisation to escape the computational domain and the later half is used to collect statistics.

4.3.2 Cold flow results

The characteristics such as the length of the recirculation zone behind the bluff-body is provided within the experimental dataset and is used to assess the adequacy of the numerical grid and appropriateness of the various boundary conditions used. This quantity is extremely important as it affects significantly the evolution of the flow field. Figure 4.12 compares the computed and measured axial velocity along the centreline when the approach turbulence intensity (TI) is 2% and 24%. No synthetic turbulence is specified at the inlet for the 2% case since the turbulence evolves as the inflow approaches the combustor entry. Synthetic turbulence is imposed using axial rms velocity and lateral length scale from experiments using the digital filter technique described in [112] in case of 24% TI. The recirculation zone length, L_r, is underestimated in the calculations using 1.8M grid and the 2.2M grid yields the correct length for both conditions

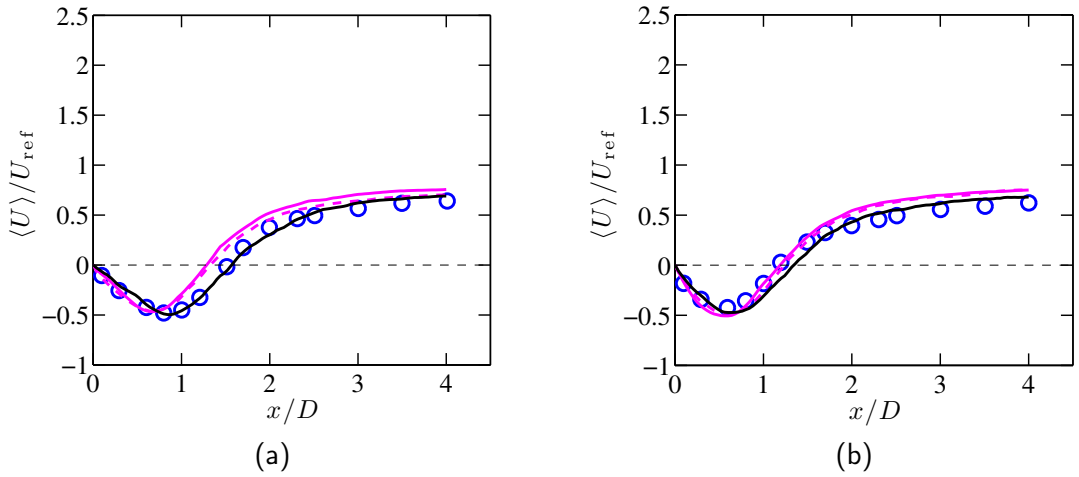

Fig. 4.12 The variation of computed (lines) and measured [176] (symbols) $\langle U \rangle / U_{\mathrm{ref}}$ along the centreline for cold flow with (a) 2% and (b) 24% TI. The results are shown for both 1.8M (——) and 2.2M (——) grid. The sensitivity to wall functions is shown for 1.8M grid (– –).

with 2% and 24% turbulence intensity. The sensitivity of L_r to the use of wall functions is also investigated and this is found to be small as shown in Fig. 4.12.

Overall, the comparison shown in this figure is very good for 2.2M grid suggesting that the numerical model used here approximates the burner flow and its attributes very well, and that the inlet turbulence technique used here [112] is appropriate.

4.4 Non piloted jet burner

The jet burner configuration studied by Furukawa *et al.* [76] is investigated as fourth and final case in this thesis. This configuration involves a cylindrical pipe of diameter $D = 26\,\mathrm{mm}$ from which a lean propane-air mixture spreads into quiescent air. A pilot was not required to stabilise the flame in the experiments because this configuration involves low velocities (the centreline velocity at the pipe exit is as low as 4.5 m/s in the cold flow) and thus the flame is stabilised on the rim of the pipe. This flame lies in the corrugated flamelets regime of the combustion diagram and thus its investigation is of interest to have a broad perspective of the combustion closures in different regimes. This flame is also prone to instabilities and flow transition, giving additional challenges for combustion modelling. Unfortunately, no cold flow measurements are available for this burner configuration. Thus, its detailed description is reminded to the reacting flow investigation in Chapter 8.

The isothermal flow results shown in this chapter suggest that the computational models, grids and boundary conditions used for the various configurations are good and represent the burner flow conditions well. The results for the reacting flows in these burners are discussed in the following chapters.

Chapter 5

Piloted flames - Algebraic closure

In this chapter the piloted flame configuration described in §4.2 is investigated. The relative performance of models and sub-models described in §3.3 is assessed by comparing LES results with experimental data [46], and an extensive analysis is conducted on properties of flamelets modelling and SDR based modelling. The algebraic closure of §3.3.1 is first explored in §5.3 using a static value for β_c in Eq. (2.22). The dynamic procedures described in §3.3.4, their advantages and limitations are assessed in §5.4.

All the simulations discussed in this chapter are listed in Table A.1 along with other simulations used to test the sensitivity to various parameters.

5.1 Experimental Cases

The piloted Bunsen flames investigated experimentally by Chen et al. [46] are considered for this study. A jet of stoichiometric methane-air mixture issues from a pipe of diameter of $D = 12$ mm into quiescent air as shown schematically in Fig. 4.6. This jet is surrounded by laminar pilot flames of stoichiometric methane-air mixture and the pilot diameter is $D_p = 68$ mm. This pilot has a cooling water jacket and thus its burnt mixture is sub-adiabatic. There are no turbulence generating devices in the reactant flow path and thus the turbulence is shear generated. Three flames F1, F2 and F3 having a bulk mean velocity of $U_b = 65$, 50 and 35 m/s respectively were investigated in [46]. These flames have Reynolds number, based on jet exit diameter and U_b, of 52,000, 40,000 and 24,000 respectively and this Reynolds number is changed by varying only U_b in the experiment. It is worth to note that, because of the large pilot, the air entrainment has an effect of dilution on the burnt gases in these flames, which can thus be supposed to operate in a premixed mode. In this regard, an analysis by Wang et al. [240] has shown that the probability to find values of equivalence ratio smaller than 0.8 is below 1% for the stoichiometric piloted flame with largest Reynolds number in [46]. Similar conclusions

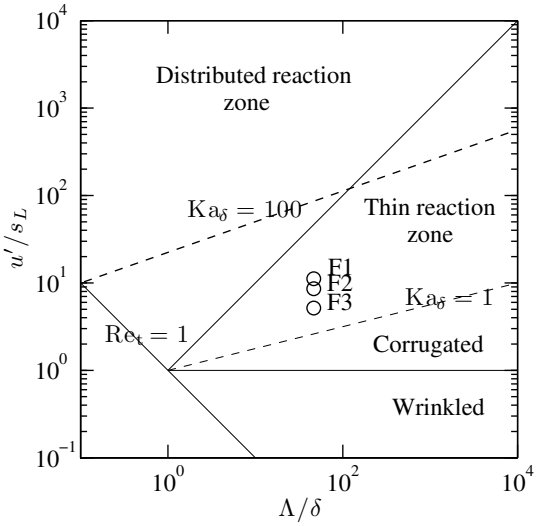

Fig. 5.1 Combustion regime diagram showing conditions of flames F1, F2 and F3.

were made by Kolla et al. [122] in terms of mixture fraction for the same configuration using RANS. Additional terms in Eq. (3.26) to account for partial premixing are thus not considered here and the effect of dilution on the thermophysical properties (heat capacity, enthalpy of formation and molecular weight) is taken into account as described in §3.4.

The radial variations of averaged temperature, fluid velocity, turbulent kinetic energy, various species mass fractions at axial locations ranging from $x/D = 2.5$ to 10.5 were measured and reported in [46]. These are useful to evaluate the overall model performance and in this respect, these flames were also considered by a number of past RANS [5, 96, 122, 143, 198, 208, 209, 222, 223] and LES [53, 56, 130, 186, 240, 243] studies using different combustion modelling. The availability of these results provides strong impetus for using these flames to address the objectives of this study.

The conditions of turbulent combustion in these flames, F1, F2 and F3, are shown in a combustion regime diagram [180] as Fig. 5.1. All of these flames are in the thin reaction zones regime [180] and the conditions of F1 to F3 are calculated using the centreline value of the turbulence RMS velocity, u', and the lateral integral length scale, Λ, of 2.4 mm measured [46] near the nozzle exit. The Zeldovich thickness is calculated as $\delta = \nu_u/s_L$ for the stoichiometric methane-air mixture at room temperature, where ν_u is the kinematic viscosity of the reactant mixture. The turbulence Reynolds number is defined as $\mathrm{Re}_T = u'\Lambda/\nu_u$. The flames F1 to F3 are simulated using LES methodology employing the models discussed in section 3.3.1 and details of these simulations are discussed next.

A value of about 0.83, based on a DNS analysis [77] is used for the Bray constant C_m in Eq. 2.19 in cases where this algebraic closure is used. Values of laminar flame speed,

thermal thickness and heat release parameter are assigned consistently from stoichiometric one-dimensional computations as $s_L \approx 0.41\,\mathrm{m/s}$, $\delta_{th} \approx 0.42\,\mathrm{mm}$ and $\tau \approx 6.48$. The heat release parameter can also be defined using mixture density as $\tau = \rho_u/\overline{\rho} - 1$ and it is observed that the numerical results to be reported in section 5.3 are not unduly influenced by this choice. If the reactant mixture is stratified then this definition is more suited as it can capture spatial variation in τ. The four closures in Eqs. (3.50) to (3.52) and (3.55) are used to model the SGS velocity scale u'_Δ required for $\widetilde{\varepsilon}_c$ closure in Eq. (2.22) and the results of this testing is discussed in §5.3. The closure for u'_Δ in Eq. (3.56) is not used here for the following reason. This model was derived specifically for use in conjunction with thickened flame model and its efficiency function requiring turbulence level of unburnt mixture that would have existed locally in the absence of heat release rate. However, it would be inappropriate to exclude the dilatational effects on u'_Δ required in Eq. (2.22) because the SGS velocity in this equation is related to the SGS kinetic energy, which must include such effects. The local gradients of c will be influenced by combustion even in the absence of turbulence and the local values of ∇c result from a fine balance among turbulent transport, heat release, advection and molecular diffusion. All of these processes will be influenced by the heat release effects and the local velocity will be affected by the acceleration induced by dilatation resulting from the flame. The model of Eq. (3.56) will be specifically used for comparisons in cases where the thermal dilation is relevant in Chapter 8 in order to assess this effect on the SGS velocity modelling.

The static value of the model parameter β_c is chosen empirically for this study and this is the only tuneable parameter in the algebraic reaction rate closure given in Eqs. (2.19) and (2.22). The values used in this study for the three flames are guided by an earlier analysis [77]. The value of β_c can be evaluated dynamically as discussed in §3.3.4 and this will be investigated in §5.4. Overall, the algebraic closure for the filtered reaction rate involving the filtered scalar dissipation rate works acceptably well and of course this closure is based on high (local) Damköhler number. The influences of local finite rate chemistry can be included in this approach using either unstrained or strained flamelets and this would be explored in Chapter 6.

5.2 Specific numerical detail

The time step used to keep the CFL below 0.3 in the simulations to be discussed later is of $3\,\mu$s ($2\,\mu$s), $4\,\mu$s ($3\,\mu$s) and $6\,\mu$s ($4\,\mu$s) respectively for flames F1, F2 and F3 using 1.5M (4.2M) grid. The sub-grid stresses are modelled using dynamic Smagorinsky model [81, 141] and the SGS scalar fluxes are computed using gradient hypothesis with dynamic Schmidt number approach [141]. The test-filter size for all dynamic procedures used in this study is $\widehat{\Delta} \approx 2\Delta$

following common practices with filter width estimated as $\Delta = (\mathscr{V}_i)^{1/3}$, where $\mathscr{V}_i$ is the volume of computational cell i.

The exit velocity for the jet is specified using its measured radial profile [46]. There is no fluctuation specified for this velocity since the turbulence in reacting region is shear generated, as discussed in §4.2. The pilot stream temperature is unspecified in the experimental study and values ranging from 1785 to 2248 K were used in past studies [5, 53, 56, 96, 122, 143, 186, 198, 208, 209, 222, 223, 240, 243] suggesting that the heat loss to the pilot burner varies from 0 [53] to 34% [56, 143]. A value of 17% was used in [96] and 20% heat loss was assumed in [186, 240]. For this study, it is taken to be 16% following [5, 122, 129], which gives 1950 K for the pilot temperature. These past studies showed that the pilot temperature uncertainty influences the temperature field only close to the jet exit ($x \leq 3D$), which is also confirmed here by changing this temperature over a range of about 200 K using for both algebraic and unstrained flamelet models. Other initial and boundary conditions are as those specified for the cold flow in table 4.3.

Out of many possibilities to define the instantaneous c, the fuel mass fraction, Y_f, is used here to define the progress variable as $c = 1 - Y_f/Y_{f,u}$ so that it takes a value of 0 and 1 in the unburnt and burnt mixtures respectively. The fuel mass fraction in unburnt mixture is denoted as $Y_{f,u}$. This definition of c avoids spurious flame that will appear numerically in the mixing layer between the pilot and coflow if it is defined using temperature T or any other species mass fraction. The filtered progress variable, $\widetilde{c}$, has a value of 0 in the jet exit and 1 for the pilot and coflowing streams. The passive fluid marker, $\widetilde{Z}$, needed for Eq. (3.70) is specified to be 1 at the jet and pilot exits, and 0 for the air inlet. The total enthalpy at these boundaries is specified to be consistent with the respective temperature and mixture composition. Other computational details such as grids and boundary conditions are discussed in §4.2. As noted in §4.2.1, these simulations are conducted using 96 cores for a period of about 32 flow-through times, defined using the computational domain length and the respective U_b. This is substantially larger than what has been used in past studies of these flames. These computations took about 12 h on the wall clock for 1.5M grid and 24 h for the 4.2M grid in the Darwin cluster at Cambridge (see §3.2.2). A period of 16 flow-through times is used for collecting statistics, after allowing the initial transient to leave the domain in the first 16 flow through times.

5.3 Results for static β_c

The algebraic reaction rate closure in Eqs. (2.19) to (2.22) and its efficacy to capture flame brush structure is explored in this section. This algebraic reaction rate closure needs a model for SGS velocity scale, u'_Δ. The models of Eqs. (3.50) to (3.52) and (3.55) have been tested in

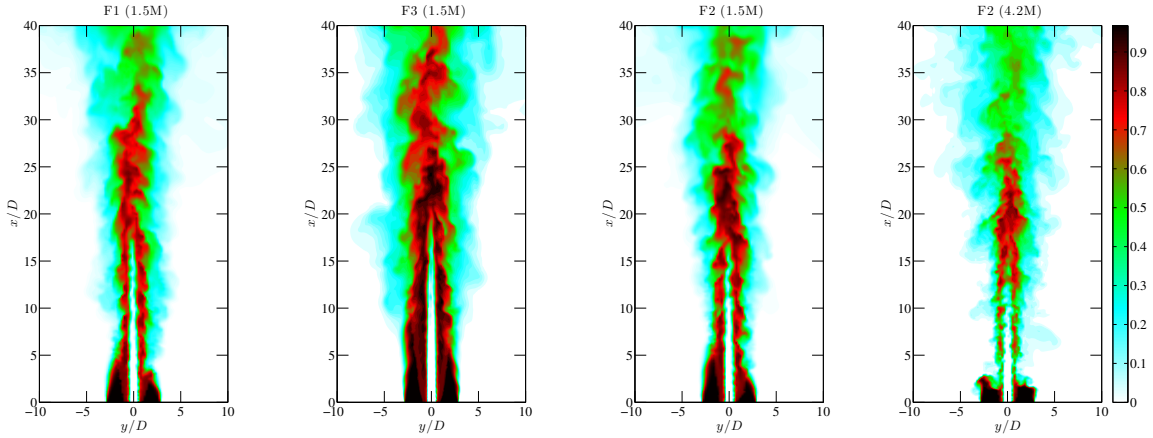

Fig. 5.2 The spatial variation of normalised filtered temperature, $\widetilde{T}^+$, field in $z = 0$ plane for the three flames, obtained using algebraic model for $\overline{\dot{\omega}}$ with $\beta_c = 7.5$. The result from 4.2M grid is shown only for F2 to depict the grid influence.

an *a priori* analysis using DNS data in [130]. The restults of this analysis show some sensitivity of the filtered dissipation rate, $\widetilde{\varepsilon}_c$, to the u'_Δ model. The sensitivity of various statistics obtained from LES results to the modelling of u'_Δ is discussed in the following section along with a discussion on grid sensitivity of LES statistics obtained using the algebraic closure.

5.3.1 General flame features

The spatial variations of temperature at an arbitrarily chosen time are shown in Fig. 5.2 for the three flames, F1, F2 and F3. The temperature is normalised as $\widetilde{T}^+ = (\widetilde{T} - T_u)/(T_b - T_u)$ and it varies from 0 in the reactant and 1 in product mixtures. The subscripts u and b respectively denote unburnt and burnt mixtures. This normalised temperature field is shown in the mid z plane from simulations using 1.5M grid for all three flames. As one would expect, the presence of shear driven Kelvin-Helmholtz instability is seen in the shear-layer region between the jet and pilot stream and this becomes more obvious in F1 because of higher Reynolds number. The potential core region, denoted by the middle region with $\widetilde{T}^+ \approx 0$, is of similar length in all the flames. When the refined grid with 4.2M cells is used for the flame F2, this length is reduced slightly and the fine scale structures emerging from the Kelvin-Helmholtz instability become more apparent. Also, the flame length is reduced substantially. Furthermore, the normalised temperature field seems to be more intermittent compared to that for 1.5M grid. The filter width implied by the numerical grid volume in 4.2M case is $\Delta^+ \leq 1$, for which the filtered reaction rate closure in Eq. (2.19) is not fully valid as has been discussed in earlier studies [61, 77, 147]. This yields locally lower temperatures in case of the 4.2M grid and this effect is seen clearly

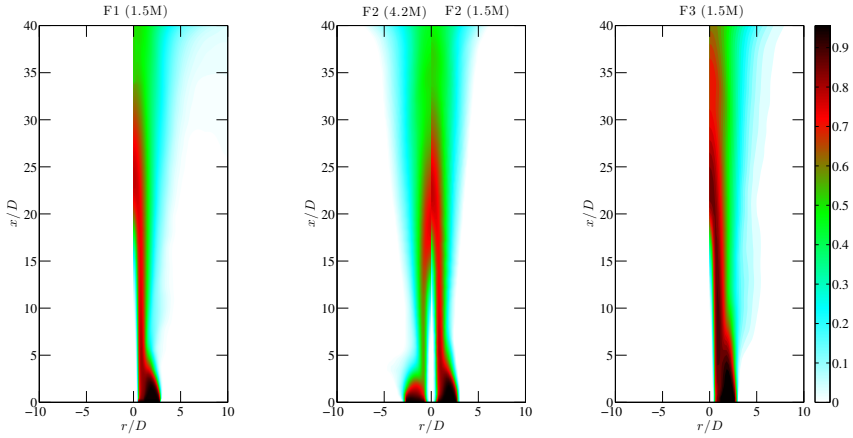

Fig. 5.3 The spatial variation of averaged and normalised temperature, $\langle \widetilde{T}^{+} \rangle$, in three flames, obtained using algebraic model for $\overline{\dot{\omega}}$ with $\beta_c = 7.5$.

in the averaged normalised temperature, $\widetilde{T}^{+}$, field shown in Fig. 5.3. The variations of $\langle \widetilde{T}^{+} \rangle$ obtained using 1.5M grid are similar to those observed in many earlier numerical studies of these flames using various combustion modelling approaches.

The normalised minimum filter sizes, Δ^{+}_{min}, implied by the minimum cell volume are respectively 1.3 and 0.8 for 1.5M and 4.2M grids. These sizes become respectively 2.8 and 1.7 if one uses the diagonal distance of the smallest numerical cell. Since the grid is spatially non-uniform the implied filter width varies spatially and a typical distribution obtained using the local cell volume is shown in Fig. 5.4 as a histogram for the two numerical grids used in this study. This histogram is constructed using the numerical grid information gathered from the whole and two different subparts of cylindrical computational domains having $0 \leq x \leq 20D$ and $0 \leq r \leq 10D$, and $0 \leq x \leq 11D$ and $0 \leq r \leq 2D$, where $r = \sqrt{y^2 + z^2}$. For the smallest subdomain considered, the most likely width for the implied filter is about $2\delta_{th}$ and $0.9\delta_{th}$ for 1.5M and 4.2M grids. This information is interesting as the reactions happen close to the jet exit and thus this subdomain is representative of the region of the reactions. When the subdomain size is increased in the axial and radial directions the most likely and averaged filter widths are increased substantially, especially for 1.5M grid. The most likely value of Δ^{+} is about 4 and the average value is about 5 to 6. There is a further increase in these values when the whole domain is considered for this analysis. The increase in the count around $\Delta^{+} \approx 14$ and about 10 respectively in Figs. 5.4a and 5.4b is due to the larger grid sizes near the lateral and outflow boundaries (see Figs. 4.6 and 4.7) of the computational domain. The above values of Δ^{+} are substantially larger than typical values used in past LES studies of these experimental flames.

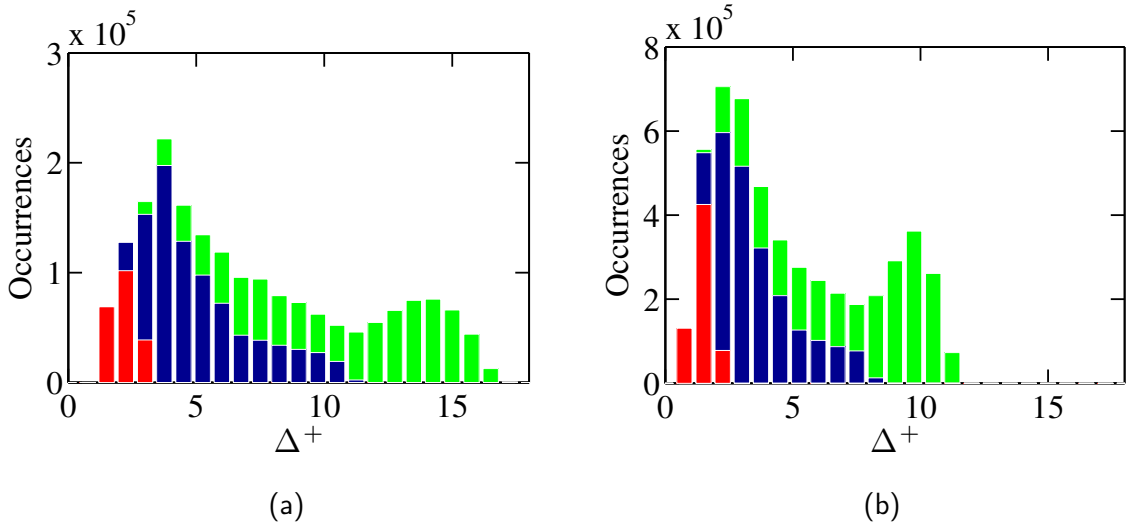

Fig. 5.4 Histogram of normalised filter width, Δ^+, for (a) 1.5M and (b) 4.2M numerical grids. Different domain sizes have been used: whole computational domain (), $0 \leq x \leq 20D$, $0 \leq r \leq 10D$ (), and $0 \leq x \leq 11D$, $0 \leq r \leq 2D$ ().

5.3.2 Sensitivities to SGS velocity modelling

As noted in §3.3.3, the SGS velocity influences the filtered reaction rate directly through the sub-grid scale scalar dissipation rate, $\widetilde{\varepsilon}_c$, modelled by Eq. (2.22). The influence of u'_Δ modelling on the filtered reaction rate computed in the LES of flame F2 is shown in Figure 5.5 for four models used in this study. Countours obtained using the k_{sgs} equation, to be discussed in more details in §5.3.4, are also shown. The reaction rate is normalised using $\rho_u s_L/\delta_{th}$ and the colourmap is shown for $\overline{\dot{\omega}}^+ > 0.01$ for an arbitrarily chosen time. The algebraic models in Eqs. (3.50) to (3.52) give relatively thinner fronts compared to that obtained using Eq. (3.55) or the k_{sgs} equation. The flame length is more or less the same for all the models and there is a slightly longer flame for the scale-similarity model in Eq. (3.51). The Lilly's model in Eq. (3.50) gives the shortest flame. Also, the peak reaction rate near the burner exit is seen only for Eq. (3.51) and k_{sgs} transport equation. The peak reaction rate predicted by the other models is relatively smaller. The averaged normalised reaction rate shown in Figure 5.6 is almost similar for the various SGS velocity models. The difference is seen only in the region close to the jet exit ($x \leq 2.5D$). The differences observed in Figures 5.5 and 5.6 suggest some sensitivity to u'_Δ modelling. It is not easy to measure the reaction rate in experiments and thus it may not be easy to assess the accuracy of these SGS velocity models. However, one can make this assessment for overall performance of these models using statistics gathered from LES and measurements as has been done next.

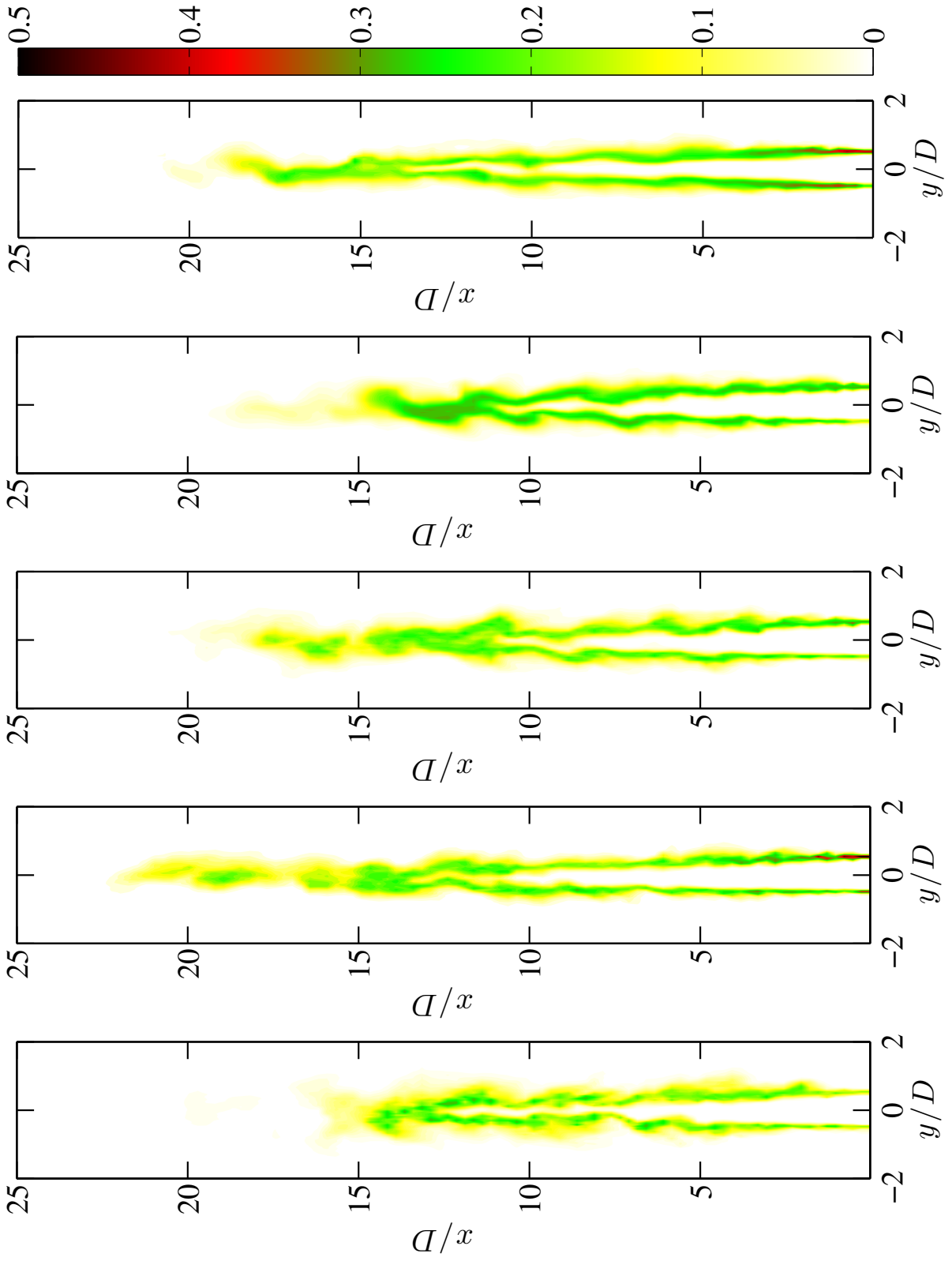

(a) Eq. (3.50) (b) Eq. (3.51) (c) Eq. (3.52) (d) Eq. (3.55) (e) Eq. (3.13)

Fig. 5.5 Colour map of normalised filtered reaction rate, $\overline{\dot{\omega}}^{+}$, for flame F2, computed for various u'_{Δ} models.

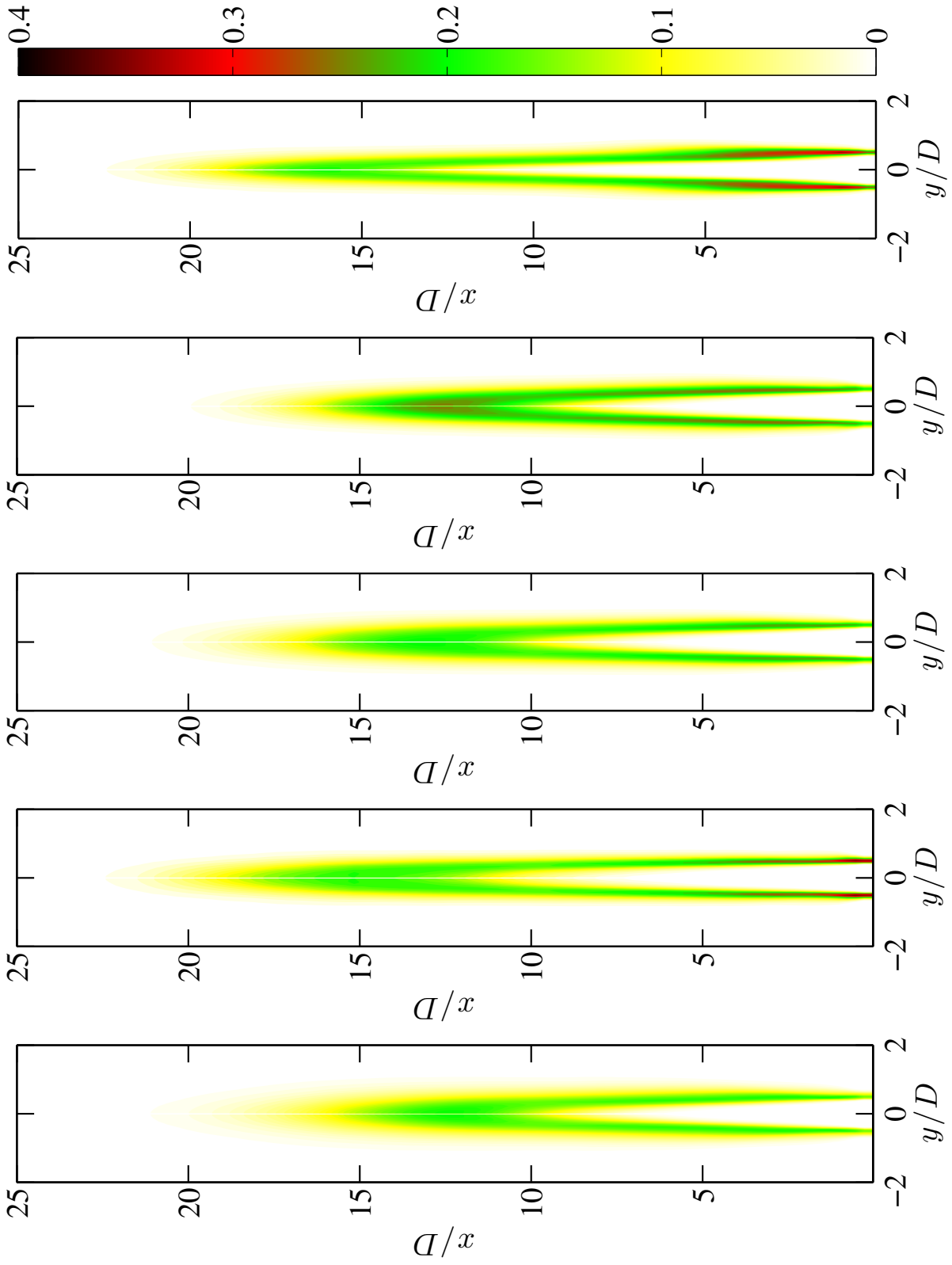

(a) Eq. (3.50) (b) Eq. (3.51) (c) Eq. (3.52) (d) Eq. (3.55) (e) Eq. (3.13)

Fig. 5.6 Colour map of normalised mean reaction rate, $\langle \overline{\dot{\omega}}^{+} \rangle$, for flame F2, computed for various u'_{Δ} models.

The flame F2 simulated using 4.2M grid is chosen for this assessment because the results for 1.5M grid is better than what is shown here. Figures 5.7 and 5.8 respectively show the sensitivity of fluid dynamic and scalar quantities to u'_Δ modelling. The radial variation of

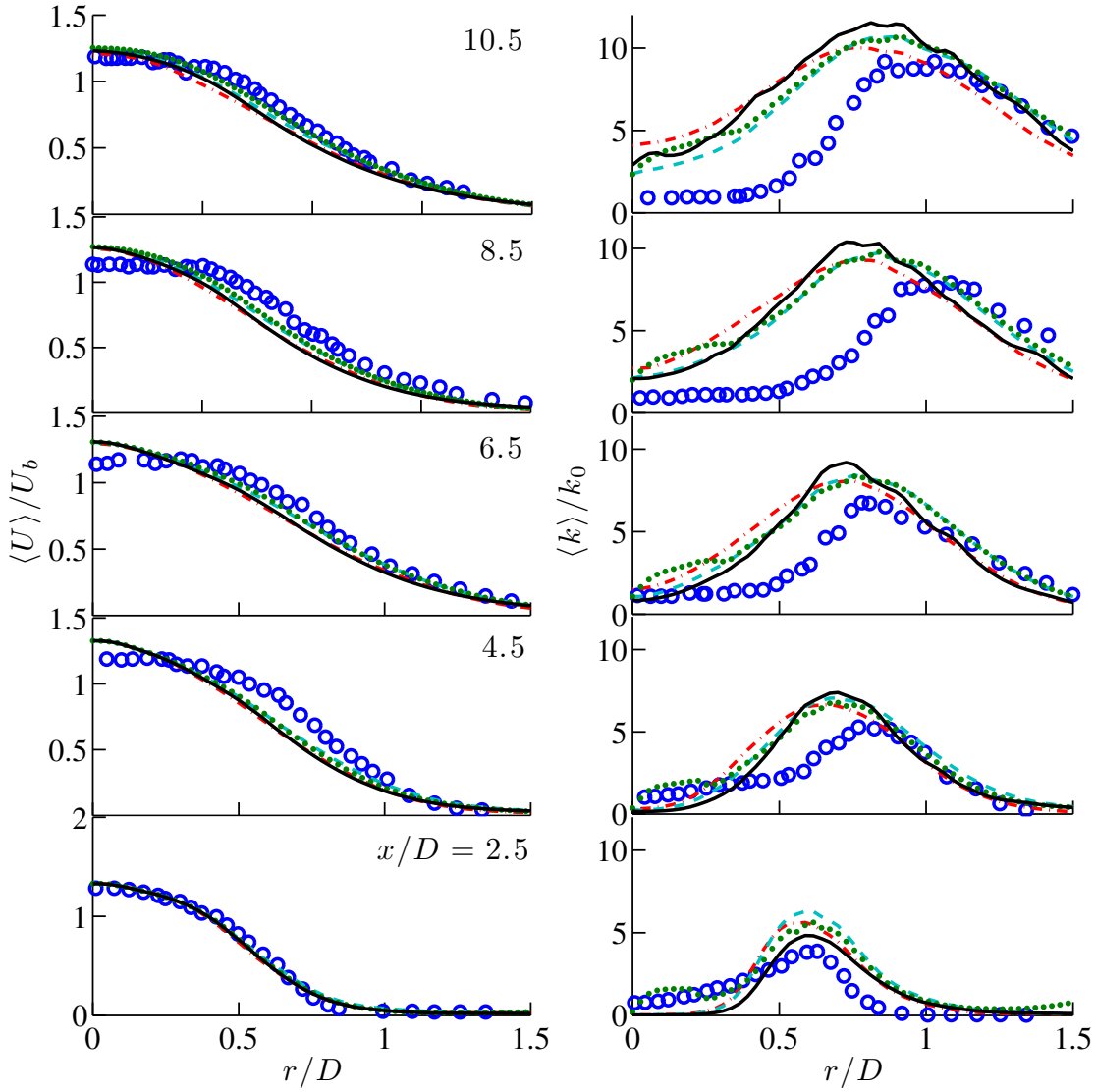

Fig. 5.7 Influence of SGS velocity modelling on averaged streamwise velocity, $\langle U\rangle$, and turbulent kinetic energy, $\langle k\rangle$, obtained using algebraic model for $\overline{\omega}$ with $\beta_c = 7.5$. Symbols (○) are experimental results [46], lines are from simulations using Eq. 3.50 (– · –), Eq. 3.51 (——), Eq. 3.52 (•••) and Eq. 3.55 (– –).

averaged streamwise velocity, $\langle U\rangle$, normalised using U_b is shown in Fig. 5.7 for five streamwise locations. The averaged normalised turbulent kinetic energy, $\langle k\rangle/k_0$, is also shown in this figure. The contribution of SGS kinetic energy to $\langle k\rangle$ is obtained using the same u'_Δ model consistently

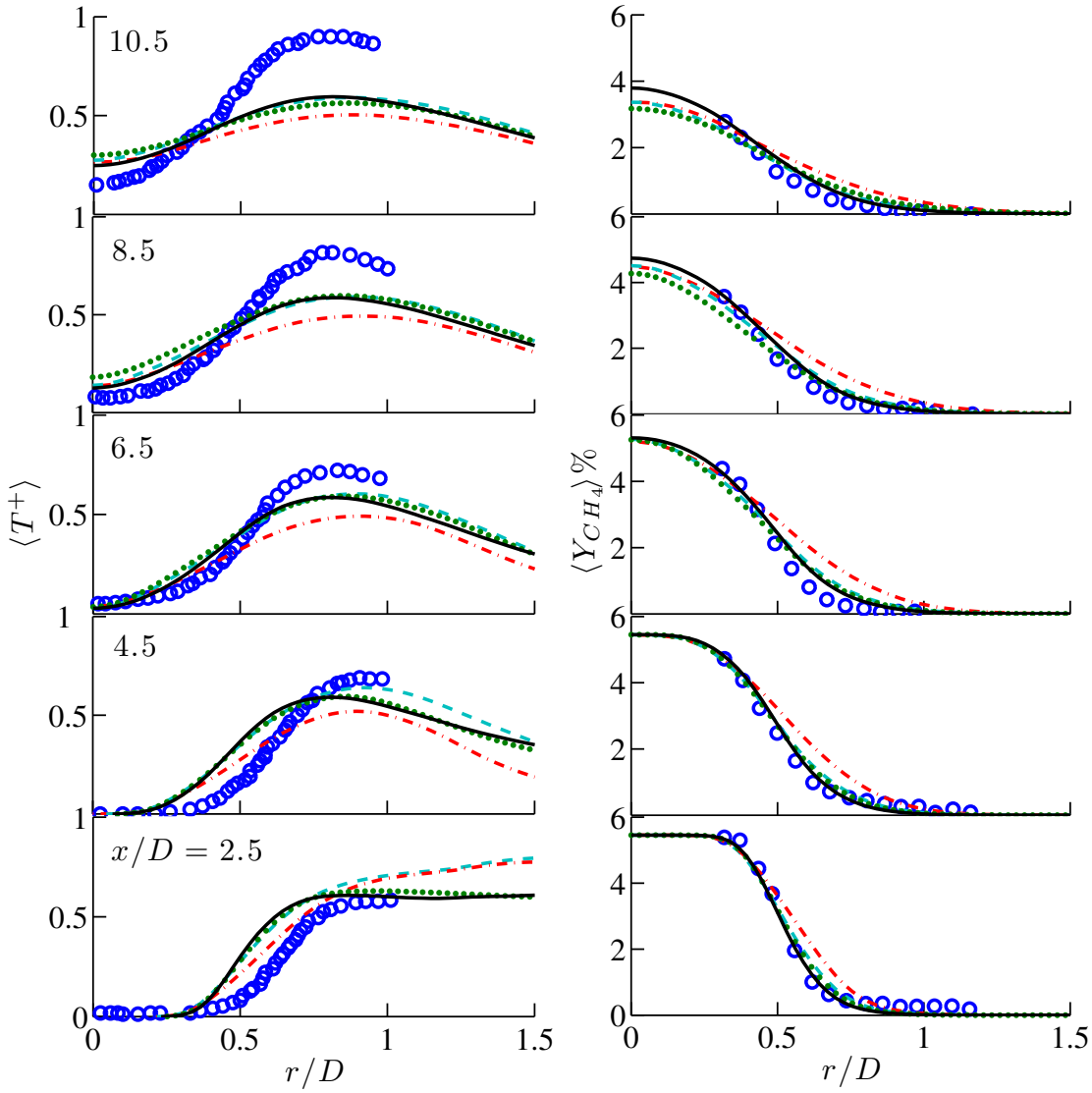

Fig. 5.8 Influence of SGS velocity modelling on averaged fuel mass fraction and normalised temperature, obtained using algebraic model for $\overline{\dot{\omega}}$ with $\beta_c = 7.5$. The legend is as in Fig. 5.7.

for four different cases discussed in section 3.3.3. The variation of $\langle U \rangle / U_b$ is observed to be very weakly sensitive to this SGS velocity modelling as seen in Fig. 5.7. However, a weak sensitivity is seen for $\langle k \rangle / k_0$ as one moves downstream. All the models overestimate $\langle k \rangle$ for $r \leq 0.8D$ when $x \geq 8.5D$ and their estimates for the outer region, $r > D$, compare reasonably well with the measured values.

The flame related quantities, fuel mass fraction and normalised temperature, are shown in Fig. 5.8. The estimates of $\langle Y_{\mathrm{CH4}} \rangle$ by the scale-similarity model in Eq. (3.51) are closer to

the measured values. Although a similar behaviour is seen for the normalised temperature there are some large underestimates for $r > 0.7D$, which is related to the performance of filtered reaction rate closure in Eq. (2.19) on 4.2M grid supporting the observation made in Figs. 5.2d and 5.3b. More elaborate discussion on this point will be provided later while discussing Fig. 5.12. Based on these assessments, the scale-similarity model in Eq. (3.51) seems appropriate for LES of reacting flows, at least for the conditions investigated in this study. The SGS stress related models in Eqs. (3.50) and the model of Bardina *et al.* in Eq. (3.52) are less satisfactory compared to the scale-similarity model in Eq. (3.51) and energy transfer based model in Eq. (3.55). It is to be noted that SGS stress based model considers only the deviatoric part of the SGS stress tensor and not the trace of this tensor while the SGS kinetic energy per unit volume is related to this trace. For these reasons, Eqs. (3.51) is selected for the following analyses.

5.3.3 Analysis of flame brush structure

De & Acharya [53] compared RANS and LES results for the experimental flames from a number of past studies and thus their results are used here for comparison. They used 1.88M and 5.91M cells in a domain of size $20D$ and $4D$ in the axial, x, and radial, r, directions respectively, and their results using a modified thickened flame approach on the 1.88M grid is used here. The RANS-strained flamelets study of Kolla and Swaminathan [122] used an axisymmetric domain of $x = 70D$ and $r = 45D$ with about few hundred thousand cells. The LES-thickened flame study of Wang *et al.* [240] used unstructured grids ranging from about 3.2M to 8.5M cells in a domain of $x = 120D$ and $r = 40D$. Their results from the 8.5M grid is used for comparison here. The recent LES-PDF study using Eulerian stochastic fields approach by Dodoulas & Navarro-Martinez [56] used a computational domain of $x = 15D$ and $r = 5D$ employing about 510k and 225k grids in the physical space and their results on their largest grid, and with 16 stochastic fields, is used here. Further detail on the combustion modelling and numerical methods used in these studies can be found in these references and the results available there are used for comparison here.

The radial variation of $\langle U \rangle / U_b$ for various streamwise locations are shown in Fig. 5.9 along with experimental measurements. Only two representative results from past studies are shown here because those results are very similar to one another. The current results are shown for the 1.5M grid and the 4.2M grid result is shown only for F2 flame because the relative behaviour is very similar for the other two flames. The difference in $\langle U \rangle / U_b$ obtained using the 1.5M and 4.2M grids is negligibly small and the values obtained using the 1.5M grid compare well with the measurements also. These results agree well with those from past studies, however, a close examination of Fig. 5.9 suggests that the agreement with the experimental data is better for the

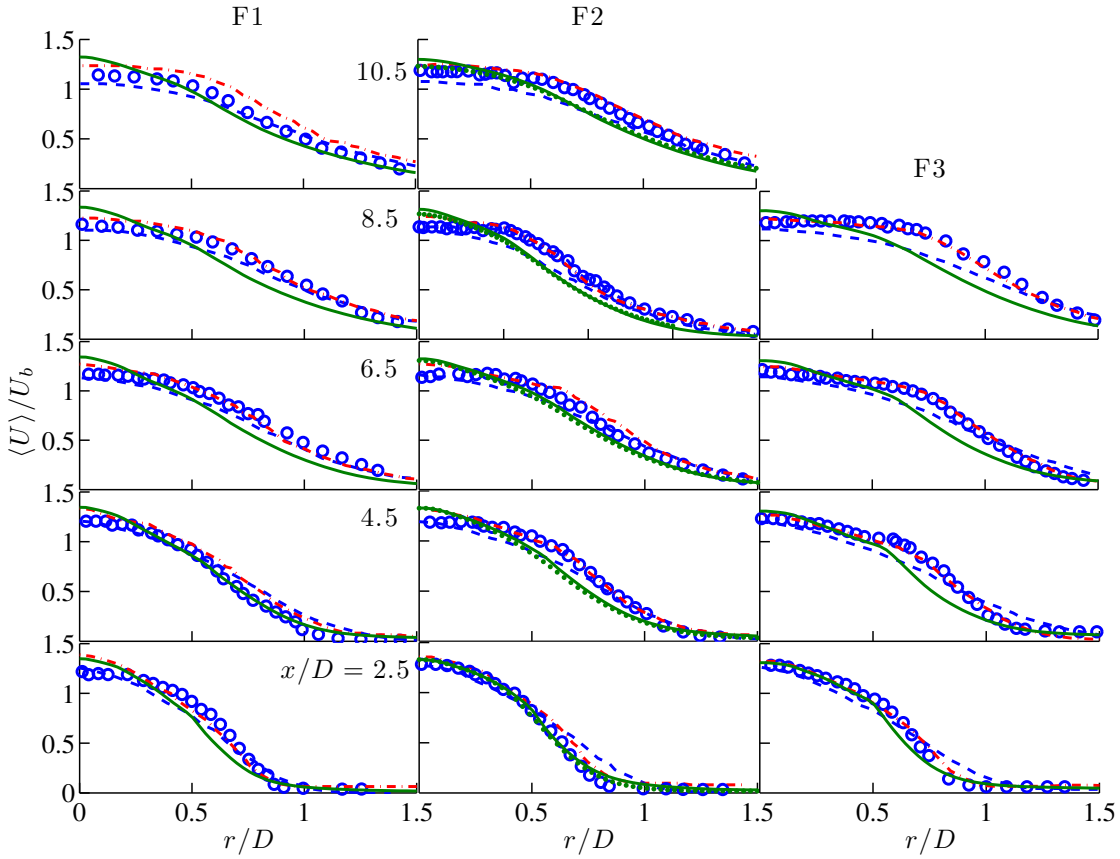

Fig. 5.9 Comparison of radial variation of normalised axial velocity, $\langle U \rangle / U_b$, in experiments [46] (symbols) and simulations (——) using Eqs. (2.19), (2.22) (with $\beta_c = 7.5$) and (3.51) on 1.5M grid. Results obtained using 4.2M grid (•••) are shown only for F2. Previous RANS [122] (– –) and LES [240] (– · –) results are also shown for comparison.

results of [240], which used 8.5M unstructured grid. Nevertheless, the difference among the numerical results and the data is observed to be small.

The radial variation of $\langle k \rangle / k_0$ at various streamwise locations is shown in Fig. 5.10 for the three flames. The statistics from LES are improved compared to previous RANS results as one would expect. The agreement between the computational results of this study and measured values improves as the turbulence Reynolds number increases (going from F3 to F1). This is due to the fact that the underlying assumption of high Reynolds number for the algebraic model of Eq. (2.19) is better verified for flame F1 and this observation is consistent with other scalars to be discussed later. The variations of $\langle k \rangle / k_0$ computed using the 4.2M grid shown for the flame F2 agree quite well with measured values in the near field and the agreement becomes poor in the inner region of the jet at downstream locations. However, the results from 1.5M and

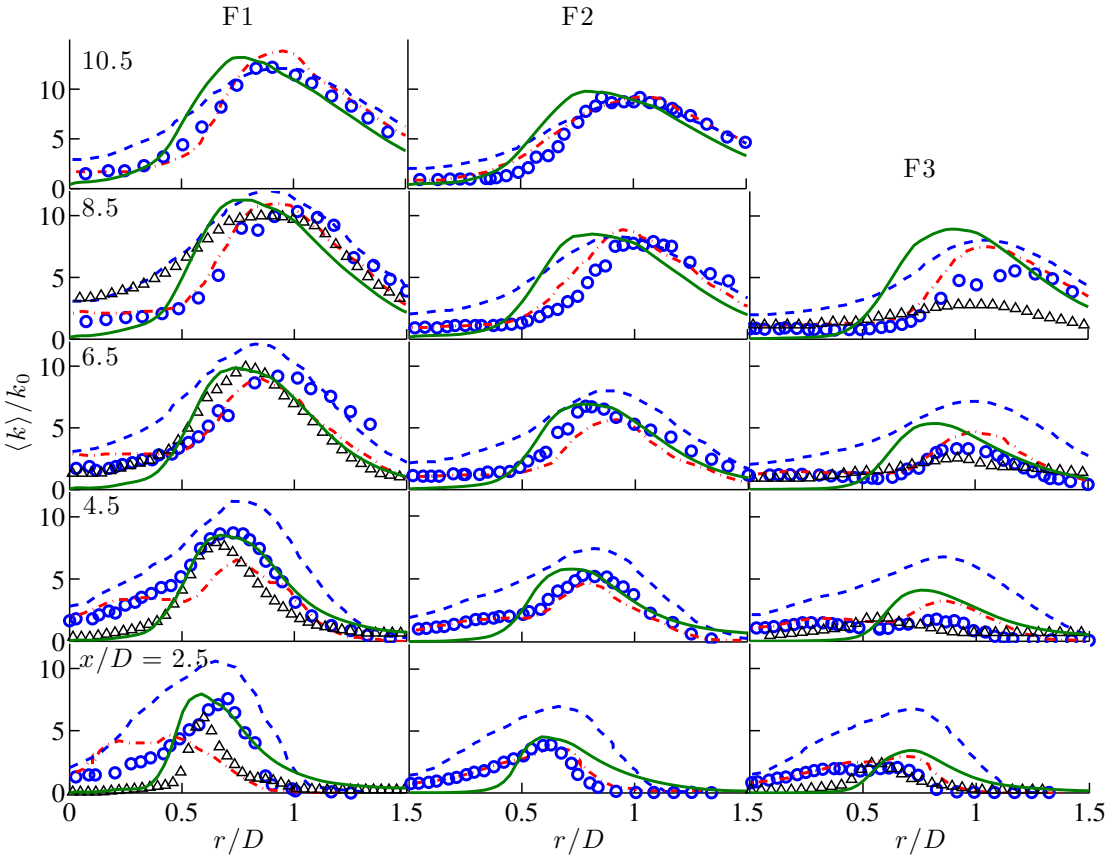

Fig. 5.10 Comparison of measured [46] (○ ○ ○) and computed (——) normalised mean TKE, $\langle k \rangle / k_0$, variation with r/D, obtained using algebraic model for $\bar{\omega}$ with $\beta_c = 7.5$. The computational results are for the 1.5M grid. Results of the 4.2M grid (•••) are shown only for F2. Previous results [53] (△), [122] (– –) and [240] (– · –) are shown for comparison.

4.2M grids agree well with measured values for $x \geq 0.8D$. Generally, second order statistics such as TKE have increased sensitivity to mesh resolution compared to first order statistics as implied in Fig. 19 of Wang *et al.* [240]. Thus, one would expect to see a better agreement for the 4.2M case of flame F2 in Fig. 5.10 and the large difference seen here is because, the combustion submodel for the filtered reaction rate is at its limit for this grid as noted earlier. This SGS combustion model underestimates the reaction rate, effects of heat release rate and their interactions with fluid dynamics as noted earlier for the 4.2M grid case (see the discussion for Figs. 5.2, 5.3, 5.7 and 5.8).

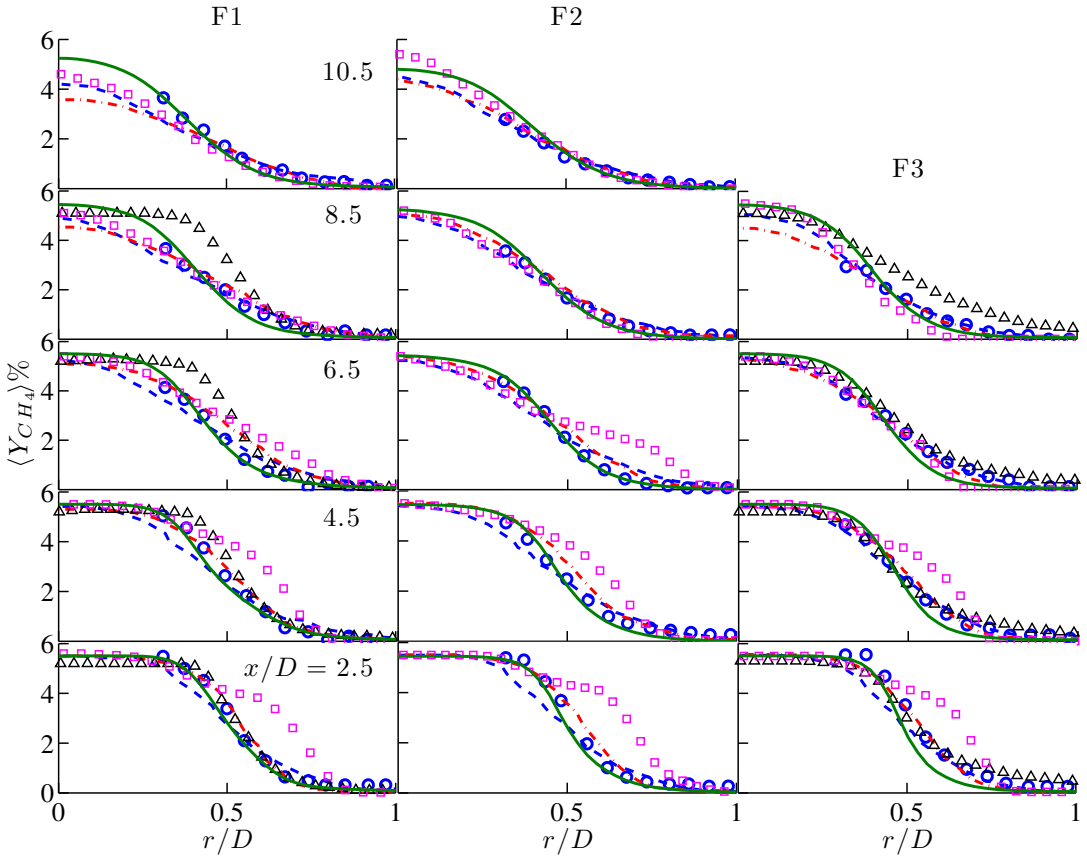

Fig. 5.11 The mean fuel mass fraction computed on the 1.5M grid (——), obtained using algebraic model for $\overline{\dot{\omega}}$ with $\beta_c = 7.5$, is compared to the measurements (○ ○ ○). Previous results [53] (△), [56] (□), [122] (– –) and [240] (–·–) are shown for comparison.

A. Comparison of reactive scalars:

The radial variation of averaged fuel mass fraction is compared to its measured values in Fig. 5.11 for all the three flames. The results of previous numerical studies are also included in this figure. The thickened flame-LES results of De & Acharya [53] agree very well with the measurements for $x \leq 6.5D$ for the high Da flame F3 and this computational results slowly move away from the experimental data as seen in this figure for the flame F1. However, the results of Wang *et al.* [240] using dynamic thickened flame approach shows a good agreement uniformly. The agreement between the measured and computed values using the LES-PDF method [56] is not uniformly good. The agreement is relatively better for $x \geq 8.5$ for the flames F1 and F2, and for the flame F3 the agreement seems to improve from $x = 6.5D$ as seen in Fig. 5.11. It had been suggested that including the differential diffusion effects could improve

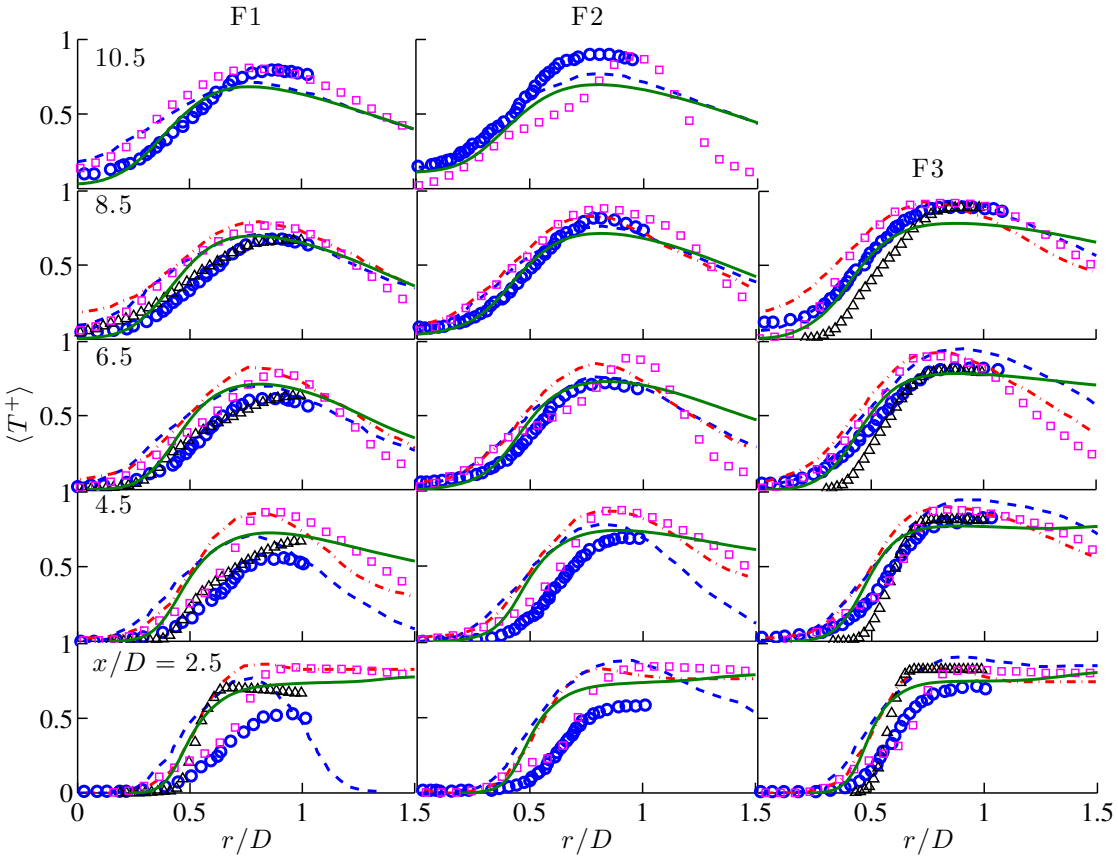

Fig. 5.12 The mean normalised temperature computed on the 1.5M grid (——), obtained using algebraic model for $\overline{\dot{\omega}}$ with $\beta_c = 7.5$, is compared to the measurements (○ ○ ○). Previous results [53] (△), [56] (□), [122] (– –) and [240] (–·–) are shown for comparison.

these estimates for the LES-PDF method. The mean fuel mass fraction computed in this study using the flamelet based algebraic model agrees very well with the measurements as shown in Fig. 5.11.

A similar comparison is shown in Fig. 5.12 for the normalised averaged temperature, $\langle \overline{T}^+ \rangle$. The values shown in Figs. 5.8 and 5.12 are calculated using Eq. (3.18) for the normalised temperature. The sub-grid variance, $\sigma^2_{T,\text{sgs}}$, needed in Eq. (3.18), is unavailable in the algebraic modelling framework since one need to solve a transport equation for $\sigma^2_{T,\text{sgs}}$ to meaningfully include the influences of reaction rate, dissipation rate, and turbulence, as discussed in §3.3.2. Although one should use $\langle \overline{T}^+ \rangle$ for comparison with measurements, no significant difference between $\langle \overline{T}^+ \rangle$ and $\langle \widetilde{T}^+ \rangle$ was observed for the flame conditions considered in this study. The flame F3 has the highest Damköhler number in the set and the computed values agree well with the data as shown in Fig. 5.12. A quite good agreement among various numerical studies

is also observed for this flame. A large overestimate seen for the flame F1 for $x \leq 4.5D$ is because of the uncertainty in the pilot temperature as it is not reported in [46]. Furthermore, the flame in the near field of the jet is expected to have quasi-laminar unsteady structure since the turbulence in these regions is low. The results in Fig. 5.12 suggest that the compounded effects of these two factors (uncertainty and quasi-laminar unsteady flames) become more apparent as the turbulent Reynolds number increases (compare the difference between the computational and experimental values at $x = 2.5D$ for all the three flames). The values of $\langle \overline{T}^{+} \rangle$ computed in this study agree well with the measurements at downstream locations as shown in Fig. 5.12. The under-prediction seen for $r > 0.6D$ at $x/D = 10.5$ is likely to be due to the missing effect of SGS fluctuations, which could not be included in Eq. (3.18) for temperature because of the reason explained earlier. A detailed analysis on the effect of the SGS fluctuations on scalars will be provided in Chapter 7. In general, a good agreement is observed for the statistics computed in this study with measurements.

The radial variations of averaged mass fractions of major, O_2, H_2O and CO_2, and minor, OH, species and intermediates, H_2 and CO, at various axial locations are shown respectively in Figs. 5.13 – 5.18, since the ability of the SGS combustion submodel to capture the flame brush structure is also of interest. The current statistics are also compared to past results available in the literature. A 2-step chemistry with empirical rate expression was used by De & Acharya [53] and 1-step chemistry was used by Wang *et al.* [240]. The LES-PDF study in [56] used a 4-step, 15-step and GRI3.0 mechanisms and the results of 15-step mechanism are used here. Because of these differences in the chemistry, a uniform comparison cannot be made for the various species measured in [46].

The mass fractions shown in these figures are obtained using Eq. (3.70) to include the dilution effect, which is elucidated using the oxygen mass fraction at axial positions of $x/D =$ 2.5, 8.5 and 10.5 for the flame F1. In the near field ($x/D = 2.5$), the influence of this effect is almost negligible and including this effect captures the oxygen mass fraction increase in the outer region, $r > 0.8D$, due to dilution with the air. The oxygen mass fraction computed using a two-step chemistry and thickened flame model by De & Acharya [53] is relatively larger compared to those obtained in the current study and those from the LES-PDF calculation in [56]. This difference increases with downstream distance. Wang *et al.* [240] did not report O_2 and CO_2 mass fractions and thus they are not shown in Figs. 5.13 and 5.15. The current results are improved over the previous RANS results as one would expect for the flames F1 and F2. This improvement is observed for H_2O, H_2 and OH. The averaged mass fraction of water vapour computed in this study agrees well with measured values and those reported in earlier LES studies. The underestimate seen for CO_2 mass fractions in Fig. 5.15 is consistent with many earlier studies [53, 56, 122] employing different combustion modelling approach. However,

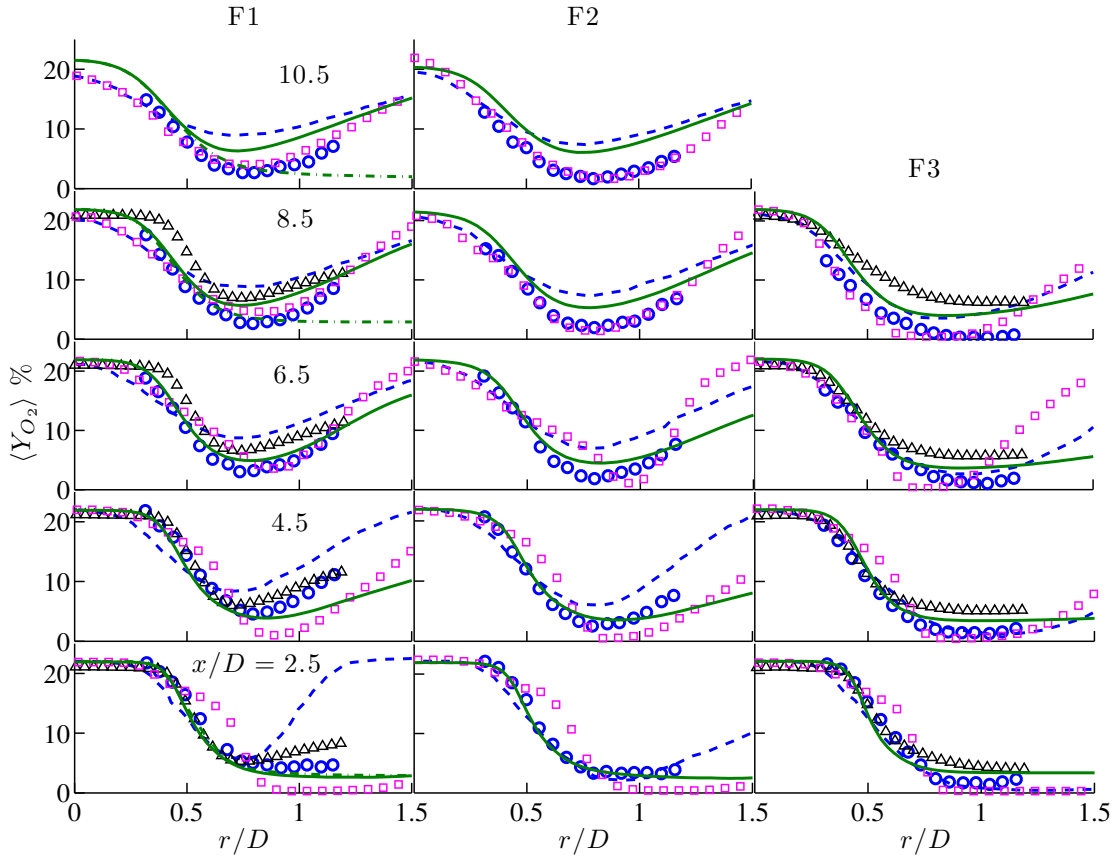

Fig. 5.13 Comparison of mean mass fraction of O_2: experimental data (○ ○ ○), results obtained using algebraic model for $\overline{\dot{\omega}}$ with $\beta_c = 7.5$ (——), [53] (△), [56] (□), and [122] (– –). The dash-dotted line (–·–) for F1 at $x/D = 2.5$, 8.5 and 10.5 shows the value obtained without using Eq. (3.70).

the values obtained using the LES-PDF method are relatively closer to the measurements for downstream locations. Although CO_2 is transported in the calculations reported in [53] there is a large underestimate inside the flame brush for $x \geq 6.5D$ for the flame F1. For high Da flame F3, the computed CO_2 mass fractions agree well with the measured values. The OH mass fractions obtained using the LES-PDF [56] and the current LES-flamelets methods agree quite well with one another and also with measurements for the flame F1. These agreements are relatively poor for upstream locations and for the largest Da flame F3 as shown in Fig. 5.16. Nevertheless, the general trend is captured well by both of these two modelling approaches.

The mean mass fraction of H_2 computed in this study agrees well with the measured values as shown in Figs. 5.17. None of the previous LES studies reported this result and thus they are not included in this figure for comparison. The slight overestimate at $x/D = 2.5$ is because of

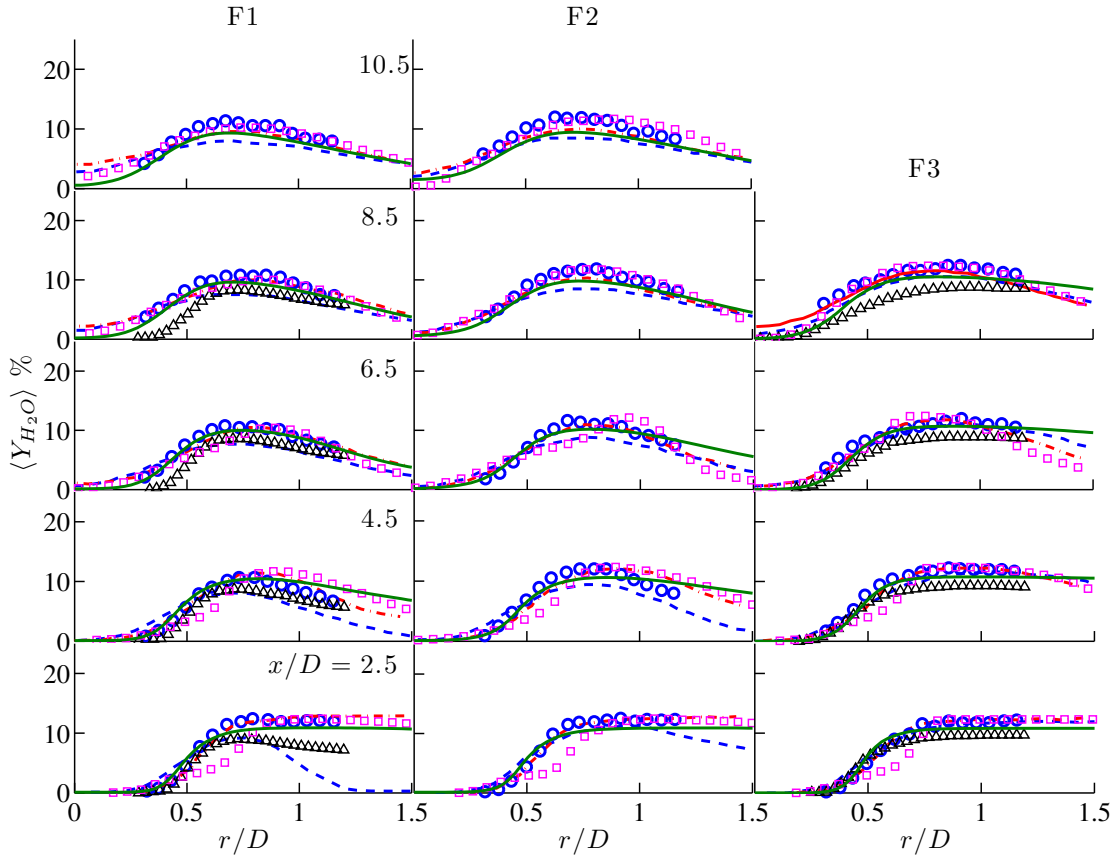

Fig. 5.14 Comparison of mean mass fraction of H_2O: experimental data (○ ○ ○), results obtained using algebraic model for $\overline{\dot{\omega}}$ with $\beta_c = 7.5$ (——), [53] (△), [56] (□), [122] (– –) and [240] (–·–).

the uncertainty in the pilot boundary condition and this uncertainty does not seem to be of any importance as one moves downstream.

The agreement for $\langle Y_{CO} \rangle$ shown in Fig. 5.18 is not good and there is a large overestimate for all the three flames. Flamelets based models are known to generally overestimate the CO mass fraction. However, a proper reason for the overestimate observed here is unclear at this time and this overestimate is consistent with the underestimate observed for the CO_2 mass fraction. A similar behaviour is seen in figure 5.18 for many previous studies using different combustion modelling. However, the CO values computed by De & Acharya [53] seem to agree quite well with the measurements but this seems to be inconsistent with the CO_2 values (see Fig. 5.15) computed by them.

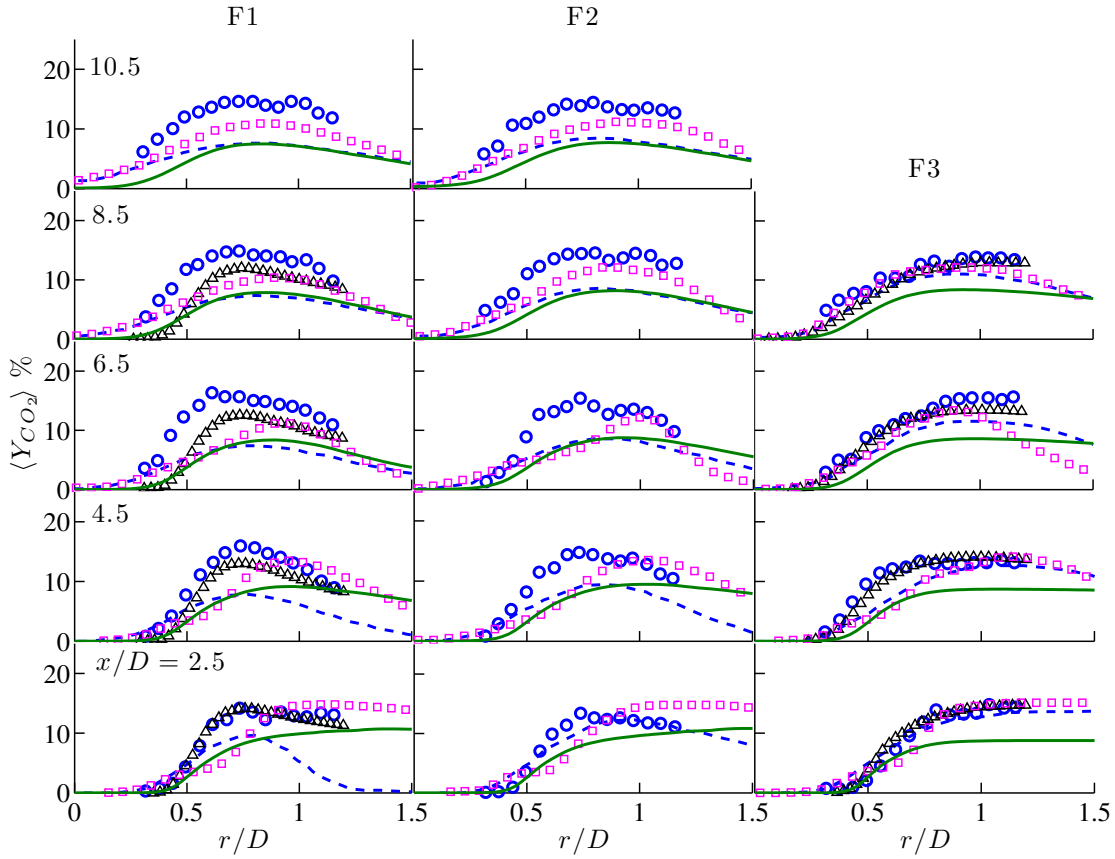

Fig. 5.15 Comparison of mean mass fraction of CO_2: experimental data (○ ○ ○), results obtained using algebraic model for $\overline{\omega}$ with $\beta_c = 7.5$ (——), [53] (△), [56] (□), and [122] (– –).

B. Flame brush thickness comparison:

Although there is a reasonable comparison between the computed and measured values of various mass fractions and temperature, it is instructive to compare the computed and measured flame brush thicknesses. This result is shown in Fig. 5.19. The flame brush thickness is calculated as $\delta_t = 1/\left(\partial\langle\overline{T}^+\rangle/\partial r\right)_{\max}$ in the experimental study [46]. Thus, one can independently calculate this value for various axial locations using the experimental data in Fig. 5.12. The values of δ_t calculated by fitting a spline curve for the measured variation of $\langle\overline{T}^+\rangle$ with r in Fig. 5.12 are compared to the δ_t reported in Fig. 16 of Chen *et al.* [46]. This comparison is shown in the top row of Fig. 5.19 for all the three flames. The values computed using $\langle\overline{T}^+\rangle$ variation are shown as diamonds and the squares represent the values, $\delta_{t,Y}$, obtained using measured $\langle\overline{Y}_{CH4}\rangle$ variation with r. The flame brush thicknesses obtained using either

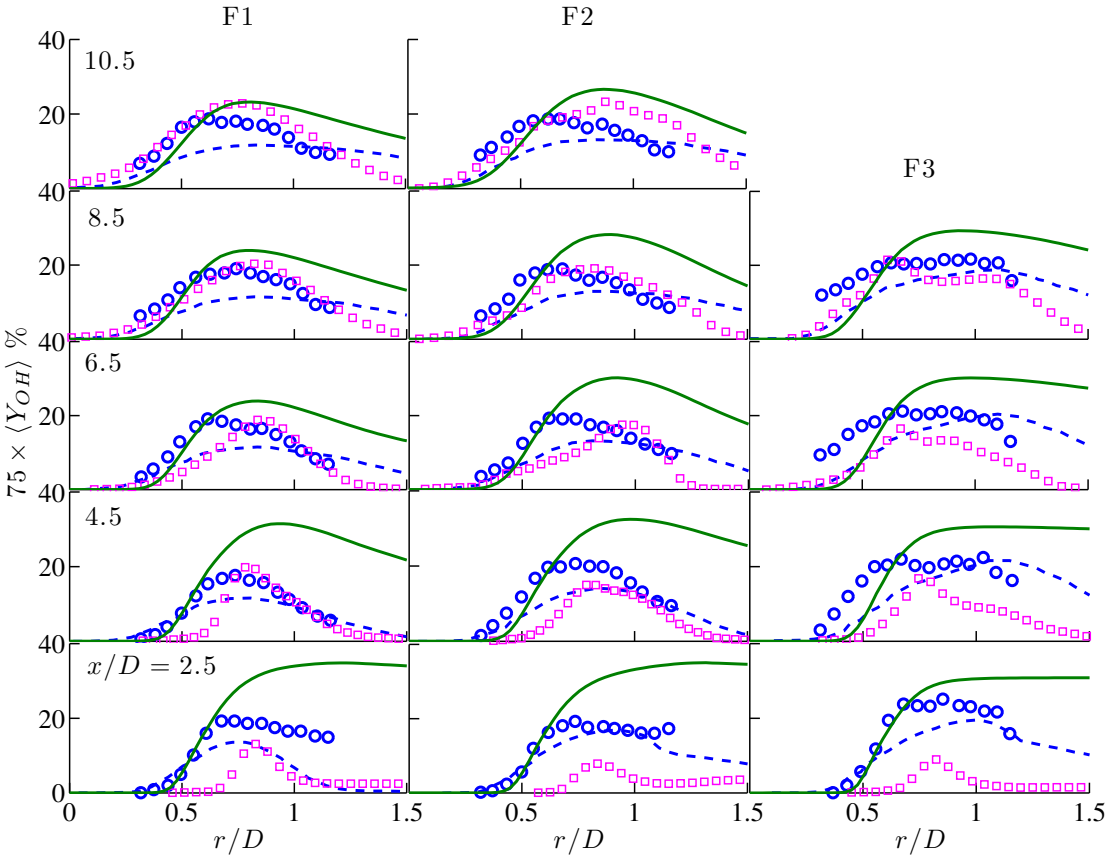

Fig. 5.16 Comparison of mean mass fraction of OH: experimental data (○ ○ ○), results obtained using algebraic model for $\overline{\dot{\omega}}$ with $\beta_c = 7.5$ (——), [56] (□) and [122] (– –).

temperature or fuel mass fraction variations are expected to be the same for adiabatic unity Lewis number flames and the stoichiometric methane-air flame has the Lewis number close to unity. This expectation holds very well for the flame F3 and also at downstream positions for the flame F2 as shown in Fig. 5.19. However, the agreement is not so good for the flame F1 and the difference between δ_t and $\delta_{t,Y}$ seen in Fig. 5.19 for F1 is because of non-adiabaticity, which is verified systematically by computing δ_t and $\delta_{t,Y}$ values using LES results. The effect of heat loss is pronounced for $x \leq 7D$ in the flame F2 and it is non-negligible over the region of measurement locations for the flame F1. These results seem to suggest that this effect also depends on the jet exit Reynolds number. The agreement between δ_t values computed here as noted above and reported by Chen *et al.* [46] is very good for the flames F2 and F3, but it is not so for the flame F1. These difference for the flame F1 raises some uncertainty on the flame

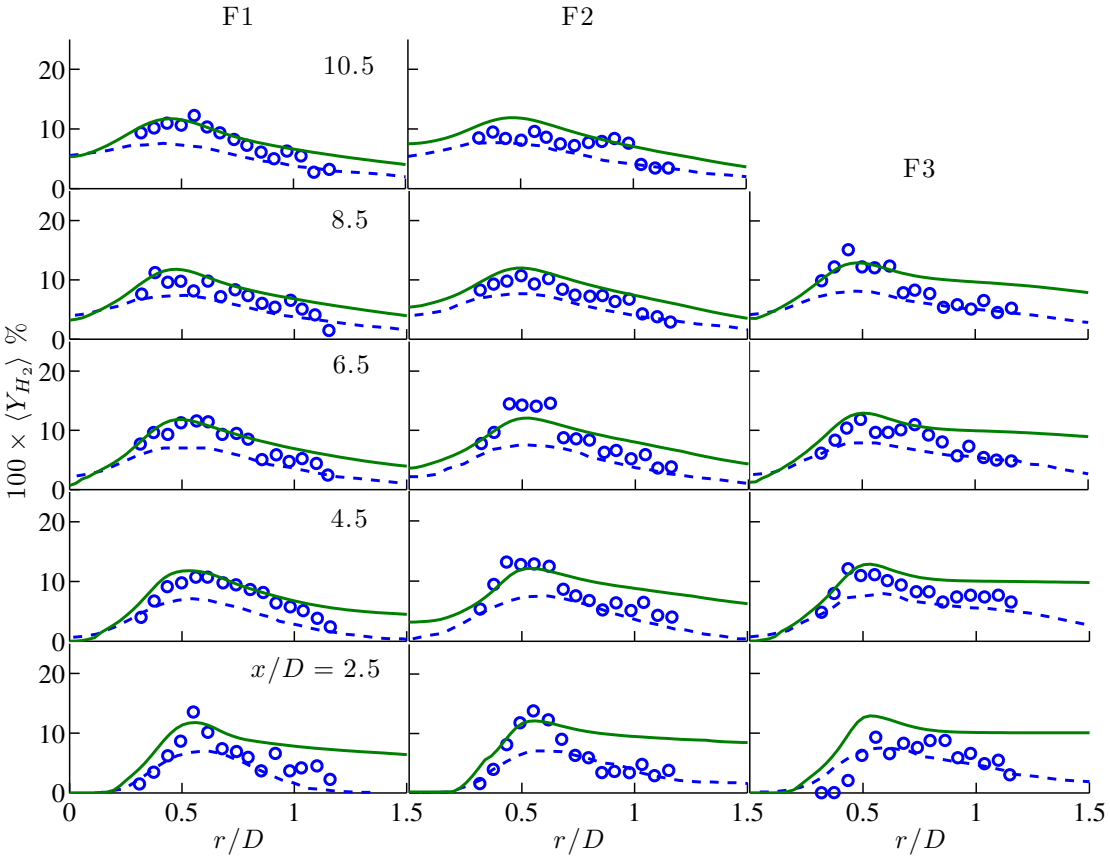

Fig. 5.17 Comparison of mean mass fraction of H_2: experimental data (○ ○ ○), results obtained using algebraic model for $\overline{\dot{\omega}}$ with $\beta_c = 7.5$ (——), and [122] (– –).

brush thickness values. One must keep this in mind while comparing the flame brush thickness obtained from LES results, or in fact from numerical simulations in general for the flame F1.

The bottom row of Fig. 5.19 compares the values of δ_t computed from the LES results with those obtained in earlier numerical studies and using the measured radial variation of $\langle \overline{T}^+ \rangle$. This choice is made for the experimental values to be consistent with the temperature comparison discussed earlier. For the F2 and F3 flames, the agreement is good. However, there are some relatively larger differences for the flame F1. The two LES simulations, this study and by Wang *et al.* [240], yield almost the same flame brush thickness for $x \leq 6D$. For the downstream positions, $x \geq 9D$, the flame brush thickness computed in this study seem to be in good agreement with the experimental values of the flame F1. The values of δ_t obtained using a modelled transport equation for k_{sgs} are also shown for comparison and these values suggest that initially the flame brushes are thicker compared to those obtained using the scale-similarity

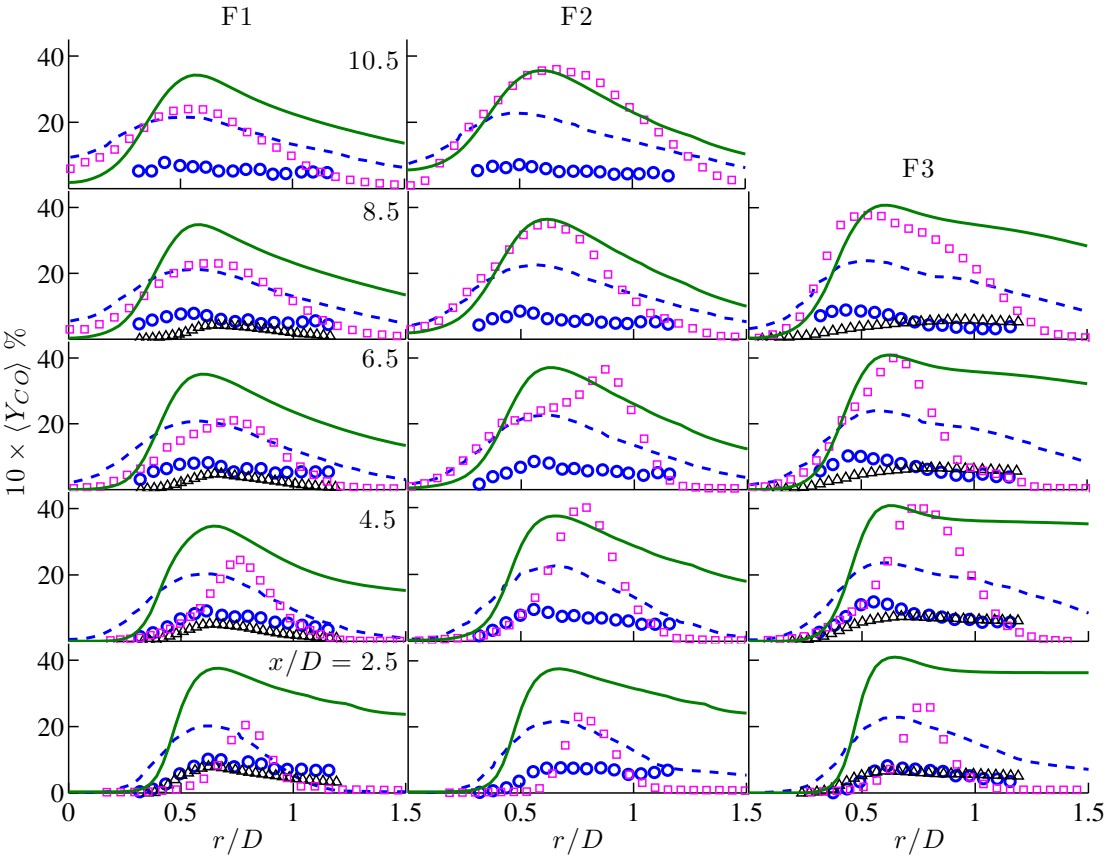

Fig. 5.18 Comparison of mean mass fraction of CO_2: experimental data (○ ○ ○), results obtained using algebraic model for $\overline{\dot{\omega}}$ with $\beta_c = 7.5$ (——), [53] (△), [56] (□), and [122] (– –).

model. However, one must not read too much into these difference for the k_{sgs} model because of the uncertainties of the sub-models used in the k_{sgs} transport equation. Overall, the flame brush structure captured using the algebraic closure for the filtered reaction rate investigated in this study is acceptable and satisfactory.

5.3.4 Analysis of SGS kinetic energy equation

Additional simulations have been performed using the additional transport equation for the SGS kinetic energy of Eq. (3.13), referred here as k_{sgs}. This equation is described in §3.1.2 and it is used in this analysis to provide a closure for the SGS velocity scale, as $u'_\Delta = \sqrt{2k_{\text{sgs}}/3}$. The sub-grid stress closure is that of Eq. (3.4) in this case, where C_v is computed dynamically for each computational cell using scale similarity. The turbulent transport is closed using a gradient hypothesis and assuming unity turbulent Schmidt number, while the dissipation of

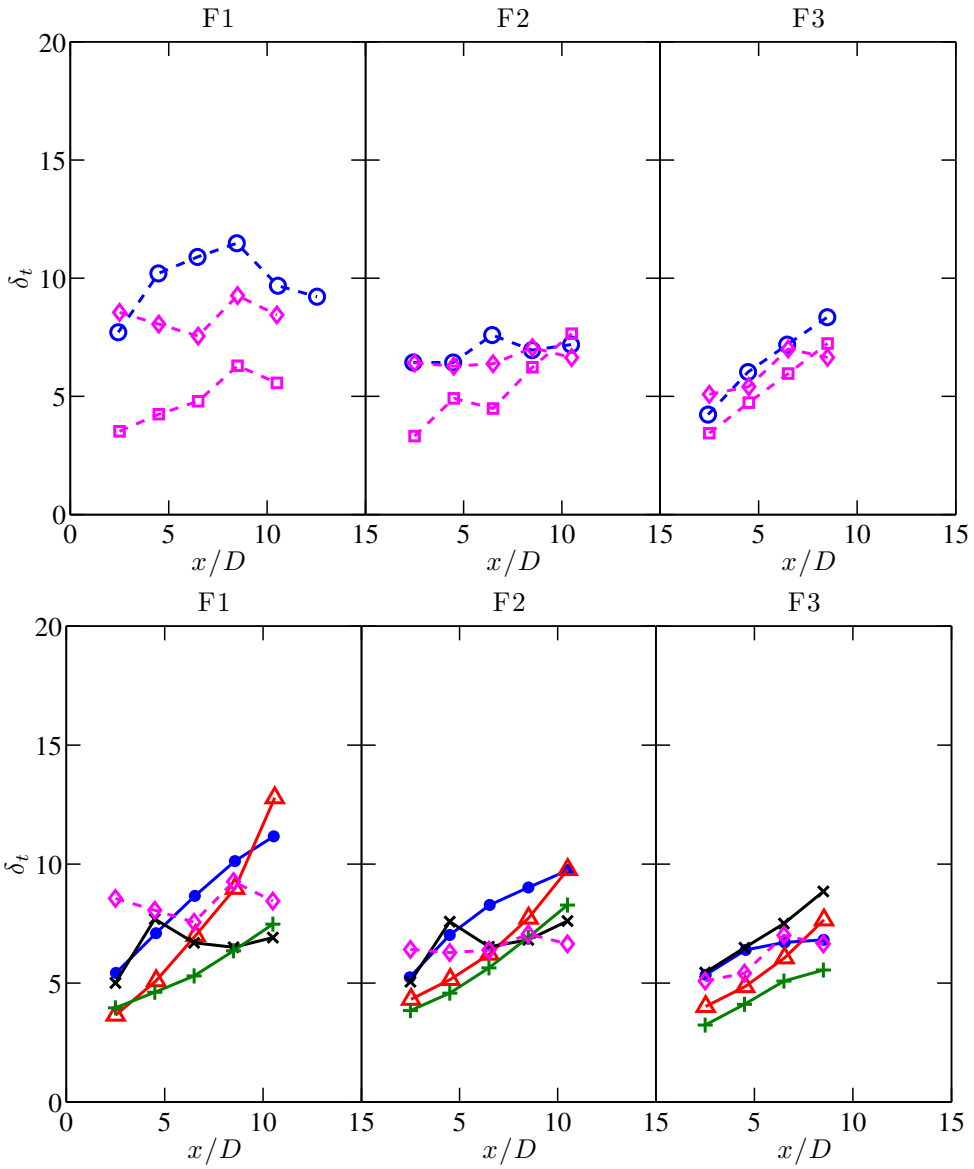

Fig. 5.19 Flame brush thicknesses, δ_t (mm), computed here using the radial variation of averaged temperature (◇) and fuel mass fraction (□) reported in [46] are compared to δ_t values reported (○) in [46] (top row). The values of δ_t obtained from LES using algebraic model for $\overline{\dot{\omega}}$ with $\beta_c = 7.5$ and SGS velocity model in Eq. (3.51) (+) and k_{sgs} transport equation (×) on 1.5M grid are compared with experimental data [46] (◇) and past RANS [122] (•) and LES [240] (△) studies in the bottom row.

k_{sgs} is computed as $\varepsilon_k = C_\varepsilon \overline{\rho} k_{\text{sgs}}^{3/2}/\Delta$. Finally, the pressure dilatation term Π is computed using Eq. (3.15). This model is used here specifically to include the dilatation resulting from heat release effects. The modelling of Π and ε_k is included systematically as listed in Table 5.1 to study their influence on LES. The case K1 excludes the pressure-related term, Π, and a static value of 0.916 is used for C_ε, whereas the case K2 includes Π. The value for C_ε is determined

Table 5.1 SGS kinetic energy models used for testing.

Case	Π-model	C_ε
K1	No	0.916
K2	Yes	0.916
K3	Yes	dynamic

dynamically in the case K3. Typical results obtained using the modelled k_{sgs} equation is shown in Fig. 5.20 for the flame F2 along with the results obtained using Eq. (3.51). The influence of

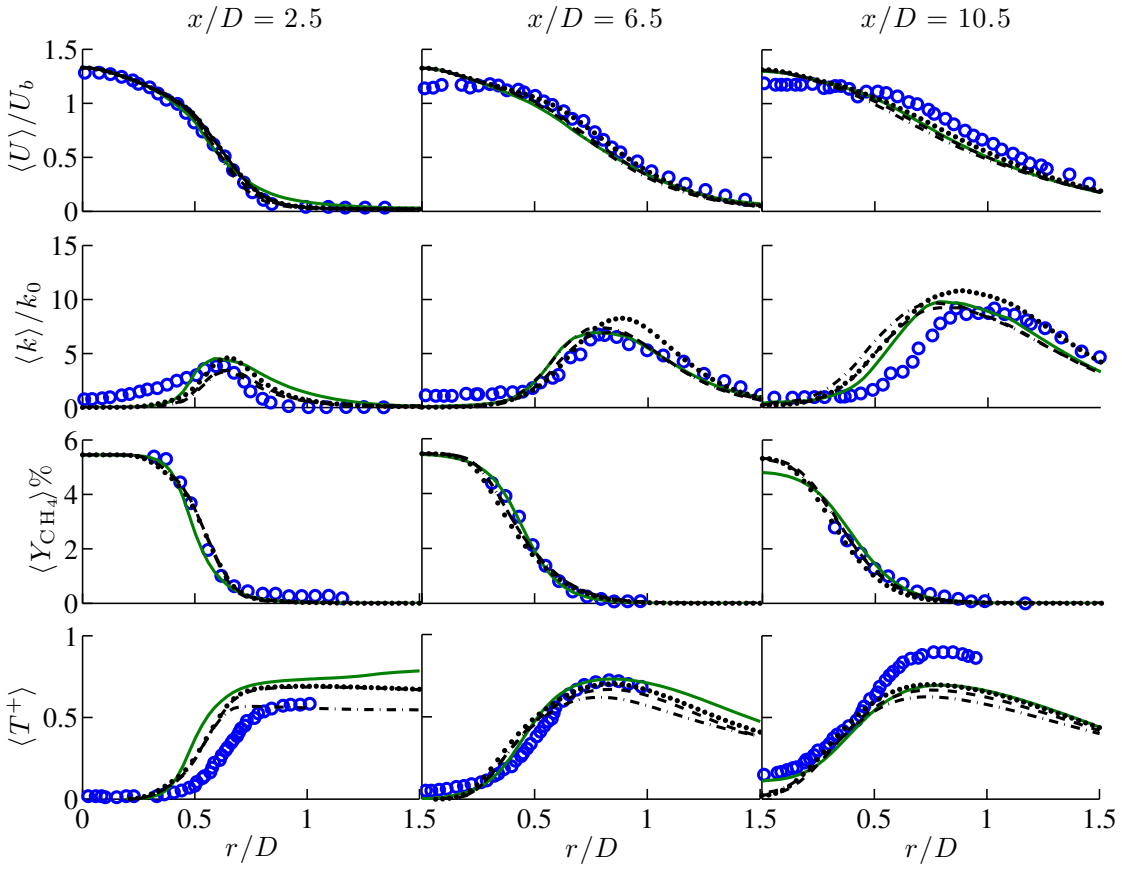

Fig. 5.20 Radial profiles of mean normalised velocity, $\langle U\rangle/U_b$, normalised TKE, $\langle k\rangle/k_0$, methane mass fraction, $\langle CH_4\rangle$ and normalised temperature, $\langle T^+\rangle$, obtained using algebraic model for $\overline{\dot{\omega}}$ with $\beta_c = 7.5$ and models K1 (–·–), K2 (– –) and K3 (•••) of table 5.1, are compared with LES results obtained using Eqs. (2.22) and (3.51) (——) and with experimental data [46] (symbols) for flame F2 and 1.5M grid.

k_{sgs} based u'_Δ modelling on $\langle U \rangle / U_b$ is negligible and the results obtained using these models are very close to those obtained using Eq. (3.51) as one observes in the top row of Fig. 5.20. A similar behaviour is observed for $\langle k \rangle / k_0$ and the averaged fuel mass fraction shown in the second and third rows of Fig. 5.20. Although there are some small differences in the near field for the normalised averaged temperature, the differences become negligible for downstream locations as seen in the bottom row of Fig. 5.20. From these results, one concludes that the results of k_{sgs} based modelling of u'_Δ are very similar to those of scale-similarity model in Eq. (3.51) and thus it does not seem to justify the additional computational effort required for k_{sgs} transport equation. On the other hand, these comparisons may suggest that the effect of the pressure dilatation is not big for these flames, and thus including this effect into modelling of u'_Δ is not critical as the contribution of shear generated turbulence is much stronger compared to flame generated turbulence effects, as one shall see in Chapter 8. Also, one must acknowledge that the various sub-modelling for k_{sgs} equation used here are *ad hoc* and more investigation is required to develop new or to improve these models.

5.4 Assessment of dynamic procedure for β_c

The results in the previous section are obtained with particular values of β_c chosen empirically after several tests, see Table A.1. As noted in §2.5.1, this parameter depends on heat release parameter and Reynolds number and so it would be ideal to evaluate it dynamically in LES. The procedure for this evaluation was discussed in §3.3.4, and it is assessed here. A similar dynamic procedure has been studied recently [79, 129] for flames with different values of Lewis and turbulent Reynolds numbers using DNS data.

Since β_c is computed dynamically, the only tunable parameter in the combustion model of Eq. (2.22) is for the SGS velocity scale, u'_Δ. The analysis in §5.3 has shown that a simple model based on scale-similarity of velocity field as in Eq. (3.51) works well. The same analysis has demonstrated further that the model in Eq. (2.22) is not unduly sensitive to u'_Δ model and thus this scale-similarity model is used for the analysis in this section. Detailed discussion in this section suggests that the dynamic procedure works well and physical insights and reasonings are provided to explain the observed behaviour.

5.4.1 Flame structure

Typical behaviour of dynamic models are elucidated using only flames F1 and F3. Figure 5.21 shows the spatial variation of mean progress variable field, $\langle \widetilde{c} \rangle$, in the flame F1 obtained using both static and dynamic approaches for β_c and the results are shown for both 1.5M and 4.2M

grid. The results for the static, $\beta_c = 7.5$, value is the same as that reported in §5.3. There

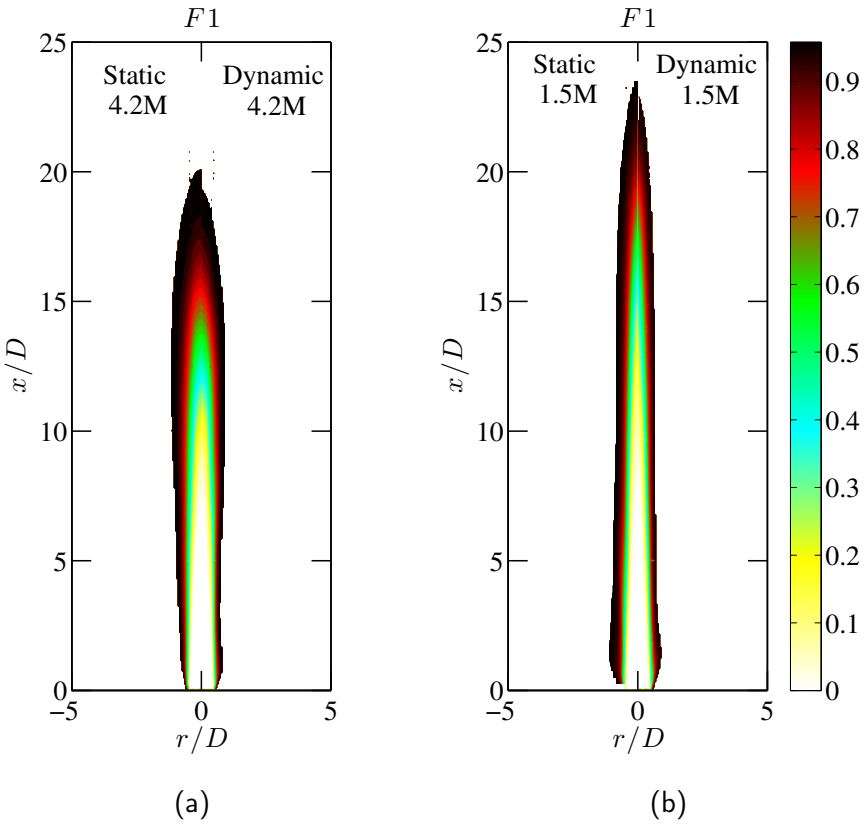

Fig. 5.21 The spatial variation of mean progress variable field for flame F1 obtained using algebraic model for $\overline{\dot{\omega}}$ with static and dynamic approaches for β_c. This comparison is shown for both 1.5M and 4.2M grids.

seems to be very small difference in the mean progress variable field obtained using either static or dynamic approach for β_c on a given numerical grid. However, a close study of this figure suggests that the flame brush is thinner for the dynamic β_c model leading to a slightly shorter flame brush as seen in Fig. 5.21. If one compares the results of 4.2M and 1.5M grids then the flame brush computed using the 1.5M grid is about 2 to 3D longer compared to that obtained using 4.2M grid. This behaviour is consistent with what is observed in Fig. 5.3 when discussing of the static formulation for β_c. The filtered reaction rate closure in Eq. (2.19) is not fully valid when $\Delta^+ < 1$ [61, 77, 147], which is the case of the 4.2M grid in the region of the strong reaction close to the jet exit, and this is reflected also in the dynamic computation.

The radial variations of averaged axial velocity, normalised using the respective bulk mean velocity at the jet exit, computed using the dynamic and static β_c values are compared to the experimental measurements [46] in Fig. 5.22 for F1 and F3 flames. The results from both

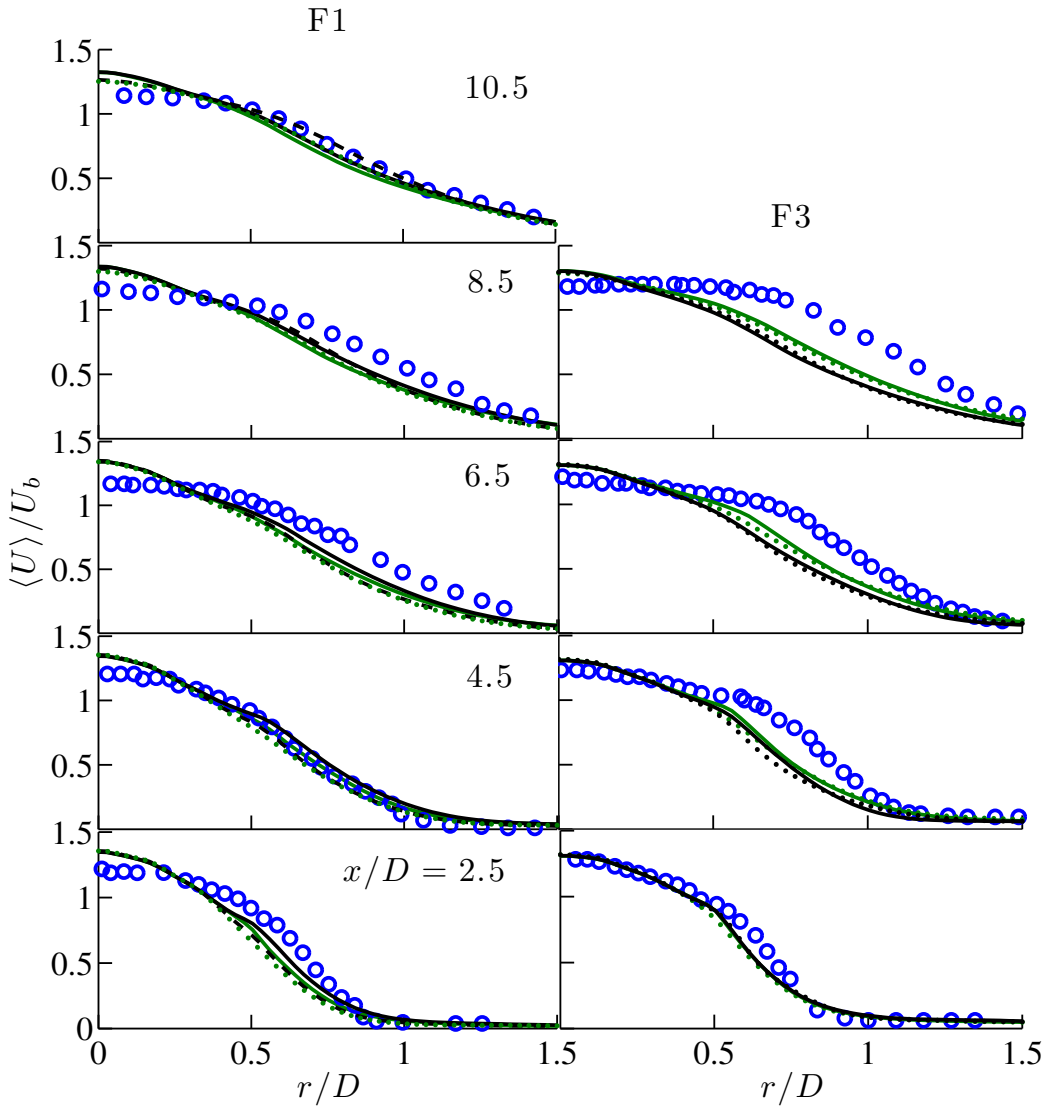

Fig. 5.22 Comparison of measured [46] (symbols) and computed (lines) radial variation of normalised axial velocity, $\langle U \rangle / U_b$, obtained using algebraic model for $\overline{\dot{\omega}}$ with dynamic (——, •••) and static (——, •••) β_c models for flames F1 and F3. The results are shown for 1.5M (solid lines) and 4.2M (dotted) grids.

1.5M and 4.2M cases are shown for few axial locations investigated in the experimental study of Chen *et al.* [46]. It is hard to distinguish the various curves for the flame F1, having the largest turbulence Reynolds number, suggesting that the computed averaged axial velocity is insensitive to the choice of β_c modelling and numerical grid. The insensitivity to numerical

grid can also be seen for the flame F3, which suggests that the chosen grids are good. A small difference is seen in $\langle U \rangle / U_b$ for the flame F3 as in Fig. 5.22 and this difference grows to be about 20% at axial location of $x = 8.5D$ and radial position of about $0.8D$. This is because the value of β_c obtained dynamically is smaller than the static value used for these locations. As one shall see later, the combustion is almost completed before this radial position for this axial location and the difference in β_c values is because of some small differences in the gradients of $\widetilde{c}$. The variations and comparisons shown in Fig. 5.22 are typical in many earlier numerical studies of these piloted Bunsen flames and thus the statistics shown here are acceptable.

The computed averaged TKE normalised using its centreline value, k_0, near the jet exit is compared to the measurements for few axial locations in F1 and F3 flames in Fig. 5.23. The values of k_0, 12.7 for F1 and 3.82 $\mathrm{m}^2/\mathrm{s}^2$ for F3, reported in [46] are used for this study. The comparisons seen in this figure are typical of many earlier studies. However, the agreement with the experimental data can be improved further than shown here by using finer grids as has been demonstrated in [240], but we restrict ourselves to relatively smaller grids to study the efficacies of the dynamic β_c modelling for the filtered reaction rate closure. This is because the closure in Eq. (2.22) works well when $\Delta^+ \gg 1$ as discussed earlier, and Δ^+ is already smaller than unity for 4.2M grid used here. Thus, refining the numerical grid further will yield $\Delta^+ \ll 1$, which would invalidate the closure in Eq. (2.22) as also noted in [61, 77, 147]. Moreover, refining the grid further would not be in line with a broader objective of this project as noted in the introductory chapter of this thesis. A close study of the results in Fig. 5.23 suggests that the peak values of $\langle k \rangle / k_0$ obtained using both static and dynamic β_c are similar to one another and also to measured values. However, the radial location of this peak value obtained using the dynamic approach agrees quite well with the measurement and the agreement, in general, at downstream positions is improved when 4.2M grid is used for the flame F1 as one would expect.

The radial variations of averaged fuel mass fraction and normalised temperature $T^+ = (\widetilde{T} - T_u)/(T_b - T_u)$ are compared with experimental results [46] in Figs. 5.24 and 5.25 respectively. The variation of averaged fuel mass fraction obtained using the power-law based model is also shown in Fig. 5.24 for both flames computed using 4.2M grid. The variation of averaged fuel mass fraction computed using this model suggests that this model is not representing the flame behaviour and it is rather representing a convective-diffusive scalar behaviour. This is because the scale-similarity for the gradient of $\widetilde{c}$ does not hold even on the finest, 4.2M, grid used in this study because $\Delta_{\mathrm{m}}\mathrm{in}^+$ is of order unity. This gradient is non-zero only inside the resolved flame suggesting that there must be at least three points within δ_{th} for this scale-similarity to hold implying that the test filter width must be smaller than $0.5\delta_{th}$. This gives severe underestimate of α in Eq. (3.60) and thus $\overline{\dot{\omega}}$ leading to the overestimate of averaged fuel mass fraction values

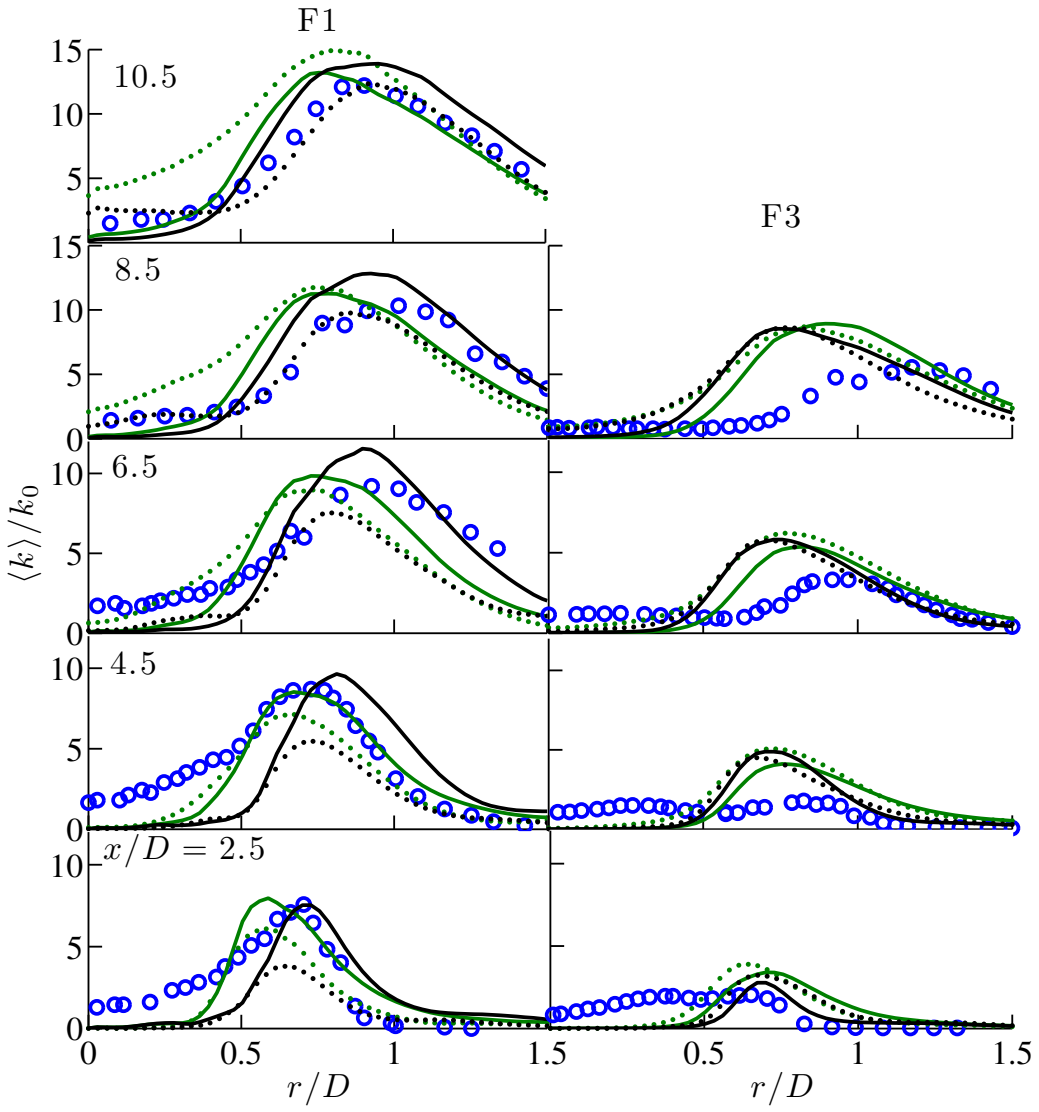

Fig. 5.23 Comparison of measured [46] (symbols) and computed (lines) radial variation of normalised mean turbulent kinetic energy, $\langle k \rangle / k_0$. The legend is as in Fig. 5.22.

seen in Fig. 5.24. The above grid requirement condition demands that the current grid should be refined at least by a factor of 27 (3 in each direction). This gives many tens of millions of grid cells, increasing the computational cost enormously, perhaps impractical for industry applications. The dynamic evaluation of β_c in Eq. (3.58) involves scale-similarity for u'_Δ and $\widetilde{c}$ (the test filter of ψ appears as sum at denominator in Eq. (3.58) and its magnitude is negligible

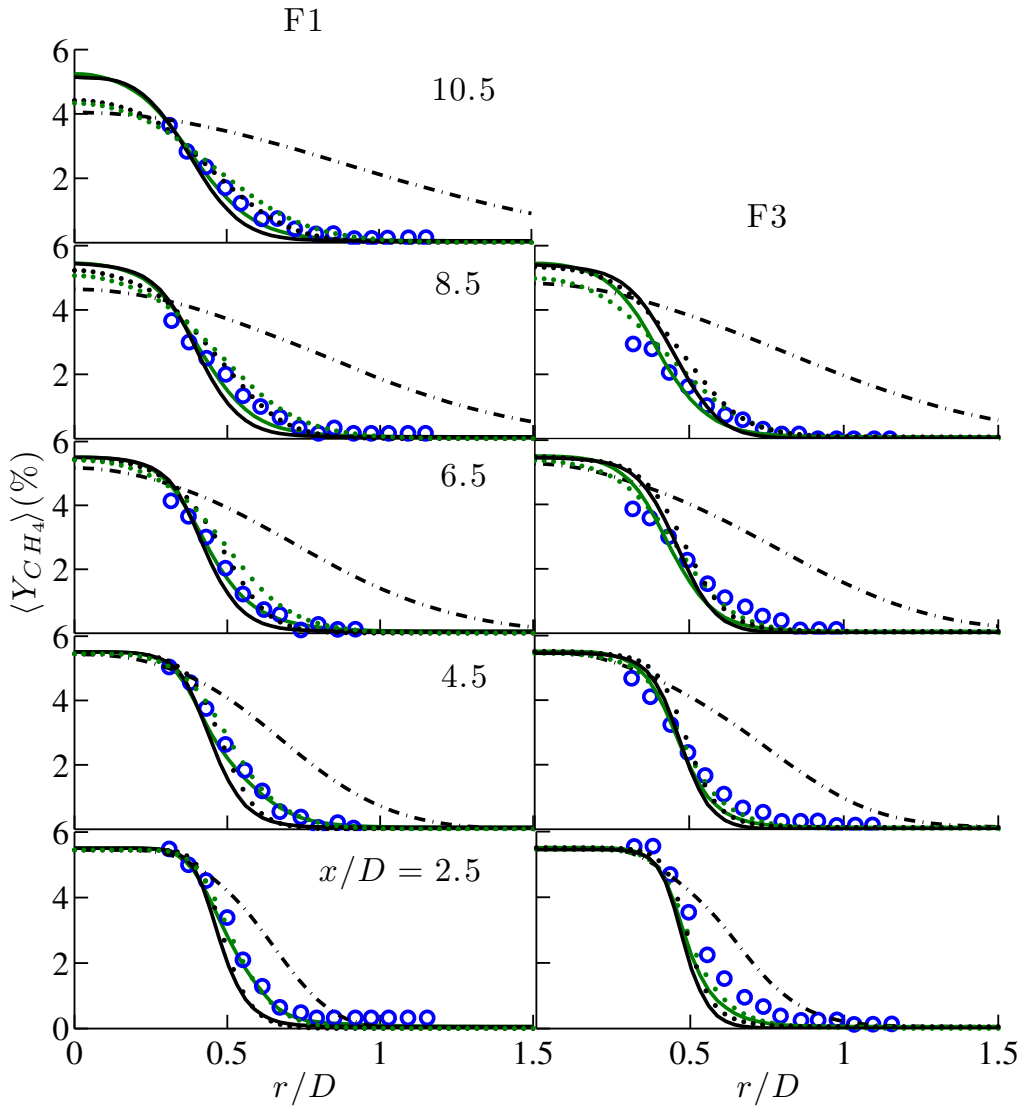

Fig. 5.24 Comparison of measured [46] (symbols) and computed (lines) radial variation of mean fuel mass fraction. The legend is as in Fig. 5.22. The dash-dotted line is for the power-law based model in Eqs. (3.60) and (3.61) for 4.2M grid.

in respect to the other terms) and thus, this assumption of scale similarity can be met with relatively coarser grid. For these reasons, the power-law based model is not considered further in this study.

The computed statistics for fuel mass fraction from static and dynamic formulation of β_c are similar on both 1.5 and 4.2M grids. The more pronounced under-prediction close to the jet

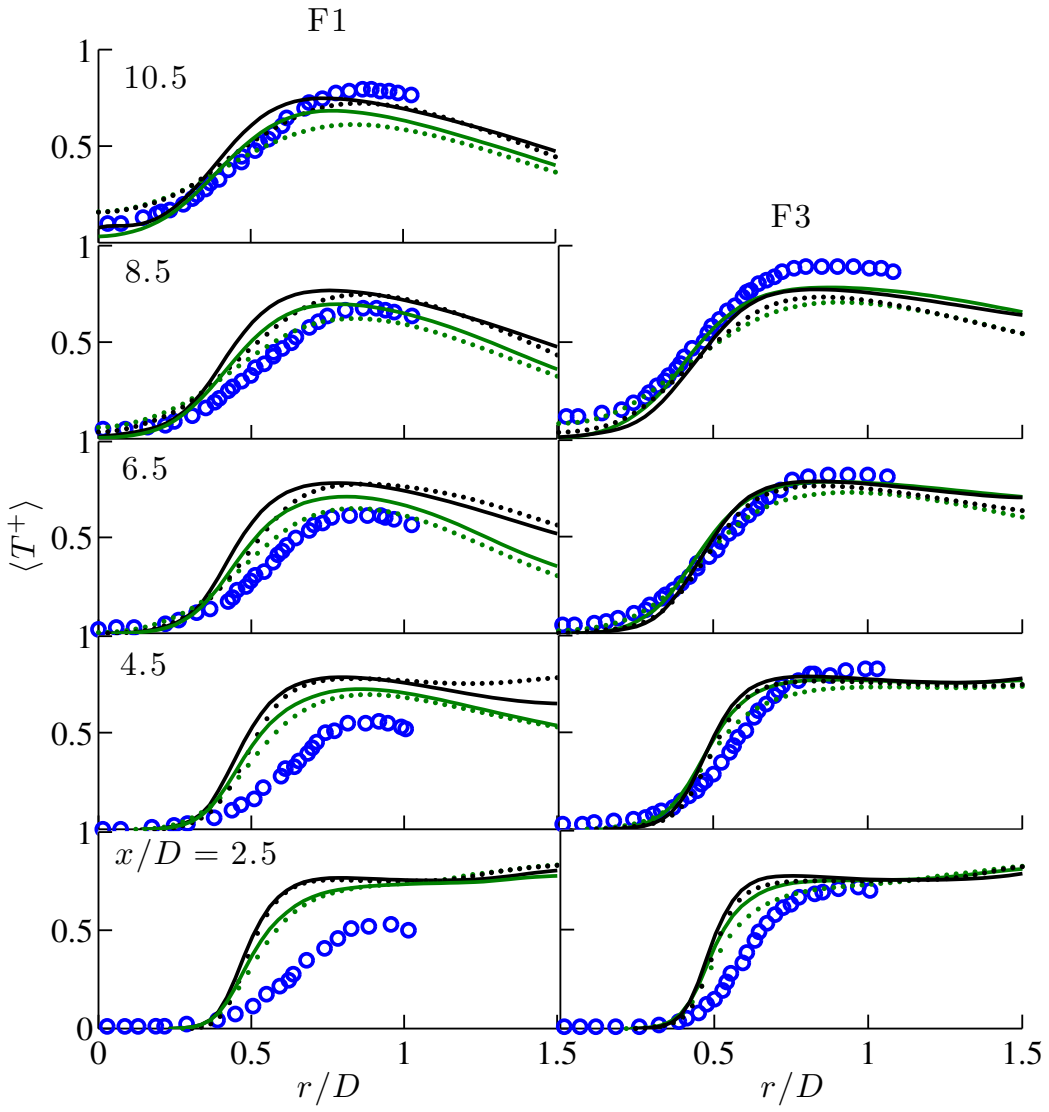

Fig. 5.25 Measured [46] (symbols) and computed (lines) radial variations of normalised mean temperature are compared above. The legend is as in Fig. 5.22.

exit in case of dynamic β_c is due to the fact that the flame in this region is quasi-laminar [46] and the dynamic formulation relies on the existence of a clear range of scales, i.e. it is weak in low-turbulence condition. The large difference in the statistics obtained using the dynamic model on 1.5M and 4.2M grids observed for $r \leq 0.3D$, especially at the downstream locations for flame F1, cannot be commented because of the absence of experimental data in these radial

positions. Overall, results for CH_4 mass fraction are good and comparable with previous studies (see for example [53, 56, 122, 240]) despite the relatively small grids used here.

The variations of averaged normalised temperature shown in Fig. 5.25 are consistent with the results for fuel mass fraction. The dynamic evaluation of β_c seems to overestimate the fuel consumption rate compared to the static case leading to an overestimate of peak temperature. The level of this overestimate decreases as one moves downstream, implying that the performance of the dynamic approach improves for both flames F1 and F3. The large overestimate of mean temperature near the jet exit results from uncertainties in pilot stream temperature as noted in §5.3 and in earlier studies [122, 240]. However, the averaged temperature computed using the current sub-grid reaction rate closure is improved as noted in §5.3 and some additional improvement from the dynamic approach is observed for downstream positions as seen in Fig. 5.25.

The radial variations of averaged mass fractions of various scalars are shown in Figs. 5.26 to 5.31. The effects of entrained air is included in the computations of these species mass fraction values as described in § 3.4. This effect is responsible for the increasing values of oxygen mass fraction for $r > 0.8D$ in Fig. 5.26 and this has been shown clearly in §5.3. The influence of dynamic evaluation of β_c on these various scalar mass fractions is found to be consistent with observations noted for averaged fuel mass fraction and temperature shown in Figs. 5.24 and 5.25. The mass fractions of H_2O and H_2 are well estimated by the method used in this study. The mass fraction of CO_2 is underestimated and the level of this underestimate is larger for the flame F1. There is a substantial overestimate in the mass fractions of CO and OH for both static and dynamic evaluation procedure for β_c. The computed increasing trend of OH mass fraction with r improves for the flame F1 at downstream positions for both static and dynamic computation of β_c and some better prediction is seen in the latter case for flame F3, as seen in Fig. 5.29. The large overestimate of CO mass fractions seen here is consistent with many past studies. As noted earlier, the difference in various statistics obtained using the dynamic and static evaluation of β_c is observed to be small for the following reason. The static value of this parameter is obtained for these two flames empirically by conducting many LES as noted in §5.3 until an overall satisfactory behaviour is noted. The dynamic procedure described here avoids this empirical testing and the average value of β_c obtained in this procedure is comparable to the static value as one shall see next.

5.4.2 The PDF of β_c

The PDF of β_c obtained by post-processing the LES data is shown in Fig. 5.32 for both flames, F1 and F3. This PDF is constructed using β_c values collected from the computational domain by imposing the limits $0.05 \leq \widetilde{c} \leq 0.95$ and $\overline{\dot{\omega}} > 0.05\langle\overline{\dot{\omega}}\rangle_{\max}$. These limits are used to avoid

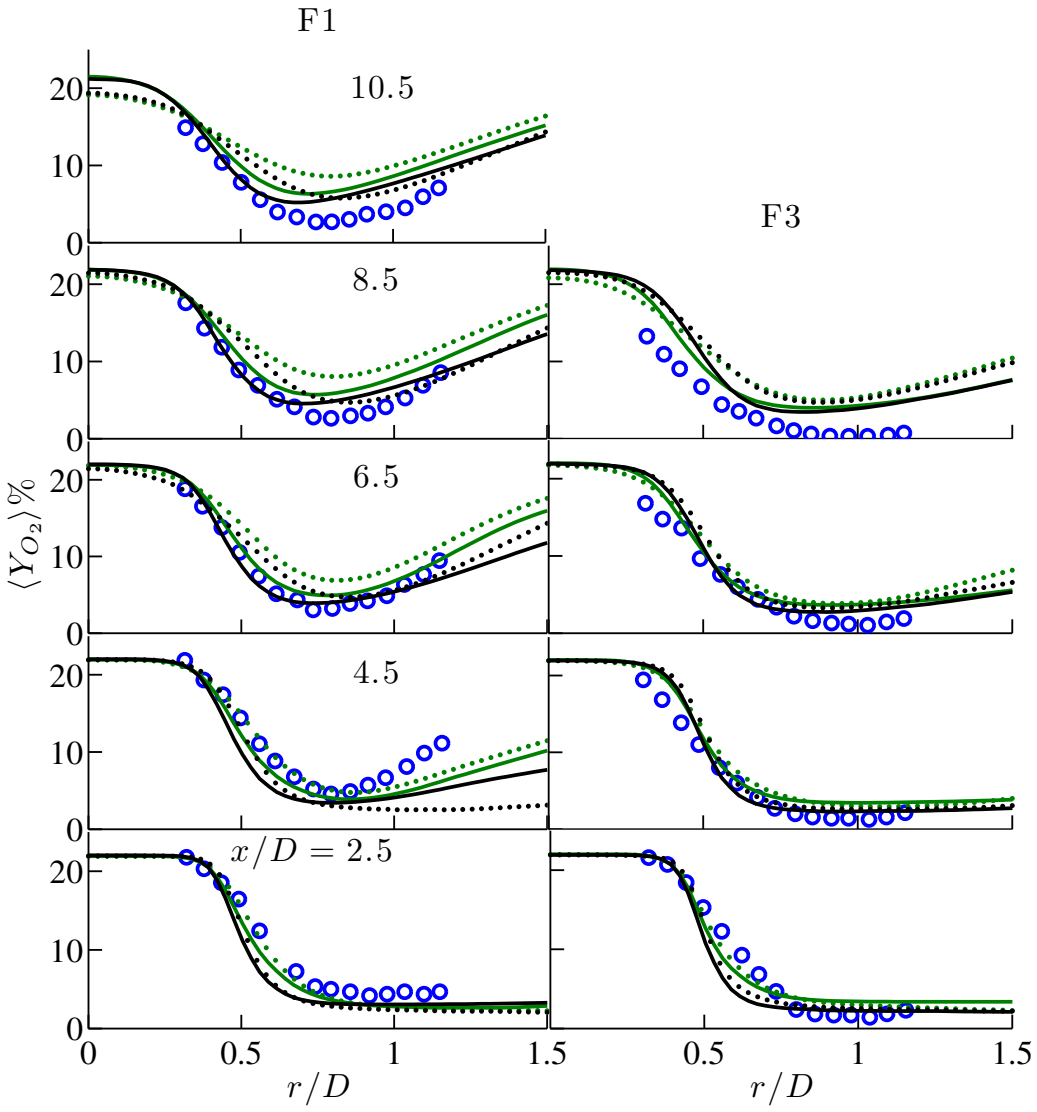

Fig. 5.26 Comparison of measured [46] (symbols) and computed (lines) mean O_2 mass fractions. The legend is as in Fig. 5.22.

regions with very low reaction rates so that the values of β_c used for this PDF are physically meaningful. The lower limit of β_c is imposed by the realisability condition in Eq. (3.59). The upper limit for F3 is nearly twice that for F1 and the PDF has a long tail for large β_c values for both of these flames. These PDFs are similar to those shown in the DNS analysis in [129]. It is worth noting that the mean values $\langle \beta_c \rangle$ given for the flames F1 and D6 are almost the same because the Damköhler and turbulence Reynolds numbers are similar for these two flames.

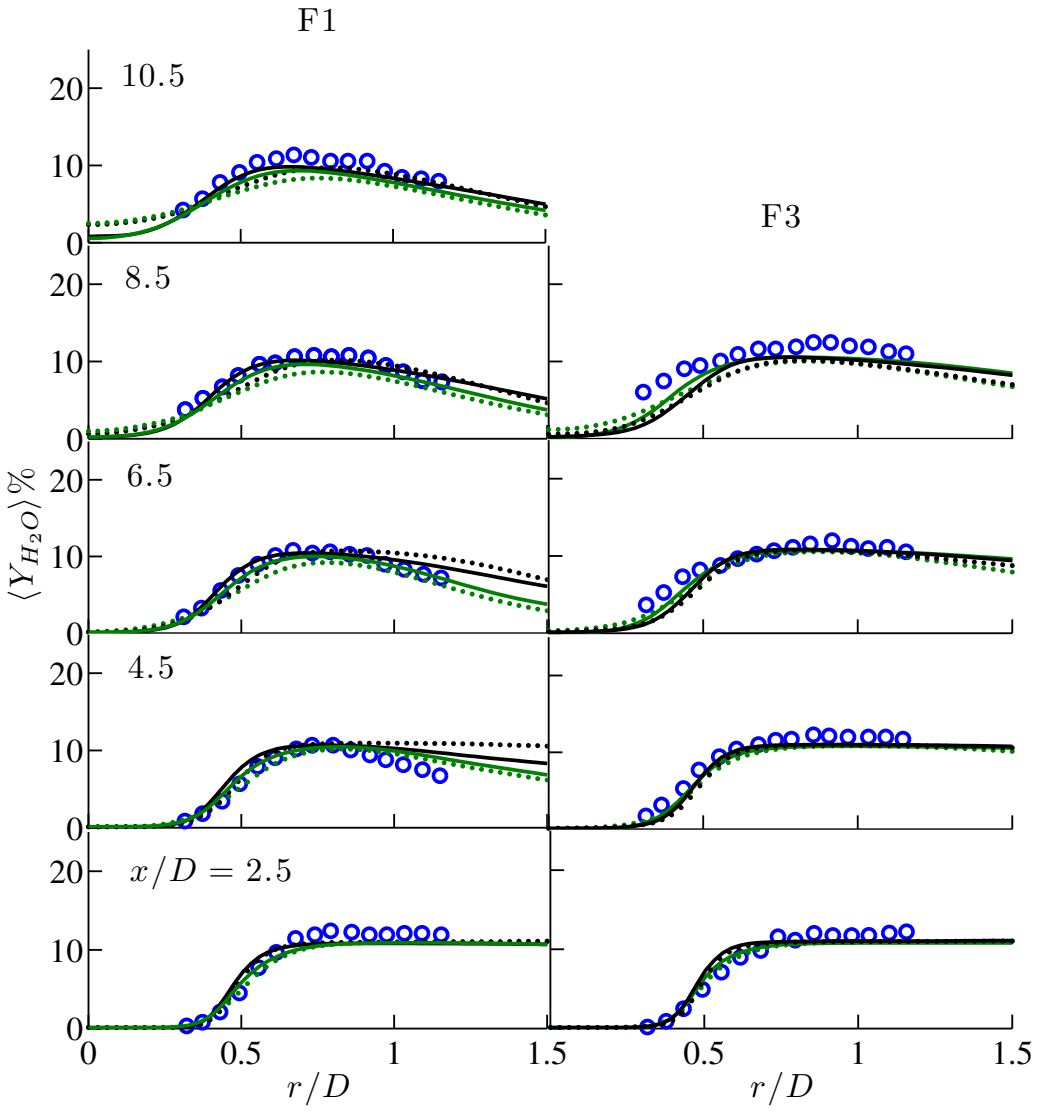

Fig. 5.27 Comparison of measured [46] (symbols) and computed (lines) mean H_2O mass fractions. The legend is as in Fig. 5.22.

This value of $\langle \beta_c \rangle \simeq 7.7$ is very close to the static value of $\beta_c = 7.5$ used for the flame F1 and thus it not surprising to observe small differences, as noted above, in various statistics obtained using the static and dynamic evaluation of β_c. The value of $\langle \beta_c \rangle = 10.5$ given in Fig. 5.32 for the flame F3 is larger than for F1 because of higher Da and lower $\mathrm{Re_t}$ values for F3, and this value is about 40% larger than the static value used for the F3 flame. This good match in the β_c values for the static and dynamic procedure for flame F1 is not coincidental. The

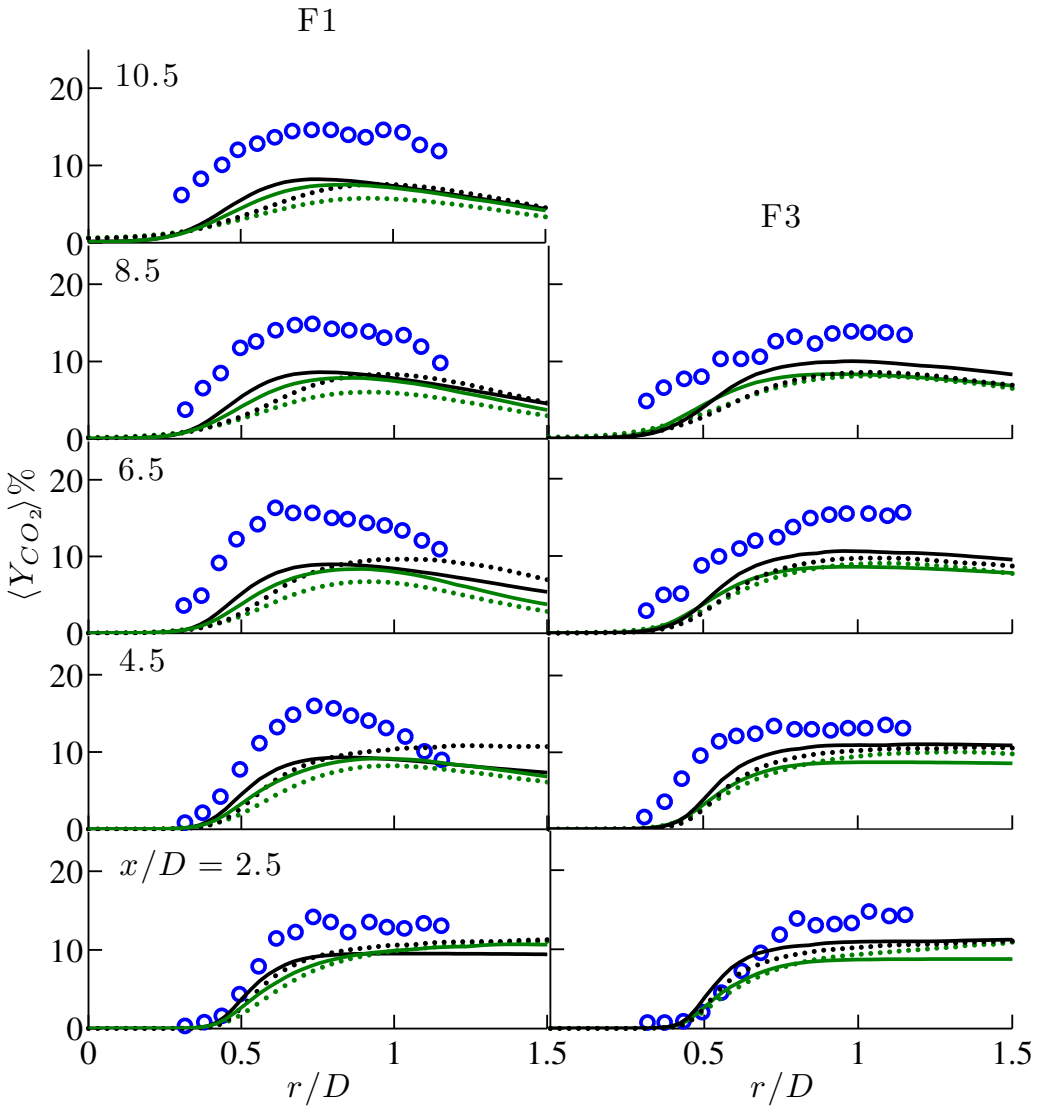

Fig. 5.28 Comparison of measured [46] (symbols) and computed (lines) mean CO_2 mass fractions. The legend is as in Fig. 5.22.

static value was obtained with empirical testing as discussed in §5.3. The dynamic procedure described here eliminates this empiricism while retaining the accuracy with a small increase in the computational cost.

The efficacy of the combustion modelling approach discussed in this paper is tested further by calculating the thicknesses of the simulated flame brushes and comparing them with measured values. The results are shown in Fig. 5.33 for both flames F1 and F3. The flame brush

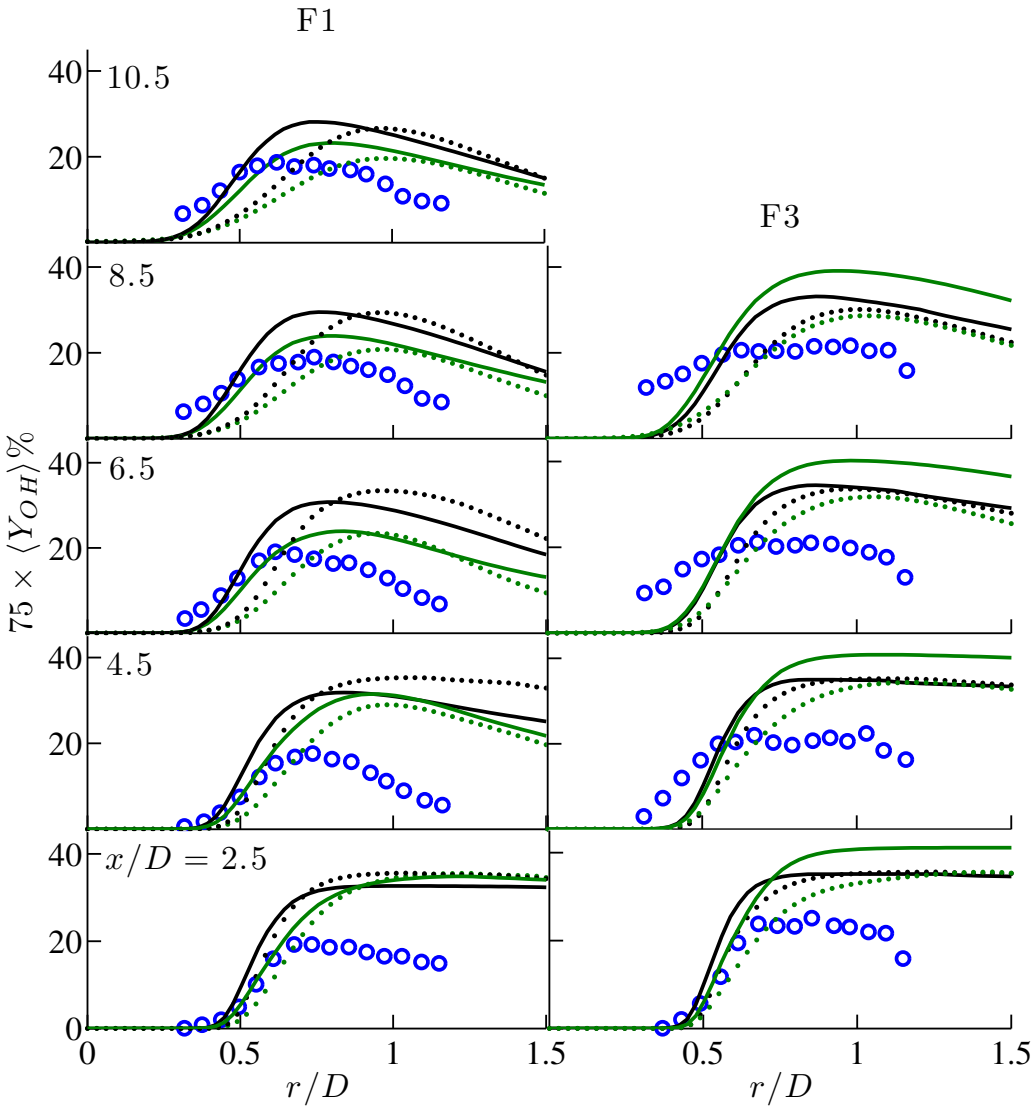

Fig. 5.29 Comparison of measured [46] (symbols) and computed (lines) mean OH mass fractions. The legend is as in Fig. 5.22.

thicknesses computed have been compared to the reconstructed experimental values [46] as discussed for Fig. 5.19 in §5.3.3. For the flame F3, the comparison shown here is reasonable. The combustion closure is at its limit for the 4.2M grid when $\Delta^+ < 1$ and this results in thicker flame brushes for both F1 and F3 flames. In other words, the closure in Eq. (2.19) is strictly valid for Δ^+ substantially larger than unity as explained in [61, 77, 147]. For the 1.5M grid case, the values of δ_t obtained using the static β_c model agrees very well with the measured

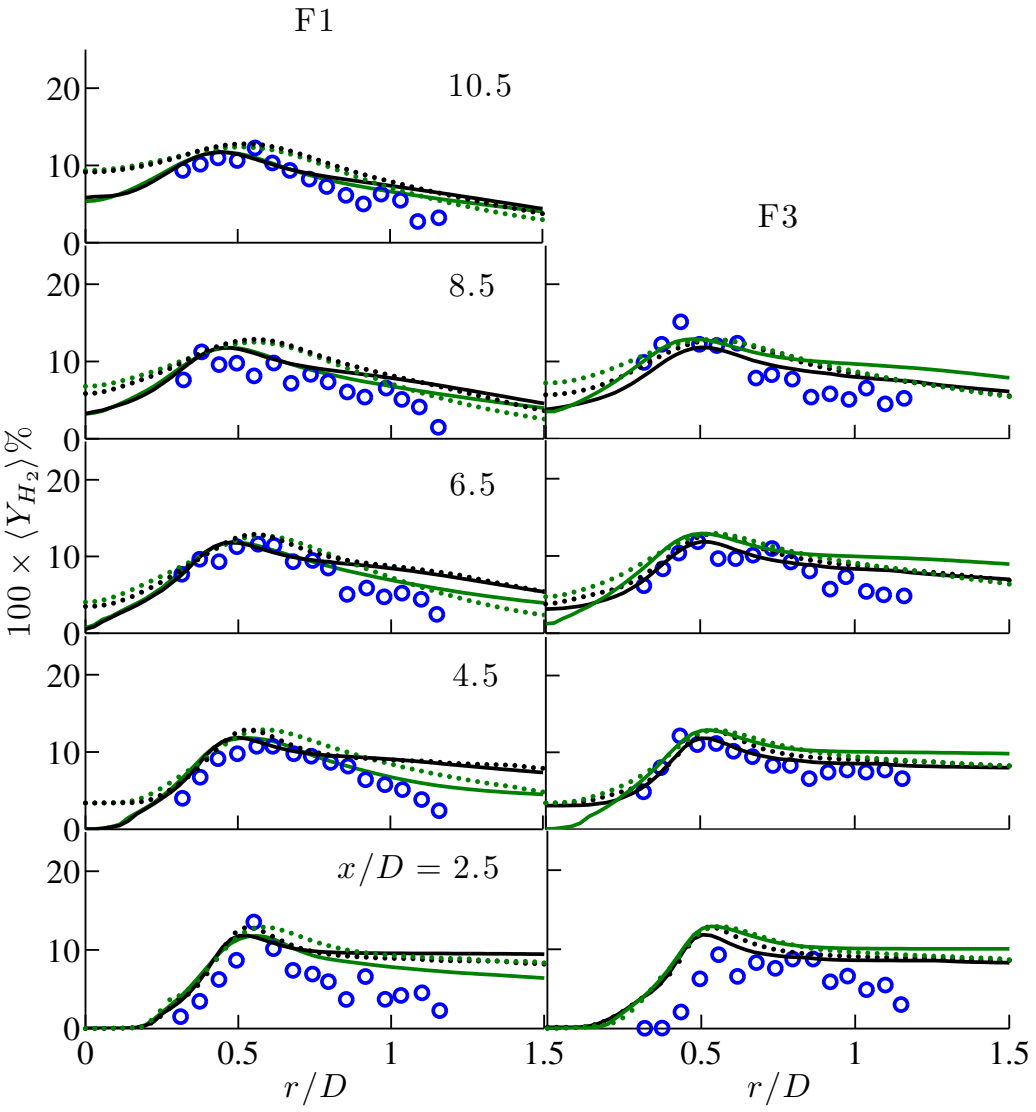

Fig. 5.30 Comparison of measured [46] (symbols) and computed (lines) mean H_2 mass fractions. The legend is as in Fig. 5.22.

values for the flame F3 as shown in Fig. 5.33. The thicker flame brush for 4.2M grid case is because of the combustion closure is at its limit for this grid as noted few times earlier. Although the difference between the measured and computed δ_t values seems large in Fig. 5.33, the maximum difference observed is about 4 mm while the maximum difference observed for the comparisons shown in the top row Fig. 5.19 is also about 4 mm (some experimental

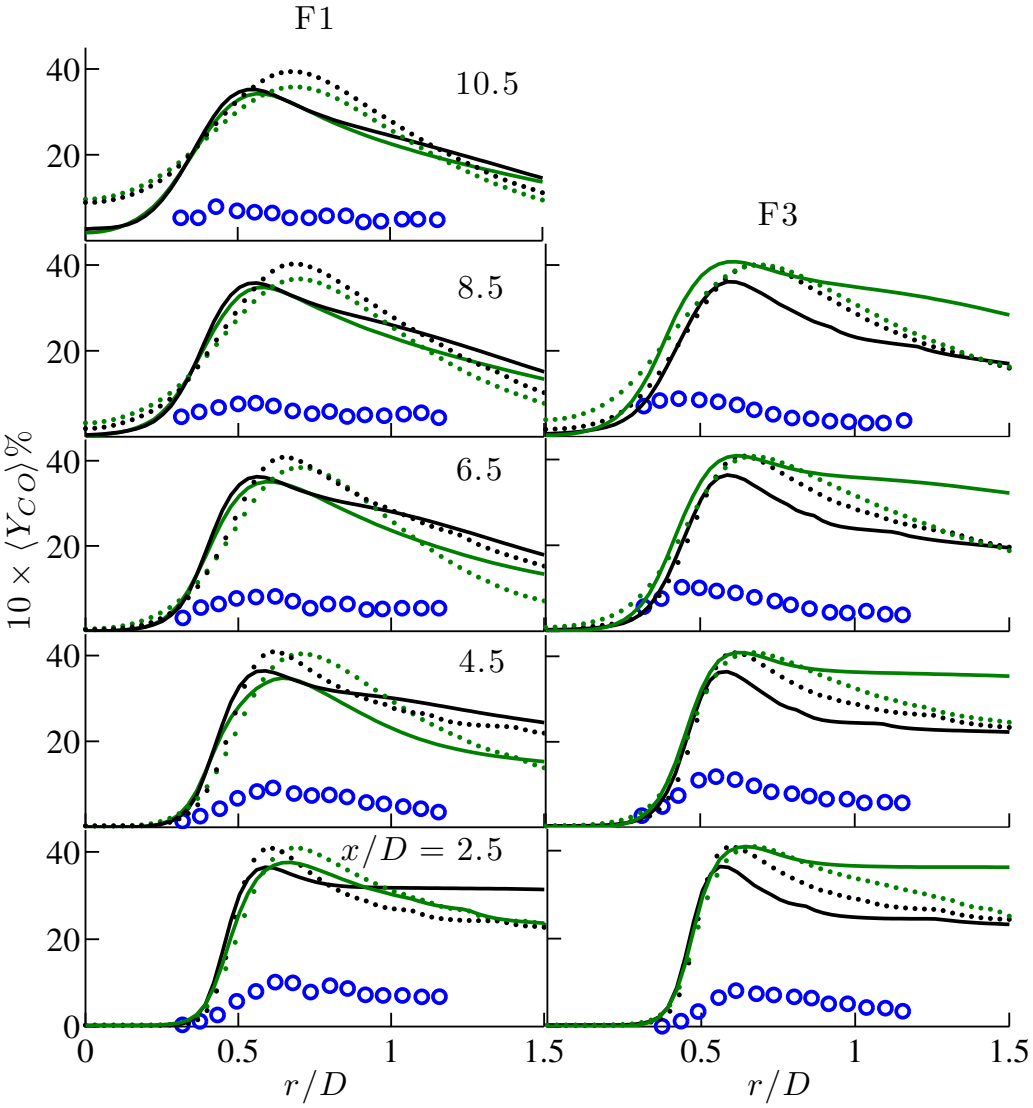

Fig. 5.31 Comparison of measured [46] (symbols) and computed (lines) mean CO mass fractions. The legend is as in Fig. 5.22.

inconsistencies). Thus, whether this difference between computed and measured values of δ_t is big or small, is an open question.

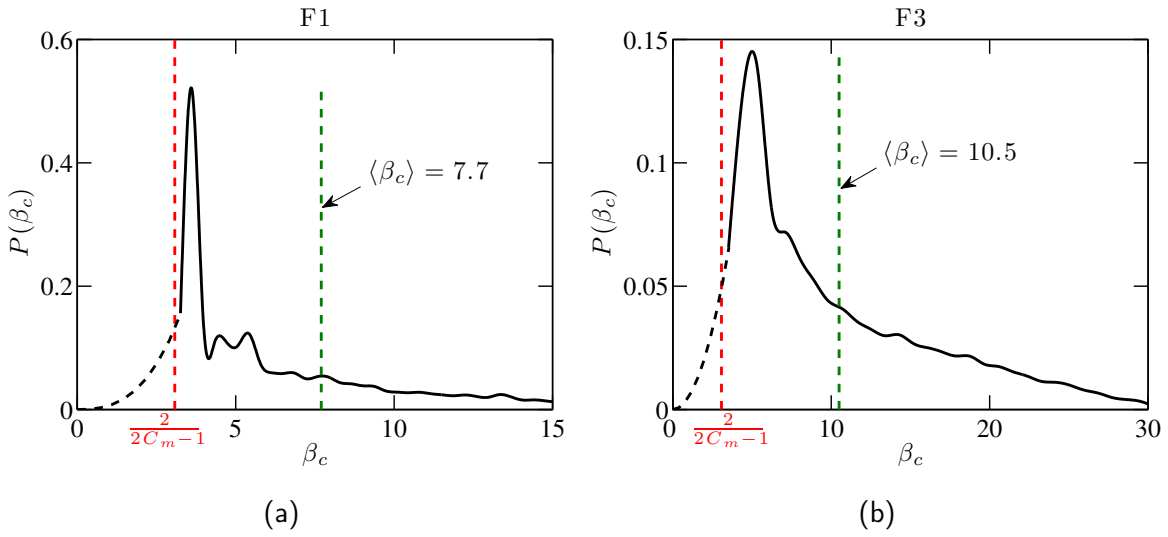

Fig. 5.32 The PDF of β_c obtained from LES of flames (a) F1 and (b) F3 using algebraic model for $\overline{\dot{\omega}}$ with dynamic computation of β_c with 1.5M grid. The average value and the lower limit imposed by Eq. (3.59) are also shown.

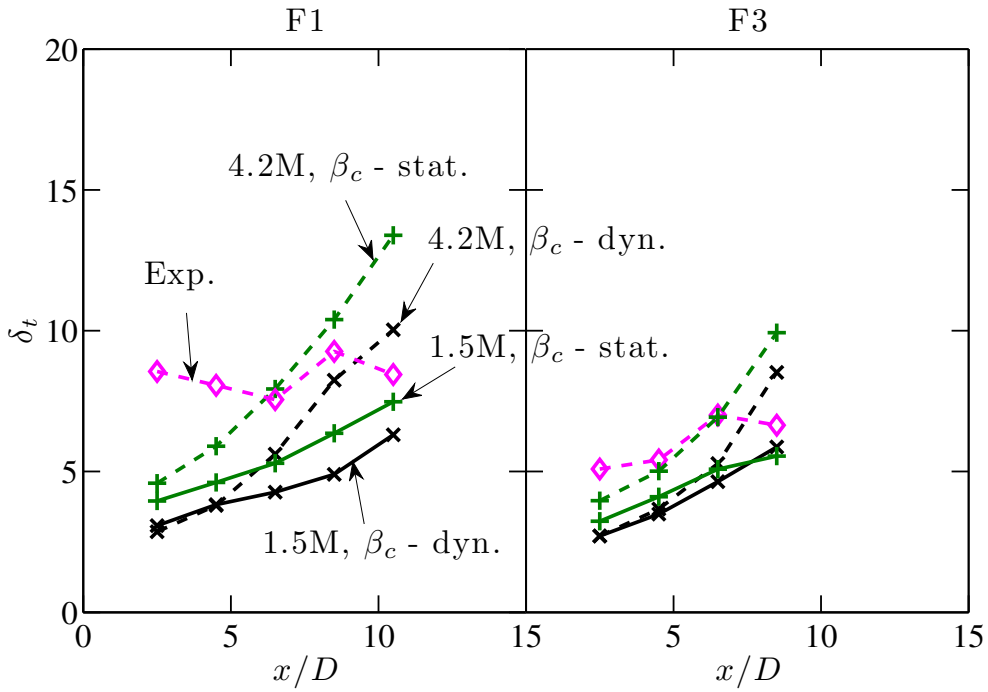

Fig. 5.33 The recomputed (◇) and LES values of flame brush thickness, δ_t, obtained using algebraic model for $\overline{\dot{\omega}}$ with dynamic computation of β_c, are compared for various cases.

5.5 Summary

The algebraic closure used for the simulation studied in this chapter inherently assumes that the local Damköhler number is very large. Thus, the influence of finite rate chemistry effects is not included. These effects are important from a practical perspective and can be included by using unstrained and strained flamelets. This is discussed in the next chapter. The dynamic evolution of β_c eliminates the empiricism and thus it will be used for further investigation in the following chapters, unless otherwise noted.

Chapter 6

Piloted flames - Presumed PDF closures

The unstrained and strained flamelets closures for filtered reaction rate described in §3.3.2 are studied in this chapter. The dynamic scales of turbulence containing about 80% to 90% of turbulent kinetic energy are resolved in a typical LES. Hence, the influences of resolved turbulent eddies on the flamelets are captured fully in the LES and of course one would need a model to represent the effects of unresolved sub-grid eddies on the flamelets and these eddies may have less than 10% of turbulent kinetic energy depending on the numerical grid employed for LES. Thus, these scales may not have enough energy to impart considerable influence on the flamelets to alter their structure and burning characteristics. This is only a conjecture here for LES and careful analyses are required to make an assessment. Similar views have been debated in the past while investigating premixed combustion regimes using DNS methodology [189] and has been suggested that the small-scale eddies do not have adequate energy to impart significant perturbations on unstrained laminar flame front structure. In the light of these observations, whether one needs strained flamelets for typical large eddy simulations of premixed combustion or not is an open question at least for configurations not involving local extinctions or blow off. This question is answered to some extent in this chapter.

All the simulations obtained using unstrained and strained closures and shown in this chapter are listed in tables A.2 and A.3 along with other simulations used to test the sensitivity of various parameters in these modelling approaches.

6.1 Specific numerical detail

The relative performances of the strained and unstrained flamelet closures are assessed by comparing numerical results from LES to experimental measurements. The numerical procedure for these closures is described in §3.3.2 and §3.4. The SGS velocity, u'_Δ, needed in Eq. (2.22), is modelled using Eq. (3.51) on the basis of the analysis of §5.3.2. The dynamic procedure for

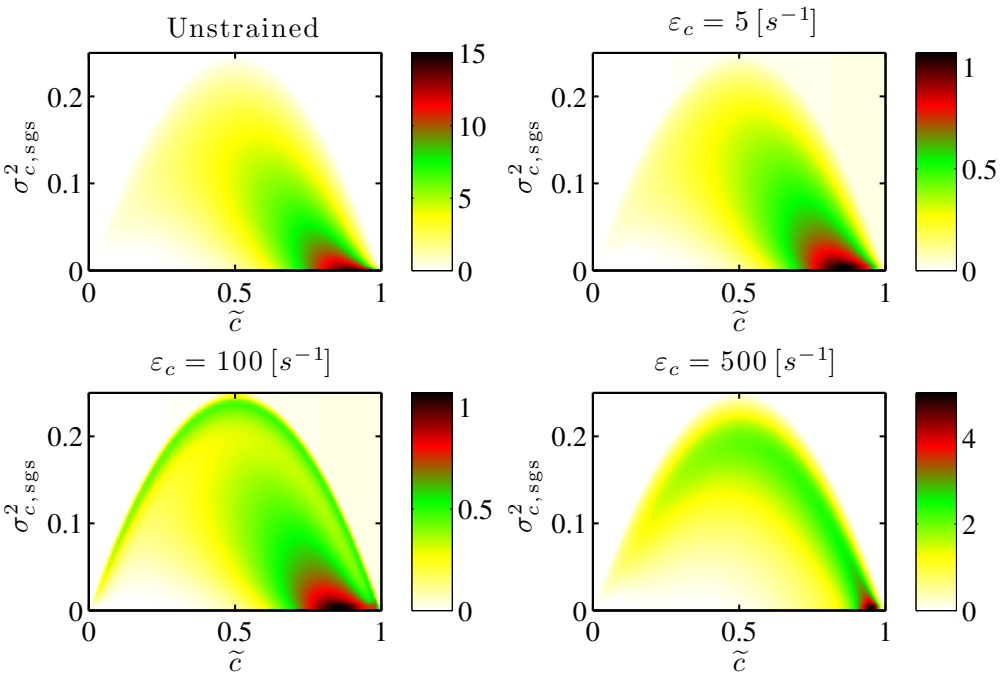

Fig. 6.1 Typical variation of normalised filtered reaction rate in unstrained and strained flamelets.

the combustion parameter β_c described in §3.3.4 is used to compute this parameter based on the results obtained in the previous section. However, comparisons with a static formulation are also discussed, if required. Grids, boundary conditions and other numerical details are discussed in §4.2, §5.1 and §5.2. The additional boundary for the SGS variance, $\sigma^2_{c,\mathrm{sgs}}$, see Eq. (3.36), is specified to be zero for all the inlets as it is generated predominantly by chemical reactions inside the domain.

6.2 Filtered reaction rate

Typical variations of filtered reaction rate, $\overline{\dot{\omega}}$, normalised by $\delta_{th}/(\rho_u s_L)$, are shown in Fig. 6.1 for the unstrained and strained flamelets as a function of the controlling parameters (see §3.3.2). This result is shown for stoichiometric methane-air flame, and similar variations are observed for other stoichiometry values. The results are shown for three values of $\widetilde{\varepsilon}_c$ for the strained flamelets model. The maximum value of $\overline{\dot{\omega}}$ occurs around $\widetilde{c} \simeq 0.8$ for very small values of $\sigma^2_{c,\mathrm{sgs}}$. For values around this $\widetilde{c}$, as the variance increases the filtered reaction rate decreases, which is because the burning part of the sub-grid PDF of c decreases as $\sigma^2_{c,\mathrm{sgs}}$ increases, which is easy to verify using the β-function employed for this study. For $0.2 \leq \widetilde{c} \leq 0.5$, the sub-grid PDF broadens as $\sigma^2_{c,\mathrm{sgs}}$ increases which implies that the burning part of the flamelet are seen occasionally leading to relatively larger reaction rate as seen in Fig. 6.1. The straining decreases

the peak reaction rate substantially as one would expect. Except for this change, the variation of filtered reaction rate is similar for the unstrained and strained flamelets. These tabulated values are used in LES to simulate the piloted flames [46] studied in the previous chapter and the results are discussed in the following sections.

6.3 Grid sensitivity

The sensitivity of the computational results to the numerical grid is discussed first. The radial variation of mean axial velocity, TKE, fuel mass fraction and normalised temperature is shown in Figs. 6.2-6.5 respectively. The results are shown for various streamwise positions for the flames F1 and F3. Typical results are shown only for the F1 and F3 flames here because they have the extreme values of Da, Ka and Re_T in the range investigated experimentally in [46]. The mean velocity is normalised using the respective bulk-mean velocity at the jet exit and the mean TKE is normalised using the values $k_0 = 12.7\ \mathrm{m}^2/\mathrm{s}^2$ for the F1 flame and 3.82 for the F3 flame reported in [46]. The temperature is normalised as $T^+ = (\overline{T} - T_u)/(T_b - T_u)$, where $\overline{T}$ is the filtered temperature calculated using $\widetilde{T}$ obtained from $\widetilde{h}$ using Eq. (3.18), and the fuel mass fraction is constructed from the computed $\widetilde{c}$. The effect of the SGS variance could not be included in $\langle \overline{T}^+ \rangle$ because this quantity is not available in the LES framework used here. These figures compare all of these quantities to their experimental values (open circles) and those reported in earlier studies. For the discussion in this section one shall focus on the present computational results obtained using 1.5M and 4.2M grids in reference to the experimental values to understand the grid sensitivity and other results shown in these figures will be discussed in later sections.

The mean velocity variations in the flames F1 and F3 show that the 1.5M grid is adequate to capture the experimental variations. The results from the 4.2M grid shown only for the flame F1 clearly demonstrates that the mean velocity is not strongly sensitive to the numerical grids used here, which has been also observed for the algebraic closure investigated in the previous sections. Similar behaviour is also observed for the strained flamelets. The TKE results shown in Fig. 6.3 also suggest similar conclusion. However, the computed TKE are relatively large for the strained flamelets and show some sensitivity to the grid as seen in Fig. 6.3. Despite this, the general variation of the TKE does not seem to be influenced by the numerical grid. The reason for the sensitivity observed for the strained flamelets model will become clearer when the results of unstrained and strained flamelets are discussed in the next subsection. The sensitivity (not shown) of mean mass fraction of methane and normalised temperature to the numerical grid is similar to that shown for $\langle U \rangle$. These results suggest that the current numerical

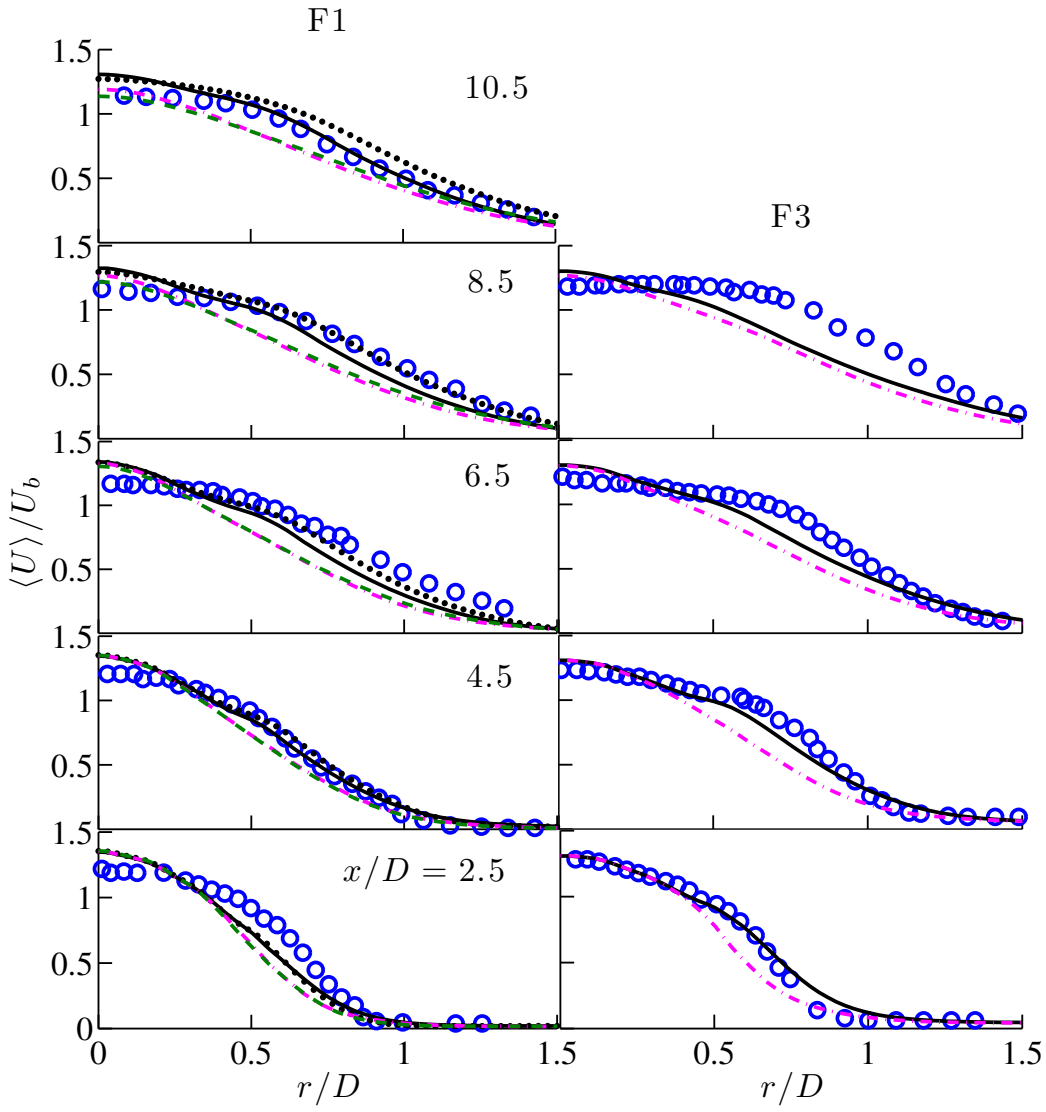

Fig. 6.2 Comparison of measured [46] (symbols) and computed (lines) radial variation of $\langle U \rangle / U_b$ for F1 and F3 flames. Unstrained flamelet result is shown for 1.5M (——) and 4.2M (•••) grids, and strained flamelets result is shown for 1.5M (– · –) and 4.2M (– –) grids. The results of 4.2M grid is shown only for the F1 flame.

results are weakly sensitive to the numerical grids employed for this study and the second order quantity such as TKE shows a sensitivity for the strained flamelets. The results of 1.5M grid are used for the subsequent analysis below because of the weak grid sensitivity observed for the mean quantities.

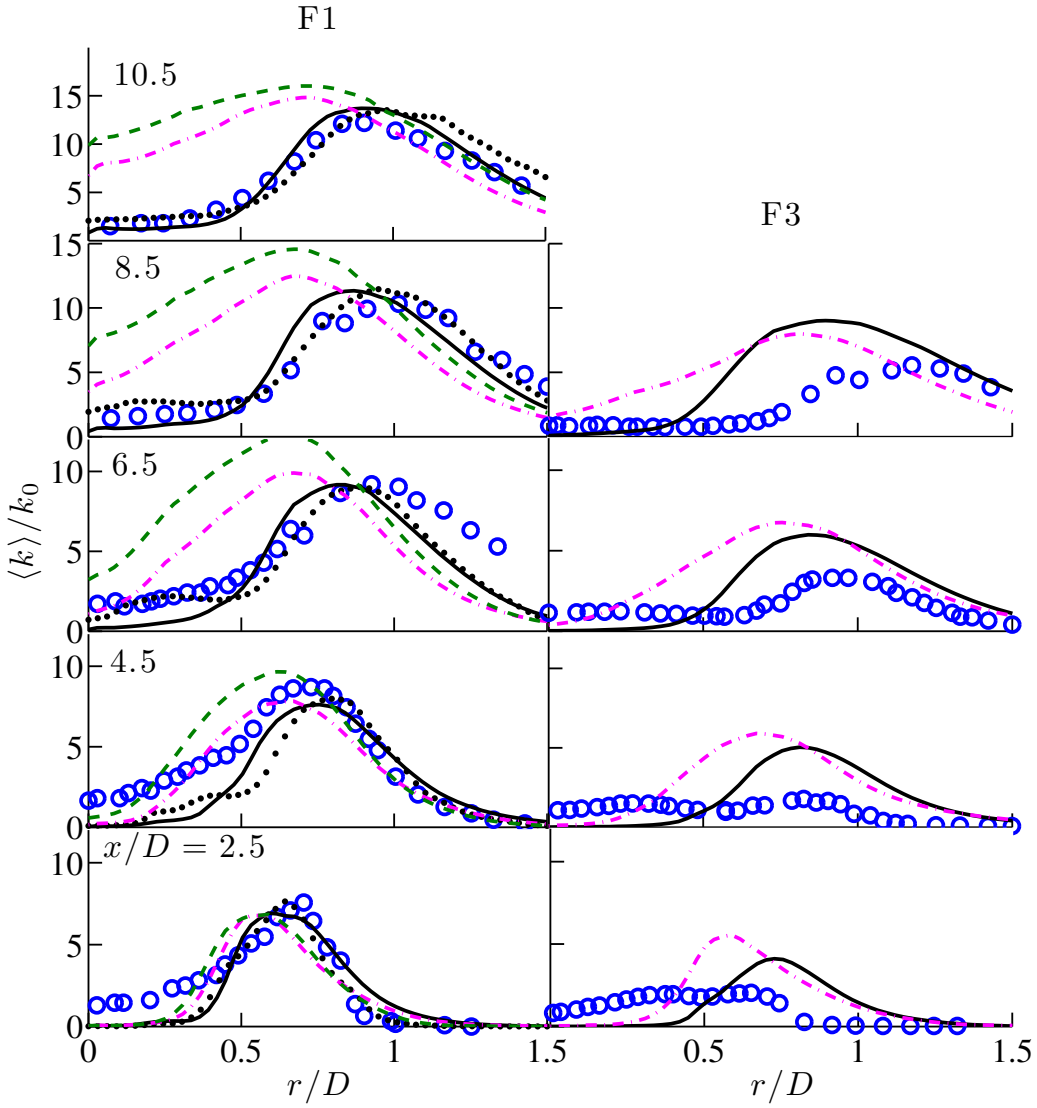

Fig. 6.3 Comparison of measured [46] (symbols) and computed (lines) radial variation of $\langle k \rangle / k_0$ for F1 and F3 flames. The legend is as in Fig. 6.2.

6.4 Unstrained vs Strained Flamelets

The fluid dynamic straining effects were shown [122] to be important in RANS calculations of the Bunsen flames of [46] using unstrained and strained flamelets. When the straining effects were excluded, the computed flame length was observed to be very much shorter than the measured length in [46] suggesting that the fuel is consumed quickly. There is only one turbulence length and time scales involved in the RANS and the effects of the spectrum of

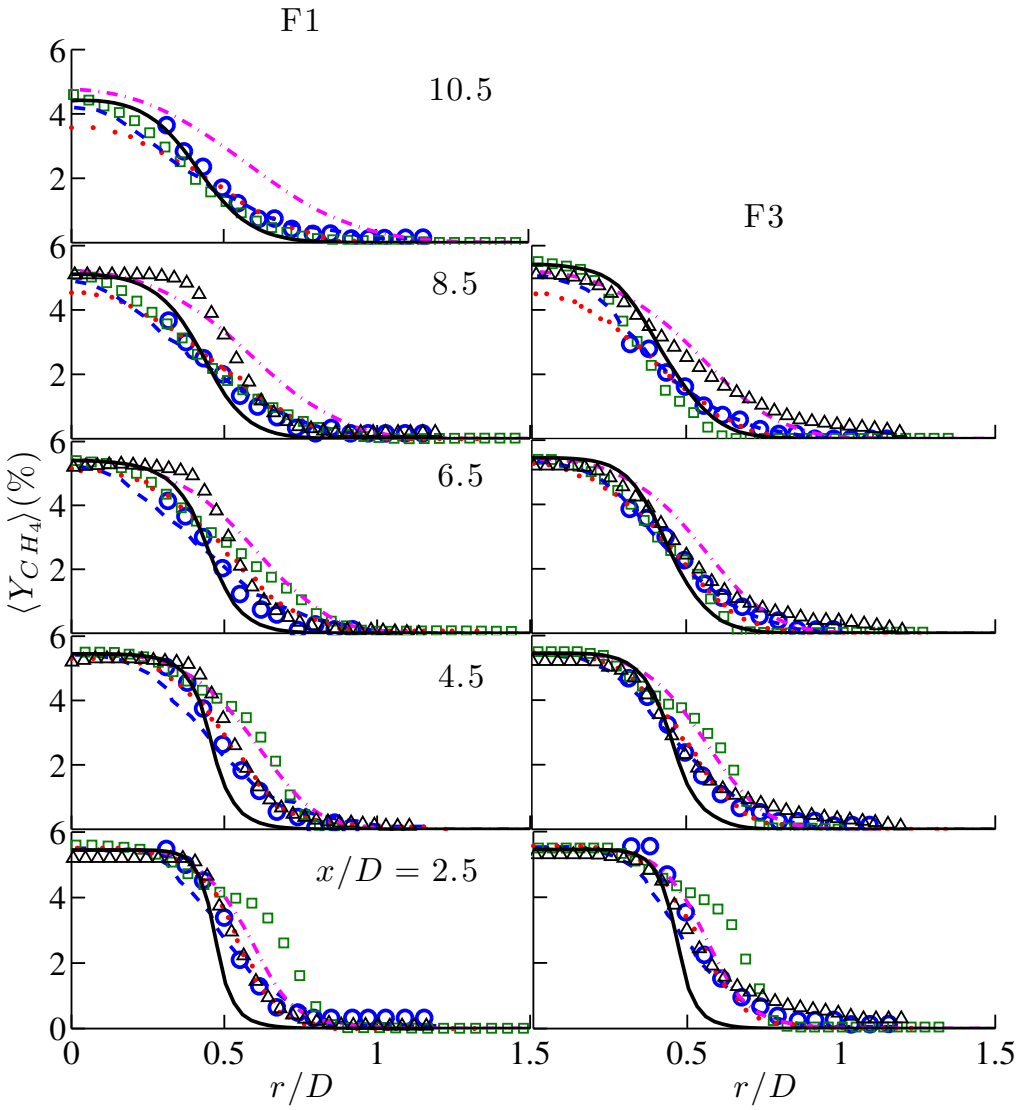

Fig. 6.4 Comparison of measured [46] (○ ○ ○) and computed mean fuel mass fraction. The computational results are shown for the 1.5M grid using unstrained (——) and strained (–·–) flamelets. Previous results [53] (△), [56] (□), [122] (– –) and [240] (•••) are shown for comparison.

turbulence scales on the flame need to be included in the combustion modelling. On the other hand, a range of scales is involved in LES, allowing the strain to be partially resolved implicitly at super-grid scales. Various approaches have been investigated in the past to include flame stretching using RANS and LES paradigm as discussed in §2.4.6. It was noted in this section that the sub-grid variance of the progress variable is modelled in earlier studies typically using an expression developed for passive scalars, and these expression is likely to

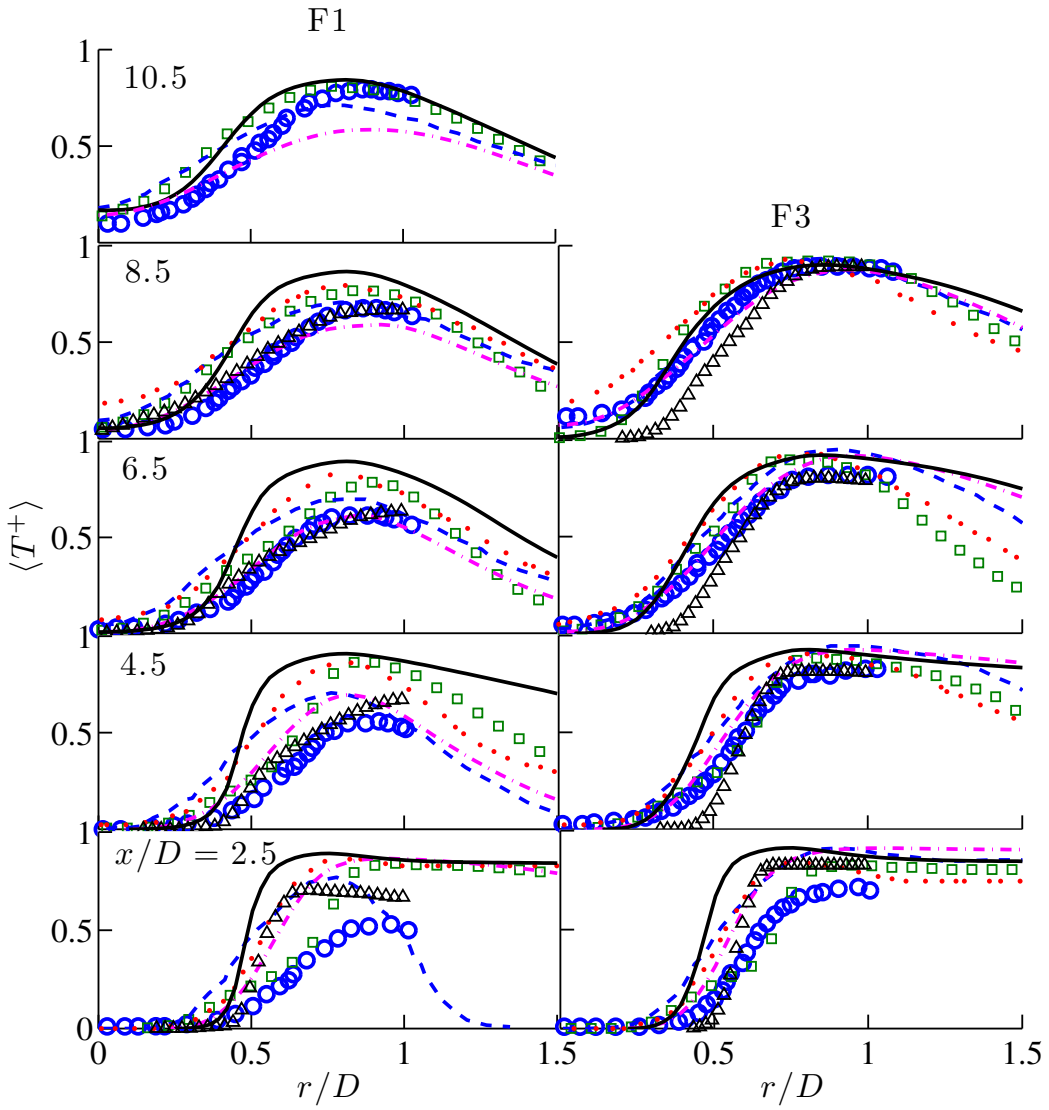

Fig. 6.5 The normalised mean temperature computed on the 1.5M grid using unstrained (——) and strained (– · –) flamelets is compared to the measurements [46] (○ ○ ○). Previous results [53] (△), [56] (□), [122] (– –) and [240] (•••) are shown for comparison.

severely under-estimate this variance across the flame, as shown in the analysis of §3.3.2. These under-prediction of SGS variance would result in an over-prediction of reaction rate in an unstrained flamelets formulation, inducing one to think that strained flamelets are required. To avoid such underestimates, a transport equation for the SGS variance of progress variable, see Eq. (3.36), must be used. Unstrained and strained flamelet models described in §3.3.2 are thus compared in this study to understand their relative behaviour in LES in light of the

above observation, and to assess if strain is effectively needed in flamelets modelling for LES in general. This assessment is done in this section by comparing radial profiles of velocity, temperature, TKE and species mass fractions obtained using unstrained and strained flamelet closures to experimental results [46].

The results shown for normalised mean axial velocity, $\langle U \rangle / U_b$, in Fig. 6.2 show that the heat release induced acceleration in the flame F3 having the highest Da is underestimated by the strained flamelets model, compared to the unstrained flamelet model, for the upstream positions as seen in this figure for $x/D = 2.5$ and 4.5. This implies that the local burning rates may be under estimated by the strained flamelets model and it seems to be the case as one shall see later while discussing Figs. 6.6 and 6.7. However, this difference becomes negligible as one moves in the streamwise direction. Similar observations are made for the highest Re_T flame F1 which has the lowest Da.

The normalised mean TKE obtained using the two flamelets is compared in Fig. 6.3 along with experimental data. The trend obtained using these two flamelets are similar for the flame F3 and there is some over estimation of the TKE in flame region, $0.55 \leq r/D \leq 0.7$. The values obtained using the strained flamelets are generally larger than those obtained for the unstrained flamelet model and the TKE values obtained using the later model compares favourably with the experimental values for the flame F1 as shown in Fig. 6.3. A closer study of this figure suggests that the shear layer, where the filtered flame is expected to be residing, is shifted slightly towards the centreline which is suggested by the shift in the peak value of the mean TKE. The production of TKE by the fluid dynamic shear is likely to be aided by the radial acceleration of the fluid resulting from the heat release effects. Because of these effects the mean TKE is overestimated for $r/D \leq 0.6$ as observed in Fig. 6.3. Nevertheless, the comparisons shown here for the unstrained flamelets are very similar to those observed in earlier studies using various SGS [53, 56, 186, 240, 243] and RANS [5, 96, 122, 130, 143, 198, 208, 209, 222, 223] combustion modelling approaches.

It is worth to investigate spatial variation of reaction rate before discussing the results in Figs. 6.4 and 6.5 in detail. This spatial variation for the unstrained and strained flamelets are compared in Figs. 6.6 and 6.7 for the flames F3 and F1 respectively. These results are shown for two different times and $\log(100\overline{\dot{\omega}}^{+})$ for $\overline{\dot{\omega}}^{+} > 0.01$, where $\overline{\dot{\omega}}^{+} = \overline{\dot{\omega}}\delta_{th}/\rho_u s_L$ is the normalised filtered reaction rate. The maximum value observed in the computations for $\overline{\dot{\omega}}^{+}$ is about 2.63 and the logarithm is used here to depict the spatial variations clearly because the combustion and thus the chemical reactions are small scale phenomena. The laminar-like structure with negligible wrinkling is observed in the F3 flame having the highest Da when the unstrained flamelet model is used. If the strain effects are included then the influence of shear layer roll-up resulting from Kelvin-Helmholtz instability on the filtered flame becomes

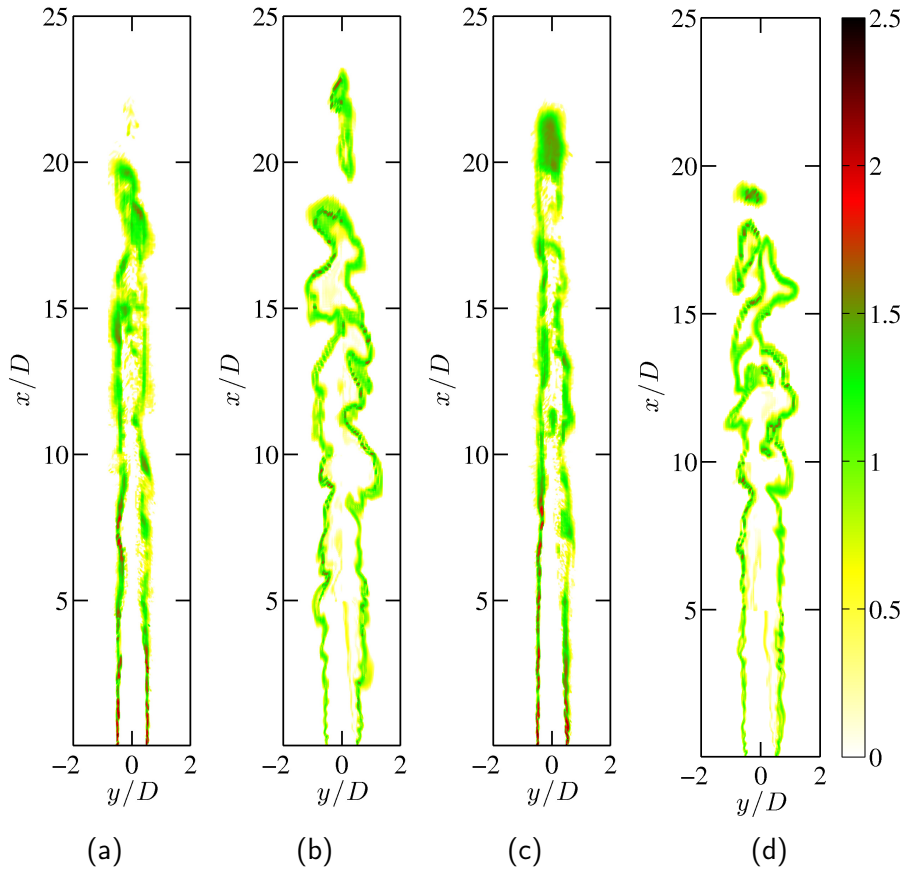

Fig. 6.6 Spatial variation of $\log(100\overline{\dot{\omega}}^{+})$ in flame F3 obtained at an arbitrarily chosen time, $t1$, using (a) unstrained and (b) strained flamelets with 1.5M grid. These results at 20 ms later are shown in (c) and (d). The contours are shown for $\overline{\dot{\omega}}^{+} > 0.01$.

apparent as in Fig. 6.6 for the two arbitrary time instances chosen. Also, the peak reaction rate occurs near the jet exit and this value is reduced considerably (see Fig. 6.1) as one would expect when the straining effects are included. The overall flame length is more or less the same and there is island formation as in Fig. 6.6 for the two combustion models used in this study.

Although the peak reaction rate is reduced for the strained flamelets model, the overall mean burning rate is maintained by the increase in flame area resulting from the increased level of flame wrinkling compared to the unstrained flamelet model. The overall mean burning rate and thus the mean heat release rate given by $\dot{m}_f \Delta H_c$, where ΔH_c is the heat of combustion, must be the same for both the model because the fuel flow rate, $\dot{m}_f$, is identical and there are no local extinction. Despite this, a distinct difference is observed for the flame F1 having the highest Re_T and lowest Da as seen in Fig. 6.7. The peak reaction rate (red colour) is spatially intermittent in Fig. 6.7a and an indication of its temporal intermittency can be seen by comparing Figs. 6.7a and 6.7c, which are expected in high Re_T flames. The most apparent difference between the

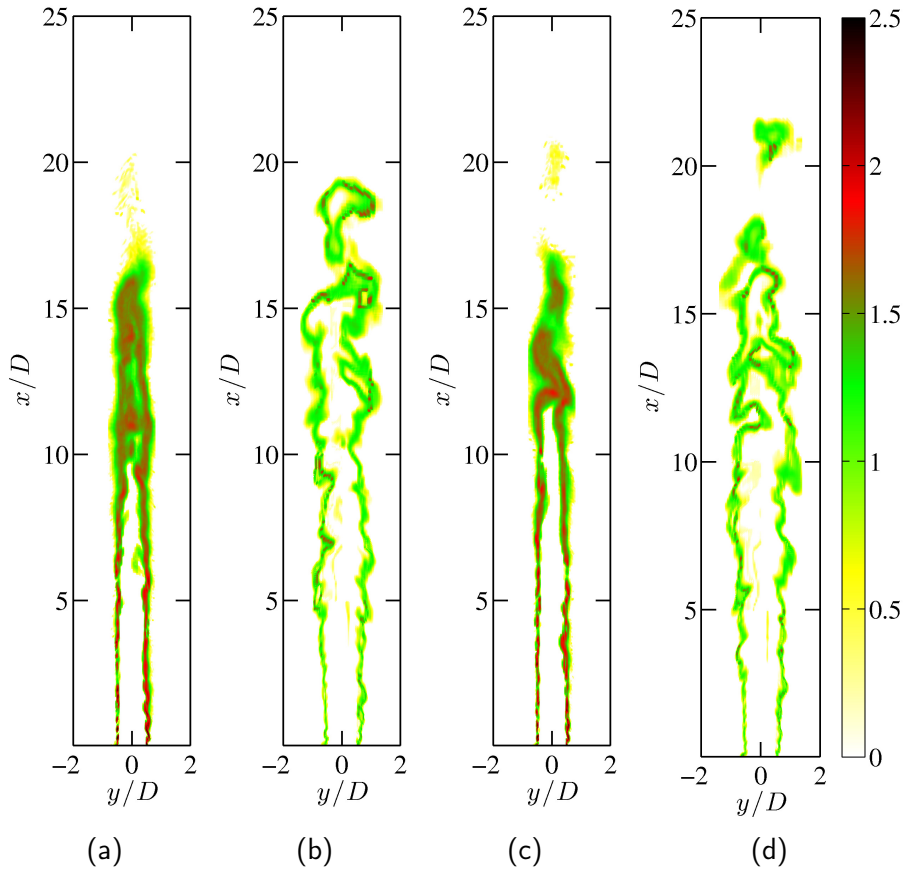

Fig. 6.7 Spatial variation of $\log(100\overline{\tilde{\omega}}^{+})$ in flame F1 obtained at an arbitrarily chosen time, $t1$, using (a) unstrained and (b) strained flamelets with 1.5M grid. These results at 20 ms later are shown in (c) and (d). The contours are shown for $\overline{\tilde{\omega}}^{+} > 0.01$.

filtered reaction rates computed using the unstrained and strained flamelet models is seen in the region $x/D \geq 10$ for the flame F1. The strained flamelets model confines the reaction rate to thin layers all the way to $x/D \approx 15$ whereas the reaction rate is distributed more or less uniformly over larger region for $x/D \geq 11$ when the unstrained flamelet model is used. A small change in the size of this region is observed if one compares Figs. 6.7a with 6.7c. It is not easy to comment which one of the behaviour shown in Figs. 6.6 and 6.7 for the unstrained and strained flamelet models is the correct behaviour because the experimental study [46] did not report results on reaction rate. Furthermore, it is not quite easy to quantitatively measure the reaction rate but it is possible to image surrogates of reaction rate qualitatively using laser diagnostics for OH, CH2O and CH species. In the absence of such information, one can compare and analyse statistics gathered from the experimental and, past and current numerical studies to further assess the relative behaviour of strained and unstrained flamelets models. The comparisons discussed above for the mean velocity suggests that both unstrained and strained

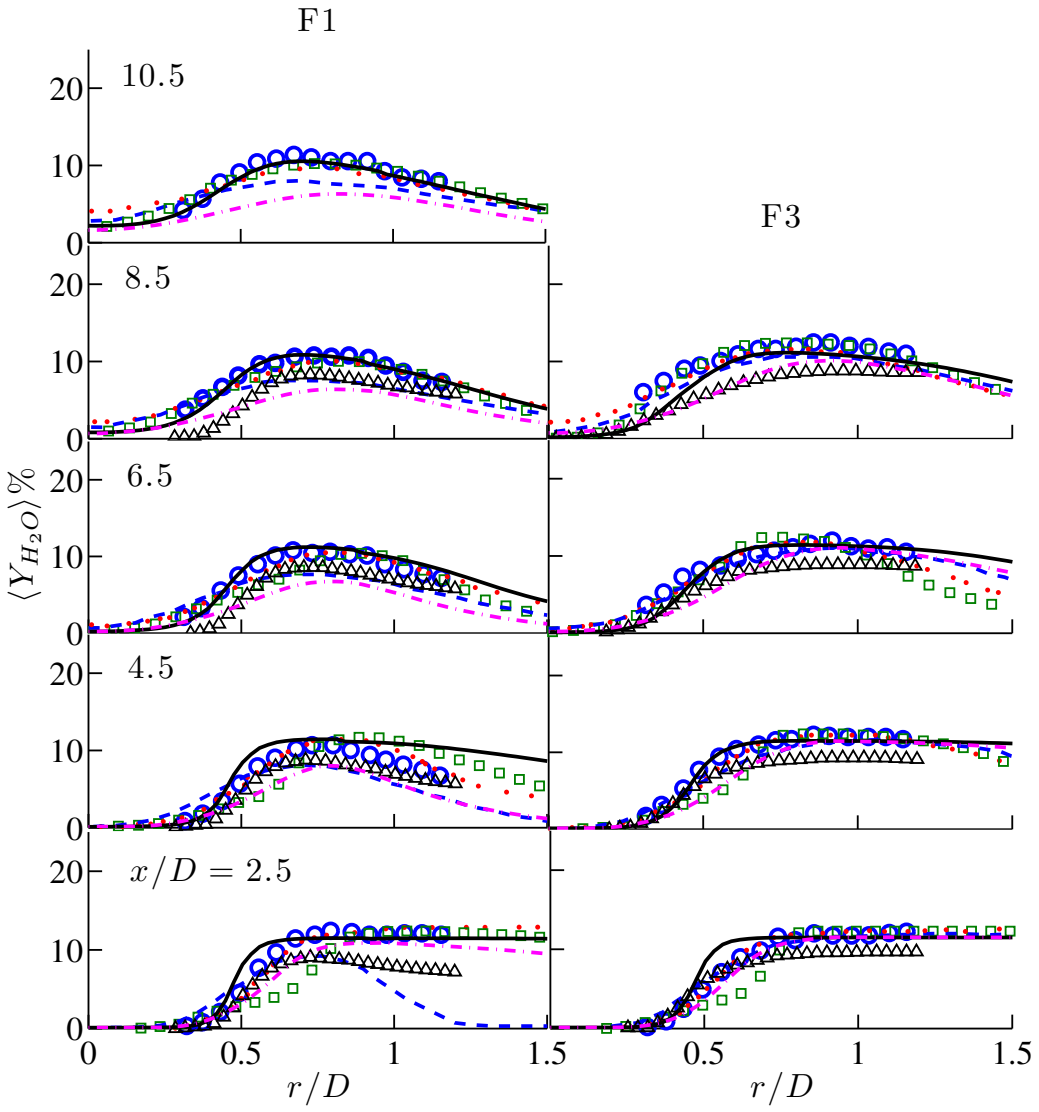

Fig. 6.8 Comparison of measured [46] and computed H_2O mass fraction. The legend is as in Fig. 6.4.

flamelets are good but the TKE variation suggests that the unstrained flamelets model may be preferred. One must also investigate the behaviour of scalar mass fractions which is conducted next.

6.4.1 Major species comparison

The radial variations of mean fuel mass fraction and normalised temperature are compared to the experimental measurements and past numerical results in Fig. 6.4. The results are

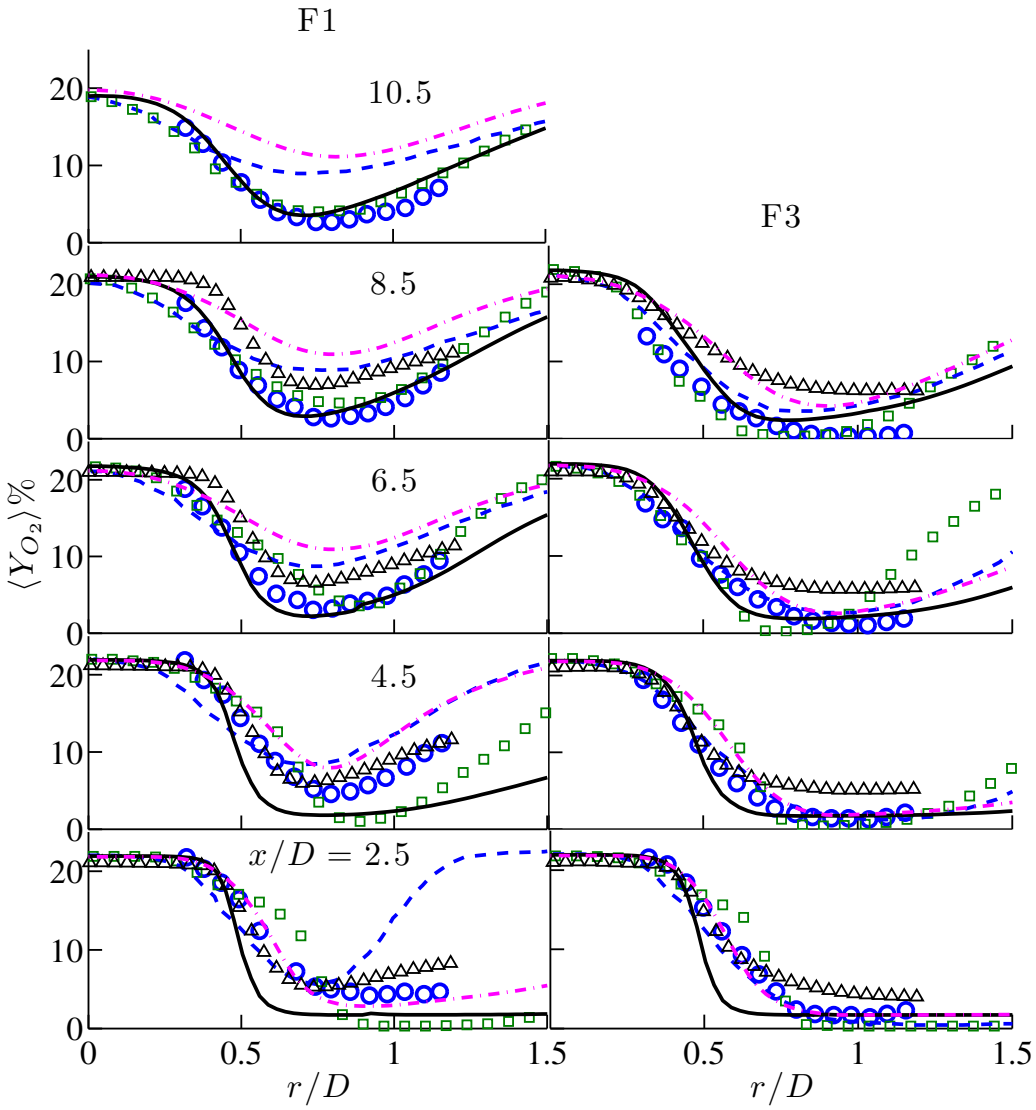

Fig. 6.9 Comparison of measured [46] and computed O_2 mass fraction. The legend is as in Fig. 6.4.

shown for various streamwise positions in the F1 and F3 flames. The averaged fuel mass fraction computed using the unstrained flamelet model is lower than the measured values for $0.5 \leq r/D \leq 0.7$ at $x/D = 2.5$ for both the F1 and F3 flames as shown in Fig. 6.4. The estimates obtained using the strained flamelets are relatively better for this location. However, the unstrained flamelet model values are closer to the measured values compared to those from the strained flamelet model as one moves in the downstream direction. Indeed, the strained flamelet model overestimates the averaged fuel mass fraction and the level of this overestimate increases with downstream distance for both the F1 and F3 flames as observed in Fig. 6.4.

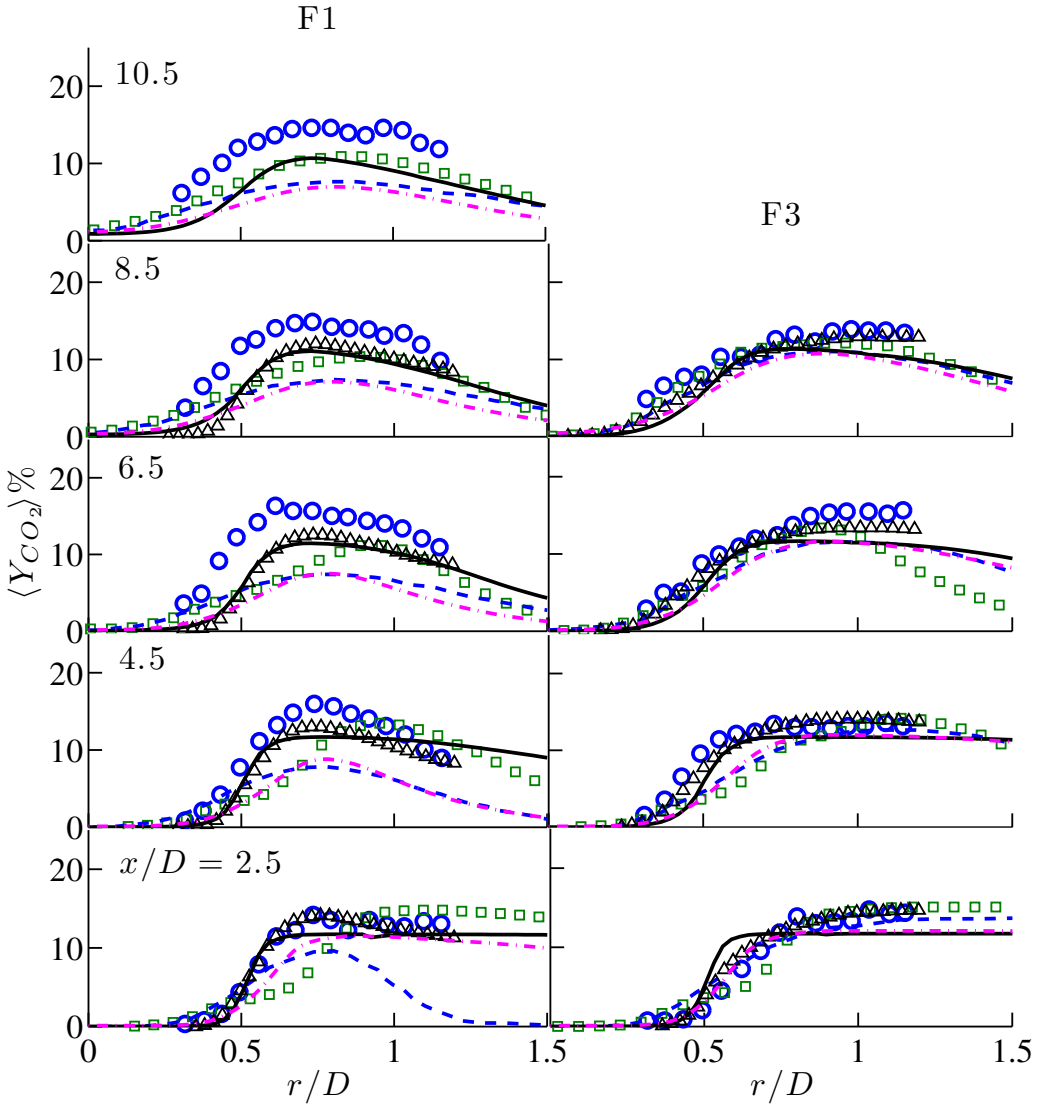

Fig. 6.10 Comparison of measured [46] and computed CO_2 mass fraction. The legend is as in Fig. 6.4.

This is consistent with the reduced reaction rate observed in Figs. 6.6 and 6.7. The results in Fig. 6.4 suggest that the unstrained flamelet model predictions are comparable to those obtained using other combustion modelling approaches such as thickened flames [53, 240] and Eulerian stochastic fields method [56].

The normalised mean temperature variation with normalised radius is shown in Fig. 6.5 for the flames F1 and F3 at various axial positions. No significant difference was observed between $\langle \overline{T}^+ \rangle$ and $\langle \widetilde{T}^+ \rangle$, and thus the mean temperature is denoted using $\langle T^+ \rangle$ in the following discussion. A significant overestimate at $x/D = 2.5$ is because of the uncertainty in the boundary

condition for the pilot stream as observed also for the algebraic closure results in the previous sections and in past studies. This overestimate decreases as one moves downstream for both F1 and F3 flames. The relative behaviour of the unstrained and strained flamelets models is consistent with that for the fuel mass fraction. Although the strained flamelets model gives a good comparison for $x/D = 6.5$ for the F1 flame, it underestimates the peak temperature for downstream positions and the level of under-prediction increases gradually with downstream distance as seen in Fig. 6.5, whereas the unstrained flamelet model prediction improves with the distance and is comparable to previous results and measured values. The difference between these two flamelet models is small for the flame F3 with the highest Da.

Figure 6.8 compares the computed values of mean mass fraction of H_2O to the measurements [46] and results of previous studies. The results of both unstrained and strained flamelet models are shown in this figure and the strained flamelets model under-predicts the mean mass fraction of water vapour, which is consistent with the fuel mass fraction variation discussed earlier. The values obtained using the unstrained flamelet model are close to the measurements for all the axial positions in both F1 and F3 flames. Also, one can observe in Fig. 6.8 that the unstrained flamelet predictions are improved compared to some of the earlier studies employing nearly 3 to 4 times the grid used in the current study. The comparisons for other major species such as O_2 and CO_2 are similar to those shown here for water vapour and fuel and are shown in Figs. 6.9 and 6.10.

6.4.2 Minor species comparison

Figures 6.11-6.13 respectively compare the radial variations of minor species, OH, H_2 and CO, mass fractions with the results of past studies and measurements. The results of past studies are shown in these figures only if they were reported in those studies. There is a severe under prediction of OH and H_2 mass fractions by the strained flamelets model whereas the unstrained flamelet model yields good prediction of these minor species for both F1 and F3 flames. The OH mass fraction comparison shown in Fig. 6.11 is much better than the comparison shown in Figs. 5.16 and 5.29 for the algebraic reaction rate closure based on high Da combustion. This improved comparison is because the unstrained flamelet model allows one to include local finite rate chemistry effects on the filtered reaction rate. Computed CO mass fraction profiles from unstrained flamelet closure are largely overestimated and is overestimation was also seen in Figs. 5.18 and 5.31 for the algebraic model and in previous studies [56, 122]. However, this over-prediction seems to be related to under-predictions seen for CO_2 in Fig. 6.10. Good predictions of CO mass fraction are observed when the strained flamelets closure is employed in case of flame F1. Nevertheless, the same quality is not observed for flame F3.

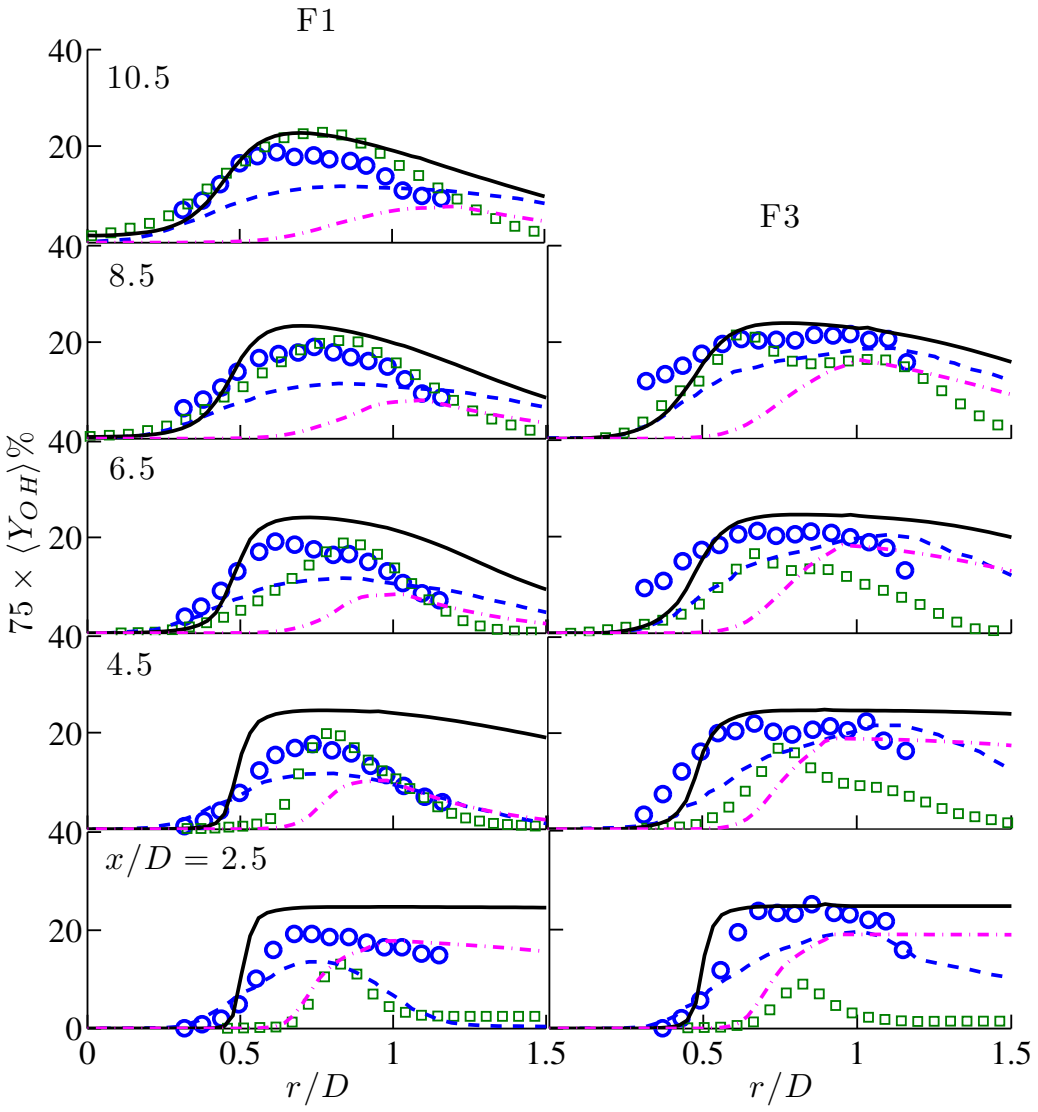

Fig. 6.11 Comparison of measured [46] and computed OH mass fraction. The legend is as in Fig. 6.4.

The results presented so far suggest that the unstrained flamelet model performs consistently better compared to the strained flamelets, which is interesting to note in the light of the observation made in [122] suggesting that the strained flamelets are required for correct prediction of these piloted Bunsen flames using RANS methodology. Furthermore, the strained flamelets model is observed to behave differently depending on the flame (F1 or F3) and the axial position, suggesting a dependence from the local Reynolds number which is not observed in case of the unstrained flamelets closure.

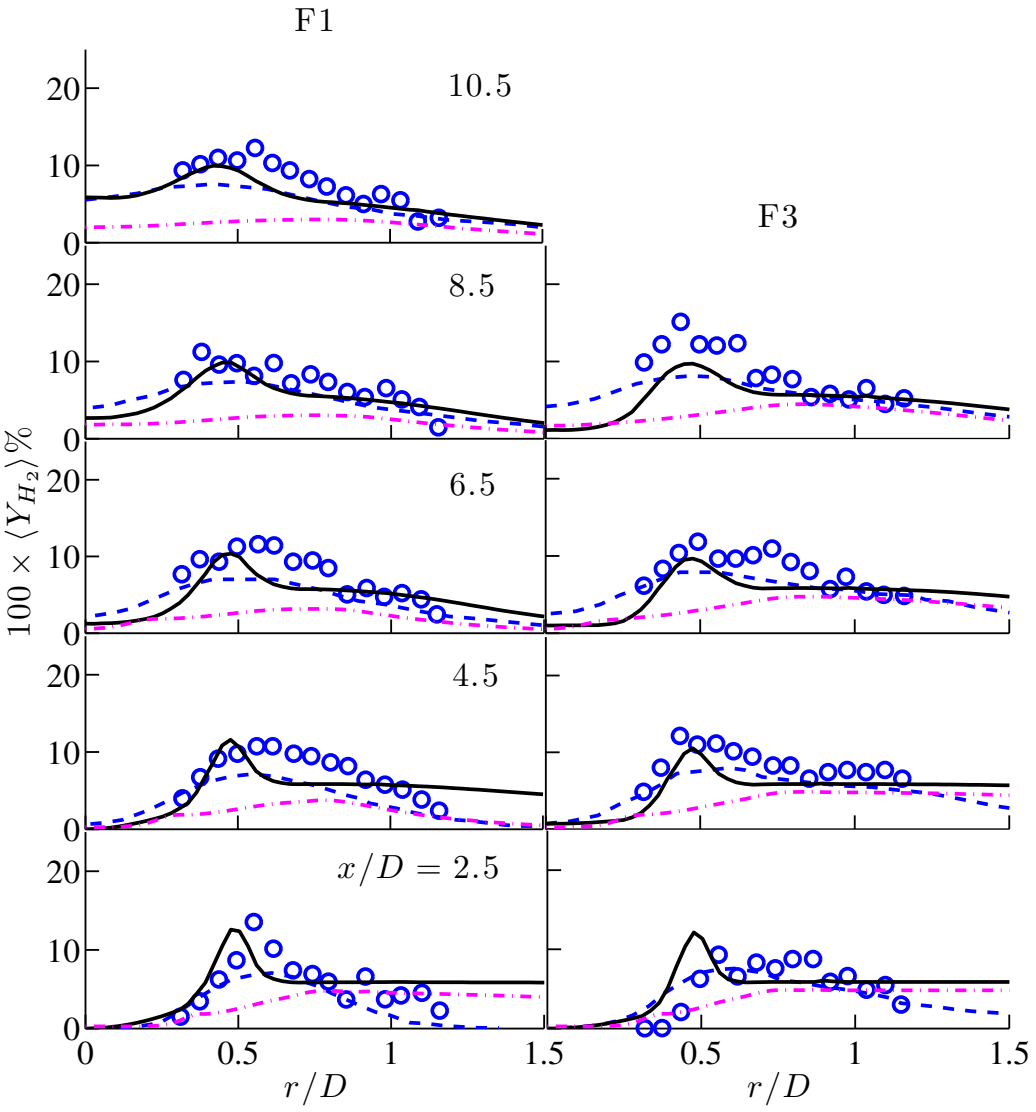

Fig. 6.12 Comparison of measured [46] and computed H_2 mass fraction. The legend is as in Fig. 6.4.

The under-predictions seen here for the strained flamelets model are because of under prediction of reaction rate observed in Figs. 6.6 and 6.7. When the flame front is stretched its reaction rate is expected to drop and the stretching is caused by straining, bending (curvature) and contortion of the flame front by the turbulent eddies. The majority of these energy containing eddies are captured in typical LES as that reported here and thus their influence on the filtered flame is included inherently through $\widetilde{c}$, $\sigma^2_{c,\text{sgs}}$ and enthalpy transport equations and their interaction with the resolved flow fields. So, including stretching effects through strained flamelets overestimates the influences of stretch. However, the stretching caused by

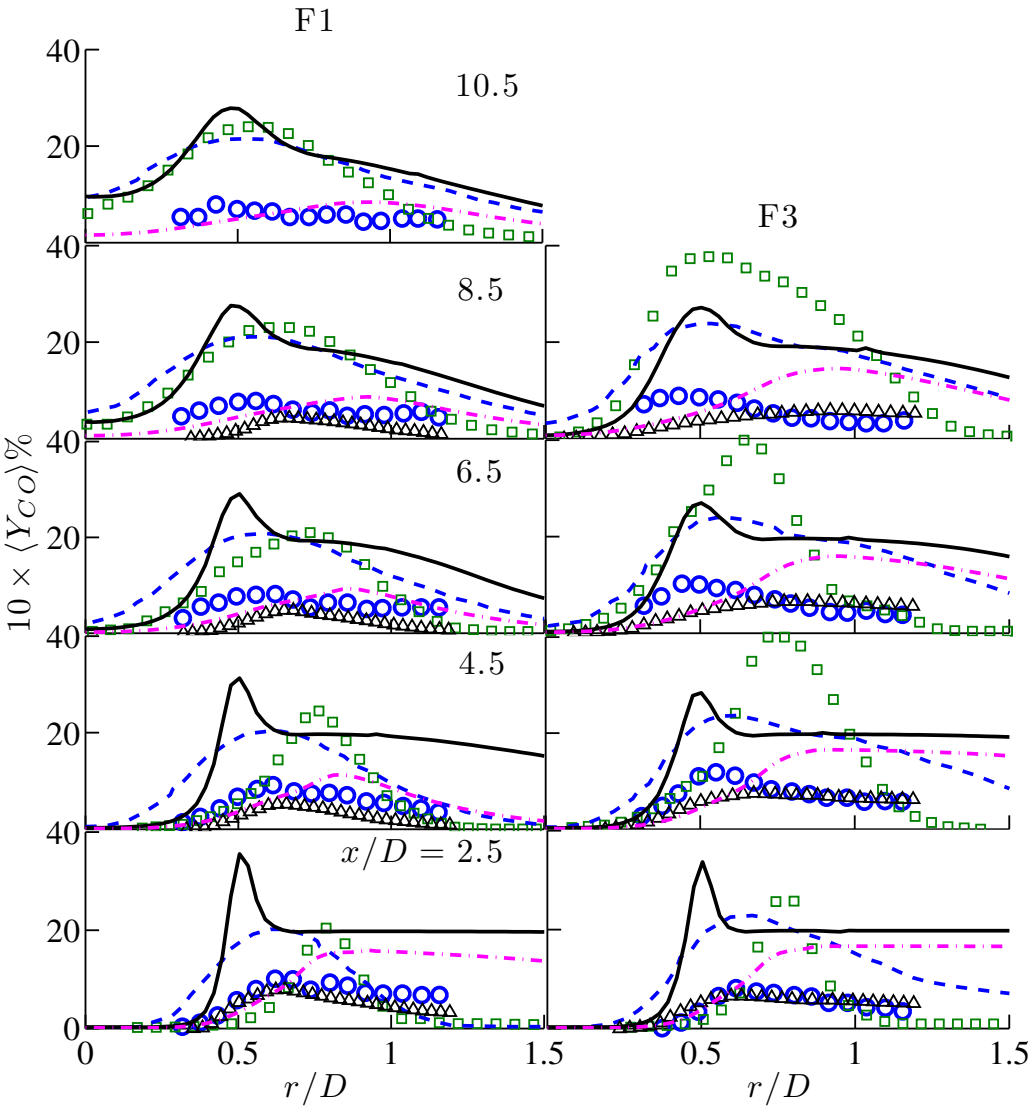

Fig. 6.13 Comparison of measured [46] and computed H_2 mass fraction. The legend is as in Fig. 6.4.

the unresolved SGS turbulent motions may not be small if the SGS kinetic energy is large. The numerical grid used here suggests that this kinetic energy is small and the comparison shown in Fig. 6.3 is good specifically for the flame F1 computed using the unstrained flamelet model. Thus, including the flame stretching effects of SGS turbulence through strained flamelets over estimates the stretching effects leading to a substantial reduction in the burning rate, which is reflected in all the scalar profiles investigated in this study. Thus, one may not need to explicitly account for flame stretching by SGS turbulence in a typical LES, which is expected to have small kinetic energy in sub-grid scales.

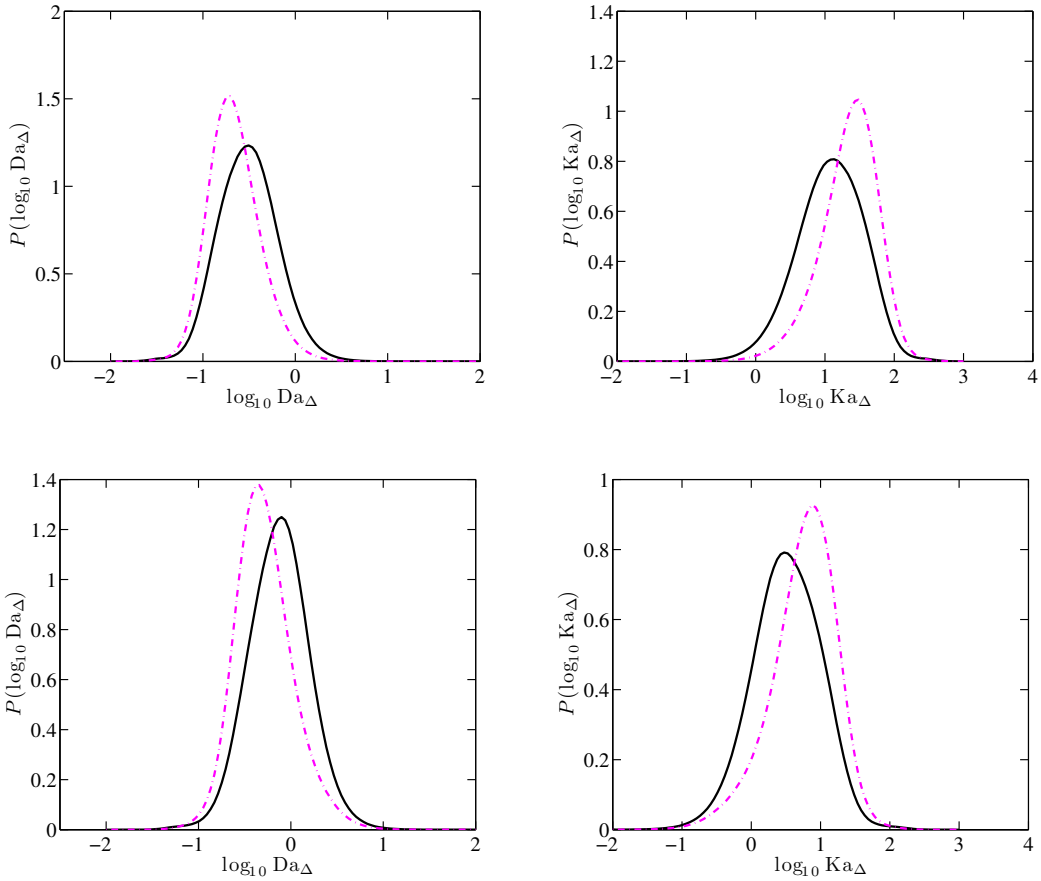

Fig. 6.14 PDFs of Da_Δ and Ka_Δ from flames F1 (top row) and F3 (bottom row). The results are shown for unstrained (——) and strained (– · –) flamelets.

It is also important to note that the SGS variance of the progress variable is computed using its transport equation rather than through a commonly used model, $\sigma^2_{c,\mathrm{sgs}} \simeq \mathscr{A}\Delta^2(\nabla\widetilde{c}\cdot\nabla\widetilde{c})$ to include correct and meaningful interactions among turbulence, scalar mixing and reactive fields, as discussed in §3.3.2. If one uses this algebraic model then $\overline{\dot{\omega}}$ is overestimated severely for unstrained flamelets (see Fig. 6.1), leading to a conclusion that one would need strained flamelets as noted in the beginning of this section. Thus, care is required for LES to maintain the consistencies among various sub models.

6.5 Analysis of Da_Δ and Ka_Δ

Figure 6.14 suggests that the typical values of Da_Δ range from about 0.1 to 1.8 in the F1 flame and 0.16 to 5 in the F3 flame. These ranges are not strongly influenced by the stretching effects included in the strained flamelets model, except that the most probable value is reduced slightly.

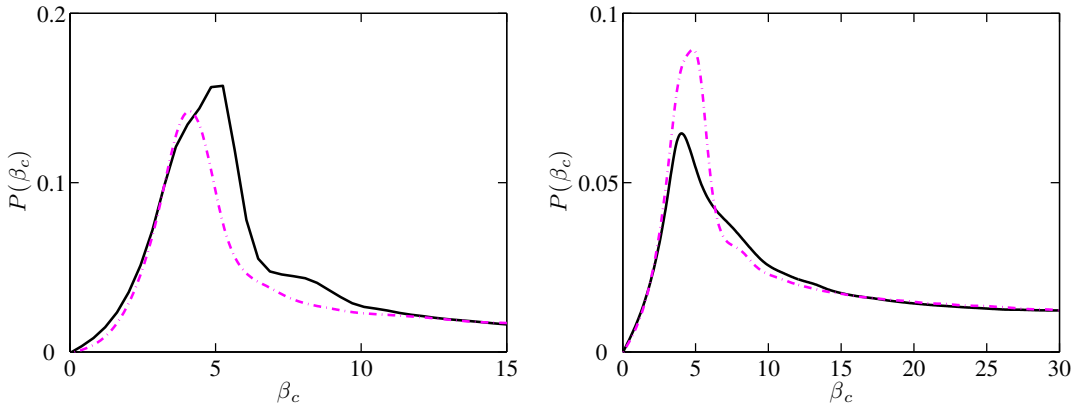

Fig. 6.15 The PDF of β_c from flame (a) F1 and (b) F3 obtained using unstrained (——) and strained (–·–) flamelets with 1.5M grid.

The relative behaviour between the unstrained and strained flamelet models does not seem to vary between F1 and F3 flames, which is consistent with the flame statistics discussed earlier. The variation of Ka_Δ PDF is similar and consistent with the PDF of Da_Δ. These two PDFs are more or less symmetric about the most probable value suggesting that they may be lognormal. However, Ka_Δ PDF shows a slightly longer negative tail because of the non-liner dependence on the small scale quantities.

The scale-dependent β_c in Eq. (2.22) is an important parameter in the SGS combustion modelling approach used in this study. This parameter is obtained dynamically using the scale-similarity methodology as discussed in section 3.3.4 and it varies spatio-temporally. The PDF of β_c obtained by post-processing the LES data is shown in Fig. 6.15 for both F1 and F3 flames. These PDFs are constructed using β_c values collected from the entire computational domain by imposing the limits $0.05 \leq \widetilde{c} \leq 0.95$ and $\overline{\dot{\omega}} > 0.05\langle\overline{\dot{\omega}}\rangle_{\max}$ to avoid regions with very low reaction rates so that the values of β_c used for this PDF are physically meaningful, which was verified in §5.4.2 and in [129] in conjunction with the algebraic closure of §3.3.1. The PDFs shown here for the unstrained and strained flamelets are similar to that in Fig. 5.32, except for a lower limit used in that study. The lower limit was set to satisfy a realisability condition of $\widetilde{N}_c \geq 0$, which was obtained by analysing the transport equation for the mean scalar dissipation rate [39]. For the reaction rate closures used in this study, the realisability condition for the filtered dissipation rate, $\widetilde{N}_c \geq 0$, is met if $C_3 \geq \tau C_4 Da_\Delta$, see Eq. (2.22), which is satisfied automatically by the functional forms of C_3 and C_4 described in §3.3.1.

The PDF of β_c is shown for both unstrained and strained flamelets for the 1.5M grid simulations. These results for the 4.2M grid are very similar to those shown here. There are no difference between the unstrained and strained flamelets and thus the flame stretching effects

introduced through the strained flamelets does not seem to influence the physical processes described by the β_c parameter.

6.6 Comparison of static and dynamic β_c

The static formulation for the combustion parameter β_c is also employed to have a direct comparison with the dynamic formulation in the context of unstrained flamelets. The differences in case of the strained flamelets closure are smaller than for the unstrained one and thus are not shown here. A value $\beta_c = 7.5$ is chosen based on the analysis of §5.3, which is also meaningful in light of the PDFs shown in Fig. (6.15). Mean profiles of fuel mass fraction obtained using static and dynamic formulation for β_c are compared to experimental data [46] in Fig. 6.16. The mean fuel mass fraction profiles obtained using static β_c compare to experimental data better than for the dynamic formulation at $x/D = 2.5$ and 4.5. This is because the separation of scales needed for the scale-similarity assumption in the dynamic computation of β_c is not completely fulfilled in the quasi-laminar region close to the jet exit, resulting in an under-prediction of β_c for this region. A similar relative behaviour was observed in §5.4.1 (Fig. 5.24) when comparing static and dynamic formulation of β_c for the algebraic closure. It is worth noting that the static value of β_c is chosen empirically and is optimal for the flame configuration. The differences in results between static and dynamic β_c formulation become smaller when one moves downstream, where the turbulence level is sufficiently large. In case of flame F1, results obtained using the dynamic formulation for β_c look better than those obtained with the static formulation at downstream locations, where the effect of air entrainment is high, and for $r < 0.5D$. This suggests that the dynamic parameter may absorb effect of air entrainment. This is also indicated by the fact that similar improvements are not seen in case of flame F3, where the air entrainment is much lower than for F1.

6.7 Summary

The analysis presented in this chapter shows that there is substantial difference between the results obtained using the unstrained and strained flamelets closures. The stretching of SGS turbulence is parameterised using the SGS dissipation rate in the strained flamelets closure used in this study. Since the numerical grids employed for the simulations resolve most of the turbulent kinetic energy the SGS kinetic energy is expected to be small implying that the SGS eddies may be weak to impart any stretching effects on the flame front. This is similar to the views expressed by Poinsot *et al.* [189] and Roberts *et al.* [202] while investigating turbulent combustion regimes. Thus, using the SGS dissipation rate or any parameter of

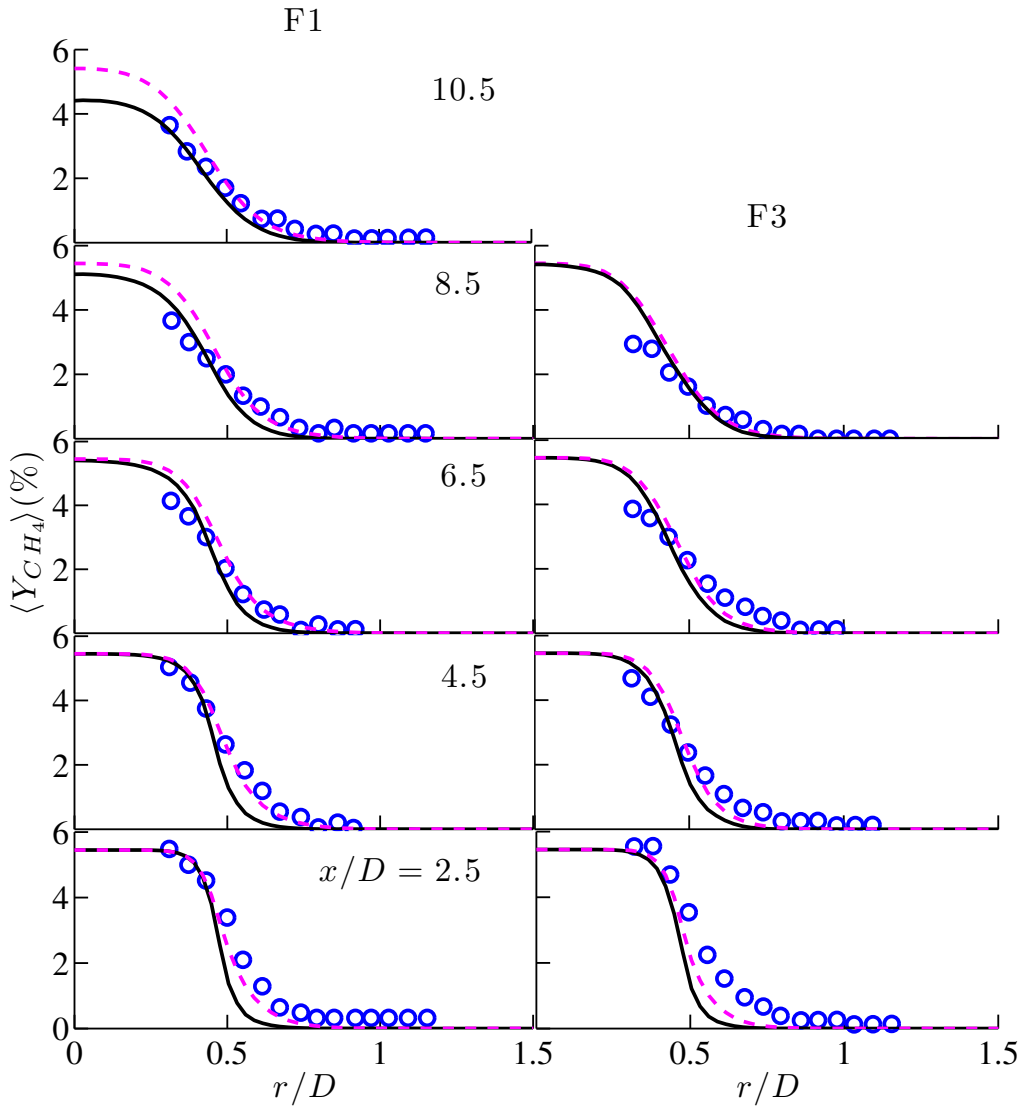

Fig. 6.16 Comparison of measured [46] (∘ ∘ ∘) and computed mean fuel mass fraction. The computational results are shown for the 1.5M grid using unstrained flamelet model with dynamic (——) and static (– –) formulation for β_c.

strained flamelets established in counterflow geometries to include the affects of SGS stretching is likely to overcompensate the SGS stretch effects compared to the influences of resolved dynamic eddies on the unstrained flamelet. Hence, the burning rate is underestimated by the strained flamelets leading to over prediction of fuel mass fraction and under-estimates of various reactive scalar mass fractions as observed in this study. The influences of resolved dynamic scales are inherently included in the unstrained flamelet closure through the various

transport equations and their interactions. The SGS variance equation plays an important role in this aspect and using an algebraic closure for $\sigma^2_{\widetilde{c},\mathrm{sgs}}$ is inadequate, which is demonstrated using order of magnitude analysis of the SGS variance equation in §3.3.2. The commonly used model, $\sigma^2_{\widetilde{c},\mathrm{sgs}} \simeq \mathscr{A}\Delta^2(\nabla\widetilde{c}\cdot\nabla\widetilde{c})$, severely underestimates the SGS variance because it excludes the combustion effects. This underestimated variance will give large reaction rate for the unstrained flamelet closure (see Fig. 6.1) implying a need for the strained flamelets, as observed for example in [116]. The results presented in this chapter suggests that the unstrained flamelet model is preferred at least for the combustion conditions investigated in this study and one must pay close attention to the modelling of SGS variance to retain the subtleties of premixed combustion physics consistently across the various SGS closures for LES of premixed combustion when flamelets closure, in general, is used with presumed PDF. Applying this modelling framework to other flame configurations such as bluff-body stabilised flames is of interest and will be explored in the next chapter.

The effect of finite rate chemistry is also of interest and it can be observed if one compares the results obtained in this chapter using unstrained flamelets closure with those for algebraic closure in previous chapter. From this comparison, it seems that a significant difference is seen only for minor species mass fractions for the piloted flame configuration analysed here. It would be ideal to evaluate this relative model performance on a different flame spanning a range of combustion regimes. For this reason the unstrained flamelet closures is also compared to the algebraic closure in the bluff body stabilised configuration which is described in the next chapter.

Chapter 7

Bluff body stabilised flame

The bluff-body stabilised flame configuration studied experimentally [168, 169, 176–178] is presented in this chapter. Bluff-body configurations are commonly used in engines and many combustion devices to provide flame anchoring mechanism. The recirculation zone behind the bluff-body provides this mechanism by increasing the residence time of the burned gas aiding combustion to sustain itself [191]. Despite a simple geometry, the physical processes involved here are complex encompassing strong interplay among turbulence, combustion and heat transfer. The performance of these type of burners, in general, is influenced by size and shape of and turbulence in the recirculation zone, which in turn is affected by a number of factors such as inlet turbulence, equivalence ratio and geometry. Thus, this configuration is ideal to further explore capabilities of flamelet based modelling.

Results obtained using the algebraic model and the unstrained flamelets model described in §3.3.1 and 3.3.2 are compared to experimental data to assess the relative performance of these two reaction rate closures and the sensitivity to a number of parameters, such as inlet turbulence, grid size and flamelet used, is studied. The SGS velocity, u'_Δ, needed for the SGS scalar dissipation rate in Eq. (2.22) is modelled using Eq. (3.51) as this model gave good results in the analysis of §5.3. The parameter β_c is computed dynamically using Eq. (3.58), as this procedure was observed to provide accurate results when turbulence level is relatively high, as seen in §5.4 and Chapter 6.

Particular emphasis is given to the investigation of sub-grid fluctuations, which are observed to play a key role in the model performances when turbulence intensity is high. This is addressed by comparing results obtained using two different conditions of turbulent intensity (TI) with related experimental measurements.

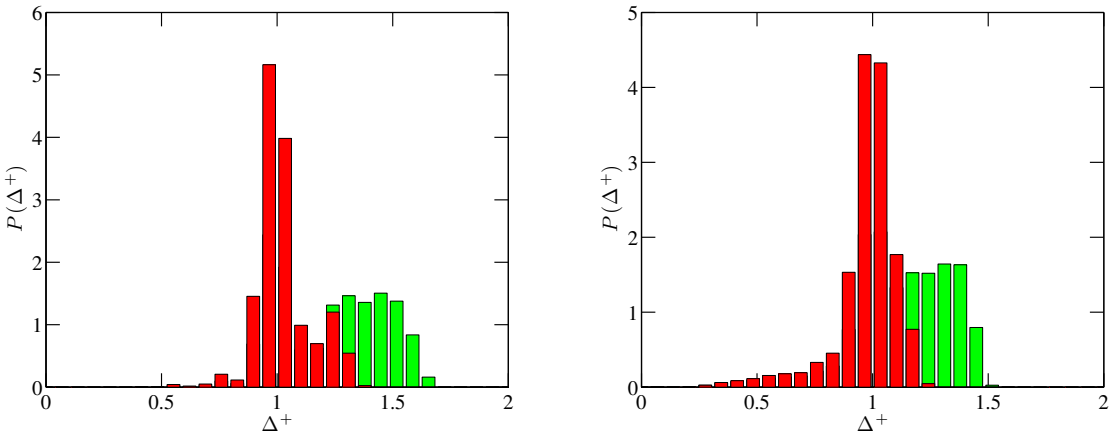

Fig. 7.1 Histograms of $\Delta^+ = \Delta/\delta_{th}$ for (a) 1.8M and (b) 2.2M grids are shown for the combustor region $0 \leq x/D \leq 6$ and a fraction of it for $r/D < 0.5$.

7.1 Experimental case

The experimental burner uses a methane-air mixture at $\phi = 0.586$. The burner configuration, its geometrical details and boundary conditions are as specified in §4.3 and Table 4.5. A sketch of geometry and boundary conditions is shown in Fig. 4.10. The domain is discretised using two meshes of 1.8M and 2.2M cells each and the difference in size between the two meshes is due to wall refinement on the bluff body surfaces for 2.2M grid. A sketch of these two grids close to the bluff body is shown in Fig. 4.11. Turbulence conditions at the inlet of the computational domain are specified using the digital filter technique [112] and the two fluctuations levels $u'/U_{\text{ref}} = 2\%$ and 24%, as for the cold flow. The integral length scales in the three directions have been assigned according to the size of the holes (3.46 mm) of the turbulence generator device. The progress variable is defined as $c = 1 - Y_{\text{CH4}}/Y^u_{\text{CH4}}$, where $Y^u_{\text{CH}_4}$ is the methane mass fraction in the reactant mixture, and is assigned to be 0 at the inlet of the computational domain. Other choices have also been explored and will be discussed in §7.5.1.

Since the algebraic closure of §3.3.1 requires filter sizes larger than the laminar flame thickness as observed in §5.3 and §5.4, an *a priori* assessment is done for the two grids. Histograms of the normalised filter size are shown in Fig. 7.1 for both grids, and the filter size is defined as $\Delta = \mathscr{V}_i^{1/3}$, where $\mathscr{V}_i$ is the volume of the cell. These histograms are shown both for the entire combustor and for a smaller region, $0 \leq r/D \leq 0.5$, to illustrate the effect of the cell size increase in the radial direction. Both grids have a peak at $\Delta^+ \approx 1$. This value is acceptable to fulfil the modelling requirements of both algebraic and unstrained flamelets models [61, 129]. Nevertheless, because of wall refinement, local values can go below 1 for the 2.2M grid, and

this restricts the use of the algebraic reaction rate closure requiring $\Delta^+ > 1$ [61]. These grids are relatively small compared to what is commonly used for LES of combusting flows if one considers that about $720k$ cells are used for the region downstream the combustor, but they are adequate to yield accurate results for the modelling framework used in this study. This was already demonstrated for a piloted jet flame configuration in §5.3 and §5.4, and will be reconfirmed in this study for a bluff-body flame.

The full list of simulations done on this configurations is shown in Table A.4. and the most relevant for this study are discussed here. All these simulations have been run for a total of 10 flow-through times as specified for the cold flow, corresponding to about 24h on a wall clock. The CFL number is kept below 0.3 everywhere in the flow using a constant time step of $10\,\mu$s and $7.5\mu s$ respectively for the 1.8M and 2.2M grids.

7.2 Flame and recirculation region

The reacting flow field was divided in three regions in [178]: (i) a first region (R1) between the flame holder and $x/L_r = 0.12$, where the flame is thin and combustion time scale is much smaller than the turbulence time scale. The assumption of flamelets holds in this region; (ii) the recirculation region (R2), $0.12 < x/L_r < 1$, where coherent structures start to grow, thickening the flame. The regime was stated to be in the thin reaction zones of the premixed regime diagram; (iii) a region (R3) further downstream of the rear stagnation point, where the flame is thick and turbulent structures strongly influence the flame. The flame condition in this region was suggested to be in the distributed reaction zones regime.

Experimental results are provided for regions (i) and (ii) for both cases with 2% and 24% TI, and the results for region (iii) are available only for the case with 24% TI. These results are compared with the LES statistics.

7.2.1 2% approach turbulence

LDA and CARS techniques were respectively used by Pan *et al.* [176, 178] to measure the fluid velocity and temperature respectively. These techniques were reported to have 1% and $\pm$30 K uncertainty respectively. The fast chemistry assumption is valid close to the bluff-body base where the flame is anchored. In this region, the flame was observed to be thin in the experiments [178]. The flame brush becomes thick as one moves downstream and it has become almost 12 times thicker at an axial location close to the rear stagnation point of the recirculation zone [178]. A similar behaviour is observed in the computational results also as shown in

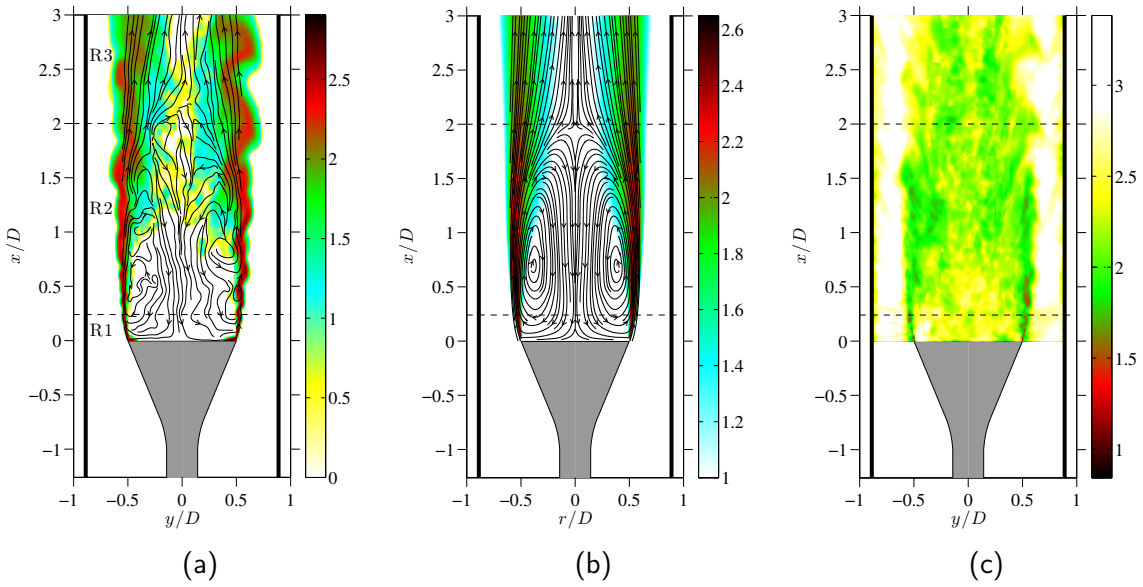

Fig. 7.2 Stream lines of (a) filtered and (b) averaged velocity fields along with contours of (filtered and averaged) $\log_{10}(1000\,\overline{\dot{\omega}}^{+})$, where $\overline{\dot{\omega}}^{+} = \overline{\dot{\omega}}\delta_{th}/(\rho_u s_L)$. The results are on the mid-plane for unstrained flamelets model and 2% TI. The contour of $\log_{10}(1000\,\mathrm{Da}_\Delta)$ is shown in (c). The three regime regions, R1, R2 and R3, are separated in the figures using dashed lines.

Fig. 7.2. The variations of filtered and averaged reaction rates are shown as colour maps in Fig. 7.2 for the mid-plane obtained from the simulation employing unstrained flamelet model. Figure 7.2a shows the filtered reaction rate along with the streamlines. The variation of averaged reaction rate and the streamlines of averaged velocity are shown in Fig. 7.2b. The variation of SGS Damköhler number, Da_Δ, in the corresponding plane is shown in Fig. 7.2c. The filtered reaction zone is very thin close to the bluff body but its width increases quickly as one moves downstream. The length of the recirculation zone is about $2D$ as seen in Fig. 7.2b and the averaged reaction zone thickness grows in the downstream direction. Also, one observes that the averaged reaction zone is already very thick at the end of the recirculation zone and thus the reaction zone structure is likely to be significantly influenced by turbulence from this location onwards and effects of finite rate chemistry become non-negligible. In particular, the algebraic model relies on the high Damköhler number assumption which is expected not to hold well in this region. Some insight can be gleaned by studying the SGS Damköhler number variation shown in Fig. 7.2c. The relatively low values of Da_Δ near the edges of bluff-body are due to intermittency in the axial velocity fluctuation and the flame in this region is expected to be quasi-laminar. The values of $\mathrm{Da}_\Delta \sim 0.01$ are because of spatio-temporal intermittency effects and a value of order unity is not observed in regions of flame suggesting that the SGS fluid dynamic time scale is typically shorter than the chemical time scale, δ_{th}/s_L. This suggests that

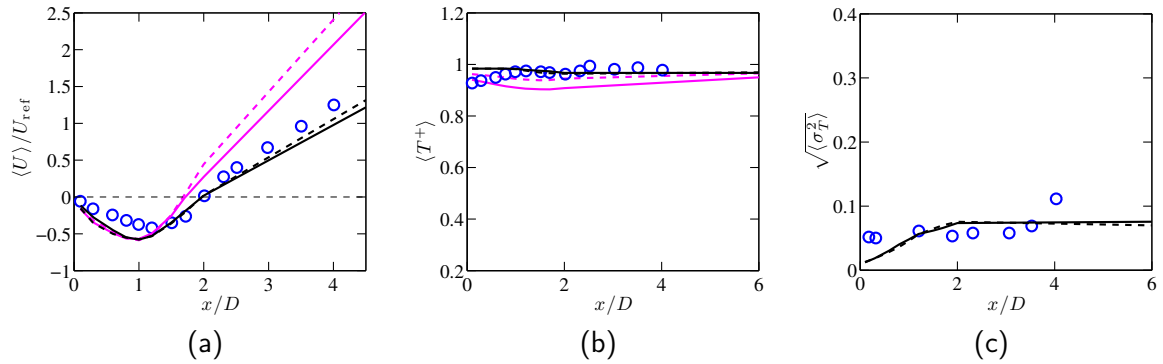

Fig. 7.3 Centreline variation of (a) $\langle U\rangle/U_{\rm ref}$, (b) $\langle T^+\rangle$, and (c) $\sqrt{\sigma_T^2}$ for 2% TI. The results with algebraic model on 1.8M (– –) and 2.2M (——) grids and with unstrained flamelets model on 1.8M (– –) and 2.2M (——) grids are compared with experimental data [176, 178] (symbols).

the finite rate chemistry effects are important in these flames. This observation must be kept in mind while comparing LES statistics obtained using the algebraic and unstrained flamelet closures with the measurements.

First and second order statistics from LES are compared next to experimental results. Both 1.8M and 2.2M grids are used for both algebraic and unstrained flamelets closures for further assessment of grid sensitivity. Wall functions with WALE model [172] are used in case of 1.8M grid. Figure 7.3a compares the averaged axial velocity, $\langle U\rangle$, obtained from LES, with measurements. This velocity is normalised using $U_{\rm ref}$ and its variation along the centreline is shown in this figure. The experimental data are taken from [176]. The algebraic and unstrained flamelets models yield similar statistics for $x/D \leq 1.1$ and the underestimate of $\langle U\rangle$ by these two models for $x < D$ is due to adiabatic wall used in the simulation. This wall treatment avoids heat losses and thus the flow accelerates more in the computation. As one moves in the downstream direction, the results of these two models differ significantly. The length of the recirculation zone, which is critical for the overall dynamics of the flow, is well estimated by the unstrained flamelets model compared to the algebraic model. It was suggested in the experimental study [176] that the flame at locations downstream of the rear stagnation point ($x \sim 2D$) is thickened and combustion is of distributed reactions regime type. Pan *et al.* [178] argued that the flame thickness near the rear stagnation point axial location is about 12 times its size near the flame holder, as noted earlier. This flame is about 5 times ticker than δ_{th} and might pose a challenge to the flamelets approach. Significant overestimates are observed in Fig. 7.3a for the algebraic model in this region independently of the grid used. However, the unstrained flamelets model captures the experimental observation suggesting that this model is sufficiently accurate for this combustion.

A typical comparison for the centreline variation of normalised mean temperature, $\langle T^+ \rangle = (\langle T \rangle - T_0)/(T_{ad} - T_0)$, computed here and measured values is shown in Fig. 7.3b. This temperature is underestimated by the algebraic model whereas the unstrained flamelets model estimates are very good apart for some overestimates nearer to the bluff-body due to adiabatic condition used for the simulations as noted earlier. The better behavior for 1.8M grid in case of algebraic model in Figs. 7.3a and 7.3b is due to the fact that the condition $\Delta^+ > 1$ [61] is not met close to the bluff body for 2.2M grid and this affects significantly the reaction rates as already noted in §5.3 and §5.4. The difference in these statistics obtained for the unstrained model using these two grids is very small implying that this model is more robust and accurate than the algebraic model. The centreline variation of rms (root-mean-square) of normalised temperature is shown in Fig. 7.3c. The rms value is estimated here using

$$\langle \sigma_T^2 \rangle = \langle \widetilde{T}^{+2} - \langle \widetilde{T}^+ \rangle^2 \rangle + \langle \sigma_{T,\mathrm{sgs}}^2 \rangle = \langle \sigma_{T,\mathrm{res}}^2 \rangle + \langle \sigma_{T,\mathrm{sgs}}^2 \rangle \tag{7.1}$$

where $\sigma_{T,\mathrm{sgs}}^2$ indicates the SGS contribution of the normalised temperature, which is approximated as $\langle \sigma_{T,\mathrm{sgs}}^2 \rangle \approx \langle \sigma_{c,\mathrm{sgs}}^2 \rangle$ because the Lewis number is close to unity for this flame and a temperature based progress variable would have the same boundary conditions as $\widetilde{c}$ in the LES domain. The above result is shown only for the unstrained flamelets model since $\sigma_{c,\mathrm{sgs}}^2$ is unavailable for the algebraic model. Higher mean temperature was seen to correspond to lower rms and *vice-versa* in the experiments [178] and this behaviour is captured by the unstrained flamelets model. The underestimate of $\sqrt{\langle \sigma_T^2 \rangle}$ for $x < D$ is related to the overestimate of mean temperature in this region resulting from adiabatic conditions used. Overall, the rms temperature variation along the centreline is captured reasonably well and this result shows negligible sensitivity to the numerical grid.

Further insight can be gained by studying radial variation of normalised mean and rms temperature shown in Fig. 7.4 for three axial locations. The latter is shown only for the unstrained flamelets model for the reasons noted earlier. The results are shown for both 1.8M and 2.2M grids. The algebraic model estimates the mean temperature variation well for $x = 0.1D$ and $0.8D$, where high Damköhler number combustion is expected to hold. Since this model works well for $\Delta^+ > 1$, the statistics obtained using 1.8M grid are closer to the measured values for these two locations. The statistically significant value of Δ^+ does not go below about 1.0 in the domain for the 1.8M grid, while it can become less than 0.8 and indeed below 0.5 in regions close to the bluff body when the 2.2M grid, involving wall refinement, is used. A severe underestimate is observed for $x = 2D$ as shown in Fig. 7.4. The radial variation of mean temperature obtained using the unstrained flamelet model compares well with the measured values for the downstream location and an overestimate of about 10% observed for $x = 0.1D$ and $0.8D$ for $0 \leq r \leq 0.5D$ is probably because of the adiabatic wall used for the bluff-body

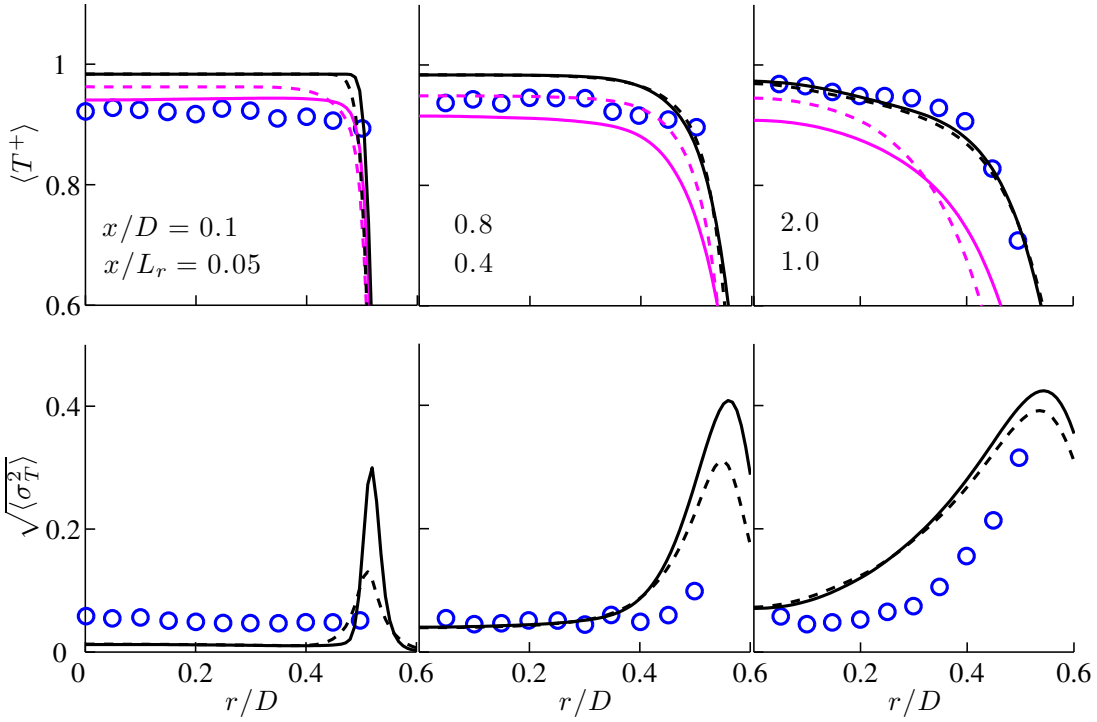

Fig. 7.4 Radial variation of $\langle T^+ \rangle$ and $\sqrt{\sigma_T^2}$ for 2% TI case with algebraic model using 1.8M (– –) and 2.2M (——) grids and with unstrained flamelets model using 1.8M (– –) and 2.2M (——) grids are compared with experimental data [176, 178] (symbols).

base. It is to be noted that the bluff-body base ends at $r \approx 0.5D$ as seen in Fig. 7.2. Although the local values of Da_Δ is low, the unstrained flamelet model is shown to work well for $x = 2D$ as it can handle finite rate chemistry effects. Also a reasonable estimate of the progress variable variance plays a role and an accurate and robust modelling of SGS dissipation rate is important for this. The comparison of radial variation of normalised temperature rms shown in Fig. 7.4 is reasonable and satisfactory although there is some room to improve this. Possible avenues to improve the rms values are yet to be explored.

7.2.2 24% approach turbulence

Increasing the level of turbulence entering the combustion chamber changes the flow dynamics and thus the combustion behaviour significantly. The experimental data [176, 178] show that the size of the recirculation region decreases from $L_r \simeq 2D$ to $1.3D$ when the incoming turbulence intensity is increased from 2% to 17%. Increasing this turbulence level further by 5%, gives

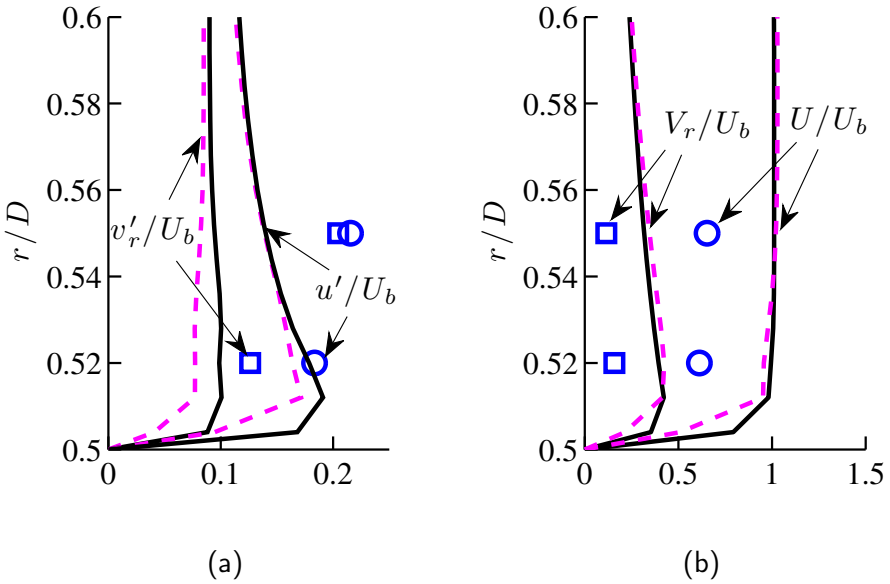

Fig. 7.5 Radial profiles of (a) rms and (b) mean velocities, obtained using the algebraic model on 1.8M grid (– –) and unstrained flamelet model on 2.2M grid (——), are compared with experimental data (symbols) for 24% TI at $x/D = 0$.

$L_r \simeq 1.1D$, i.e. the recirculation zone length decreases by about 15%. In a recent LES [9] of this flame, the turbulence at the inlet was underestimated leading to larger recirculation length. The sensitivity of L_r to incoming turbulence level and the lack of a full characterisation of this turbulence in the experiment poses additional challenges for CFD simulations. An attempt is made in this work to simulate the case with 24% approach turbulence intensity since a good set of scalar measurements were reported for this flame in [168, 169, 176, 178]. The turbulence levels reported in the experimental work by measuring the rms velocity in the axial direction at the flame holder station are 18% and 22% of TI for $r/D = 0.52$ and $r/D = 0.55$ respectively. This TI is defined in reference to the velocity, U_{ref}. Mean and rms values of radial and axial velocities from LES are compared with the experimental data in Fig. 7.5. The 24% nominal T.I. has been varied by a small amount ($\approx 3\%$) until the condition at the burner entrance for the cold flow is matched with the experimental measurements, yielding the results in Fig. 4.12b. This condition is then maintained for the reacting flow simulation, which produces a mean level of turbulence intensity of 19% (for the region $0.5 \leq r/D \leq 0.7$) but turbulence is higher closer to the bluff-body edge before vanishing very quickly on the wall, as seen in Fig. 7.5. This mean value is about 2% smaller than that obtained for the cold flow, which is probably because of the heat release effects. About 2% and 10% difference exists between the algebraic and unstrained flamelet models, respectively for the axial velocity, u', and the radial velocity,

v'_r, rms values, as seen in Fig. 7.5a. The results of the algebraic model are obtained using 1.8M grid for the reason noted earlier. The differences observed for the combustion models are thus due to the differences in flow evolution along the bluff body wall for the two grids, with better estimates on the 2.2M grid. Mean velocities from the two models are very similar, but both models overestimate the experimental values, as seen in Fig. 7.5b. These results suggest that the computed boundary layer is somewhat thinner than in experiments. These differences at the burner entrance may have a non-negligible effect on the flow field. Improved comparisons would be possible if one uses non-homogeneous inlet turbulence, which is not easy to control in the digital filter framework [112] used for the simulations of this study. Instead, matching u' value at $x/D = 0.52$ was set as a target, since the turbulence level close to the bluff body is expected to have stronger influence on the flow field than in farer regions. The overall estimates of the flame and flow characteristics obtained using this approach is reasonable as one shall see next.

A. Reaction zones

In Fig. 7.6 typical instantaneous contours of $\overline{\dot{\omega}}^+$ obtained with algebraic and unstrained flamelets models, are shown on the mid-plane. The combustion is nearly complete in the recirculation zone, as was observed in experiments [169]. Also, the flame front is much more wrinkled and corrugated than for 2% TI case shown in Fig. 7.2a, because of the increased TI at the inlet. This alters the flow dynamics in downstream regions due to the interplay of turbulence, combustion, shear stresses and pressure gradients, resulting in an overall increase of turbulent kinetic energy and reduction of the length of the recirculation zone [176], as will be observed later. Another characteristic observed in Fig. 7.6 is that the flame predicted by the algebraic model is thicker than that predicted by the unstrained flamelet model. Moreover, the algebraic model suggests that high values of the reaction rate extend further downstream compared to the unstrained flamelet model. In both cases, the flame is anchored to the bluff-body. However, very large reaction rate, $\overline{\dot{\omega}}^+ > 1.3$, are in the flame anchoring region for the algebraic model, and the unstrained flamelet model predicts these regions to be slightly in the downstream location as observed in Fig. 7.6. The large scale wrinkling of the reaction zones is very different for these two models as shown by $\overline{\dot{\omega}}^+ = 0.1$ contours in Fig. 7.6. This will reflect in the averages of flame related quantities to be discussed in section 7.5.

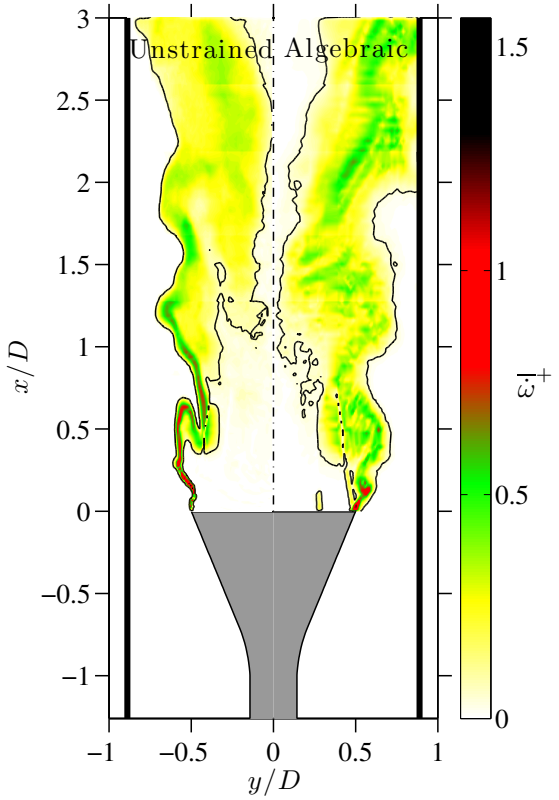

Fig. 7.6 Contours of filtered normalised reaction rate $\overline{\dot{\omega}}^{+} = \overline{\dot{\omega}}\delta_{th}/(\rho_u s_L)$ at an arbitrary chosen time. The results are on the mid-plane for unstrained flamelet and algebraic models with 24% TI. Isolines having $\overline{\dot{\omega}}^{+} = 0.1$ are also shown.

B. Axial variations

The centreline variations of normalised mean axial velocity and temperature are shown in Fig. 7.7 for the case with 24% turbulence intensity. The recirculation zone length is over-estimated by $\approx 12\%$ by both models because of its strong sensitivity to the inlet turbulence, noted in the earlier part of this section. Other attributes of this comparison are similar to those observed for the 2% case. The centreline variation of normalised mean temperature is almost constant throughout the combustor, and it is underestimated by both models as seen in Fig. 7.7b, This under-estimation was also observed in [9] and it was suggested that fluid dynamic strain might be responsible for this. Here, it is observed that the SGS variance of temperature has substantial influence on this underestimate. The normalised averaged temperature is computed using Eq. (3.18), as noted for the 2% TI case, where the SGS variance is approximated using the SGS variance of the progress variable in case of unstrained flamelets closure. Using this approximation an analysis of the influence of SGS variance on temperature can be performed

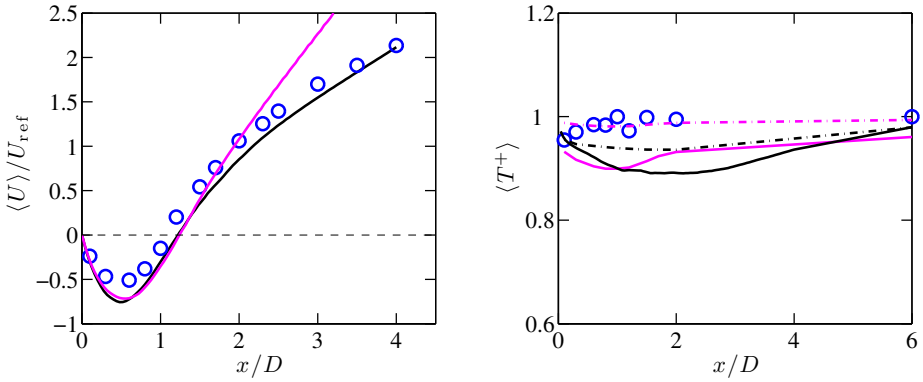

Fig. 7.7 Centreline variation of (a) $\langle U\rangle/U_{\rm ref}$ and (b) $\langle T^+\rangle$ obtained with algebraic model using 1.8M (——) grid, and with unstrained flamelet model using 2.2M (——) grid are compared to experimental data [176, 178] (symbols) for 24% TI case. The influence of $\langle\sigma^2_{T,\rm SGS}\rangle$ on $\langle\overline{T}^+\rangle$ is shown for the unstrained flamelet (– · –) and algebraic (– · –) models.

and results of this analysis are discussed first before discussing Fig. 7.7b. Figure 7.8 is a scatter plot of the Favre averaged progress variable, indicated as $\langle\widetilde{c}\rangle$, and the Reynolds averaged values, indicated as $\langle\overline{c}\rangle$. The Reynolds averaged value is obtained using Eq. (3.18). If the SGS variance is excluded while calculating $\langle\overline{c}\rangle$ then the difference between $\langle\widetilde{c}\rangle$ and $\langle\overline{c}\rangle$ is not large as seen in Fig. 7.8a. However, a significant difference is seen if one includes the SGS contribution in the analysis, and thus this contribution cannot be neglected for this flame.

Figure 7.9 shows a scatter plot of the total variance of progress variable obtained as a sum of resolved and SGS part, $\sigma_c^2 = \left(\langle\widetilde{c}^2\rangle - \langle\widetilde{c}\rangle^2\right) + \langle\sigma^2_{c,\rm sgs}\rangle$, and $\langle\widetilde{c}\rangle$. The total variance increases along the axial direction until $x/D \approx 3$ and then decreases. Nevertheless, the total variance is very high in the combusting region and close to the maximum possible value, $\langle\widetilde{c}\rangle(1-\langle\widetilde{c}\rangle)$. This suggests that the maximum possible variance may be used as a good approximation if the sub-grid variance is unavailable, as in the case of the algebraic model used here.

The mean temperature obtained including the SGS variance is shown as dash-dotted line in Fig. 7.7b for both models. A good improvement is seen for $x \leq 2D$ because the temperature variance was observed to be high in these regions in experiments [168, 169, 178] and a similar observation is also made, which will be discussed later while discussing Fig. 7.11. Thus, one cannot ignore the influence of variance, specifically the sub-grid scale variance, $\langle\sigma^2_{c,\rm sgs}\rangle$. This information is not available for the algebraic model used in this study and so the maximum variance, obtained as $\langle\widetilde{c}\rangle(1-\langle\widetilde{c}\rangle)$, is used to include the effect of SGS variance as suggested by the results in Fig. 7.9. If this correction is made to $\langle\overline{T}^+\rangle$ obtained from the algebraic model then a very good agreement with the experimental data is seen in Fig. 7.7b. Thus, the SGS variance plays an important role to obtain the measured mean temperatures.

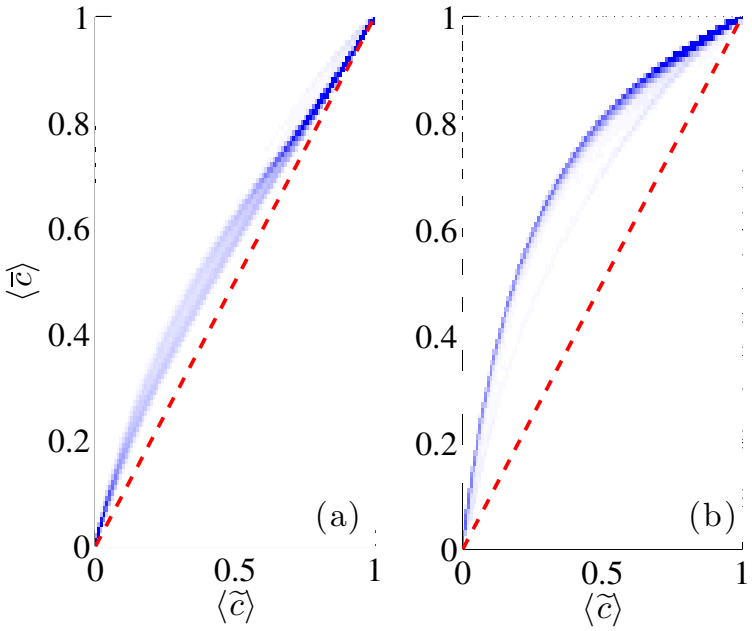

Fig. 7.8 Scatter plots of $\langle\widetilde{c}\rangle$ and $\langle\overline{c}\rangle$ for unstrained flamelet model with 24% TI. The Reynolds average is obtained using Eq. (3.18) (a) without and (b) with SGS variance, $\langle\sigma^2_{c,\mathrm{sgs}}\rangle$.

C. Statistics of velocity and temperature

The radial variations of $\langle U\rangle/U_{\mathrm{ref}}$ and $\langle V_r\rangle/U_{\mathrm{ref}}$, where V_r is the radial component of velocity, are shown in Fig. 7.10 for six axial locations inside the recirculation zone having a length of $L_r \approx 1.1D$ [176]. The velocity variations are captured well and there is some underestimate at the end of the recirculation zone, which is consistent with the centreline variation shown in Fig. 7.7.

The radial profiles of $\langle\overline{T}^+\rangle$ and $\sqrt{\langle\sigma^2_T\rangle}$ are shown in Fig. 7.11. Experimental results for $\sqrt{\langle\sigma^2_T\rangle}$ are unavailable for $x > 0.6D$ and thus they are not shown in Fig. 7.11. Temperature data reported for 24% approach turbulence level was obtained using Rayleigh technique and it was observed not to change very much with turbulence level for $x \leq 2D$ and $r \leq 0.3D$ [178]. A similar behaviour is observed in this study only if the SGS temperature variance, $\langle\sigma^2_{T,\mathrm{sgs}}\rangle$, is included in the analysis. This is shown as dash-dotted line in Fig. 7.11 for both the algebraic and the unstrained flamelet models. Similar values of mean temperature are observed for the two closures considered for this study. When the effect of SGS variance is taken into account,

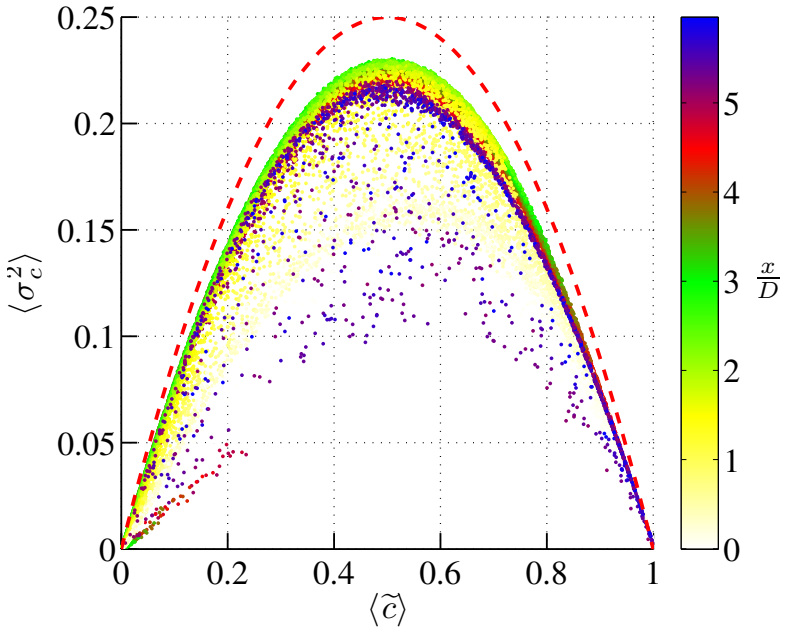

Fig. 7.9 Scatter plot of mean progress variable and total variance, $\langle \sigma_c^2 \rangle$ (sum of resolved and SGS parts), for unstrained flamelet model with 24% TI. Colours represent the axial locations, x/D, for the data. The maximum possible variance, $\langle \widetilde{c} \rangle (1 - \langle \widetilde{c} \rangle)$ is also shown (--).

clear improvements are seen as in Fig. 7.11, confirming that the SGS contribution cannot be neglected. Some overestimation is seen in $r/D > 0.5$ for the algebraic model, because the maximum variance is used. This can be observed in the radial variation of normalised temperature rms, shown in Fig. 7.11. The solid lines denote the resolved part and the dash-dotted lines include the SGS part as noted in Eq. (7.1). The maximum possible variance used for the algebraic model does not vanish at $r/D = 0$ because $\langle \widetilde{T}^+ \rangle$ predicted by the algebraic model at this position is slightly smaller than unity. The rms values computed from the unstrained flamelet model are reasonable for $x = 0.1D$ and some overestimates are seen for $x = 0.3D$ and $x = 0.6D$ in the region $0.2D \leq r \leq 0.5D$. In the shear region, $0.4 \leq r/D \leq 0.6$, the temperature rms values are underestimated substantially when the contribution from the SGS part is ignored. Overall, the various comparisons shown in this figure are acceptable.

7.3 Post-flame region

At the end of the recirculation zone the combustion is nearly complete [169] and for this reason the region downstream of the recirculation zone is referred as 'post-flame' region. The flame

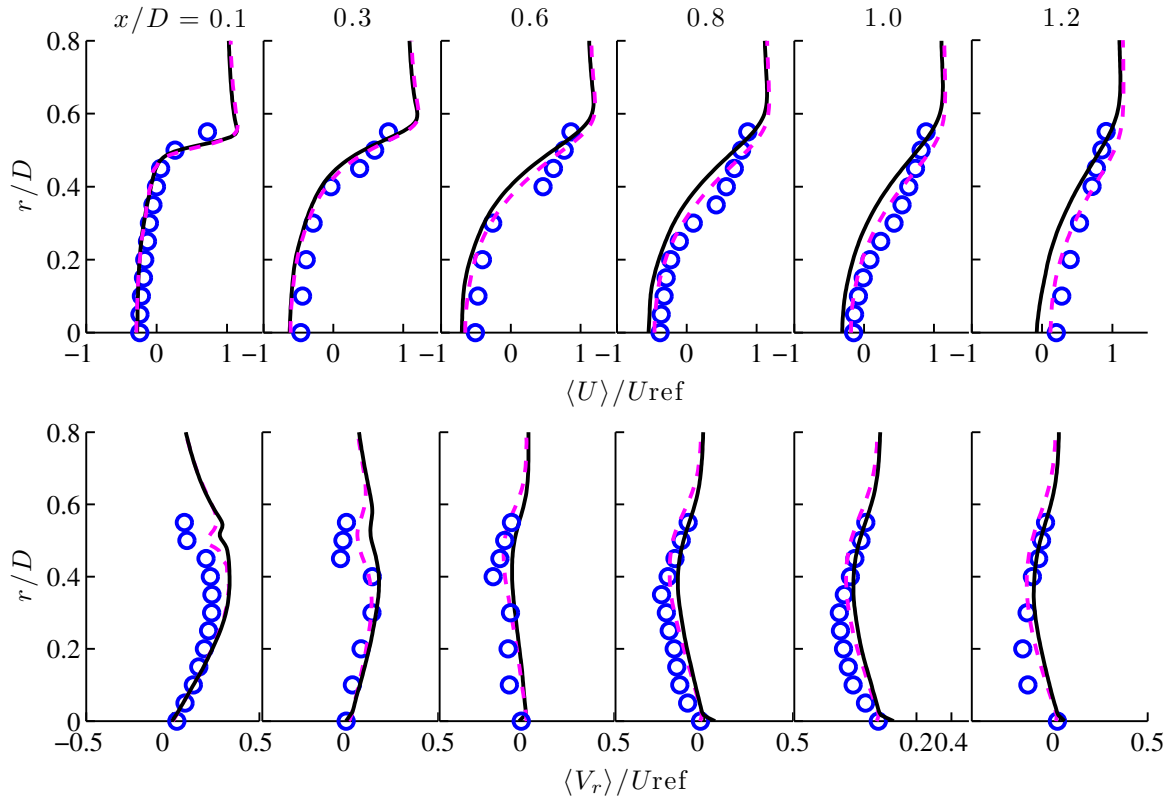

Fig. 7.10 Radial variation of $\langle U \rangle / U_{\text{ref}}$ and $\langle V_r \rangle / U_{\text{ref}}$, obtained with algebraic model using 1.8M (– –) grid and with unstrained flamelets model using 2.2M (——) grid are compared with measurements [176, 178] (symbols) for 24% TI within the recirculation region.

front in this region the flame front has been thickened by turbulent eddies and the combustion condition lies in the distributed reaction zones of the premixed regime diagram [176, 178]. LES results of mean radial profiles of velocities are compared with experimental data in Fig. 7.12, which are available up to $x = 2D$ for these quantities [176]. Some underestimation is seen for the axial velocity obtained from the unstrained flamelet model and it is related to a small overestimation of the recirculation zone length (see Fig. 7.7a). The algebraic model is observed to overestimate this velocity and this overestimate is expected to increase further in downstream regions, as suggested by the centreline variation in Fig. 7.7a. However, the computed radial velocity are observed to agree very well with measured values for both models.

The computed radial profiles of $\langle \overline{T}^{+} \rangle$ and $\sqrt{\langle \sigma_T^2 \rangle}$ are compared with experimental results [168, 169] in Fig. 7.13. Experimental data for $\sqrt{\langle \sigma_T^2 \rangle}$ are available only for $x = 6D$ location. A close agreement with the experimental data when the SGS variance is included in the analysis suggests the importance of this variance, specifically for locations $x = 1.5D$ and $2D$. This is because the level of fluctuation increases until $x \approx 3D$ and then decreases, as discussed

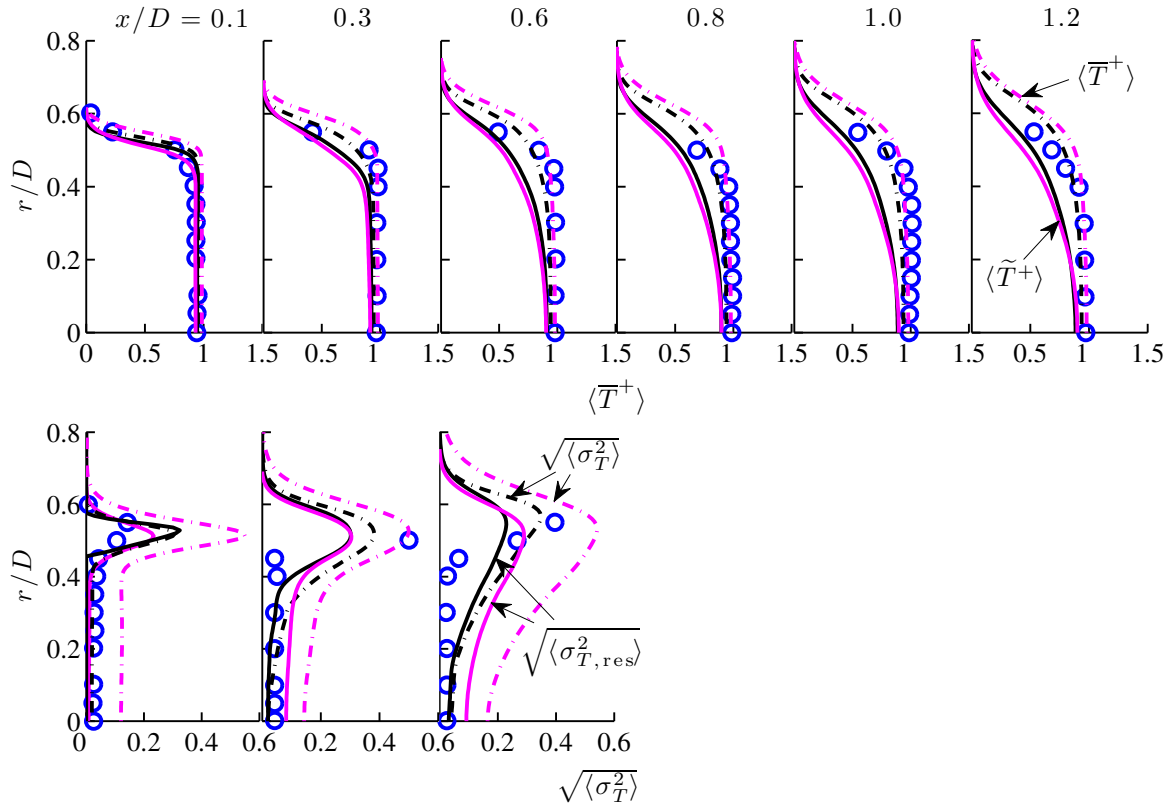

Fig. 7.11 Radial variation of normalised averaged temperature and its rms, obtained using the algebraic model with 1.8M (——) grid and unstrained flamelet model with 2.2M (——) grid are compared with measurements [168, 169, 176, 178] (symbols) for 24% TI case within the recirculation region. The influence of $\langle \sigma^2_{T,\mathrm{sgs}} \rangle$ on $\langle \overline{T}^+ \rangle$ is shown for the unstrained flamelet (– · –) and algebraic (– · –) models.

in Fig. 7.9. The predictions from both models are very good despite the distributed reaction zones regime combustion suggested in the experimental study [168, 169]. The total variance calculated using the unstrained flamelet model is good for $x = 6D$ location, despite some over-estimation for $0.4 \leq r/D \leq 0.6$. The maximum variance approximation used for the algebraic model yields an overestimate as seen in Fig. 7.13, especially close to the centreline. This is because of the following reason. As $\langle \overline{T}^+ \rangle$ approaches unity, the maximum variance is expected to approach zero. An error of 1% in $\langle \overline{T}^+ \rangle$ would produce $\sqrt{\langle \sigma_T^2 \rangle} \approx \sqrt{\langle T^+ \rangle (1 - \langle T^+ \rangle)} \approx 0.1$, a 10% error in the rms value. This must be kept in mind while studying these results.

7.4 Implication of local Damköhler and Karlovitz numbers

Local SGS Damköhler, Da_Δ, and Karlovitz, Ka_Δ, numbers can be used to individuate the local combustion regime at the SGS level. In Fig. 7.14, PDFs of Da_Δ and Ka_Δ are shown. Only points

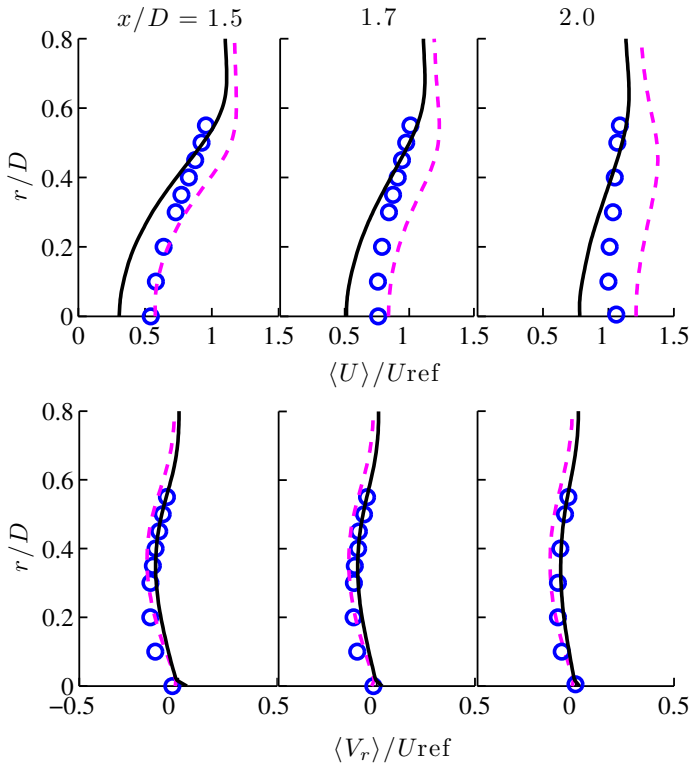

Fig. 7.12 Radial variation of $\langle U \rangle / U_{\text{ref}}$ and $\langle V_r \rangle / U_{\text{ref}}$ are compared with measurements [176, 178] for 24% TI in the post-flame region. The legend is as in Fig. 7.10.

where $u'_\Delta > 0$ and $\overline{\dot{\omega}} > 0$ have been used to compute the PDFs to be physically meaningful because Da_Δ and Ka_Δ are undefined outside the flame. PDFs obtained using the unstrained and algebraic model are similar to each other, and the effect of increasing TI is of narrowing the PDF width towards lower Damköhler numbers and higher Karlovitz numbers. Representative values suggested by this distributions are $\text{Da}_\Delta \approx 0.1$ and $\text{Ka}_\Delta \approx 35$ for 24% TI case. Since LES involves the modelling of the SGS, these global values may affect model performance rather than Da and Ka at the integral scale, which would partly explain why the flamelet models used in this study remain accurate in the distributed reaction zones regime. In case of the unstrained flamelet model, local values of $\widetilde{c}$ and its SGS variance, $\sigma^2_{c,\text{sgs}}$, imply a certain shape of the β-PDF used to compute $\overline{\dot{\omega}}$, which in turn affects the statistical behaviour at large scales. Depending on local values of $\widetilde{c}$ and $\sigma^2_{c,\text{sgs}}$, the β-PDF can assume a shape close to bimodal or Gaussian distribution. However, the assumption of high Damköhler number in the algebraic model implies that the statistical behaviour at SGS level implied by this model is bimodal. The statistical behaviour in the distributed reaction zones regime is far from being bimodal, and this seems to set limits to the algebraic model. On the other hand, predictions shown in section 7.3 using the algebraic model are reasonable. In order to explain this, a statistical

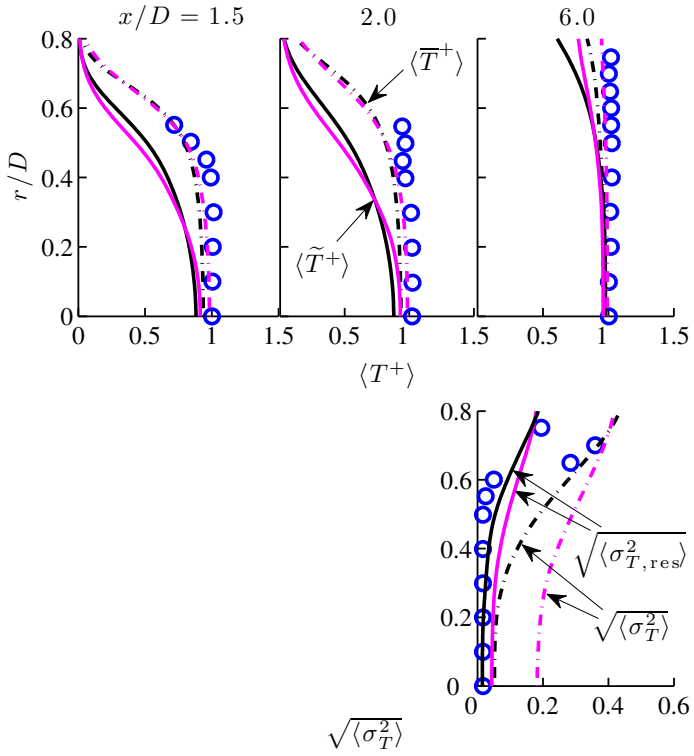

Fig. 7.13 Radial variation of mean normalised temperature and its rms are compared with measurements [168, 169] for 24% TI in the post-flame region. The legend is as in Fig. 7.11.

analysis of $\widetilde{c}$ has been done and its results are shown in Fig. 7.15. The PDFs in this figure have been computed using the algebraic model results at two axial locations with different variance, one within and one downstream of the recirculation region. Three radial positions are shown within the shear layer in order to span the flame brush from $\langle \widetilde{c} \rangle \approx 0.2$ to $\langle \widetilde{c} \rangle \approx 0.8$. β-PDFs computed using $\langle \widetilde{c} \rangle$ and its resolved variance are also shown. These PDFs match very well those obtained from LES data and are representative of the large scales. The SGS PDFs are also shown and they are computed as β-functions using the values of $\langle \widetilde{c} \rangle$ and its mean SGS variance, $\langle \sigma^2_{c,\mathrm{sgs}} \rangle$. The SGS variance is estimated using results from the unstrained flamelet model, since this quantity is not computed in the algebraic model framework. The SGS PDFs are close to bimodal distribution because the SGS variance is high. Thus, this plots suggest that non-bimodal behaviours at resolved scales can be captured using the algebraic model as long as the SGS statistical behaviour of the flame under investigation is bimodal, i.e. the SGS variance is high. However, this condition verified for the flame configuration studied in this work may not work for configurations having different values of Da_Δ and Ka_Δ. Moreover, the velocity field estimated using the algebraic model becomes inaccurate for $x > 2D$, as observed in Fig. 7.7a, suggesting some limitation of the algebraic model. The unstrained flamelet model

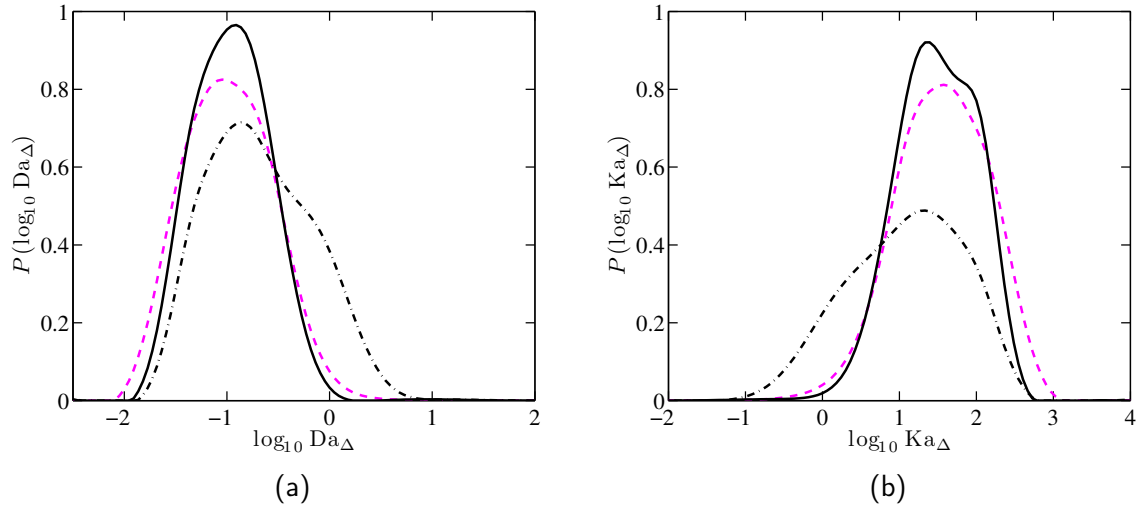

Fig. 7.14 PDF of (a) SGS Damköhler, Da_Δ, and (b) Karlovitz, Ka_Δ, numbers in the combusting region are shown for the unstrained flamelet model on 2.2M grid with 2% (−·−) and 24% (——) TI, and algebraic model on 1.8M grid with 24% TI (−−).

gives good predictions for all quantities investigated and it is more robust from this point of view.

7.5 Species comparisons

Species mass fractions are provided within the experimental dataset [168, 169]. LES statistics are compared with measurements for CH_4, O_2, CO_2, H_2O, H_2, CO and OH. Spontaneous Raman scattering was used to measure the first six, while Laser Induced Fluorescence (LIF) was used to measure OH [169]. Species were found at adiabatic equilibrium values in the exhaust at $x/D = 6$. Super-equilibrium values were observed for OH and CO in the shear layer region.

Based on the analysis in section 7.2.2, SGS variance must be taken into account when comparing mean values. Reynolds averaged mass fraction of species i can be computed by accessing the pre-filtered table *a posteriori* with local values of $\langle\overline{c}\rangle$ in case of the algebraic model, and as

$$\langle\overline{Y}_i\rangle = \int_0^1 Y_i\, \overline{P}(c;\langle\overline{c}\rangle,\langle\overline{c'^2}\rangle)\,\mathrm{d}c \tag{7.2}$$

in case of the unstrained flamelet model, where $\overline{P}(c;\overline{c},\overline{c'^2})$ is the β-PDF of c, parameterised on the Reynolds averaged quantities $\langle\overline{c}\rangle$ and $\langle\overline{c'^2}\rangle$. The first is obtained using Eq. (3.18), where

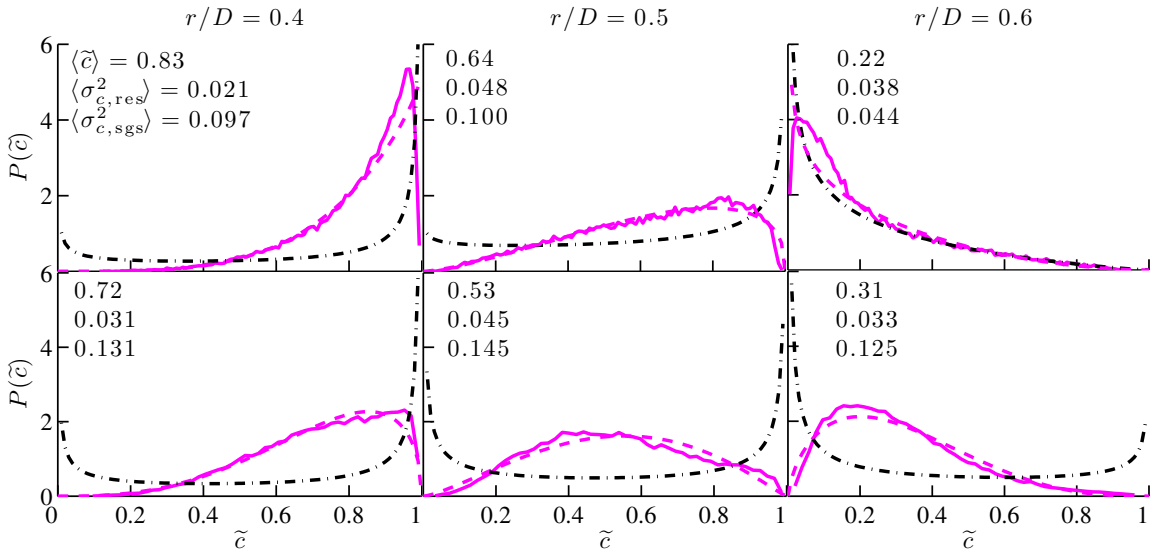

Fig. 7.15 PDFs of $\widetilde{c}$ from LES using algebraic model on 1.8M grid (——) at $x/D = 0.6$ (top) and $x/D = 2.0$ (bottom) and for three radial positions along the shear are compared with β-PDFs computed using $\langle\widetilde{c}\rangle$ and resolved variance $\langle\sigma^2_{c,\mathrm{res}}\rangle = \langle\widetilde{c}^2\rangle - \langle\widetilde{c}\rangle^2$ (– –), and using $\langle\widetilde{c}\rangle$ and mean SGS variance, $\langle\sigma^2_{c,\mathrm{sgs}}\rangle$ (– · –).

the total variance is substituted by the maximum possible variance in case of algebraic model for the reason explained in section 7.2.2. The Reynolds variance, $\langle\overline{c'^2}\rangle = \left(\langle c^2\rangle - \langle c\rangle^2\right)$, is computed as [122]

$$\langle\overline{c'^2}\rangle = \frac{\langle\widetilde{c}\rangle^2 + \sigma_c^2}{1+\tau\langle\widetilde{c}\rangle}\left[\frac{1+\tau(\langle\widetilde{c}\rangle^2(1-\langle\widetilde{c}\rangle)+\sigma_c^2(2-\langle\widetilde{c}\rangle))}{\sigma_c^2+\langle\widetilde{c}\rangle(1-\langle\widetilde{c}\rangle)}\right] - \langle\overline{c}\rangle^2 \tag{7.3}$$

Mean quantities have to be used as the resolved variance must also be taken into account in Eq. (7.3), and it is not defined for filtered quantities. An additional analysis has been done using Eq. (3.18) with mean SGS variance instead of total variance, and comparing the results with those obtained by applying Eq. (3.18) to the filtered quantities before averaging. The differences in the results obtained using these two ways of computing the species statistics are small (not shown), and thus computing species as a post-processing step is acceptable.

Using the property $\rho\overline{P}(c) = \overline{\rho}\widetilde{P}(c)$ [122], $\langle\overline{Y}_i\rangle$ can be also computed, in case of the unstrained flamelet model, as

$$\frac{\langle\overline{Y}_i\rangle}{\langle\rho\rangle} = \int_0^1 \frac{Y_i}{\rho}\,\widetilde{P}(c;\langle\widetilde{c}\rangle,\langle\sigma^2_{c,\mathrm{sgs}}\rangle)\,\mathrm{d}c \tag{7.4}$$

A comparison between Eqs. (7.2), (7.4) and experimental data [168, 169] is shown for CH_4 mass fraction in Fig. 7.16. The relative error increases in the radial direction, as the level of

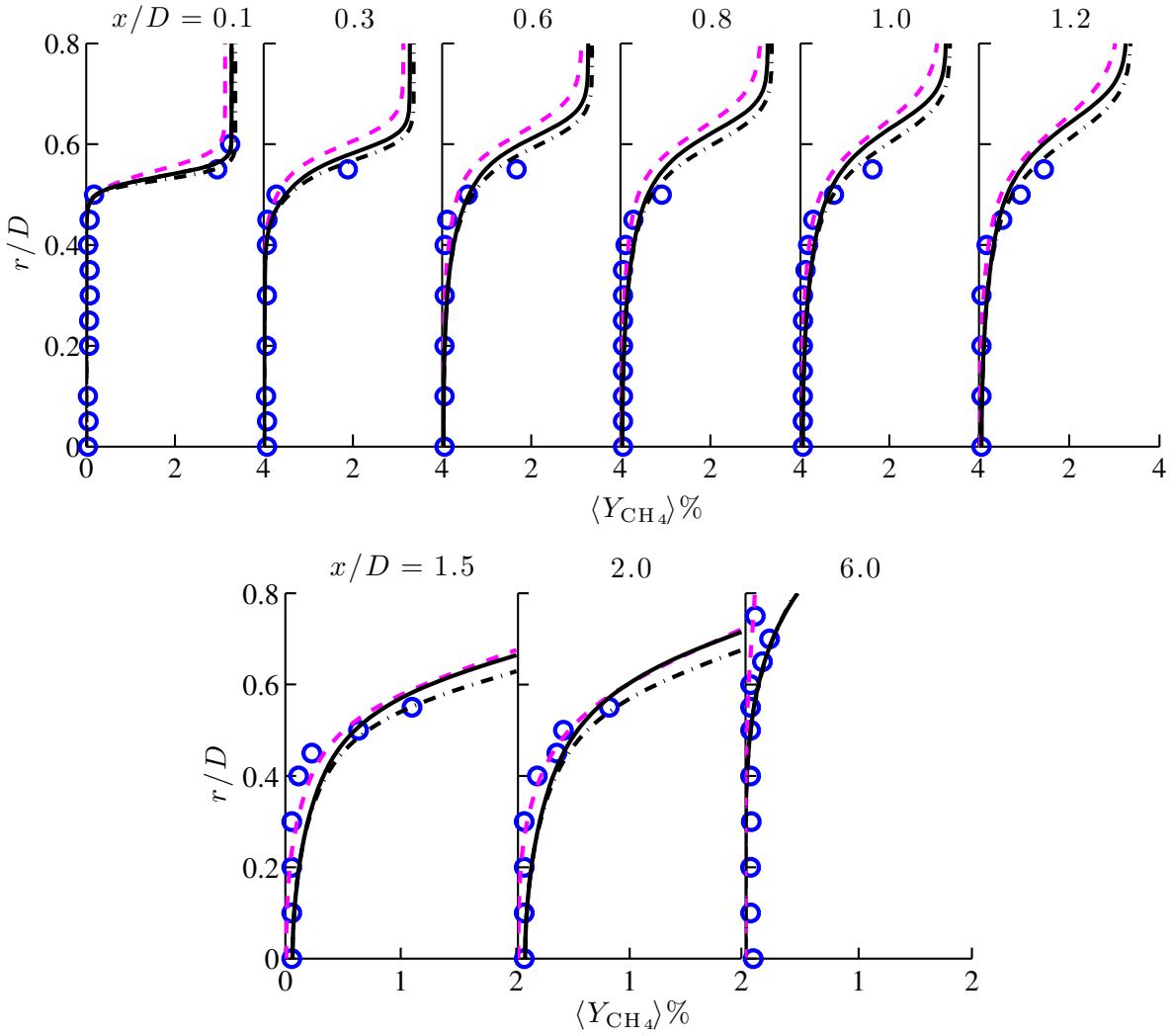

Fig. 7.16 Radial profiles of CH_4 mass fraction, obtained using the algebraic model with 1.8M grid (– –) and the unstrained flamelet model on 2.2M grid using Eq. (7.2) (——), are compared with experimental data [168, 169] (symbols) for (a) six axial locations within the recirculation region and (b) three locations in the post-flame region. Results obtained using Eq. (7.4) (– · –) are also shown.

fluctuation is also increasing in this direction. Since Y_{CH_4} is directly related to c by its definition, $\langle \overline{Y}_{CH_4} \rangle$ can be also computed directly from $\langle \overline{c} \rangle$ as

$$\langle \overline{Y}_{CH_4} \rangle = (1 - \langle \overline{c} \rangle) Y^u_{CH_4} \tag{7.5}$$

where $Y^u_{CH_4}$ is the value of Y_{CH_4} in unburnt mixture. Profiles obtained using Eq. (7.5) have been found to be very similar to those obtained using Eq. (7.2) and thus they are not shown. Moreover, using Eq. (7.2) is more consistent with the definition used for algebraic model, and is therefore preferred for comparison purposes.

The algebraic and unstrained flamelet model predictions of Y_{CH_4} are similar and they match well the experimental data in both recirculation and post-flame region. Other major species predictions are shown in Figs. 7.17 to 7.19. Comparisons with experimental results are very good using both models and for both recirculation and post-flame region, with the unstrained flamelet model giving some better predictions. The equilibrium value at $x/D = 6$ is also very well captured by both the models. Some underestimation is seen for CO_2 for both models. This is not unexpected, as similar underestimations were seen for this quantity on a different configuration using either RANS [122] or LES in Chapter 5. Thus, this underestimate seems to be related to the flamelet framework and an additional insight is given in section 7.5.1. Overall the agreement is very good.

Radial profiles of minor species mass fractions, obtained using algebraic and unstrained flamelets models, are compared with experimental data [168, 169] in Figs. 7.20-7.22. Error bars are shown when the measure error is larger than the symbol size. Prediction of CO from unstrained flamelet model is reasonable and improves moving in the axial and radial direction, where the level of fluctuations increases. A significant overestimation is seen for $x \leq 0.6D$, where the regime is between flamelet regime and thin reaction zones regime. A similar overestimation was seen in both RANS [122] and LES in Chapter 6 using the same flamelet framework for a piloted flame lying in the thin reaction zones regime. This may suggest that the unstrained flamelet model predictions of CO improve with high level of SGS variance. The equilibrium value at $x = 6D$ is also overestimated. H_2 mass fraction prediction from the unstrained flamelet model improves moving in the axial direction up to $x = 2D$, while the equilibrium value is under-predicted at $x = 6D$, where the level of fluctuation has decreased (see Fig. 7.9). The algebraic model results for CO and H_2 are similar to those of the unstrained flamelet model at $x = 0.1D$, but large overestimates are seen overall when moving downstream, suggesting some limitation in the assumptions of high Damköhler number.

Predictions of OH mass fraction are reasonable for $x/D \leq 0.8 \leq 2$, but large inaccuracies are seen from both models outside this region and close to the centreline. The value of Y_{OH} at $x = 0.1D$ and $r/D = 0$ is severely overestimated despite the flow contains fully burnt mixture. This inaccuracy is related to the choice of methane as progress variable, as will be discussed below.

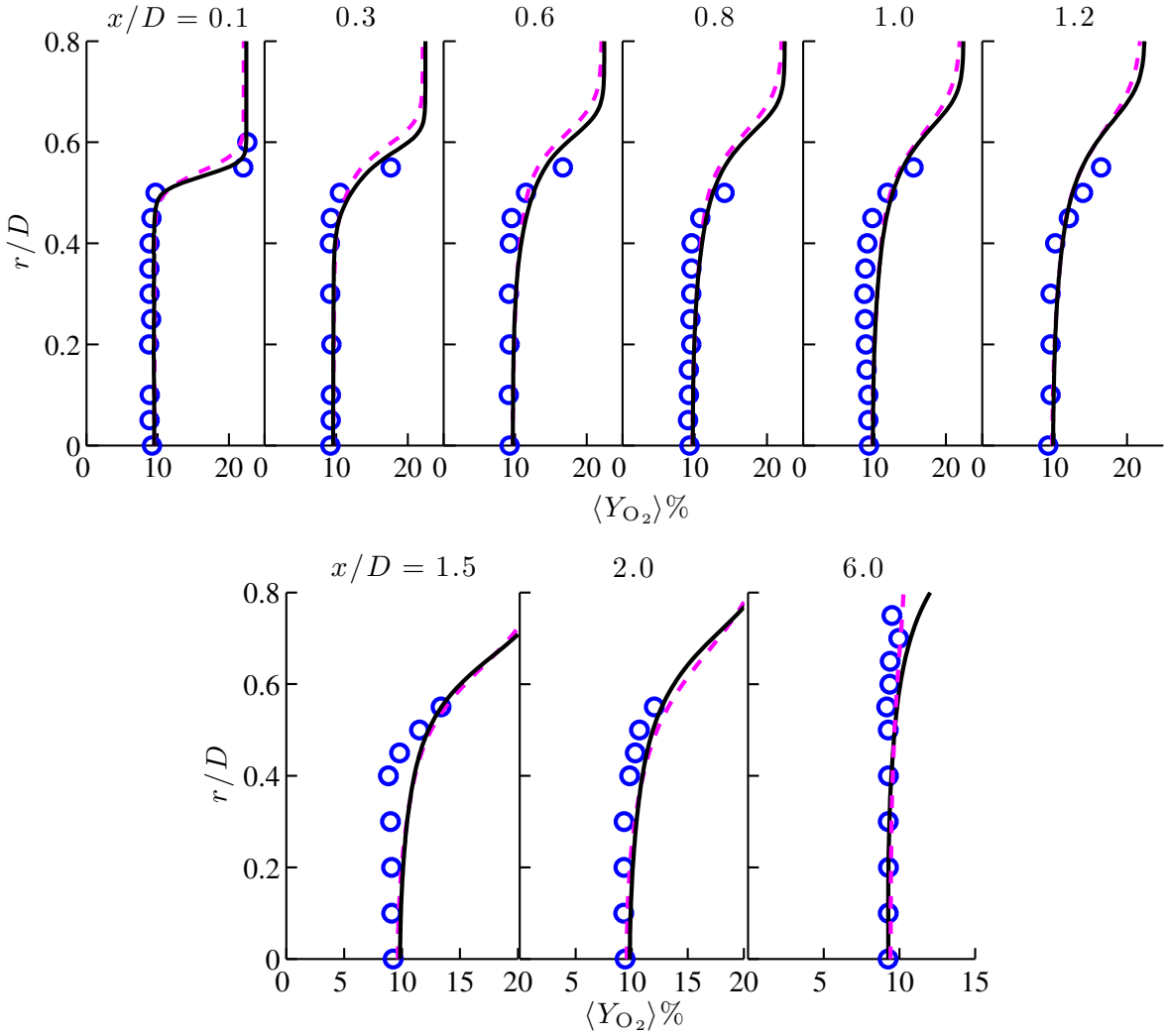

Fig. 7.17 Radial profiles of O_2 mass fraction are compared with experimental data [168, 169] for six axial locations within the recirculation region (top) and three locations in the post-flame region (bottom). The legend is as in Fig. 7.16.

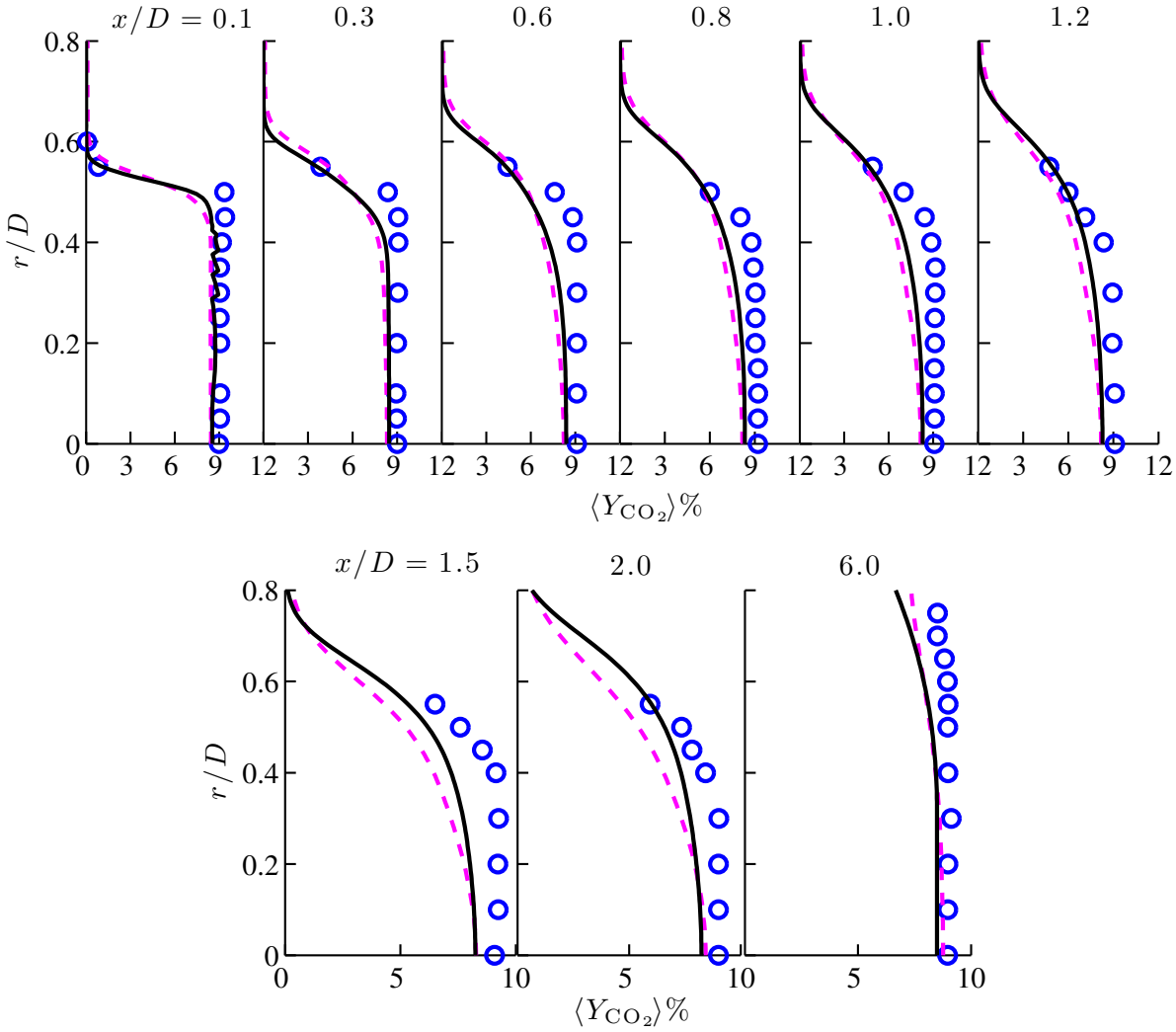

Fig. 7.18 Radial profiles of CO_2 mass fraction are compared with experimental data [168, 169] for six axial locations within the recirculation region (top) and three locations in the post-flame region (bottom). The legend is as in Fig. 7.16.

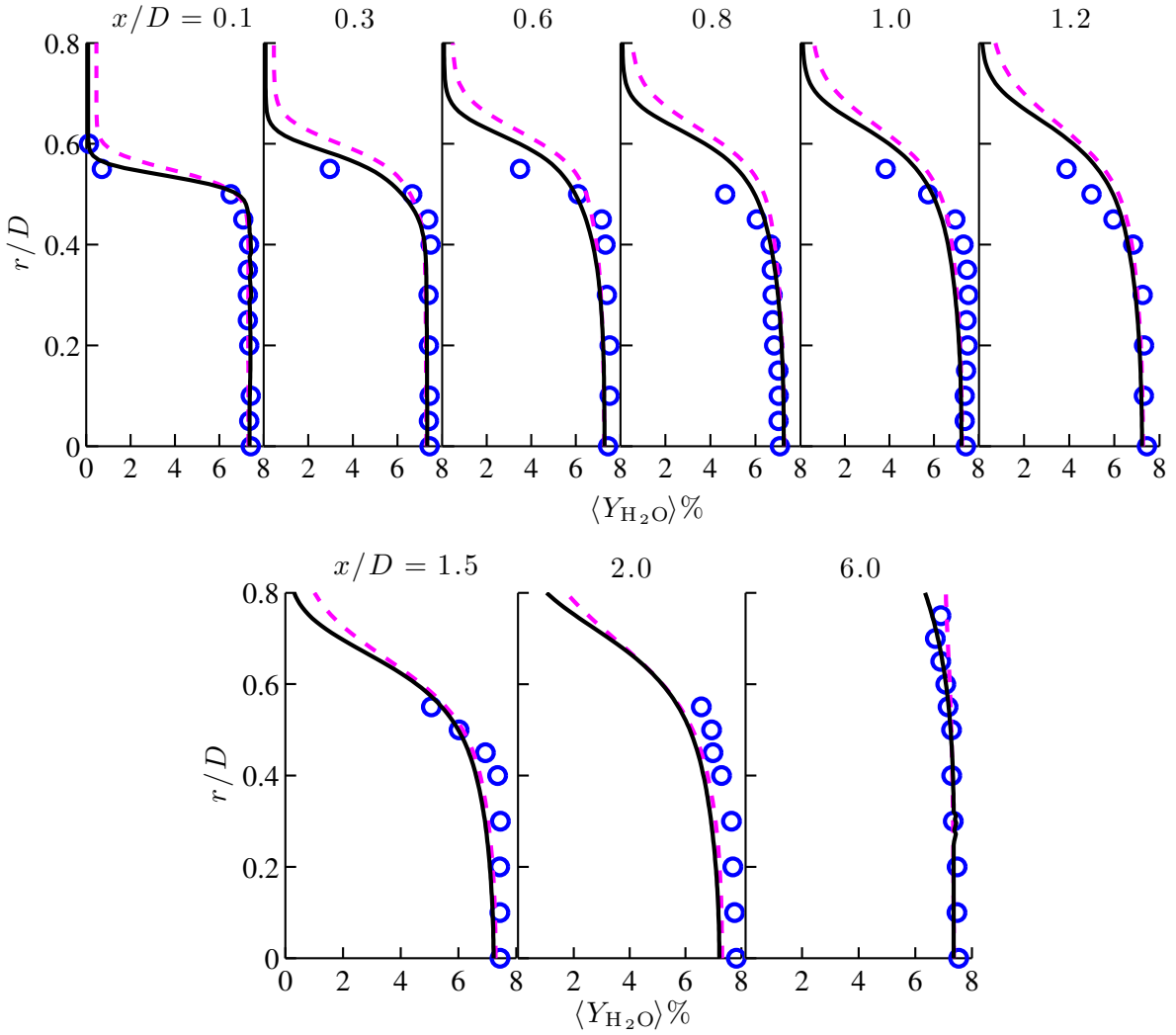

Fig. 7.19 Radial profiles of H_2O mass fraction are compared with experimental data [168, 169] for six axial locations within the recirculation region (top) and three locations in the post-flame region (bottom). The legend is as in Fig. 7.16.

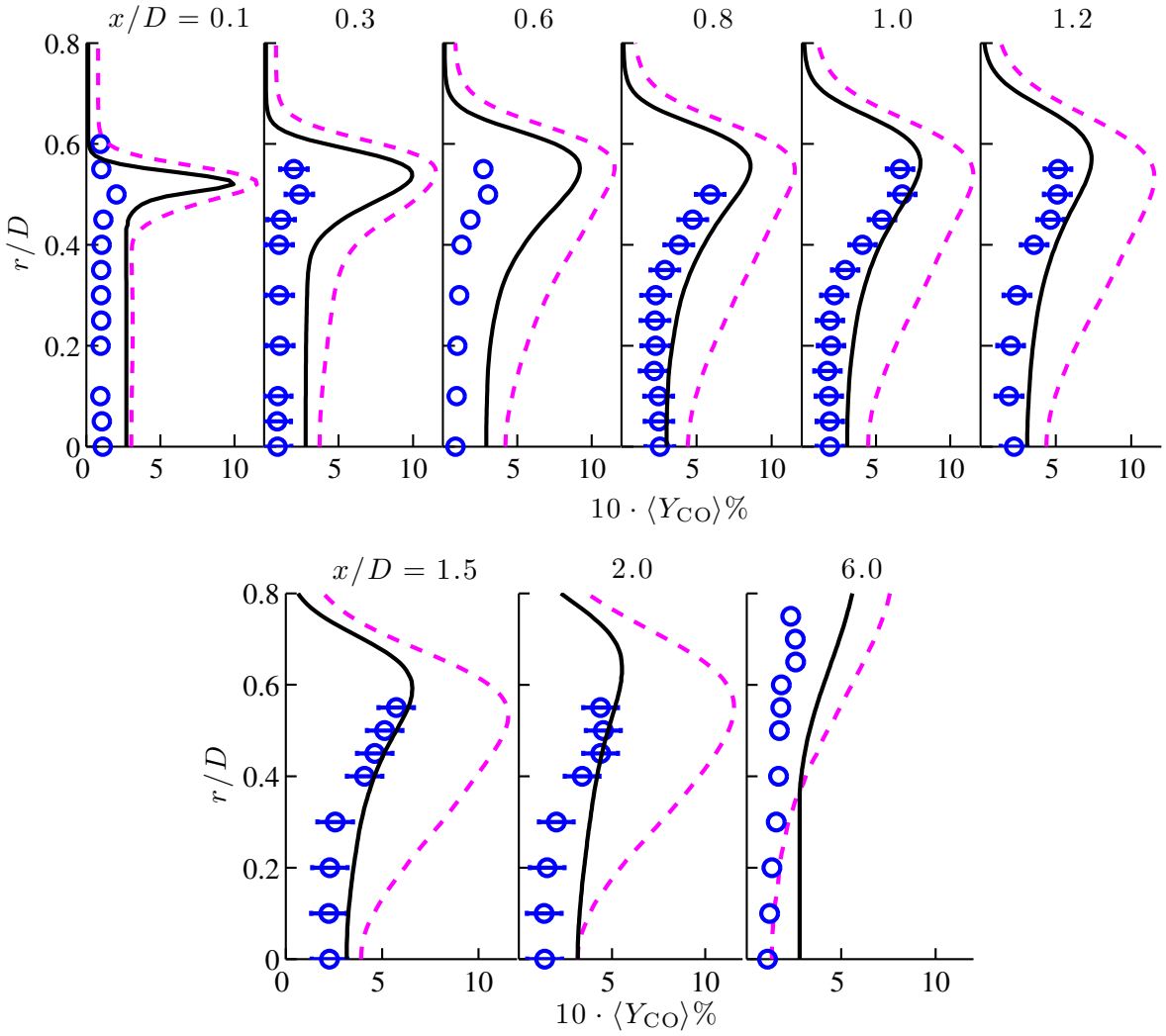

Fig. 7.20 Radial profiles of CO mass fraction are compared with experimental data [168, 169] for six axial locations within the recirculation region (top) and three locations in the post-flame region (bottom). The legend is as in Fig. 7.16.

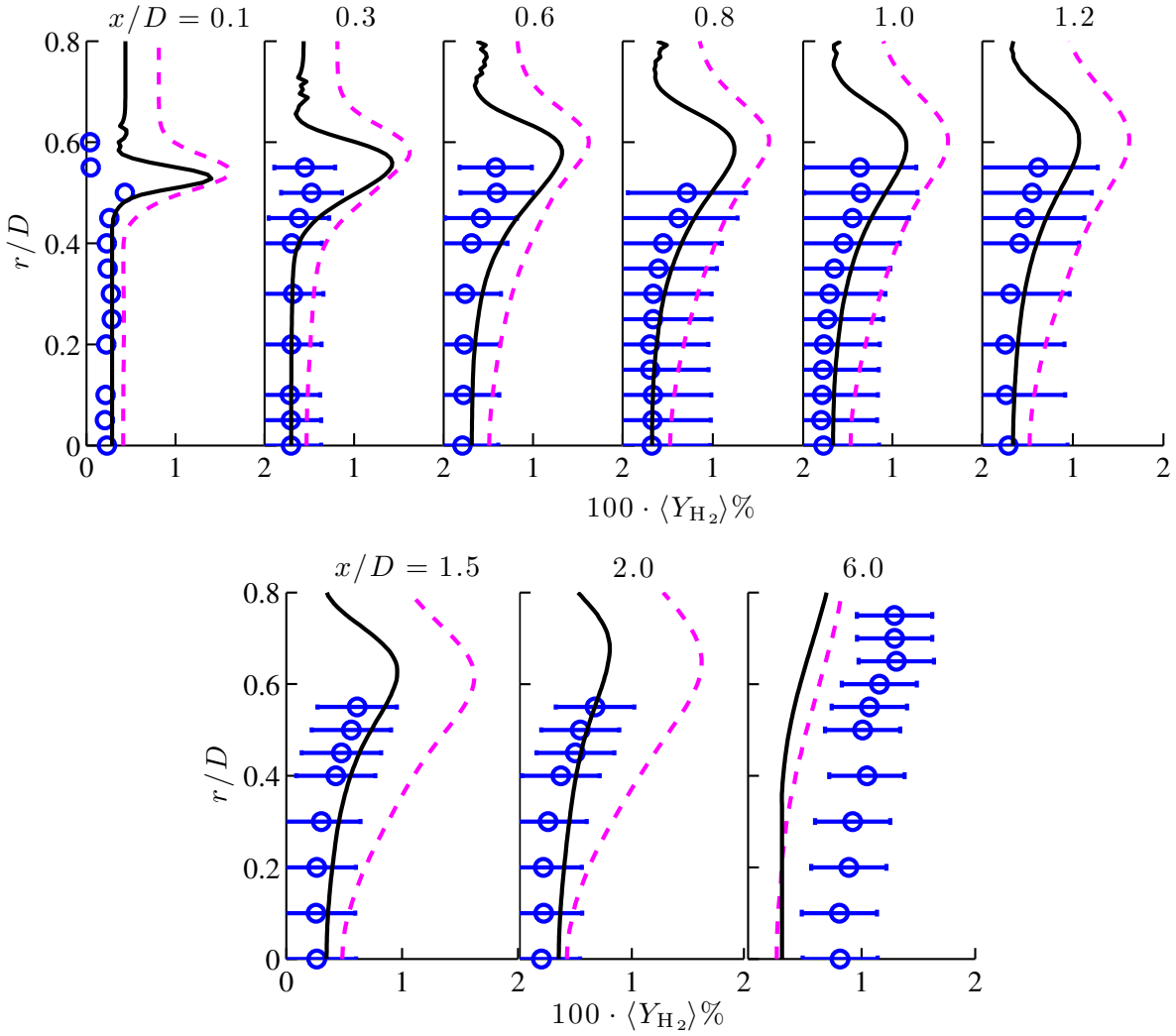

Fig. 7.21 Radial profiles of H_2 mass fraction are compared with experimental data [168, 169] for six axial locations within the recirculation region (top) and three locations in the post-flame region (bottom). The legend is as in Fig. 7.16.

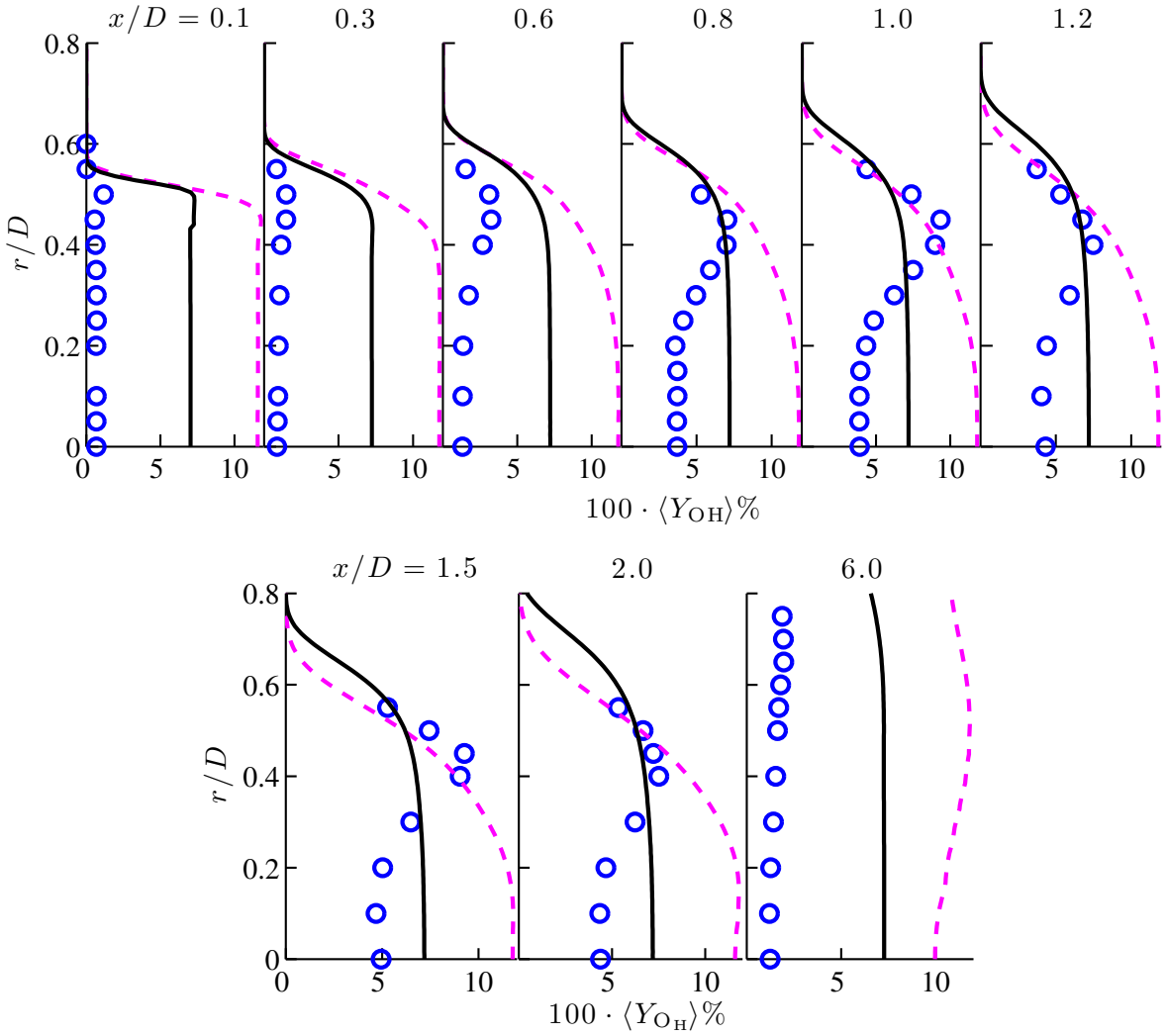

Fig. 7.22 Radial profiles of OH mass fraction are compared with experimental data [168, 169] for six axial locations within the recirculation region (top) and three locations in the post-flame region (bottom). The legend is as in Fig. 7.16.

7.5.1 Sensitivity to choice of progress variable

Strong gradients of species mass fractions can be found in laminar flamelets depending on the particular choice of the progress variable. To exemplify this situation, variation of major and minor species from laminar flamelets for three different definitions of the progress variable are shown in Fig. 7.23. These progress variable are $c = 1 - Y_{CH4}/Y^u_{CH_4}$, used for this study, $c = Y_{H_2O}/Y^b_{H_2O}$ and $c = (Y_{CO_2} + Y_{CO})/(Y^b_{CO_2} + Y^b_{CO})$, where superscripts u and b refer to unburnt and burnt conditions respectively. Gradients of Y_{CO}, Y_{CO_2} and Y_{OH} are very strong close to $c = 1$ when the methane-based progress variable is used. An enlargement of the region $0.999 \leq c \leq 1$

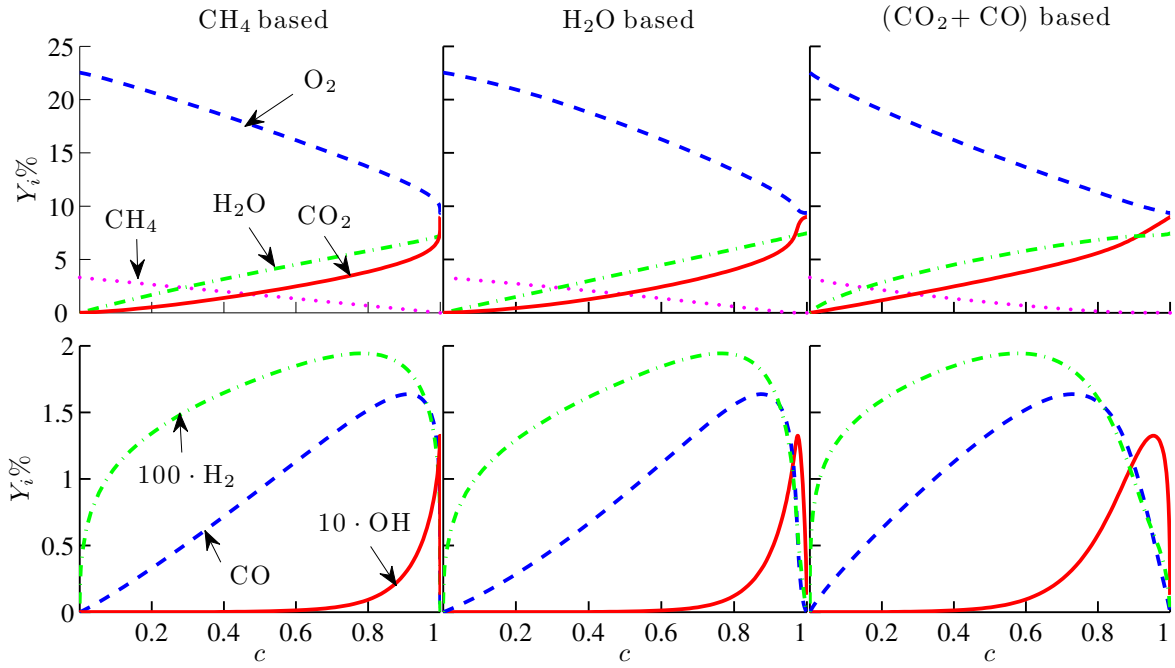

Fig. 7.23 Mass fractions variation of major and minor species using different progress variable definitions for a stoichiometric methane-air flamelet.

is shown for OH in Fig. 7.24, using the three definitions of progress variable described earlier. The pre-integrated table used for species computation in the unstrained flamelet model uses 1000 points to discretise c and linear interpolation is performed between two values of c. When $\sigma^2_{c,sgs} \to 0$ in a LES, $\widetilde{c} \to c$ and the flamelet behaviour is laminar. An error of 0.01% on c will produce an error of 90% on Y_{OH}. The value of $\langle c \rangle$ at $x/D = 0.1$ and $r/D = 0$ is $\langle c \rangle \approx 0.9998$, therefore an error of 0.02% is present and this explains why OH mass fraction does not vanish for $r \to 0$ close to the bluff body in Fig. 7.22. Similar considerations can be done for CO and CO_2 for locations where $\langle c \rangle \to 1$.

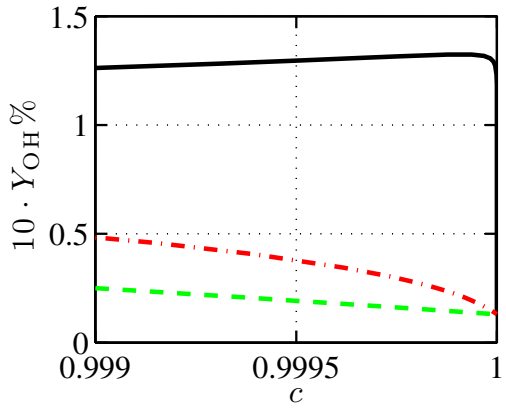

Fig. 7.24 Enlargement of OH mass fraction in Fig. 7.23 on the burnt side using different definitions of c: $c = 1 - Y_{CH4}/Y^u_{CH_4}$ (——), $c = Y_{H_2O}/Y^b_{H_2O}$ (– –) and $c = (Y_{CO_2} + Y_{CO})/(Y^b_{CO_2} + Y^b_{CO})$ (– · –).

Radial profiles of major and minor species mass fractions, obtained using the unstrained flamelet model with c based on CH_4, are compared with those obtained using definitions of c based on H_2O and $(CO_2 + CO)$ and with experimental results in Figs. 7.25 to 7.31 for six axial locations in the combusting region. The computed profiles converge on each other for all species for $r/D \geq 0.6$, i.e. when $\langle c \rangle \to 0$ or $\langle \sigma_c^2 \rangle \to 0.25$. Major species predictions are almost insensitive to the progress variable choice, apart for CO_2 in the region where $\langle c \rangle \to 0$, because of the presence of strong gradients in the laminar flamelet. Under-prediction of Y_{CO_2}, seen for methane- and water-based flamelets for $0.6 \leq x/D \leq 2$, are much smaller when the flamelets is based on $(CO_2 + CO)$ instead. Significant improvements are seen in CO predictions when H_2O and $(CO_2 + CO)$ based flamelets are used, and results are very good, apart some over-prediction at $x = 0.6D$. Similar results are obtained using the three definitions of c for H_2 mass fraction, with some better predictions for the methane-based c at $x/D = 0.1$ and $x/D = 6$. Also, clear improvements are seen for OH mass fractions at $x/D = 0.1$, $x/D = 0.6$ and $x/D = 6$ when H_2O and $(CO_2 + CO)$ based progress variables are used. However, there is a large underestimate for $1 \leq x/D \leq 2$, although the qualitative behaviour is captured. Equilibrium values at $x/D = 6$ are well captured for major species using any of the definitions of c, while minor species seem to be more sensitive to the choice of the progress variable. Overall the matches are very good irrespective of the combustion regime, suggesting that the unstrained flamelets model investigated here is robust and accurate.

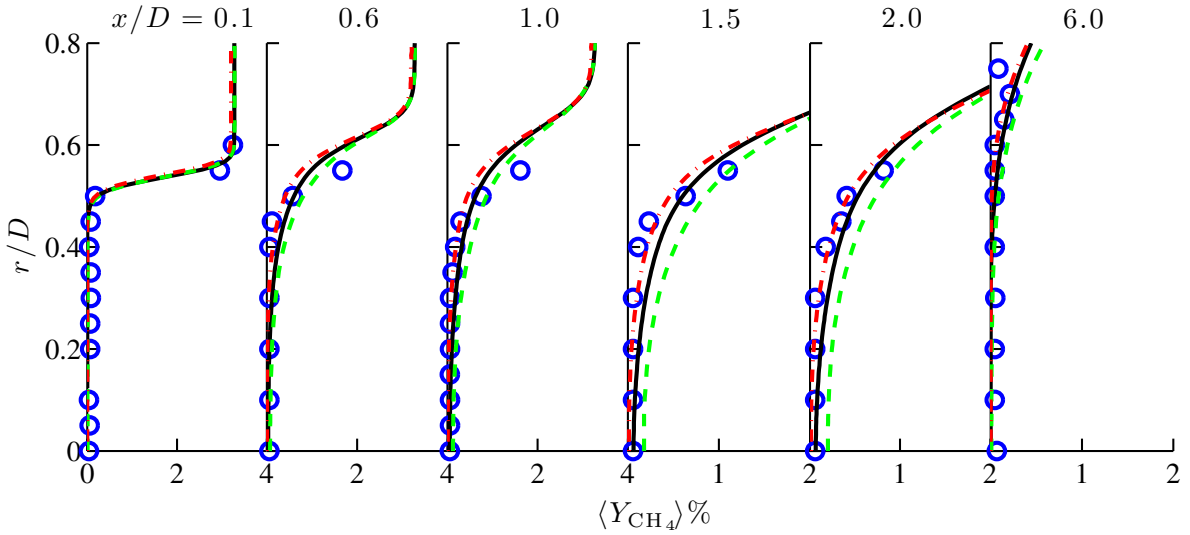

Fig. 7.25 Radial profiles of CH_4 mass fraction, obtained using the unstrained flamelets model with 2.2M grid using Eq. (7.2) for three different definition of c, $c = 1 - Y_{CH4}/Y^u_{CH_4}$ (——), $c = Y_{H_2O}/Y^b_{H_2O}$ (– –) and $c = (Y_{CO_2} + Y_{CO})/(Y^b_{CO_2} + Y^b_{CO})$ (– · –), are compared with experimental data [168, 169] (symbols) for six axial locations.

7.6 Analysis of β_c PDF

The PDF of the combustion parameter β_c in Eq. (2.22), computed dynamically, is shown in Fig. 7.32 for the 24% TI case. The result is shown for both algebraic and unstrained flamelet closures, and the data is taken from the entire domain obeying the conditions noted in §6.5. The realisability limit for algebraic model [39], $2/(2C_m - 1)$, is also shown in the figure. Both PDFs have their maximum for $\beta_c \approx 4$. The PDF has a longer tail for the unstrained flamelet closure, which is related to the different flow dynamics in the region downstream of the recirculation region, as was shown in Fig. 7.6. Because of this difference, the mean value of β_c is $\langle \beta_c \rangle \approx 4$ for the algebraic model, which is close to the maximum probable value, whereas $\langle \beta_c \rangle \approx 12$ for the unstrained flamelet model. Additional simulations with constant β_c have shown that an optimum value for this parameter is also around 4 for both algebraic and unstrained flamelets closures. DNS analyses [77] show that β_c increases with the heat release parameter, τ, which is $\tau \approx 4.2$ for the lean premixed configuration studied here. This is consistent with the LES analysis on stoichiometric piloted flames in Chapter 5, as an optimum value of $\beta_c = 7.5$ was found in that case for $\tau \approx 6.4$. This analysis is an useful indication of which value to set for β_c when a dynamic formulation is not possible, i.e. in cases of low turbulence, as will be discussed in the next chapter.

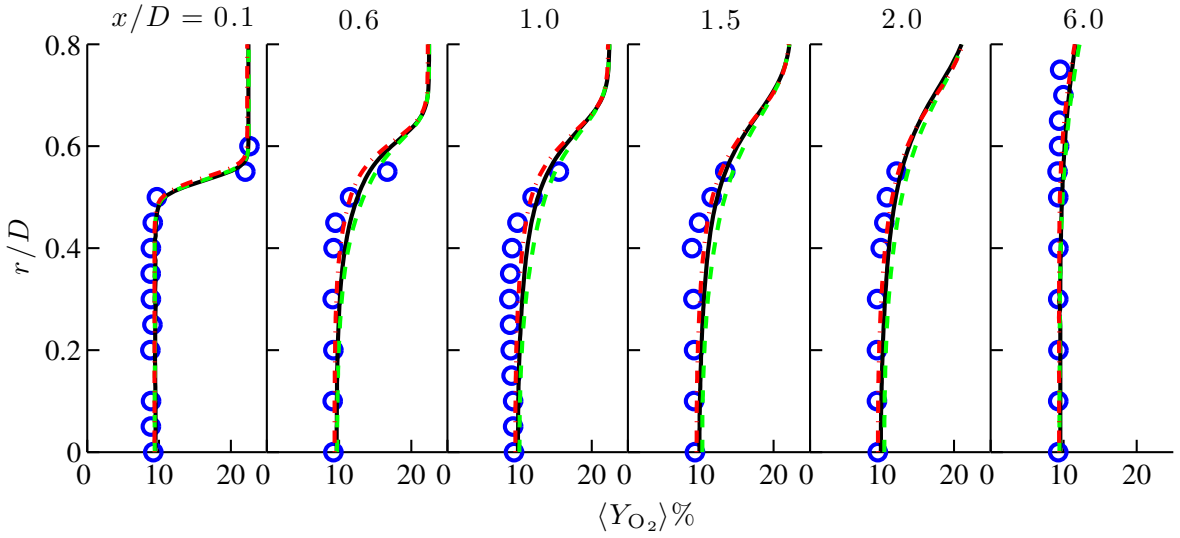

Fig. 7.26 Radial profiles of O_2 mass fraction from LES, obtained using three different definitions of the progress variable, are compared with experimental data [168, 169] for six axial locations. The legend is as for Fig. 7.25.

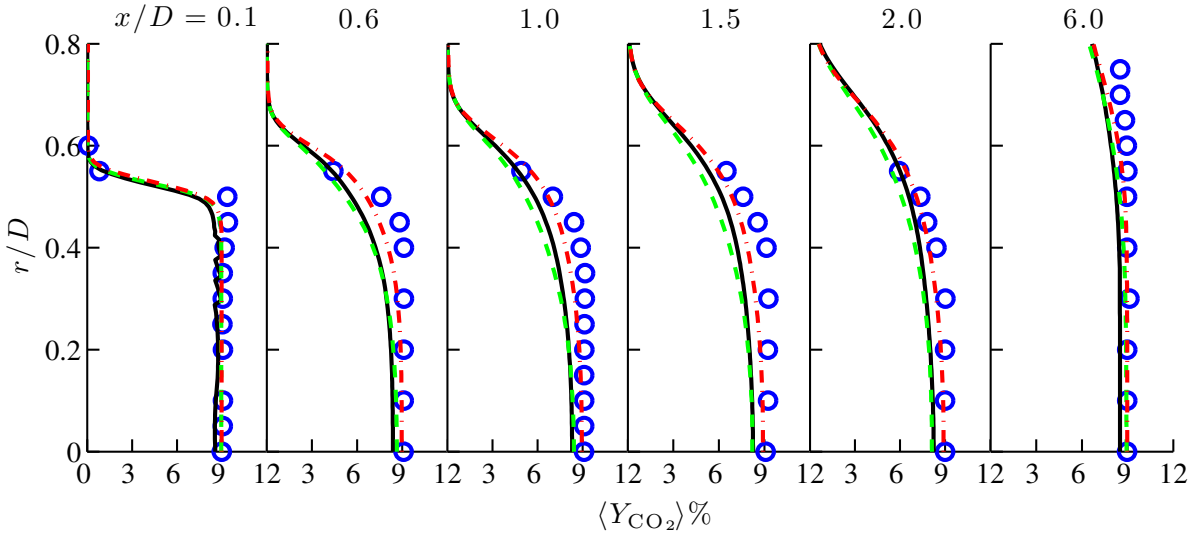

Fig. 7.27 Radial profiles of CO_2 mass fraction from LES, obtained using three different definitions of the progress variable, are compared with experimental data [168, 169] for six axial locations. The legend is as for Fig. 7.25.

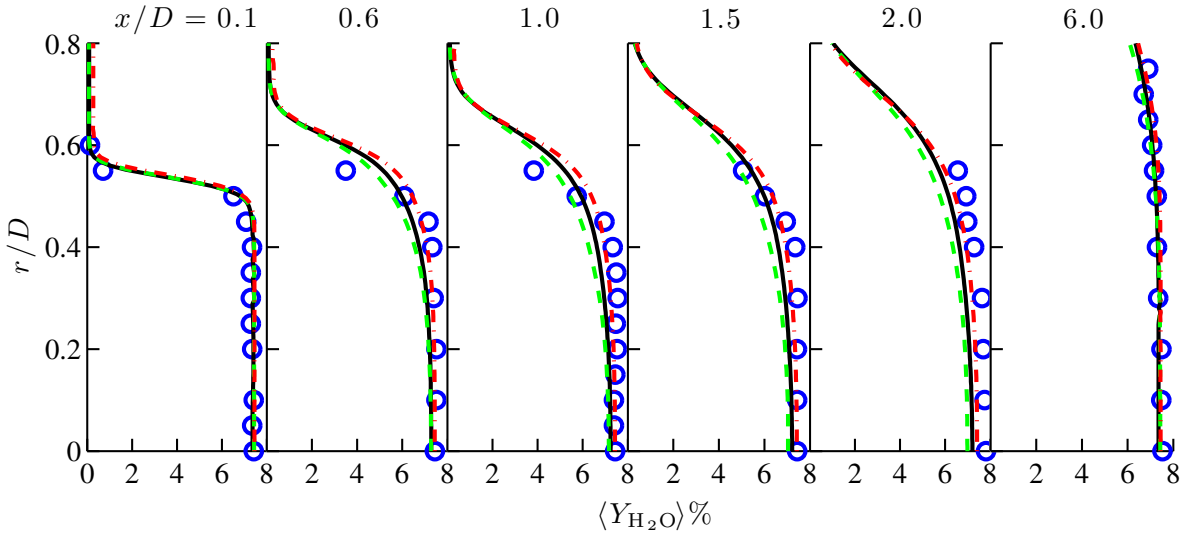

Fig. 7.28 Radial profiles of H_2O mass fraction from LES, obtained using three different definitions of the progress variable, are compared with experimental data [168, 169] for six axial locations. The legend is as for Fig. 7.25.

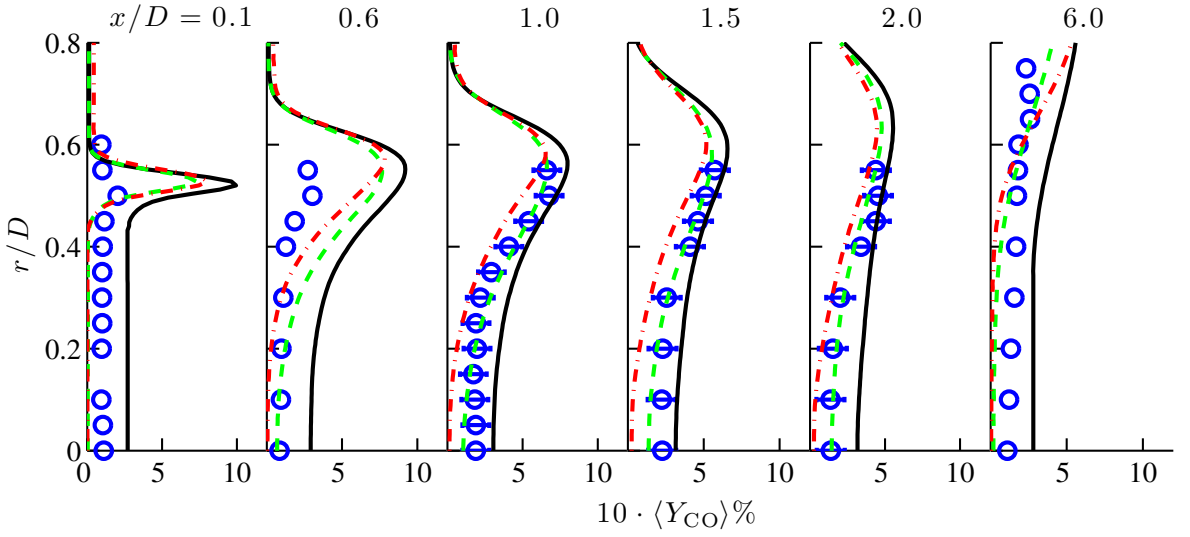

Fig. 7.29 Radial profiles of CO mass fraction from LES, obtained using three different definitions of the progress variable, are compared with experimental data [168, 169] for six axial locations. The legend is as for Fig. 7.25.

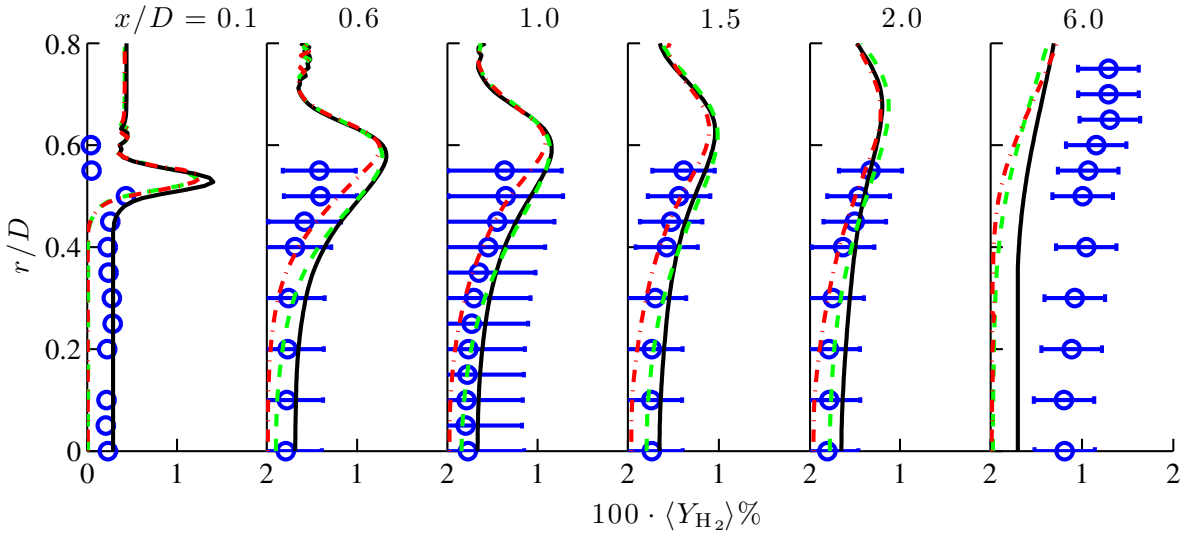

Fig. 7.30 Radial profiles of H_2 mass fraction from LES, obtained using three different definitions of the progress variable, are compared with experimental data [168, 169] for six axial locations. The legend is as for Fig. 7.25.

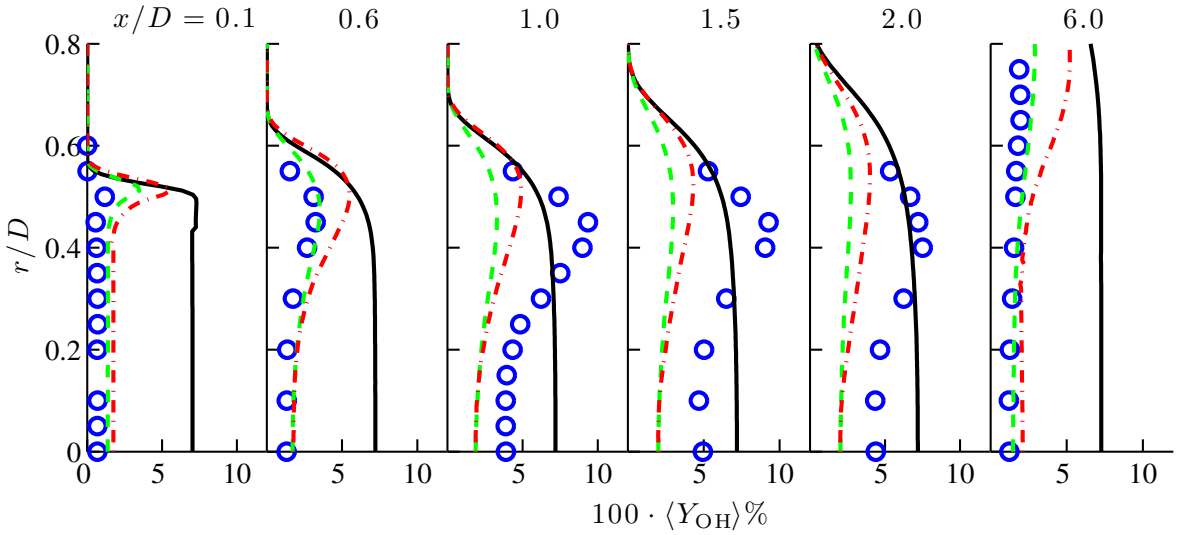

Fig. 7.31 Radial profiles of OH mass fraction from LES, obtained using three different definitions of the progress variable, are compared with experimental data [168, 169] for six axial locations. The legend is as for Fig. 7.25.

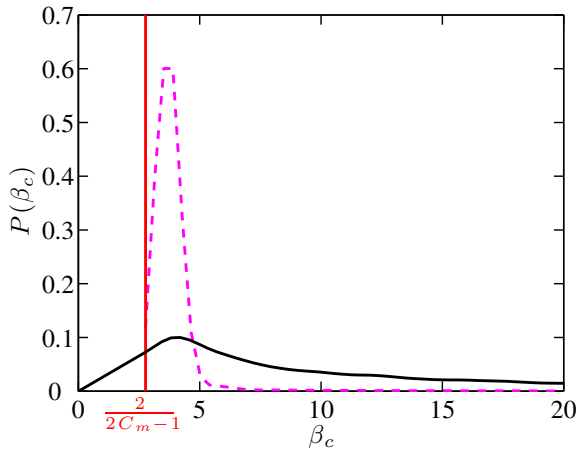

Fig. 7.32 PDF of β_c for algebraic (– –) and unstrained flamelet (——) models and 24% TI. The realisability limit, $2/(2C_m-1)$, is also marked.

7.7 Summary

The unstrained flamelet closure is found to be reasonably accurate in this configuration which involves different regimes. The effect of finite rate chemistry is found to be important in the region of distributed reactions downstream of the recirculation region, where the unstrained flamelet closures is indeed more accurate than the algebraic closure, which assumes fast chemistry instead. However, the flames analysed here and in the previous chapters involve relatively high turbulence. It is interesting to assess the potentiality of the unstrained flamelet closure in conditions of low turbulence, where effects of thermal dilatation become strong and may substantially affect the combustion and thus its modelling. This analysis is done in the next chapter.

Chapter 8

Non piloted jet flame

In this chapter a low-turbulence, lean propane-air flame is simulated. This flame lies in the corrugated flamelets regime of the combustion diagram. Flames in this regime are likely to experience turbulence resulting from flame induced effects such as heat release and flame intermittency because of low levels of background turbulence. The series of experiments in [72–75] is a good example for this case. Recently, Furukawa *et al.* [76] reported statistics of gas velocities and reaction progress variable fields in a non-piloted lean propane-air premixed Bunsen flame in quiescent ambient environment, and remarked that those statistics and certain aspects such as "bubble formation" and "bimodal radial velocity" are useful for testing combustion modelling. Thus, these premixed flames offer additional challenges for numerical modelling and the sub-grid scale models must cater for the subtleties of turbulence-combustion interaction physics in the corrugated flamelets regime. It is worth noting that the air entrainment does not affect the flame in this configuration as one shall see next, which thus operates in a fully premixed mode.

The aim of this chapter is to shed light on this interaction by simulating the lean propane-air flame in [76]. Despite the low velocities involved, this flame is prone to instabilities and flow transition which are challenging for combustion modelling. This provides a good opportunity to gather insights on the capabilities and limitations of the statistical flamelet model for SGS combustion in LES of this flame. Since the shear-produced turbulence does not affect this flame, as one shall see in the results section, the turbulence level experienced by the flame results mainly from flame oscillation and thermal expansion effects. These are sub-grid scale (SGS) phenomena in a practical LES and thus they would affect the SGS velocity which needs to be modelled. It may be debatable whether one needs to include dilatation effect in this velocity modelling or not as propositions have been made in the past to exclude this effect in general [47]. The SGS velocity models of Eqs. (3.50), (3.51) and (3.56) are considered to assess their influence on the premixed combustion, as these models treat the thermal-expansion

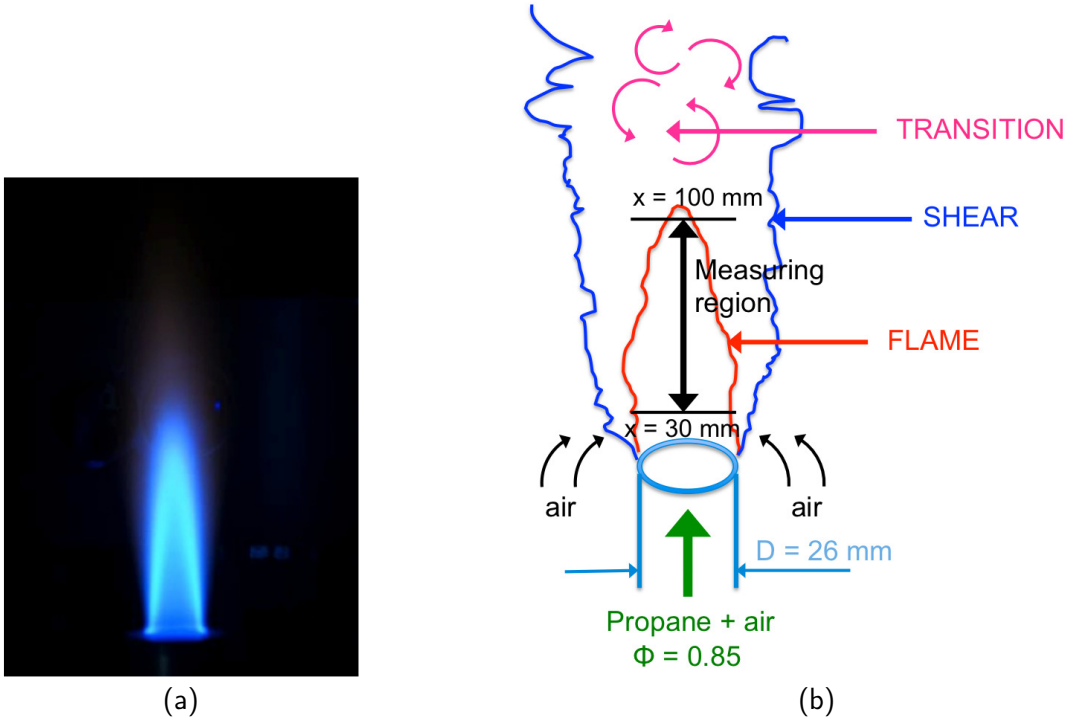

Fig. 8.1 A direct photograph (a) and a schematic (b) of the lean propane-air flame of [76].

effects differently. Models of Eqs. (3.52) and (3.55) are respectively similar to models of Eqs. (3.51) and (3.50) from this point of view and thus will not be considered in this analysis.

8.1 Experimental case

The experimental dataset of [76] includes a lean and a rich flames of propane-, and methane-air mixtures and these non-piloted flames belong to the corrugated flamelets regime of the turbulent premixed combustion regime diagram. These reactant mixtures have the same laminar flame speed, $s_L = 0.34$ m/s and these flames were observed to be similar except for the differential diffusion effects in the rich propane flame. So, the lean propane-air flame having an equivalence ratio of $\phi = 0.85$, having a laminar flame thermal thickness of $\delta_{th} = 0.4$ mm, is chosen for this study to better understand the turbulence-flame interaction in corrugated flamelets and their modelling implications without differential diffusion effects. The influences of differential diffusion will be studied in future.

A direct photograph of the lean flame of [76] is shown in Fig. 8.1a. The reactant mixture issuing from a pipe of diameter $D = 26$ mm spreads into an open environment as shown schematically in Fig. 8.1b. The bulk mean velocity based on the mass flow rate at cold

condition is $U_b = 4$ m/s. The air entrainment caused by the reactant jet creates a shear layer surrounding the flame as sketched in this figure and this is quite different from the case of piloted turbulent premixed flames where the flame resides inside the shear layer between reactant and pilot streams. Since the flame is not in the shear layer for this configuration the turbulence experienced by the flame comes from the inlet, produced by thermal expansion effects and flame-front intermittency. This insight is obtained indeed through LES to be discussed in later sections. Furthermore, the turbulence produced by the shear through the Kelvin-Helmoltz instability is not expected to affect the flame as one shall see later. A 3D LDV system having a spherical probe of about 0.2 mm diameter was used to measure three components of velocity, which were used to deduce various characteristics of the flame. These measurements along the centreline were taken from $h = 10$ to 110 mm and along the radius for $r \leq 15$ mm at given height, h, ranging from 30 to 90 mm. These measurement regions did not include the shear layer or region where the potential core of the jet starts to breakdown (marked as "Transition" in Fig. 8.1b). In other words, the measurements were focused in regions where shear generated turbulence effects are weaker. This experiment offers a good challenge for combustion modelling because the flame induced turbulence and mutual interactions are important in these flames and thus the combustion and other submodels have to cater for this physics. This flame is simulated here using LES paradigm which is described next.

8.2 Numerical details

The algebraic closure in Eq. (2.19) will not be used for this flame because the assumption in this closure involves relatively high Reynolds numbers, which is not met. The unstrained flamelets model described in §3.3.2 is used along with the numerical procedure of §3.4. The dilution effect due to air entrainment is accounted by using a transport equation for a passive marker as described in that section. As noted before, the air entrainment does not affect the flame structure in this configuration, as will be also shown next, thus additional terms in Eq. (3.26) accounting for partial premixing effects are not required and the procedure of §3.4 is adequate. The instantaneous progress variable is $c = 1 - Y_f/Y_{f,u}$, where $Y_{f,u}$ is the fuel mass fraction in the unburnt mixture. The sub-grid stresses are closed using a localised dynamic Smagorinsky model [81, 141] and the SGS scalar fluxes are computed using gradient hypothesis with dynamic Schmidt number approach [141]. The SGS velocity, u'_Δ, is modelled using the models of Eqs. (3.50), (3.51) and (3.56) as these models represent differently the dilatational effects which are of interest in this study. The dynamic approach [79, 130] for the scale-dependent parameter β_c in Eq. (2.22) cannot be used for the flame investigated here because of the low turbulence. Thus, a static value is used as detailed in section 8.3.1.

The cylindrical computational domain with $D_c \times L_c = 1\,\mathrm{m} \times 1\,\mathrm{m}$ is discretised using a non-uniform grid having 278×506 cells in the radial and axial directions respectively, with 44 cells for the jet diameter, D. This grid results in 5.4M cells in total for the chosen computational volume. The filter size, based on the numerical cell volume, has a minimum of $\Delta \approx 1.3\delta_{th}$ close to the jet exit. Another refined grid having about 23M cells, by increasing the number of cells by about 60% in all three directions, is used to test grid dependency of the flame statistics. The progress variable is assigned to be 0 and 1 for the reactant jet and entrainment inlet boundaries respectively. A small velocity of 0.1 m/s and a temperature of 298 K are assigned for the entrained air at the respective inlet boundary. The inlet jet velocity cannot be prescribed using the bulk mean, U_b, and centreline, $U_0 = 4.5\,\mathrm{m/s}$, velocities reported by [76] from cold flow measurements for the reasons discussed below.

The measured centreline variation of axial velocity is shown in Fig. 8.5, to be discussed in detail later, using symbols. The increase in the axial velocity at around 100 mm is due to acceleration through the flame tip. The axial velocity at the centreline is about 5.5 m/s at about one diameter distance from the jet exit implying a strong acceleration over this distance if it were 4.5 m/s at the jet exit. A careful considerations and further measurements of jet tube wall temperature suggested that this results from heating of reactant mixture inside the tube when the flame is present. To capture these influences correctly, a preliminary RANS simulation using Fluent (a commercial CFD code) is performed for the computational domain and conditions illustrated in Fig. 8.2. This cylindrical domain is discretised using 31×775 cells in radial and axial directions respectively. The measured mass flow rate of propane-air mixture at 298 K is specified at the inlet with flat profiles. A linear temperature profile as shown in the figure is specified near the exit based on the experimental estimates. This linear profile gives a temperature gradient of about 3 K/mm. The radial variations of temperature and axial velocity at the jet exit obtained from this RANS calculation are shown in Fig. 8.3. The temperature at the jet exit is nonuniform which accelerates the flow. The centreline value of axial velocity is about 5.4 m/s, which is close 5.5 m/s observed in the experiment at $1D$ from the jet exit. These computed profiles are specified as boundary conditions for the LES.

Although a rms value of 0.22 m/s reported by [76] is low at the jet exit, it is important to include this because the flame experiences this turbulence and does not see the shear generated turbulence as noted earlier. So, a synthetic turbulence having similar characteristics as in the experiment is obtained using the digital filter technique [112] and is added to the velocity U shown in Fig. 8.3a for the jet exit. The values of rms velocities needed for the digital filter method are taken from the RANS simulation along with the measured length scale.

The grid size is also increased by 1.6 in all directions resulting in 23M cells for the same computational volume as noted earlier to test grid sensitivity. The CFL number is kept below

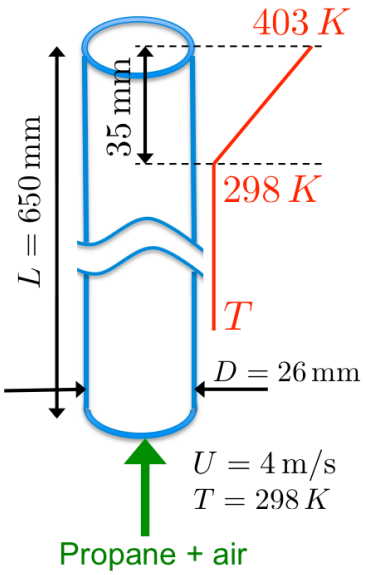

Fig. 8.2 Numerical domain for the preliminary RANS.

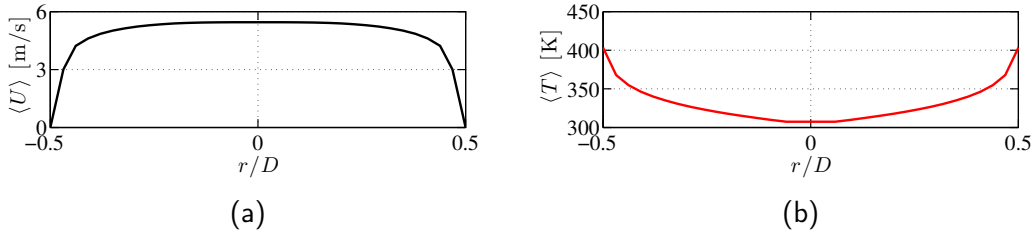

Fig. 8.3 Profiles of (a) mean axial velocity and (b) mean temperature at the jet exit, computed using RANS.

0.3 everywhere in the domain using a constant time step of 30 μs and 50 μs respectively for 23M and 5.4M grids. The LES are run for 1.6 s of real time using 208 cores for 23M and 32 cores for 5.4M grids, of which the later half (0.8 s) is used for collecting statistics. These simulations took about 72h on a wall clock.

8.3 Results

8.3.1 Role of SGS velocity modelling

The SGS velocity will be influenced by dilatation resulting from combustion and thus u'_Δ values obtained using Eqs. (3.50), (3.51) and (3.56) can be significantly different as these models presume the role of the dilatation differently. The difference in u'_Δ gives different $\widetilde{\varepsilon}_c$, see

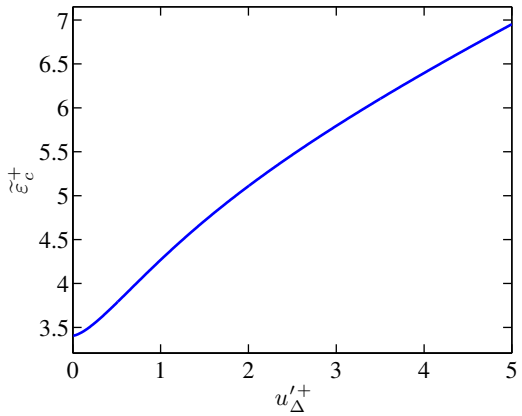

Fig. 8.4 Variation of $\widetilde{\varepsilon}^+ = \widetilde{\varepsilon}\delta_{th}/s_L$, with $u'^+_\Delta = u'_\Delta/s_L$, for $\Delta/\delta_{th} = 1.4$.

Eq. (2.22), influencing $\sigma^2_{c,\mathrm{sgs}}$. This can influence the filtered reaction rate which can affect the u'_Δ. Thus, the combustion model used here has two-way coupling between flame and turbulence.

Figure 8.4 shows the sensitivity of $\widetilde{\varepsilon}_c$, normalised using δ_{th}/s_L, to u'_Δ while keeping other parameters in Eq. (2.22) to be constant and $\Delta^+ = 1.4$ to be a representative value for the flame regions based on the grid used here. The quantity $\sigma^2_{c,\mathrm{sgs}}/\beta_c$ is taken to be unity for the purpose of this analysis. The variation is almost sublinear for the range shown and a 100% change in u'^+_Δ produces only about 20% change in $\widetilde{\varepsilon}^+$. This implies that the same variation could be obtained by changing β_c by about 20%. Since the incoming turbulence influences u'_Δ any difference in its value obtained synthetically can also influence $\widetilde{\varepsilon}^+$. The sub-grid velocity can be written as $u'_\Delta = Cu'^*_\Delta$ with a constant $C \neq 0$ and u'^*_Δ given by Eqs. (3.50) to (3.56) without their respective model constants. The $\widetilde{\varepsilon}_c$ in Eq. (2.22) can then be expressed as

$$\widetilde{\varepsilon}_c = \mathscr{F} f(u'_\Delta, \Delta)\frac{\sigma^2_{c,\mathrm{sgs}}}{\beta_c} = \mathscr{F} f_1(u'^*_\Delta, \Delta) f_2(C)\frac{\sigma^2_{c,\mathrm{sgs}}}{\beta_c} \tag{8.1}$$

where $f(u'_\Delta, \Delta) = f_2(C) f_1(u'^*_\Delta, \Delta)$ is found by comparing Eqs. (8.1) and (2.22). The variation of $\widetilde{\varepsilon}_c$ for $f_2(C) = 1$ is shown in Fig. 8.4. From Eq. (8.1) one can define $\beta'_c = \beta_c/f_2(C)$ which can be used instead of C and β_c and this approximation is plausible because of the quasi-linearity of $\widetilde{\varepsilon}_c$ with u'_Δ observed in Fig. 8.4. The value of β'_c for the various u'_Δ models is chosen by matching the computed and measured flame lengths and this length is estimated to be the location of the peak axial velocity from the jet exit along the centreline for a meaningful comparative analysis. The values of β'_c obtained using the three u'_Δ models given in Eqs. (3.50) to (3.56) are shown in Table 8.1. The β'_c for Lilly's model is larger than those for the other two models suggesting that the SGS velocity estimated by it is also different as one shall see later. The computed axial velocity along the centreline is compared to the measured values in Fig. 8.5 for the three u'_Δ

models. Practically there is no difference among the computed values which also agree well with measurements.

The variation of $\widetilde{\varepsilon}_c^+$ within the filtered flame is shown in Fig. 8.6 for the three u'_Δ models. The values obtained using Eqs. (3.51) and (3.56) for u'_Δ look similar, with the latter exhibiting more scatter. These large values are due to the effects of intermittency of the interface between the reacted jet fluid and entrained air at locations closer to the jet exit. The sub-grid SDR for Lilly's model, Eq. (3.50), is smaller due to the higher value of β'_c. This can be also interpreted that this model needs reduced dissipation to achieve the same flame length or this model overestimates u'_Δ.

Further insights can be obtained by studying the spatial variation of $\langle u'^*_\Delta \rangle$, which is time averaged u'^*_Δ, and a typical variation is shown in Fig. 8.7 for the mid-plane. Formally, this quantity is u'^*_Δ (see Eq. 8.1), which is normalised using the respective maximum value so that it varies from 0 to 1 and to make the comparison sensible because of the difference in β'_c. A significantly larger value and wider region is seen for the shear layer for Colin *et al.* model compared to Pope model and it seems to be the case even for non-reacting regions. Although Colin *et al.* model in Eq. (3.56) is derived from Eq. (3.51) there is no guarantee that the SGS velocities predicted with these two models will be the same for non-reacting regions. The maximum values of u'^*_Δ given in the figure occur near the jet exit. The same values inside the shear layer at $x \approx 150$ mm are 0.15, 0.3 and 1.19 m/s for Eqs. (3.50), (3.51) and (3.56) respectively. The peak value from the model in Eq. (3.56) is nearly 4 times larger compared to that from Eq. (3.51) for non-reacting regions where similar values are expected.

A second region having non-zero u'_Δ is seen in Fig. 8.7 for Eq. (3.51) and it results from flame induced effects. This flame induced u'_Δ inside the flame brush is of similar magnitude of those produced in the shear layer region. The flame induced SGS velocity is not visible for Colin *et al.* model as it is designed to exclude the dilatation effect. Nevertheless, the dimensional $\langle u'^*_\Delta \rangle$ inside the flame brush obtained using Eqs. (3.51) and (3.56) are found to be about 0.2 m/s , which is masked by the very large value in non-reacting region.

For Lilly's model in Eq. (3.50), the value of $\langle u'^*_\Delta \rangle$ in the region of the flame brush is about 0.02, which is an order of magnitude smaller than those of the other two models. Since the viscosity is computed dynamically, the dilatational part in Lilly's model coming from the strain rate is masked by the fact that the Smagorinsky constant goes to zero in quasi-laminar laminar

Table 8.1 Values of β'_c obtained using the SGS velocity models in Eqs. (3.50), (3.51) and (3.56).

Model	Lilly (Eq. 3.50)	Pope (Eq. 3.51)	Colin *et al.* (Eq. 3.56)
β'_c	10.0	6.0	6.0

region. For the same reason u'_Δ approaches zero even in the shear region close to the jet exit as seen in Fig. 8.7b. It is worth noting that Lilly's model was originally derived from the stresses without involving any dynamic constant.

The above analysis shows the potentials of the various SGS velocity models considered here. The flame length in this analysis is tuned by selecting an appropriate value for β'_c and this parameter alters the amount of sub-grid SDR in Eq. (8.1), which in turn alters the value of $\sigma^2_{c,\mathrm{sgs}}$ and thus $\overline{\dot{\omega}}$. Since $\beta'_c = \beta_c / f(C)$, the role of β'_c can be interpreted as that of controlling the magnitude of u'_Δ to maintain the correct value of $\widetilde{\varepsilon}_c$. The above analysis of u'_Δ models suggests that either the dilatation effect should be included in or a different value for c_2 is required for Eq. (3.56). Lilly's model in Eq. (3.50) is not suitable for the present flame conditions because the dynamic viscosity used in this model goes to zero as the magnitude of u'_Δ goes to zero in laminar regions irrespective of flame induced effects.

8.3.2 Comparison of statistics

Figure 8.8 shows axial velocity contours, both instantaneous and time averaged, along with a contour of mean progress variable of $\langle \widetilde{c} \rangle = 0.5$. These contours indicate the positions of the shear layer and flame, and it is seen that these two regions do not overlap. The jet becomes highly turbulent at $x \approx 200$ mm but the flame height is only about 100 mm. The acceleration through the flame tip is visible at $x \approx 100\,\mathrm{mm}$, which is consistent with the experimental data as seen in Fig. 8.5.

The computed rms of radial velocity fluctuation along the centreline is compared to the experimental data in Fig. 8.9 for the three SGS velocity models. The values shown here are only the resolved part, which is found to be insensitive to the u'_Δ model and the computed values agree well with the experimental data. A small underestimate is seen toward the tip of the flame and the reason for this will become clear in the next section.

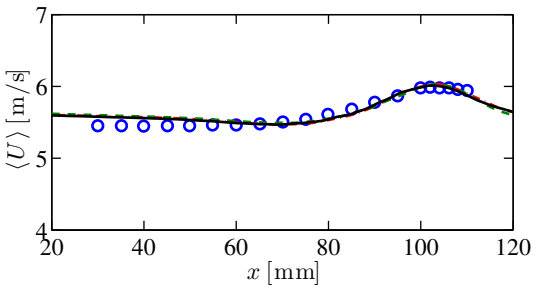

Fig. 8.5 Comparison of measured (symbols) and computed axial velocity along the centreline; Eq. 3.50 (dashed line), Eq. 3.51 (continuos line) and Eq. 3.56 (dash-dotted line).

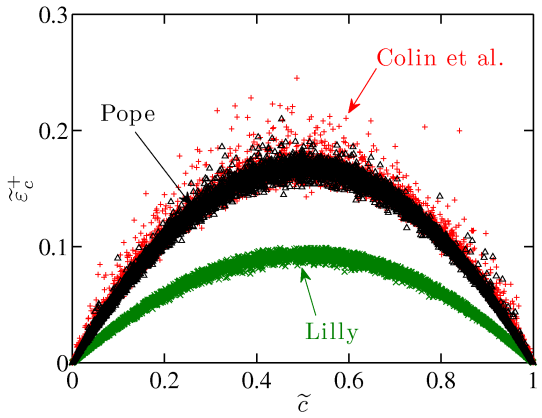

Fig. 8.6 Scatter plot of normalised sub-grid SDR versus progress variable, obtained using models of Eq. (3.50) (Lilly), Eq. (3.51) (Pope) and Eq. (3.56) (Colin *et al.*) for u'_Δ.

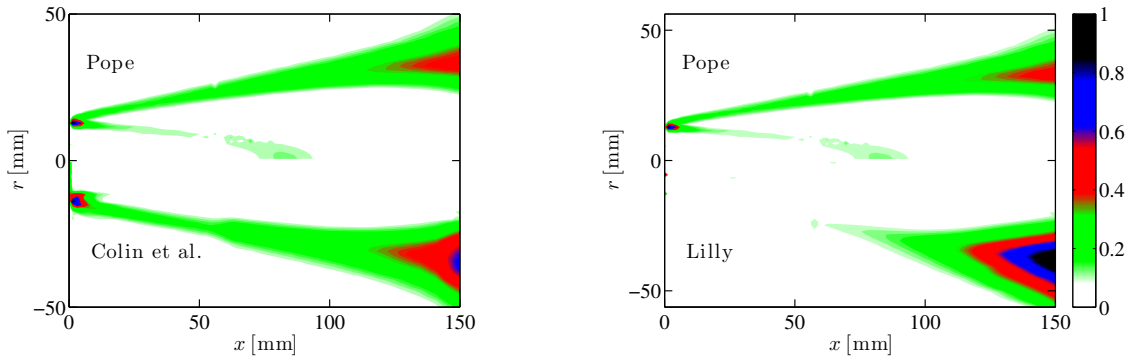

Fig. 8.7 Contours of $\langle u'^*_\Delta \rangle / \langle u'^*_\Delta \rangle_{\max}$ in the mid-plane. The values of $\langle u'^*_\Delta \rangle_{\max}$ are 0.15, 0.80 and 2.03 m/s respectively for Lilly, Pope and Colin *et al.* models.

The radial variations of computed mean and rms velocities are compared to the experimental results in Fig. 8.10. These statistics are also insensitive to the u'_Δ model, and $\langle U \rangle$, $\sqrt{\langle u'^2 \rangle}$, and $\sqrt{\langle v'^2_t \rangle}$ compare quite well with the experimental data. Some under-prediction is seen in both mean and rms radial velocities close to the jet exit and for $10 \leq r \leq 15$ mm, i.e in the flame region. This under-prediction is related to the dilatation effects and bimodal radial velocity, which is investigated in detail in the next section.

Reynolds- and Favre-averaged progress variable statistics are also available from the experiments by deducing the progress variable using bimodal velocity data [76]. This approach could not be used for the LES because the flame is broadened at least to size of $\Delta > \delta_{th}$. The transported methane-based progress variable is used here. The radial variations of the Favre-averaged progress variable are compared to those from the experiment in Fig. 8.11. Error

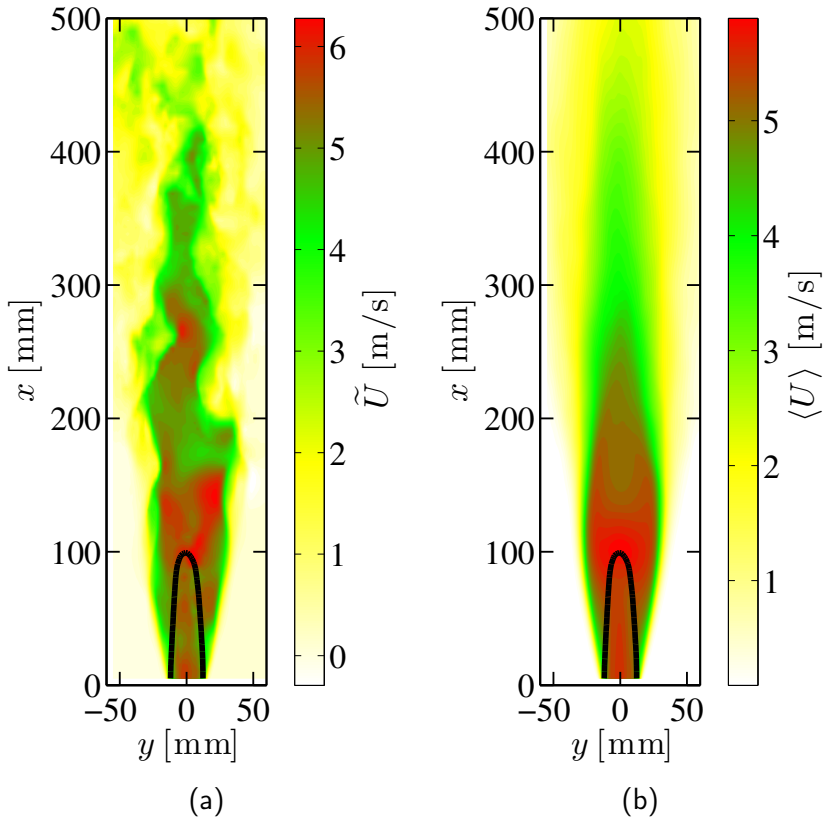

Fig. 8.8 Contours of (a) filtered, $\widetilde{U}$, and (b) mean, $\langle U \rangle$, axial velocity, obtained using Eq. (3.51) for SGS velocity. The mean progress variable isoline $\langle c \rangle = 0.5$, is also shown (black line).

bars are shown for the experimental data at $x = 40$ mm and similar errors can be expected for other locations. All SGS velocity models predict similar variation with some difference in the flame region ($10 \leq r \leq 15$ mm). However, the variations are within the error limits. The Reynolds averaged values are also shown for $x = 40$ mm and these values are computed using Eq. (3.18) [122]. Furukawa *et al.* [76] used an expression similar to Eq. (3.18) while analysing their experimental data. The significant difference between Favre- and Reynolds-averaged values observed in the figure implies that the variance of the progress variable in both experiments and LES is large. Since the flame is quasi-laminar at these locations, this variance is predominantly produced by combustion, which is at SGS level for the LES. The radial variations of resolved and SGS variance are shown in Fig. 8.12. The results from 23M grid will be discussed later in section 8.3.4. The SGS variance is nearly 4 to 5 times the resolved part for the location close to the jet exit and the resolved part is smaller than SGS part for all locations shown here. The relative contribution of the resolved part is increasing as one moves downstream because of a relative increase in turbulence level and flame thickness.

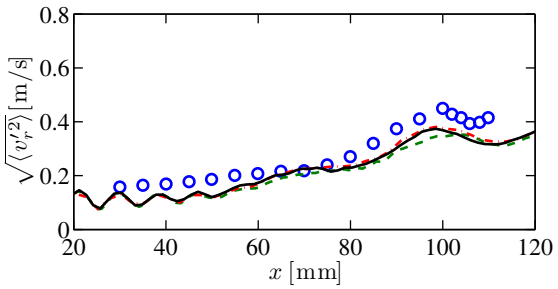

Fig. 8.9 Comparison of measured and computed centreline variation of radial rms velocity. The legend is as in Fig. 8.5.

These observations suggest that models for $\sigma^2_{c,\mathrm{sgs}}$ deduced from passive scalar scenario would be inappropriate, as discussed in the order analysis of §3.3.2.

Figure 8.13a compares the flame position deduced from the experiments by [76] using Favre-averaged progress variable of 0.5 with those obtained in the computations using $\langle\widetilde{c}\rangle = 0.5$. The flame brush width computed as $\delta_t = 1/|\partial\langle\widetilde{c}\rangle/\partial r|_{\max}$ is compared in Fig. 8.13b. These comparisons are good and the curves marked as 23M will be discussed in section 8.3.4. The flame brush thickness is slightly thinner for the Lilly and Colin et al models for u'_Δ, which is consistent with results in Fig. 8.11. The bubble in the measured flame position, suggested by the local minimum for r locations at $x = 60$ in Fig. 8.13a is not captured in the LES even with a grid of 23M. The reasons for this difference is unclear at this time and will be explored in future.

In summary, the results suggest that the flame statistics are not influenced by u'_Δ modelling if the parameter β_c is chosen carefully to match the measured flame length and the SGS variance of c is obtained using its transport equation. Thus, the unstrained flamelet model can be used with careful selection of SGS sub-modelling to capture the relevant physical aspects.

8.3.3 Bimodal of radial velocity

Figure 8.14, taken from [76] and shown here for the sake of convenience, shows that the bimodal behaviour is seen only for the radial velocity. This bimodal behaviour results from the flame intermittency, back and forth flame movement in the radial direction, as suggested by [73]. Since the flame is very thin because of the weak turbulence, a probe in the region of this flickering would register a fast turnover of cold and hot gases provided the probe size is small enough for the flame to be completely on either side of it at a given time. It is worth to note that this behaviour is less likely when the flame is situated inside the shear layer because the shear-generated turbulence is likely to increase the front thickness smearing the flame effects. The probe size, which is also the sampling size in the radial direction denoted as

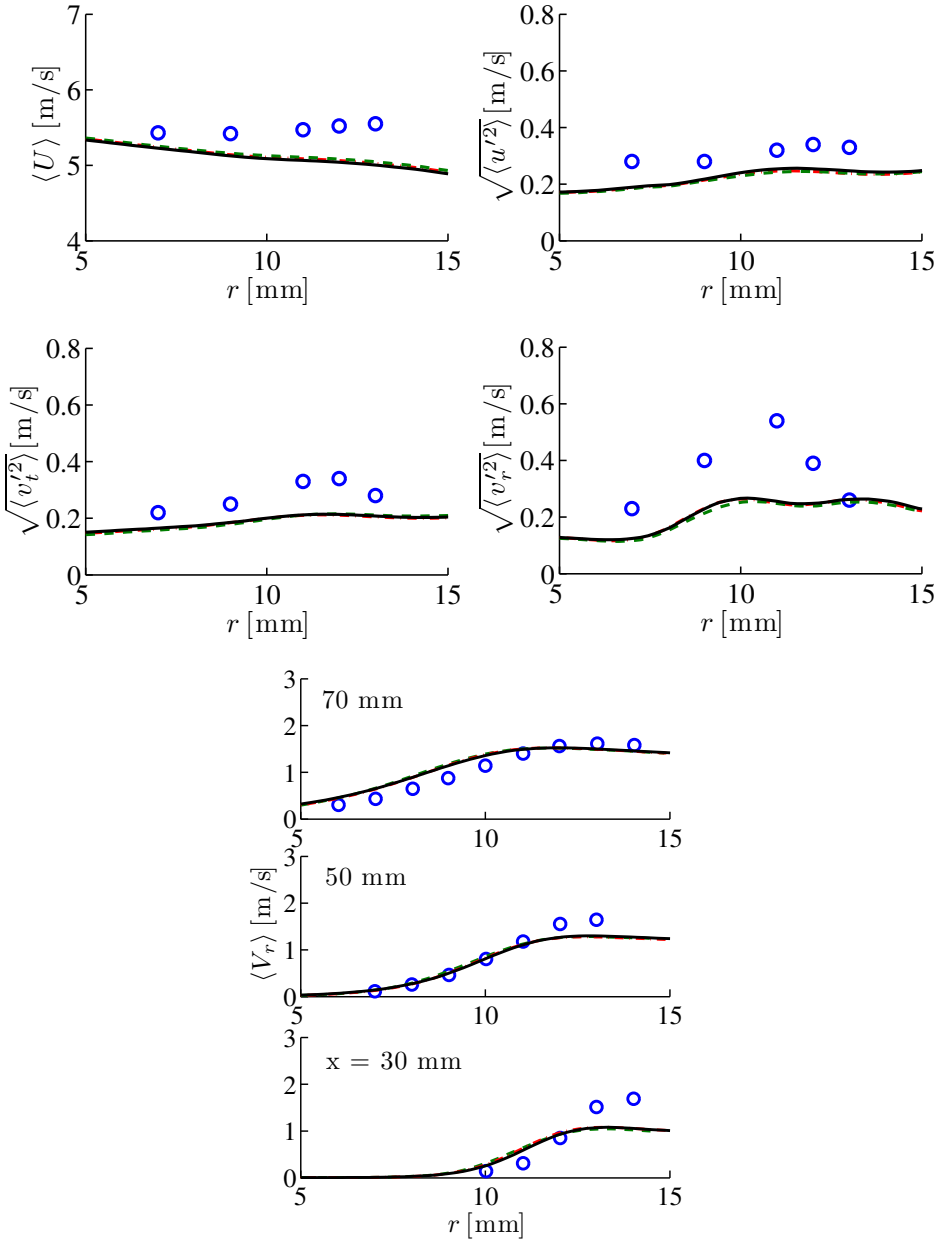

Fig. 8.10 Radial variations of mean and rms velocities in axial and radial directions. The rms of tangential velocity is also shown. The legend is as in Fig. 8.5.

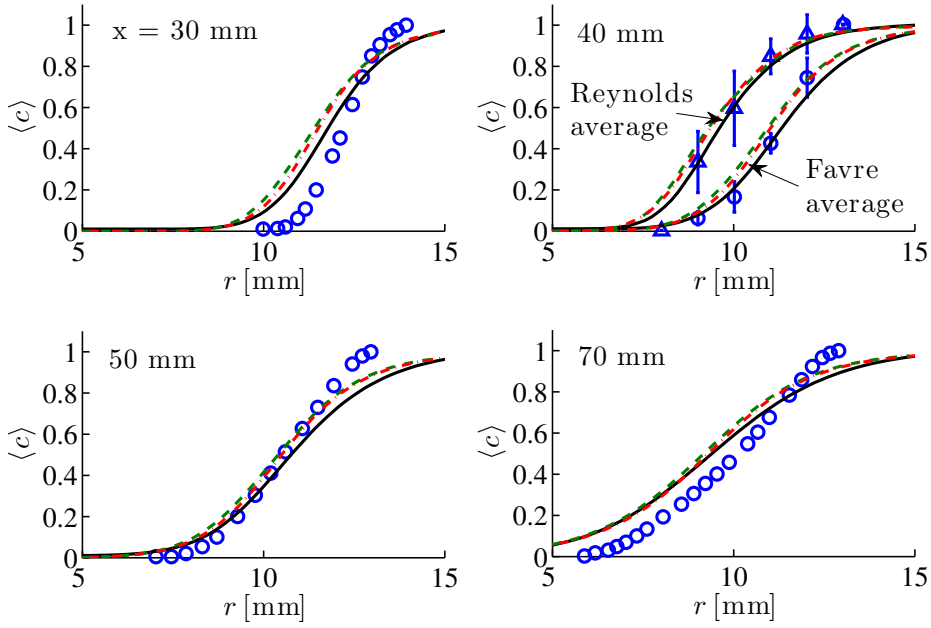

Fig. 8.11 Comparison of measured and computed Reynolds- and Favre-averaged progress variable variation. The legend is as in Fig. 8.5. Error bars are also shown.

δ_{samp} below, is a sphere with a diameter of about 0.2 mm in the experiments of Furukawa *et al.* [76]. A strong bimodal behaviour is observed in the experiments for $r = 11$ mm, where the probability of finding radial velocity equal to its mean is about one fifth of the maximum probability (or N/N_s) seen in Fig. 8.14. Let us denote this ratio using a symbol $\widehat{\Psi}$ which is 0.2 for the experimental flame.

Furukawa *et al.* [76] observed that the tangential rms velocity had a local maximum for $r = 11$ mm at $x = 50$ mm. LES results are shown in Fig. 8.15 only for the radial position of $r \approx 10.2$ mm, as at this position the strongest bimodal behaviour is observed. This position is slightly different from the experimental location of 11 mm, but within the experimental uncertainty of about 2 mm shown in Figure 8.13. These results show a weak sensitivity to the u'_Δ modelling. As for the experiments, the bimodal behaviour is seen only for the radial component and this behaviour is seen to depend on the sampling width, δ_{samp}, used for data collection in the LES. The bimodality is not seen when the $\delta_{\text{samp}} = 0.25$ mm for the LES is about that for the experiments, implying that the sampling point is always within the filtered flame which is suggested by the most probable radial velocity seen in the top row of Fig. 8.15. The results for the other two velocity components are similar to those from experiments. The bimodal behaviour starts to appear when the sampling width is increased gradually so that the radial movements of the filtered flame could be captured through the collected velocity data. The minimum sampling width for which bimodality occurs is found for $\delta_{\text{samp}} \approx 3$ mm for the

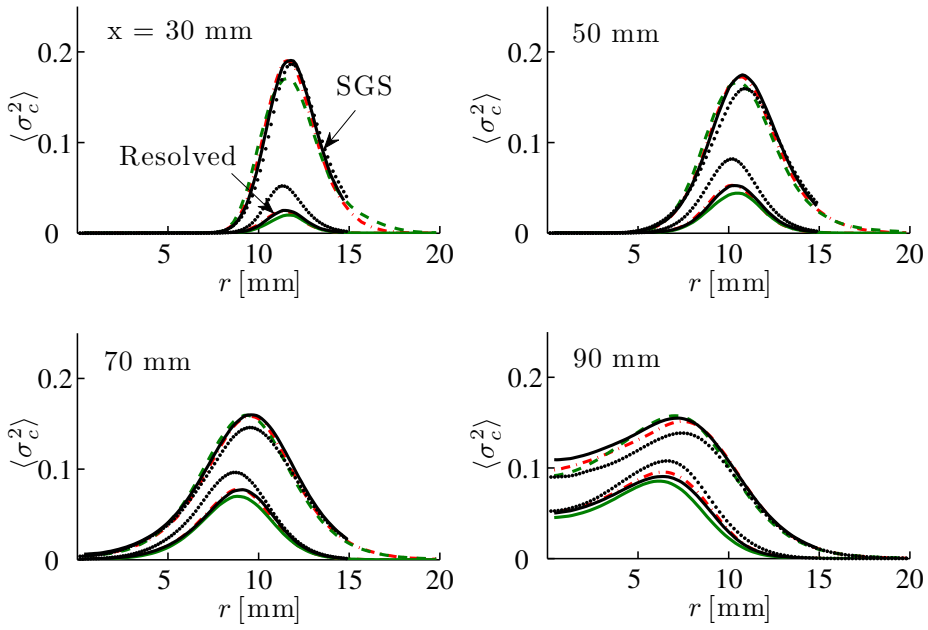

Fig. 8.12 Resolved and SGS variance of the progress variable. The legend is as in Fig. 8.5 and the dotted line is for 23M grid.

5.4M grid. When the sampling width is increased to 6 mm, which is $15\delta_{th}$ whereas it is about $0.5\delta_{th}$ for the experiments, then the bimodal behaviour is seen clearly with $\widehat{\Psi} \approx 0.5$, which is larger than the experimental value of 0.2. This is because, only the resolved velocity is used to construct the results shown in Figure 8.15. Strictly, one must use instantaneous velocity which includes the SGS fluctuations and these fluctuations are unavailable in LES framework unless the grid is refined to a level so that they become negligible. Indeed, one can refine the grid to have $\Delta < \delta_{th}$ so the filtered flame width become comparable to the flamelet thickness to capture the bimodal behaviour. The minimum filter width based on the numerical cell volume is about $\Delta^+ = 1.4$ for the 5.2M grid and to have a filter width of $\Delta^+ \approx 0.5$, which is comparable to the experimental probe size, one needs a grid with about 120M cells which would be a very expensive calculation and thus it is not attempted here. However, another grid with about 23M cells are used to test the sensitivity of the statistics shown above and this sensitivity is discussed next.

It is worth to note that the rms of radial velocity fluctuation is observed to have a local maximum near the sampling location and not the tangential component as noted for the experiment.

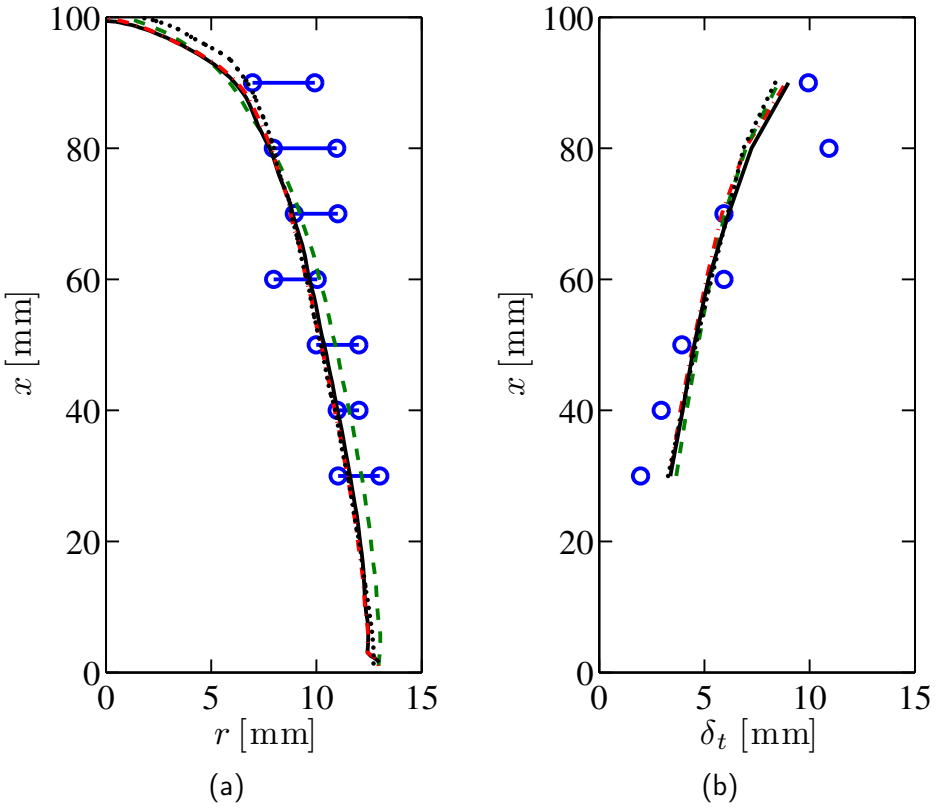

Fig. 8.13 The computed isolines of $\langle \widetilde{c} \rangle = 0.5$ are compared to the experimental result in (a) along with the uncertainty for the measurements. A comparison of flame brush thickness is shown in (b). The legend is as in Fig. 8.5. The dotted line is for 23M grid.

8.3.4 Influence of numerical grid

The first order statistics obtained using 23M grid are very similar to those from the 5.4M grid, for example see $\langle \widetilde{c} \rangle = 0.5$ contour shown in Fig. 8.13, and thus they are not shown here. The second order statistics show some sensitivity to grid resolution as seen in Fig. 8.16. Since the filter size decreases with increase in grid resolution the SGS velocity fluctuations are expected to decrease which is seen in this figure. However, u'_Δ values are still high compared to the rms values for the three velocity components and this is because the flame effects are responsible for predominant part of the SGS kinetic energy in these regions. The rms of axial velocity fluctuation for 23M grid compares well with the experimental data, tangential component does not show any sensitivity, and there is some improvement for the radial component. However, there is substantial difference between the computed and measured $\sqrt{\langle v_r'^2 \rangle}$ because of the missing subgrid part which is related to the flame intermittency effects. The probability distribution of V_r (indeed only the resolved part) does not seem to change between 5.4M

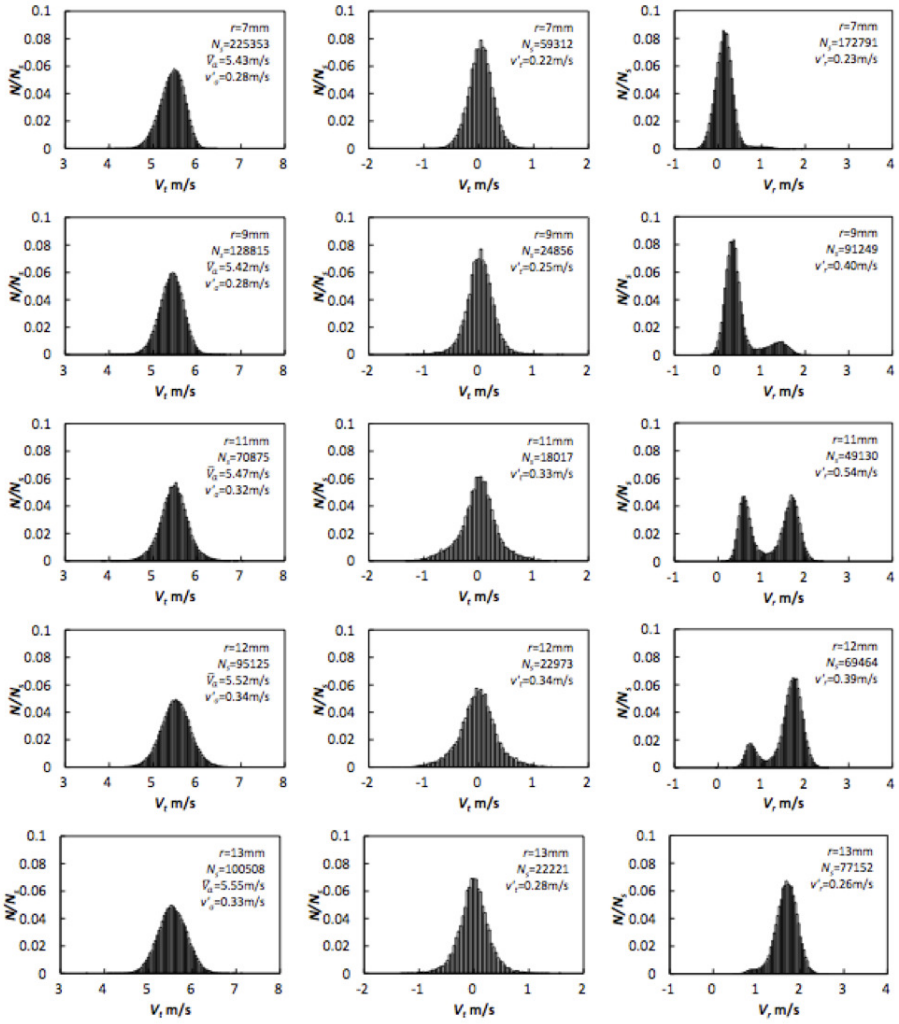

Fig. 8.14 Normalised histograms of [76] for three velocity components at $x = 50$ mm for various radial locations.

and 23M grids as shown in Fig. 8.15, suggesting that the statistics influenced by background turbulence effects are captured quite well and depends weakly on the grid. It is worth to note that the minimum sampling width at which bimodality in the radial velocity occurs has been observed to decrease in case of the 23M grid from 3 mm to 2.4 mm because the filtered flame width is also smaller in this case, as one would expect.

The SGS variance, $\sigma^2_{c,\mathrm{sgs}}$, does not seem to be sensitive to the grid resolution and the resolved part increases with grid resolution as one would expect. The difference in the resolved part also becomes less sensitive to the grid as one moves downstream. All of these points can be observed in results for 23M grid shown in Fig. 8.12. This suggests that the SGS combustion process is captured well by the reaction rate closure used for this study. However, the influence

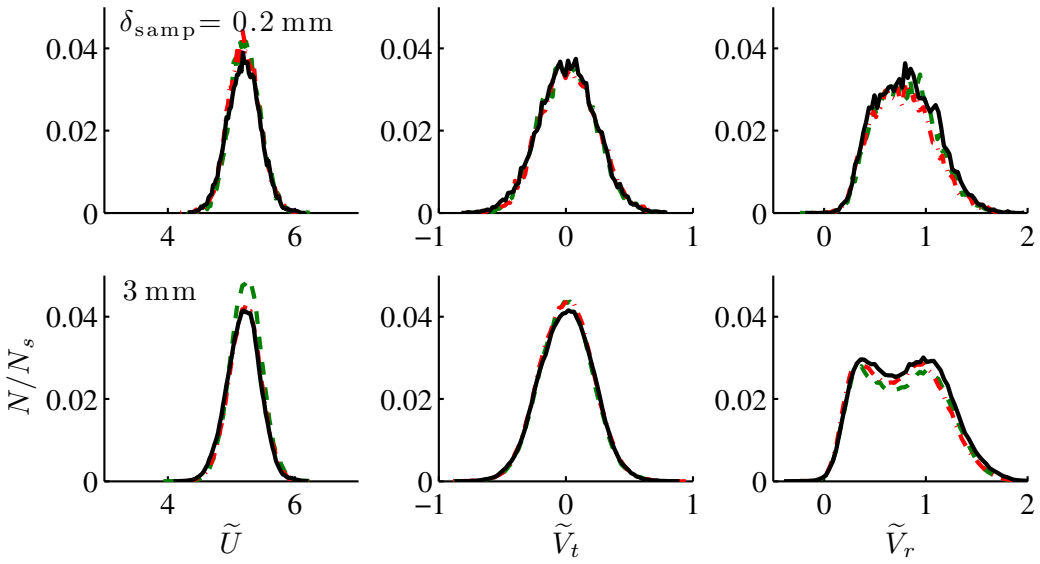

Fig. 8.15 Normalised histograms from LES for the three components of velocity at $x = 50$ mm and $r = 10.2$ mm for various values of δ_{samp}. The legend is as in Fig. 8.5. The result for 23M grid (•••) is also shown for v_r for comparison.

of the flame intermittency and resulting acceleration effects on the SGS velocity fluctuation is not represented directly by the commonly used SGS velocity models. Thus, the experimentally observed bimodality of the radial velocity is not captured fully.

8.3.5 Influence of bimodal PDF on statistics

The probability density function (PDF) constructed using the normalised histograms in Figs. 8.14 and 8.15 for the radial velocity is shown in Fig. 8.17 for the experimental and simulated flames. Although the shapes of measured, in Fig. 8.17a, and computed, the solid line in Fig. 8.17b, compare quite well there is a substantial difference. The analysis discussed below outlines reasons for this and tries to identify limitations of the LES and SGS models used in this study.

The bimodal PDF shown in the above figure can be seen as a double-Gaussian PDF for the given conditional means and variances. The first Gaussian results when the flame is completely on one side of the sampling region suggesting that the sampling point is in the unburnt mixture. The second Gaussian arises when the flame is on the other side, i.e. the sampling point lies completely in the burnt mixture. The required conditional means and variances of the radial velocity are obtained by collecting samples satisfying the conditions $\widetilde{c} \leq 0.05$ and $\widetilde{c} \geq 0.95$ for the two branches respectively. The PDF constructed thus is shown in Fig. 8.17b and it is worth noting that the velocities collected are only resolved components. The left branch has a mean of $\mu_L = 0.25$ and a standard deviation of $\sigma_L = 0.143$, and the right branch has

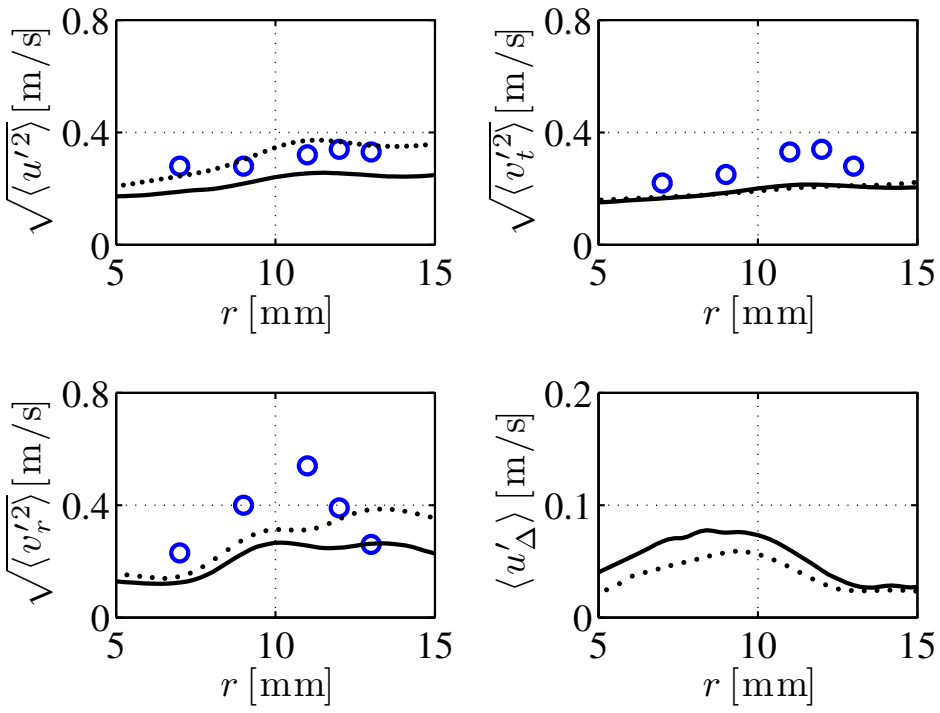

Fig. 8.16 RMS and SGS velocity profiles for 5.4M (continuous line) and 23M (dotted line) grids are compared to the experimental data (symbols) at $x = 50$ mm.

$\mu_R = 1.06$ and $\sigma_R = 0.176$. These two standard deviations are due to the turbulence effect (resolved part only) in unburnt and burnt conditions, and $\sigma_R > \sigma_L$ suggesting that the turbulent kinetic energy is increased across the flame as one would expect for the corrugated flamelets regime of premixed combustion. The computed radial velocity rms at the sampling location of $r = 10.2$ mm is about 0.33 as seen in Fig. 8.16 and this value is very close to the $(\sigma_R + \sigma_L)$. This observation can be further ascertained by collecting sample from a single numerical cell located at $r = 10.2$ mm and $x = 50$ mm, and constructing the PDF which is shown in Fig. 8.18. This PDF is compared to the a Gaussian model having the same mean as for the sample and a standard deviation of $(\sigma_L + \sigma_R)$. The mean value is almost equal to $\langle \widetilde{V}_r \rangle$ shown in Figure 8.10 for $r = 10.2$ mm and $x = 50$ mm.

The computed PDF in Fig. 8.17b suggests that the peak-to-peak velocity difference is about 0.98 m/s which compares well with that of about 1.1 m/s for the experimental data. However, the whole PDF is shifted to the lower values of the radial velocity in the computations, which comes from the missing flamelet physics in the SGS velocity models although the acceleration across the flame brush is captured quite well as seen in Figure 8.10. Reason for the above shift and the difference in peak-to-peak values is as follows. The measured V_r is the instantaneous velocity and it would not be easy to reconstruct this from LES because of the missing sub-grid

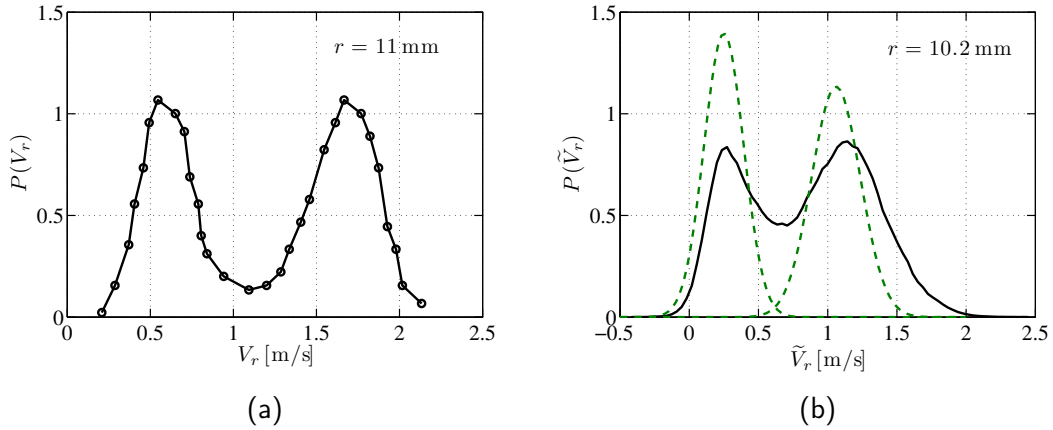

Fig. 8.17 The PDF of (a) measured and (b) computed radial velocity component v_r at $x = 50$ mm. The modelled values using two Gaussians are shown in (b) for the mean and variance of unburnt ($\widetilde{c} \leq 0.05$) and burnt ($\widetilde{c} \geq 0.95$) mixtures in LES data.

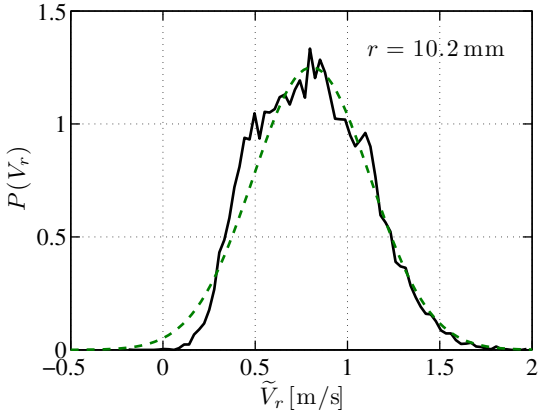

Fig. 8.18 The PDF (continuous line) obtained with samples collected from a single numerical cell ($\delta_{\text{samp}} < \Delta$) at $x = 50$ mm and $r = 10.2$ mm is compared to a Gaussian model with the same mean and standard deviation of $\sigma_L + \sigma_R$ (dashed line).

fluctuation and the u'_Δ models discussed in section 3.3.2 gives only a statistical measure of this fluctuation. Thus, one must be cautious while comparing PDFs generated from practical LES to those from measurements. If one uses very fine grid to make these fluctuations to be negligible then it is possible to compare the computed and measured PDFs and such LES, indeed it must be at least a coarse DNS (direct numerical simulation), is very expensive for the present flame conditions as noted in section 8.3.3.

The difference of 0.12 m/s in the peak-to-peak value is almost equal to the difference between the measured $\sqrt{\langle v_r'^2 \rangle} \approx 0.46$ (see Fig. 8.16) and $(\sigma_L + \sigma_R)$, where the later is the resolved part. This can be seen clearly if one consider the joint PDF $P(\varphi, \zeta) = P(\varphi|\zeta)P(\zeta)$,

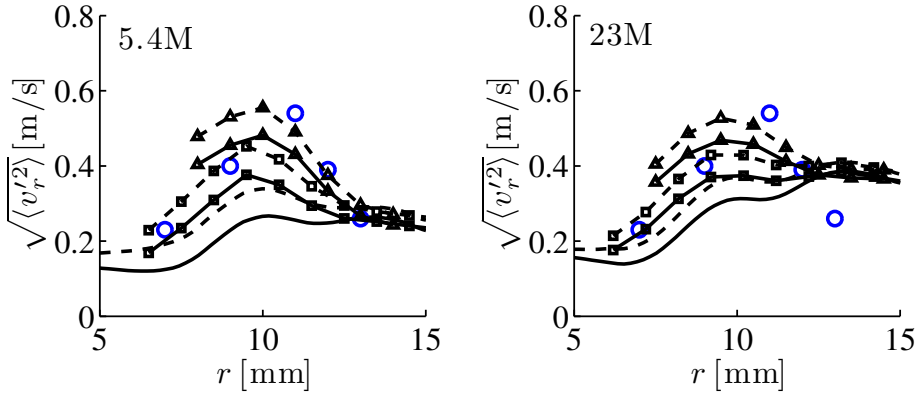

Fig. 8.19 Radial variation of measured (open circle) and computed (lines) rms of radial velocity at $x = 50$ mm. Results are shown for 5.4M (left) and 23M (right) grids. The effect of δ_{samp} is shown for $\delta_{\text{samp}} < \Delta$ (continuous line), $\delta_{\text{samp}} = 3$ mm for 5.4M or 2.4 mm for 23M grids (continuous line with squares); $\delta_{\text{samp}} = 6$ mm for 5.4M or 5 mm for 23M grids (continuous line with triangles). The dashed lines represent the corresponding curves when the $v'_{r,\Delta}$ is included.

where φ is the sample space variable for the velocity. If one presumes the marginal PDF to be BML as has been done by [136] and [29] then

$$\begin{aligned}\langle v_r'^2 \rangle = \int (\varphi_r - \langle \varphi_r \rangle)^2 \; P(\varphi_r|\zeta = 0) \; d\varphi_r + \int (\varphi_r - \langle \varphi_r \rangle)^2 \; P(\varphi_r|\zeta = 1) \; d\varphi_r \\ + \gamma \int (\varphi_r - \langle \varphi_r \rangle)^2 \; P(\varphi_r|\zeta) \; d\varphi_r \\ = \left(\sigma_L^2 + \sigma_R^2\right) + \gamma \sigma_f^2 \end{aligned} \tag{8.2}$$

where γ is the burning mode part of the marginal PDF, $P(\zeta)$ which can be obtained by integrating the β-PDF used for the reaction rate closure between the limits of $\zeta = 0.05$ and 0.95, but it is not straightforward to get σ_f as it is related to the effects of combustion on SGS velocity fluctuation. Furthermore, this contribution will be highly anisotropic in corrugated flamelets regime and a way to include this contribution to SGS modelling for a practical LES is an open question.

The above difference in the rms value results from the missing flame intermittency effects on the flow field in general for the SGS velocity models and grids used. The influence of this effect on the resolved part can be seen by increasing the width for the data sampling as one would expect. This is shown in Fig. 8.19 comparing the measured and computed rms of radial velocity (compare the solid lines). The sub-grid contribution has to come through u'_Δ. A good comparison of $\sqrt{\langle u'^2 \rangle}$ shown in Fig. 8.16 suggests that axial SGS velocity fluctuation is very small and thus the u'_Δ computed using Eq. (3.51) is taken to be from the radial and tangential fluctuations because the flame can be intermittent in these two directions. However,

their relative contribution is unknown and is not easy to estimate. But, if one presumes, guided by the experimental result in Fig. 8.14, that $v'_{r,\Delta} = u'_{\Delta}$ then the comparison of computed rms of radial velocity with experimental data improves further for flame regions. These observations apply equally for the results shown in Figure 8.19b for the 23M grid also. It seems that the flame induced anisotropy in the SGS velocity need to be captured as these effects are strong in corrugated flamelets regime and thus improved modelling strategies are required for the SGS velocity for practical LES.

Chapter 9

Concluding remarks

9.1 Summary and final considerations

The efficacy of sub-grid scale (SGS) reaction rate closure in the flamelet framework has been investigated In this work. Different turbulent premixed flame configurations, spanning from the corrugated flamelets regime to the distributed reaction zones regime of the premixed combustion diagram [180], have been investigated in order to assess potentials and limitations of flamelets modelling in the context of Large Eddy Simulation. As result of this investigation, two model for LES of turbulent lean premixed combustion of industrial relevance have been identified and analysed. These models involve algebraic closure and presumed PDF based closure, and they need a closure for the scalar dissipation rate of a progress variable, which is modelled with a newly developed expression [61]. The sensitivity to numerical and physical parameters has also been investigated. These models have been tested in the context of LES for the first time.

All simulations have been performed using Precise-MB, which requires multi-block structured grids. The scalar dissipation rate (SDR) based flamelets approaches investigated are shown to work well on relatively smaller grid sizes and with low computational cost.

The first investigation in this study has been on the efficacy of the SDR-based algebraic model for the SGS reaction rate closure in the light of recent developments on the modelling of filtered scalar dissipation rate of the reaction progress variable. The closure for the SGS scalar dissipation rate needs a model for the SGS velocity scale, u'_Δ. Four different models for this velocity scale have been studied and evaluated. These models are based on the shear stress related closure of Lilly [140], scale-similarity for velocity [196] and kinetic energy [11] and a hypothesis of constant kinetic energy transfer down to the filter scale, Δ. Results on piloted Bunsen flames lying in the thin reaction zone regime using these four models for u'_Δ suggests a weak sensitivity of the combustion model to these closures, at least for what concerns first and second order statistics. The model in Eq. (3.51) based on the scale-similarity of velocity works

well in general and thus it has been used for detailed analysis for further study. A modelled transport equation for SGS kinetic energy, k_{sgs}, is also used to obtain u'_{Δ}. The additional gain in computational accuracy is found to be small and this could be because of various *ad hoc* models used in k_{sgs} transport equation. Further work to develop appropriate models for the unclosed terms in k_{sgs} transport equation is needed. On the other hand, results of a quasi-laminar jet flame belonging to the corrugated flamelets regime show that these u'_{Δ} models do not contain physics relevant to represent the flame induced effects such as flame intermittency, thermal expansion effects and the associated anisotropic fluctuating velocity fields.

The algebraic filtered reaction rate closure given in Eqs. (2.19) and (2.22) is assessed to work well if the filter width normalised by the laminar flame thermal thickness, δ_{th}, is large, which is consistent with past DNS studies [61, 77]. This assessment is made by using two numerical grids having 1.5M and 4.2M cells on a piloted Bunsen flame configuration, and it is further verified on a bluff-body configuration. This condition is barely met for the 4.2M grid in the piloted Bunsen flames, thus the difference in the reacting flow results is because of underestimate of the fuel consumption rate when $\Delta^{+} < 1$ and this observation from LES is consistent with *a priori* analysis using DNS data [130]. This underestimate leads to lower peak temperature and product scalar mass fractions in a consistent manner. The results obtained using 1.5M grid compare quite well with the measurements and earlier RANS and LES results, and similar observation are done for the bluff body configuration when Δ is kept larger than the flame thickness. Such limit is not observed in case of unstrained flamelets model. These two models behave similarly well when the Karlovitz number, Ka, is relatively small, while effect of finite chemistry are evident when the Karlovitz number increases, which is the case in the buff body configuration. In this case both algebraic and unstrained flamelet closures have been observed to predict the recirculation zone and the statistics well when the local Karlovitz number is relatively small. Some statistics obtained using algebraic closure in regions downstream of the rear stagnation point of the recirculation zone do not compare well with experimental data because the high Damköhler number assumption used for this model may not hold, while the unstrained flamelet model do not show such sensitivity and is observed to work reasonably well, suggesting that the effect of finite rate chemistry is to be taken into account in these conditions. An additional analysis in this study has indicated that the local SGS Damköhler and Karlovitz numbers, rather than their integral values, may be in control of the model performance in a LES, and thus the correct statistical behaviour can be predicted if the combustion model is consistent with the physics at SGS level, which may be different to that at larger scales. This gives additional insights on flamelets capabilities in light of the recent advancement in the literature.

A weak sensitivity to the grid resolution has been observed for the unstrained flamelets model for all the flames analysed, at least when the grid satisfies the 80% turbulent kinetic energy criteria [196]. Other analysis show that the unstrained flamelets model is also insensitive to the choice of the progress variable, but strong gradients in the laminar flamelets may affect substantially minor species predictions when the variance is low on the burnt side. A substantial difference is observed between the results obtained using the unstrained and strained flamelet closures. These two closures are compared on the piloted flame configuration. Since the numerical grids employed for the simulations resolve most of the turbulent kinetic energy the SGS kinetic energy is expected to be small implying that the SGS eddies may be weak to impart any stretching effects on the flame front. This is similar to the views expressed by Poinsot *et al.* [189] while analysing their DNS data to investigate turbulent combustion regimes. Thus, using the SGS dissipation rate or any parameter of strained flamelets established in counterflow geometries to include the effects of SGS stretching is likely to overcompensate the SGS stretch effects compared to the influences of resolved dynamic eddies on the unstrained flamelet. Hence, the burning rate is underestimated by the strained flamelets leading to over prediction of fuel mass fraction and under-estimates of various reactive scalar mass fractions, suggesting that a dependence on the filter width should be included in the modelling of the SGS strain. The influences of resolved dynamic scales are inherently included in the unstrained flamelet closure through the various transport equations and their interactions. In particular, an order of magnitude analysis indicates that simple algebraic models for the progress variable variance would result in an inaccurate reaction rate. This is also verified by *a posterori* analysis in LES of different flames investigated. This central role of the SGS variance implies that it must be predicted accurately in the unstrained flamelets model and therefore a transport equation is necessary in this case. When the SGS variance is well predicted, as long as the most of the strain is at the resolved level, a simple unstrained flamelets model is sufficient to predict the flow field over different regimes. The importance of the SDR is evident in this case as it directly controls the SGS variance. Finally, the contribution of SGS variance of temperature and species has also been found to play a critical role in some configurations and under certain condition of turbulence, as the SGS level of fluctuation affects the macroscopic scales. A simple scaling used in this thesis has been found to be effective in including this influence into the main statistics.

The sensitivity to the model parameter β_c is also investigated in both algebraic and unstrained flamelets model. This parameter is related to the physics of flame front curvature effects induced by turbulence, chemical reactions, molecular dissipation, and their interactions at sub-grid level. This parameter was also shown to depend on heat release parameter and

turbulence Reynolds number in earlier studies [77, 79] and possibly on filter width also because of the influence of the above physical processes. Thus, a dynamic evaluation of this parameter is ideal and has been evaluated. A power-law based model has also been considered for the filtered scalar dissipation rate. The various statistics, specifically, averaged fuel mass fraction variation in radial direction at a number of axial positions has shown that the power-law based model is unable to see a flame when the filter size is of order of δ_{th} because the scale-similarity of the progress variable gradient does not hold. For this scale-similarity to hold, one needs a very fine grid, which is impractical. However, the scale-similarity of SGS velocity and filtered progress variable, $\widetilde{c}$, required for the dynamic evaluation of β_c is easy to satisfy on relatively small grids, and the only limitation is found to be the level of turbulence, which must be high enough in order to have a range o scales for the dynamic procedure to be effectively used. The various statistics obtained from LES compare well with the measured values of these quantities for the cases where this procedure is employed. The difference in various statistics in respect to results obtained with the empirical (static) evaluation of β_c is found to be small because the empirically determined β_c values for the configurations analysed are similar to the averaged value of β_c obtained in the dynamic evaluations, which is verified by analysing the PDF of β_c. The evolution of flame brush thickness with axial distance computed from LES results also compares quite well with measured values where they are available.

Effects of thermal dilatation on the SGS modelling have also been investigated by simulating a non-piloted flame lying in the corrugated flamelets regime. The turbulence-chemistry interaction in this case is driven by flame induced effects rather than shear-produced turbulence. The modelling of u'_Δ is expected to play a role and three different models treating the dilation effects differently have been considered for this analysis. The computed statistics compare well with the experimental results and the grid sensitivity of the statistics is found to be negligible in this configuration. There is some under-prediction for the statistics of radial velocity which was observed to be bimodal in experiments. Results suggest that the bimodal behaviour can only be seen if the sampling width is larger than Δ for situations with $\Delta > \delta_{th}$, which is typical for LES, and thus one would need very large grids to implicitly capture this behaviour in the current LE framework. If this condition is not met then the PDF is observed to be Gaussian rather than bimodal, because the filtered flame is thicker than the flamelet and will not move back and forth adequately about the sampling point to give bimodal behaviour. Nevertheless, this flame broadening due to filtering does not unduly influence the first order statistics, indicating that these statistics are not a good indicator of the appropriateness of a LES. This analysis suggests that the commonly used u'_Δ models are to be improved to handle SGS physics and this is specifically so for the corrugated flamelets regime because of the dominant effect of thermal

dilatation in this case.

In conclusion, the algebraic and unstrained flamelets models are found to be simple, accurate, computationally efficient and robust over a range a different conditions and configurations. The key role of the SDR has been demonstrated as it controls directly the reaction rate in the algebraic model, and it controls the variance of the SGS progress variable variance in the unstrained flamelets model, and this quantity has been shown to be fundamental for the modelling. Since finite rate chemistry can be taken into account in the unstrained flamelets, this model represents a valid choice in industrial and academic environments.

9.2 Future work

- The models developed in this thesis can be applied on a real combustor geometry in order to assess their relative performance on practical configurations; the success of this implementation will give additional useful information on the advantages and limitations of the flamelets modelling;
- The SGS kinetic energy transport equation can be employed to further investigate on the effects of dilation on the flow field. This investigation is conditional to the finding of appropriate models for the thermal dilation, which possibly account for anisotropy and are regime-adaptive. This will need investigations using both DNS and LES on different configurations.
- Despite the β-PDF has been shown to work reasonably well, alternative choices of the SGS PDFs can be used and tested for the pre-integration of the reaction rate, like the modified laminar flamelet PDF, in order to assess the relative model sensitivity. According to the literature, this type of PDFs may better represent bimodal behaviours at SGS level;
- An analysis on the interplay between turbulence, strain, heat release and pressure dilation and their influence on the size of the recirculation zone on bluff body configurationss would be beneficial for the understanding of this mode of combustion. Ideally, a unique scaling for both cold and reacting flow exists and can be found with this analysis;
- A significant contribution of rms temperature is lost at sub-grid scales in LES. Approximating this contribution using rms of progress variable is not always possible because the Lewis number is not always unity or may change in the flame, and may lead to inaccuracies as shown for example in §7.2.1 for Fig. 7.4. Improved models for rms

temperature which, for example, account for the covariance of temperature and progress variable are worth an investigation;

- Identify avenues to extend these models for partially premixed combustion of practical relevance would be worthwhile.

References

[1] Abdel-Gayed, R. G., Bradley, D., Hamid, M. N., and Lawes, M. (1984). Lewis number effects on turbulent burning velocity. *Proc. Combust. Inst.*, 20:505–512.

[2] Ahmed, I. and Swaminathan, N. (2013). Simulation of spherically expanding turbulent premixed flames. *Combust. Sci. Technol.*, 185(10):1509–1540.

[3] Ahmed, I. and Swaminathan, N. (2014). Simulation of turbulent explosion of hydrogen-air mixtures. *Int. J. Hydrogen Energy*, 39:80–115.

[4] Amzin, S. and Swaminathan, N. (2013). Computations of turbulent lean premixed combustion using CMC. *Combust. Theory Modelling*, 17(6):1125–1153.

[5] Amzin, S., Swaminathan, N., Rogerson, J. W., and Kent, J. H. (2012). Conditional moment closure for turbulent premixed flames. *Combust. Sci. Technol.*, 184(10-11):1743–1767.

[6] Anand, M. S. and Pope, S. B. (1985). Diffusion behind a line source in grid turbulence. In Bradbury, L. J. S., Durst, F., Launder, B. E., Schmidt, F. W., and Whitelaw, J. H., editors, *Turbulent Shear Flows*, volume 4, pages 46–61. Springer-Verlag, Berlin.

[7] Anand, M. S. and Pope, S. B. (1987). Calculations of premixed turbulent flames by PDF methods. *Combust. Flame*, 67(2):127–142.

[8] Anand, M. S., Zhu, J., Connor, C., and Razdan, M. (1999). Combustor flow analysis using an advanced finite-volume design system. In *International gas turbine and Aeroengine Congress and Exhibition*, volume 99-GT, page 273, Indianapolis. ASME.

[9] Andreini, A., Bianchini, C., and Innocenzi, A. (2014). Large eddy simulation of a bluff body stabilized lean premixed flame. *Journal of Combustion*, 2014(710254):18.

[10] Auzillon, P., Gicquel, O., Darabiha, N., Veynante, D., and Fiorina, B. (2012). A filtered tabulated chemistry model for LES of stratified flames. *Combust. Flame*, 159(2704-2717).

[11] Bardina, J., Ferziger, J. H., and Reynolds, W. C. (1980). Improved subgrid scale models for large-eddy simulation. *Am. Inst. Aeronaut. Astronaut.*, 80:1357.

[12] Batchelor, G. (1952). The effect of homogeneous turbulence on material lines and surfaces. *Proc. R. Soc. Lond. A*, 213(349–366).

[13] Bilger, R. W. (1993). Conditional moment closure for turbulent reacting flow. *Phys. Fluids*, 5:436–444.

[14] Birol, F. (2014). World energy investment outlook. Technical report, International Energy Agency, http://www.worldenergyoutlook.org/investment/.

[15] Blint, R. J. (1986). The relationship of the laminar flame width to flame speed. *Combust. Sci. Technol.*, 49:79–92.

[16] Boersma, B. J. (2000). Entrainment boundary conditions for free shear flows. *IJCFD*, 13:357–363.

[17] Boger, M., Veynante, D., Boughanem, H., and Trouvé, A. (1998). Direct numerical simulation analysis of flame surface density concept for large eddy simulation of turbulent premixed combustion. *Proc. Combust. Inst.*, 27:917–925.

[18] Borghi, R. (1990). Turbulent premixed combustion: Further discussions on the scales of fluctuations. *Combust. Flame*, 80(304-312).

[19] Bose, S. T., Moin, P., and You, D. (2010). Grid-independent large-eddy simulation using explicit filtering. *Phys. Fluids*, 22:105103–1–11.

[20] Bradley, D., Gaskell, P. H., Gu, X. J., and Sedaghat, A. (2005). Premixed flamelet modelling: Factors influencing the turbulent heat release rate source term and the turbulent burning velocity. *Combust. Flame*, 143:227–245.

[21] Bradley, D., Kwa, L. K., Lau, A. K. C., and Missaghi, M. (1988). Laminar flamelet modelling of recirculating premixed methane and propane-air combustion. *Combust. Flame*, 71:109–122.

[22] Bray, K. N. C. (1979). The interaction between turbulence and combustion. *Proc. Combust. Inst*, 17:223–233.

[23] Bray, K. N. C. (1980). Turbulent flows with premixed reactants. In Libby, P. A. and Williams, F. W., editors, *Turbulent Reacting Flows*, volume 44 of *Topics in Applied Physics*, chapter 4, pages 115–183. Springer Berlin Heidelberg.

[24] Bray, K. N. C. (1995). Turbulent transport in flames. *Proc. R. Soc. London*, 451:231–256.

[25] Bray, K. N. C. (2011). Laminar flamelets and the Bray, Moss, and Libby model. In Swaminathan, N. and Bray, K. N. C., editors, *Turbulent Premixed Flames*, chapter 2, pages 50–52. Cambridge University Press, Cambridge, UK.

[26] Bray, K. N. C., Champion, M., and Swaminathan, N. (2011). Scalar dissipation and mean reaction rates in premixed turbulent combustion. *Combust. Flame*, 158:2017–2022.

[27] Bray, K. N. C., Domingo, P., and Vervisch, L. (2005). Role of the progress variable in models for partially premixed turbulent combustion. *Combust. Flame*, 141:431–437.

[28] Bray, K. N. C., Libby, P. A., and Moss, J. B. (1984). Flamelet crossing frequencies and mean reaction rates in premixed turbulent combustion. *Combust. Sci. Technol.*, 41:143–172.

[29] Bray, K. N. C., Libby, P. A., and Moss, J. B. (1985). Unified modeling approach for premixed turbulent combustion – part I: General formulation. *Combust. Flame*, 61:87–102.

[30] Bray, K. N. C. and Moss, J. B. (1977). A unified statistical model of the premixed turbulent flame. *Acta Astronaut.*, 4:291–319.

[31] Bulat, G., Jones, W. P., and Marquis, A. J. (2014). NO and CO formation in an industrial gas-turbine combustion chamber using LES with the Eulerian sub-grid PDF method. *Combust. Flame*, 161(7):1804–1825.

[32] Butz, D., Gao, Y., Kempf, A. M., and Chakraborty, N. (2015). Large eddy simulations of a turbulent premixed swirl flame using an algebraic scalar dissipation rate closure. *Combust. Flame*, 162:3180–3196.

[33] Cant, R. S. (2011). RANS and LES modelling of turbulent combustion. In Echekki, T. and Mastorakos, E., editors, *Turbulent combustion modelling: Advances, new trends and perspectives*, pages 63–87. Springer, Heidelberg.

[34] Cant, R. S. and Mastorakos, E. (2008). *An Introduction to Turbulent Reacting Flows*. Imperial College Press.

[35] Chai, X. and Mahesh, K. (2012). Dynamic k-equation model for large eddy simulation of compressible flow. *J. Fluid Mech.*, 699:385–413.

[36] Chakraborty, N. and Cant, R. S. (2007). A priori analysis of the curvature and propagation terms of the flame surface density transport equation for large eddy simulation. *Phys. Fluids*, 19:105101.

[37] Chakraborty, N. and Cant, R. S. (2011). Effects of lewis number on flame surface density transport in turbulent premixed combustion. *Combust. Flame*, 158:1768–1787.

[38] Chakraborty, N. and Klein, M. (2008). A priori direct numerical simulation assessment of algebraic flame surface density models for turbulent premixed flames in the context of large eddy simulation. *Phys. Fluids*, 20:085108.

[39] Chakraborty, N., Rogerson, J. W., and Swaminathan, N. (2008). A priori assessment of closures for scalar dissipation rate transport in turbulent premixed flames using direct numerical simulation. *Phys. Fluids*, 20:045106.

[40] Chakraborty, N. and Swaminathan, N. (2011). Effects of Lewis number on scalar variance transport in premixed flames. *Flow Turb. Combust.*, 87:261–292.

[41] Chakravarthy, V. K. and Menon, S. (2001). Large-eddy simulation of turbulent premixed combustion in the flamelet regime. *Combust. Sci. Technol.*, 162:175–222.

[42] Charlette, F., Meneveau, C., and Veynante, D. (2002a). A power-law flame wrinkling model for LES of premixed turbulent combustion, part I: Nondynamic formulation and initial tests. *Combust. Flame*, 131:159–180.

[43] Charlette, F., Meneveau, C., and Veynante, D. (2002b). A power-law flame wrinkling model for LES of premixed turbulent combustion, part II: dynamic formulation. *Combust. Flame*, 131:181–197.

[44] Chatakonda, O., Hawkes, E. R., Aspden, A. J., Kerstein, A. R., Kolla, H., and Chen, J. H. (2013). On the fractal characteristics of low Damköhler number flames. *Combust. Flame*, 16:2422–2433.

[45] Chen, Y.-C. and Bilger, R. W. (2001). Simultaneous 2-D imaging measurements of reaction progress variable and OH radical concentration in turbulent premixed flames: instantaneous flame-front structure. *Combust. Sci. Technol.*, 167:187–222.

[46] Chen, Y.-C., Peters, N., Schneemann, G. A., Wruck, N., Renz, U., and Mansour, M. S. (1996). The detailed flame structure of highly stretched turbulent premixed methane-air flames. *Combust. Flame*, 107:223–244.

[47] Colin, O., Ducros, F., Veynante, D., and Poinsot, T. J. (2000). A thickened flame model for large eddy simulations of turbulent premixed combustion. *Phys. Fluids*, 12:1843.

[48] Colucci, P. J., Jaberi, F. A., Givi, P., and Pope, S. B. (1998). Filtered density function for large eddy simulation of turbulent reacting flows. *Phys. Fluids*, 10:499.

[49] Cook, A. W. (1997). Determination of the constant coefficient in scale similarity models of turbulence. *Phys. Fluids*, 9:1485.

[50] Cook, A. W. and Riley, J. J. (1994). A subgrid model for equilibrium chemistry in turbulent flows. *Phys. Fluids.*, 6(8):2868–2870.

[51] Cruz, A. P. D., Dean, A. M., and Granda, J. M. (2000). A numerical study of the laminar flame speed of stratified methane/air flames. *Proc. Combust. Inst.*, 28(2):1925–1932.

[52] Davidson, P. A. (2004). *Turbulence: An Introduction for Scientists and Engineers*. Oxford University Press.

[53] De, A. and Acharya, S. (2009). Large eddy simulation of a premixed Bunsen flame using a modified thickened-flame model at two Reynolds number. *Combust. Sci. Technol.*, 181(10):1231–1272.

[54] Deardorff, J. W. (1974). Three-dimensional numerical study of the height and mean structure of a heated planetary boundary layer. *Boundary-Layer Meteorology*, 7:81–106.

[55] Deardorff, J. W. (1980). Stratocumulus-capped mixed layers derived from a three-dimensional model. *Boundary-Layer Meteorol.*, 18:495–527.

[56] Dodoulas, I. A. and Navarro-Martinez, S. (2013). Large eddy simulation of premixed turbulent flames using the probability density function approach. *Flow Turb. Combust.*, 90:645–678.

[57] Domingo, P., Vervisch, L., Payet, S., and Hauguel, R. (2005). DNS of a premixed turbulent V flame and LES of a ducted flame using FSD-PDF subgrid scale closure with FPI-tabulated chemistry. *Combust. Flame*, 143:566–586.

[58] Doormaal, J. P. V. and Raithby, G. D. (1984). Enhancements of the simple method for predicting incompressible fluid flows. *Numerical Heat Transfer*, 7(2):147–163.

[59] Dunn, M. J., Masri, A. R., and Bilger, R. W. (2007). A new piloted premixed jet burner to study strong finite-rate chemistry effects. *Combust. Flame*, 151:46–60.

[60] Dunn, M. J., Masri, A. R., Bilger, R. W., Barlow, R. S., and Wang, G. H. (2009). The compositional structure of highly turbulent piloted premixed flames issuing into a hot coflow. *Proc. Combust. Inst.*, 32(2):1779–1786.

[61] Dunstan, T. D., Minamoto, Y., Chakraborty, N., and Swaminathan, N. (2013). Scalar dissipation rate modelling for large eddy simulation of turbulent premixed flames. *Proc. Combust. Inst.*, 34:1193–1201.

[62] Dunstan, T. D., Swaminathan, N., and Bray, K. N. C. (2012). Influence of flame geometry on turbulent premixed flame propagation: a DNS investigation. *J. Fluid Mech.*, 709:191–222.

[63] Duwig, C. (2007). Study of a filtered flame formulation for large eddy simulation of premixed turbulent flames. *Flow Turb. Combust.*, 79(4):433–454.

[64] Ferziger, J. H. (1997). *New Tools in Turbulence Modelling*, pages 29–47. Springer-Verlag Berlin Heidelberg.

[65] Ferziger, J. H. and Peric, M. (1999). *Computational Methods for Fluid Dynamics*. Springer.

[66] Fiorina, B., Veynante, D., and Candel, S. (2015). Modeling combustion chemistry in large eddy simulation of turbulent flames. *Flow Turb. Combust.*, 94:3–42.

[67] Fiorina, B., Vicquelin, R., Auzillon, P., Darabiha, N., Gicquel, O., and Veynante, D. (2010). A filtered tabulated chemistry model for LES of premixed combustion. *Combust. Flame*, 157:465–475.

[68] Frank, J. H., Kalt, P. A. M., and Bilger, R. W. (1999). Measurements of conditional velocities in turbulent premixed flames by simultaneous OH PLIF and PIV. *Combust. Flame*, 116:220–232.

[69] Frisch, U. (1996). *Turbulence, the legacy of A.N. Kolmogorov*. Cambridge University Press.

[70] Fureby, C. and Möller, S. I. (1995). Large eddy simulation of reacting flows applied to bluff body stabilized flames. *AIAA J.*, 33:2339–2347.

[71] Fureby, C., Tabor, G., Weller, H. G., and Gosman, A. D. (1997). A comparative study of subgrid scale models in homogenous isotropic turbulence. *Phys. Fluids*, 9:1416.

[72] Furukawa, J., Noguchi, Y., Hirano, T., and Williams, F. A. (2002). Anisotropic enhancement of turbulence in large-scale, low-intensity turbulent premixed flames. *J. Fluid Mech.*, 462:209–243.

[73] Furukawa, J. and Williams, F. A. (2003). Flamelet effects on local flow in turbulent premixed Bunsen flames. *Combust. Sci. Technol.*, 175:1835–1858.

[74] Furukawa, J., Yoshida, Y., Amin, V., and Williams, F. A. (2013a). Changes of gas velocities in passing through flamelets ina premixed turbulent Bunsen flame. *Combust. Sci. Technol.*, 185:200–211.

[75] Furukawa, J., Yoshida, Y., and Williams, F. A. (2013b). Evolution of gas velocities behind flamelets in a premixed turbulent bunsen flame. *Combust. Sci. Technol.*, 185:661–671.

[76] Furukawa, J., Yoshida, Y., and Williams, F. A. (2015). Structures of methane-air and propane-air turbulent prmixed Bunsen flames. *Combust. Sci. and Technol.*, in review.

[77] Gao, Y., Chakraborty, N., and Swaminathan, N. (2014a). Algebraic closure of scalar dissipation rate for large eddy simulations of turbulent premixed combustion. *Combust. Sci. Technol.*, 186:1309–1337.

[78] Gao, Y., Chakraborty, N., and Swaminathan, N. (2014b). Scalar dissipation rate transport in the context of LES for turbulent premixed flames with non-unity lewis number. *Flow Turb. Combust.*, Accepted.

[79] Gao, Y., Chakraborty, N., and Swaminathan, N. (2015). Dynamic closure of scalar dissipation rate for large eddy simulations of turbulent premixed combustion: A direct numerical simulations analysis. *Flow Turb. Combust.*, Accepted:DOI 10.1007/s10494–015–9631–3.

[80] Gardiner, C. W. (1985). *Handbook of stochastic methods*. Springer-Verlag, second edition.

[81] Germano, M., Piomelli, U., Moin, P., and Cabot, W. H. (1991). A dynamic subgrid-scale eddy viscosity model. *Phys. Fluids A*, 3:1760.

[82] Ghanshyam, S. T., Sundarajan, T., and Shet, U. S. P. (1999). Entrainment and mixing studies for a variable density confined jet. *Numerical Heat Transfer*, 35:205–223.

[83] Ghosal, S., Lund, T., Moin, P., and Akselvoll, K. (1995). A dynamic localization model for large-eddy simulation of turbulent flows. *J. Fluid Mech.*, 286:229–255.

[84] Giacomazzi, E., Battaglia, V., and Bruno, C. (2004). The coupling of turbulence and chemistry in a premixed bluff-body flame as studied by LES. *Combust. Flame*, 138:320–335.

[85] Gicquel, L. Y. M., Staffelbach, G., and Poinsot, T. (2012). Large eddy simulations of gaseous flames in gas turbine combustion chambers. *Prog. Energy Combust. Sci.*, 38:782–817.

[86] Gicquel, O., Darabiha, N., and Thévenin, D. (2000). Laminar premixed hydrogen/air counterflow flame simulation using flame prolungation of ILDM with differential diffusion. *Proc. Combust. Inst.*, 28:1901–1908.

[87] Givi, P. (2006). Filtered density function for subgrid scale modelling of turbulent combustion. *AIAA J.*, 44(1):16–23.

[88] Gubba, S. R., Ibrahim, S. S., and Malalasekera, W. (2012). Dynamic flame surface density modelling of flame deflagration in vented explosion. *Combust. Expl. Shock Waves*, 48:393–405.

[89] Gulder, O. (1990). Turbulent premixed flame propagation models for different combustion regimes. In *Symp. (Int.) on Combustion*, volume 23, pages 743–835, Pittsburg. The Combustion Institute.

[90] Hartung, G., Hult, J., Kaminsky, C. F., Rogerson, J. W., and Swaminathan, N. (2008). Effect of heat release on turbulence and scalar-turbulence interaction in premixed combustion. *Phys. Fluids*, 20:035110.

[91] Hawkes, E., Chatakonda, O., Kolla, H., Kerstein, A. R., and Chen, J. H. (2012). A petascale direct numerical simulation study of the modelling of flame wrinkling for large-eddy simulations in intense turbulence. *Combust. Flame*, 159:2690–2703.

[92] Hawkes, E. R. and Cant, R. S. (2001a). Implications of a flame surface density approach to large eddy simulation of premixed turbulent combustion. *Combust. Flame*, 126:1617–1629.

[93] Hawkes, E. R. and Cant, R. S. (2001b). Physical and numerical realizability requirements for flame surface density approaches. *Combust. Theory Model.*, 5:699–720.

[94] Haworth, D. C. and Pope, S. B. (2011). Transported probability density function methods for Reynolds-averaged and large-eddy simulations. In Echekki, T. and Mastorakos, E., editors, *Turbulent Combustion Modelling*. Springer.

[95] Hélie, J. and Trouvé, A. (1998). Turbulent flame propagation in partially premixed combustion. *Proc. Combust. Inst.*, 27(1):891–898.

[96] Herrmann, M. (2006). Numerical simulation of turbulent Bunsen flames with a level set flamelet model. *Combust. Flame*, 145:357–375.

[97] Hirschfelder, J. O., Curtiss, C. F., and Byrd, R. B. (1969). *Molecular theory of gases and liquids*. John Wiley & Sons.

[98] Hu, L. Y., Zhou, L. X., and Luo, Y. H. (2007). LES modelling of a swirling diffusion flame and validation of different SGS stress and combustion models. In *Fifth International Conference on Fluid Mechanics*, pages 119–122.

[99] Hughes, T. J. R., Wells, G. N., and Wray, A. A. (2004). Energy transfers and spectral eddy viscosity in large-eddy simulations of homogeneous isotropic turbulence: comparison of dynamic Smagorinsky and multiscale models over a range of discretizations. *Phys. Fluids*, 16:4044.

[100] Im, H. G., Lund, T. S., and Ferziger, J. H. (1997). Large eddy simulation of turbulent front propagation with dynamic subgrid models. *Phys. Fluids*, 38:3826–3833.

[101] Janicka, J. and Sadiki, A. (2005). Large eddy simulation of turbulent combustion systems. *Proc. Combust. Inst.*, 30:537–547.

[102] Jones, W. P., Marquis, A. J., and Prasad, V. N. (2012). LES of a turbulent premixed swirl burner using the eulerian stochastic field method. *Combust. Flame*, 159:3079–3095.

[103] Jones, W. P., Marquis, A. J., and Wang, F. (2015). Large eddy simulation of a premixed propane turbulent bluff body flame using the eulerian stochastic field method. *Fuel*, 140:514–525.

[104] Jones, W. P. and Navarro-Martinez, S. (2007). Large eddy simulation of autoignition with a sub-grid probability density method. *Combust. Flame*, 150:170–187.

[105] Kaul, C. and Raman, V. (2013). Analysis of a dynamic model for subfilter scalar dissipation rate in large eddy simulation based on the subfilter scalar variance transport equation. *Combust. Theory Model.*, 17(5):804–834.

[106] Kee, R. J., Grcar, J. F., Smooke, M. D., and Miller, J. A. (1985). A fortran program for modeling steady laminar one-dimensional premixed flames. Technical Report SAND85-8240, Sandia National Labortories.

[107] Kemenov, K. A. and Pope, S. B. (2011). Molecular diffusion effects in LES of a piloted methane-air flame. *Combust. Flame*, 158:240–254.

[108] Keppeler, R. and Pfitzner, M. (2015). Modelling of Landau–Darrieus and thermo-diffusive instability effects for CFD simulations of laminar and turbulent premixed combustion. *Combust. Theory Model.*, 19(1):1–28.

[109] Kerstein, A., Ashurst, W., and Williams, F. A. (1988). Field equation for interface propagation in an unsteady homogeneous flow field. *Phys. Rev. A*, 33:2728–2731.

[110] Kerstein, A. R. (1991). Linear-eddy modeling of turbulent transport. Part 6. Microstructure of diffusive scalar mixing fields. *J. Fluid Mech.*, 231:361–394.

[111] Kirkpatrick, M. P., Armfield, S. W., Masri, A. R., and Ibrahim, S. S. (2003). Large eddy simulation of a propagating turbulent premixed flame. *Flow Turb. Combust.*, 70:1–19.

[112] Klein, M., Sadiki, M., and Janicka, J. (2002). A digital filter based generation of inflow data for spatially developing direct numerical or large eddy simulations. *J. Comp. Phys.*, 186:652–665.

[113] Klimenko, A. Y. and Bilger, R. W. (1999). Conditional moment closure for turbulent combustion. *Prog. Energy Combust. Sci.*, 25(6):595–687.

[114] Knikker, R., Veynante, D., and Meneveau, C. (2002). *A priori* testing of a similarity model for large eddy simulations of turbulent premixed combustion. *Proc. Combust. Inst.*, 29:2105–2111.

[115] Knikker, R., Veynante, D., and Meneveau, C. (2004). A dynamic flame surface density model for large eddy simulations of turbulent premixed combustion. *Phys. Fluids*, 16:91.

[116] Knudsen, E., Kolla, H., Hawkes, E. R., and Pitsch, H. (2013). LES of a premixed jet flame DNS using a strained flamelet model. *Combust. Flame*, 160:2911–2927.

[117] Knudsen, E. and Pitsch, H. (2008). A dynamic model for the turbulent burning velocity for large eddy simulation of premixed combustion. *Combust. Flame*, 154(4):740–760.

[118] Knudsen, E. and Pitsch, H. (2012). Capabilities and limitations of multi-regime flamelet combustion models. *Combust. Flame*, 159:242–264.

[119] Kolla, H. (2010). *Scalar dissipation rate based flamelet modelling for turbulent premixed flames*. PhD thesis, University of Cambridge, Cambridge, UK.

[120] Kolla, H., Rogerson, J. W., Chakraborty, N., and Swaminathan, N. (2009). Scalar dissipation rate modeling and its validation. *Combust. Sci. Technol.*, 181:518–535.

[121] Kolla, H. and Swaminathan, N. (2010a). Strained flamelets for turbulent premixed flames, I: Formulation and planar flame results. *Combust. Flame*, 157:943–954.

[122] Kolla, H. and Swaminathan, N. (2010b). Strained flamelets for turbulent premixed flames II: Laboratory flame results. *Combust. Flame*, 157:1274–1289.

[123] Kolla, H. and Swaminathan, N. (2011). Influence of turbulent scalar mixing physics on premixed flame propagation. *Journal of Combustion*, 2011:451351.

[124] Krajnovic, S. and Davidson, L. (2002). A mixed one-equation subgrid model for large-eddy simulation. *International Journal of Heat and Fluid Flow*, 23:413–425.

[125] Kravchenko, A. and Moin, P. (2000). Numerical studies of flow over a circular cylinder at $\mathrm{Re}_d = 3900$. *Phys. Fluids*, 12:403–417.

[126] Kronenburg, A. and Mastorakos, E. (2011). The conditional moment closure model. In Echekki, T. and Mastorakos, E., editors, *Turbulent Combustion Modelling*. Springer Science.

[127] Kuenne, G., Seffrin, F., Fuest, F., Stahler, T., Ketelheun, A., Geyer, D., Janicka, J., and Dreizler, A. (2012). Experimental and numerical analysis of a lean premixed stratified burner using 1D Raman/Rayleigh scattering and large eddy simulation. *Combust. Flame*, 159:2669–2689.

[128] Landenfeld, T., Sadiki, A., and Janicka, J. (2002). A turbulence-chemistry interaction model based on a multivariate presumed beta-PDF method for turbulent flames. *Flow Turb. Combust.*, 68:111–135.

[129] Langella, I., Swaminathan, N., Gao, Y., and Chakraborty, N. (2015a). Assessment of dynamic closure for premixed combustion LES. *Combust. Theory Model.*, 19:628–656.

[130] Langella, I., Swaminathan, N., Gao, Y., and Chakraborty, N. (2015b). LES of premixed combustion: Sensitivity to SGS velocity modelling. *Combust. Sci. Technol.*, in review.

[131] Lecocq, G., Richard, S., Colin, O., and Vervisch, L. (2010). Gradient and counter-gradient modeling in premixed flames: theoretical study and application to the LES of a lean premixed turbulent swirl-burner. *Combust. Sci. Technol.*, 182:465–479.

[132] Lecocq, G., Richard, S., Colin, O., and Vervisch, L. (2011). Hybrid presumed pdf and flame surface density approaches for large-eddy simulation of premixed turbulent combustion: Part 1: formalism and simulation of a quasi-steady burner. *Combust. Flame*, 158:1201–1214.

[133] Lee, D. and Huh, K. Y. (2012). Validation of analytical expressions for turbulent burning velocity in stagnating and freely propagating turbulent premixed flames. *Combust. Flame*, 159:1576–1591.

[134] Leonard, A. (1974). Energy cascade in large-eddy simulations of turbulent fluid flows. *Adv. in Geophysics A*, 18:237–248.

[135] LeVeque, R. J. (2007). *Finite Volume Methods for Hyperbolic Problems*. Cambridge University Press.

[136] Libby, P. A. and Bray, K. N. C. (1980). Implications of the laminar flamelet model in premixed turbulent combustion. *Combust. Flame*, 39:33–41.

[137] Libby, P. A., Bray, K. N. C., and Moss, J. B. (1979). Effect of finite reaction rate and molecular transport in premixed turbulent combustion. *Combust. Flame*, 34:285–301.

[138] Libby, P. A. and Williams, F. A. (1982). Structure of laminar flamelets in premixed turbulent flames. *Combust. Flame*, 44:287–303.

[139] Lilly, D. K. (1966). On the application of the eddy viscosity concept in the inertial sub-range of turbulence. Technical Report 123, NCAR, Boulder, CO, USA.

[140] Lilly, D. K. (1967). The representation of small-scale turbulence in numerical simulation experiments. In Goldstine, H. H., editor, *Proceedings of the IBM Scientific Computing Symposium on Environmental Sciences*, number 320-1951, pages 195–210. IBM.

[141] Lilly, D. K. (1992). A proposed modification of the Germano subgrid scale closure method. *Phys. Fluids A*, 4:633–635.

[142] Lindstedt, R. P. (2011). Transported probability density function methods for premixed turbulent flames. In Swaminathan, N. and Bray, K. N. C., editors, *Turbulent Premixed Flames*, chapter 2, pages 114–121. Cambridge University Press, Cambridge, UK.

[143] Lindstedt, R. P. and Vaos, E. M. (2006). Transported PDF modeling of high-Reynolds-number premixed turbulent flames. *Combust. Flame*, 145:495–511.

[144] Lipatnikov, A. N. and Chomiak, J. (2010). Effects of premixed flames on turbulence and turbulent scalar transport. *Prog. Energy Combust. Sci.*, 36:1–102.

[145] Lipatnikov, A. N. and Sabelnikov, V. A. (2013). Transition from countergradient to gradient scalar transport in developing premixed turbulent flames. *Flow Turb. Combust.*, 90:401–418.

[146] Lutz, A. E., Kee, R. J., Grcar, J. F., and Rupley, F. P. (1997). OPPDIF: a fortran program for computing opposed-flow diffusion flames. Technical Report SAND96-8243, Sandia National Laboratories.

[147] Ma, T., Gao, Y., Kempf, A. M., and Chakraborty, N. (2014). Validation and implementation of algebraic LES modelling of scalar dissipation rate for reaction rate closure in turbulent premixed combustion. *Combust. Flame*, page DOI:10.1016/j.combustflame.2014.05.023.

[148] Maas, U. and Pope, S. B. (1992). Implementation of simplified chemical kinetics based on low-dimensional manifold. *Proc. Combust. Inst.*, 24:719–729.

[149] Magnussen, B. F. and Hjertager, B. H. (1977). On the mathematical modeling of turbulent combustion with special emphasis on soot formation and combustion. In *Symp. (Int.) on Combustion*, volume 16, pages 719–729. The Combustion Institute.

[150] Mantel, T. and Bilger, R. W. (1995). Some conditional statistics in a turbulent premixed flame derived from direct numerical simulations. *Combust. Sci. Technol.*, 110-111:393–417.

[151] Martin, S. M., Kramlich, J. C., Kosaly, G., and Riley, J. J. (2003). The premixed conditional moment closure method applied to idealized lean premixed gas turbine combustors. *J. Eng. Gas Turb. Power*, 125(4):895–900.

[152] Matalon, M. (2009). Flame dynamics. *Proc. Combust. Inst.*, 32:57–82.

[153] Mathew, J., Lechner, R., Foysi, H., Sesterhenn, J., and Friedrich, R. (2003). An explicit filtering method for large eddy simulation of compressible flows. *Phys. Fluids*, 15:2279–2289.

[154] Meneveau, C. and Katz, J. (2000). Scale-invariance and turbulence models for large-eddy simulation. *Annu. Rev. Fluid Mech.*, 32:1–32.

[155] Meneveau, C. and Poinsot, T. (1991). Stretching and quenching of flamelets in premixed turbulent combustion. *Combust. Flame*, 86:311–332.

[156] Menon, S., Yeung, P.-K., and Kim, W.-W. (1995). Effect of subgrid models on the computed interscale energy transfer in isotropic turbulence. *Computers & Fluids*, 25(2):165–180.

[157] Mercier, R., Moureau, V., Veynante, D., and Fiorina, B. (2015a). LES of turbulent combustion: on the consistency between flame and flow filter scales. *Proc. Combust. Inst*, 35:1359–1366.

[158] Mercier, R., Schmitt, T., Veynante, D., and Fiorina, B. (2015b). The influence of combustion SGS submodels on the resolved flame propagation. Application to the LES of the Cambridge stratified flames. *Proc. Combust. Inst*, 35:1259–1267.

[159] Métais, O. and Lesieur, M. (1992). Spectral large-eddy simulation of isotropic and stably stratified turbulence. *J. Fluid Mech.*, 239:157–194.

[160] Meyers, J. and Sagaut, P. (2006). On the model coefficients for the standard and the variational multi-scale Smagorinsky model. *J. Fluid Mech.*, 569:287–319.

[161] Meyers, J. and Sagaut, P. (2007). Is plane-channel flow a friendly case for the testing of large-eddy simulation subgrid-scale models? *Phys. Fluids*, 19:048105.

[162] Möller, S. I., Lundgren, E., and Fureby, C. (1996). Large eddy simulation of unsteady combustion. *Proc. Combust. Inst.*, 26:241–248.

[163] Moureau, V., Domingo, P., and Vervisch, L. (2011). From large-eddy simulation to direct numerical simulation of a lean premixed swirl flame: filtered laminar flame-PDF. *Combust. Flame*, 158:1340–1357.

[164] Moureau, V., Fiorina, B., and Pitsch, H. (2008). A level set formulation for premixed combustion LES considering the turbulent flame structure. *Combust. Flame*, 156(4):801–812.

[165] Mueller, C., Driscoll, J. F., Reuss, D., Drake, M., and Rosalik, M. (1998). Vorticity generation and attenuation as vortices convect through a premixed flame. *Combust. Flame*, 112:342–358.

[166] Mukhopadhyay, S., Bastiaans, R. J. M., van Oijen, J. A., and de Goey, L. P. H. (2015). Analysis of a filtered flamelet approach for coarse DNS of premixed turbulent combustion. *Fuel*, 144:388–399.

[167] Mura, A. and Borghi, R. (2003). Towards an extended scalar dissipation equation for turbulent premixed combustion. *Combust. Flame*, 133:193–196.

[168] Nandula, S. P. (2003). *Lean premixed flame structure in intense turbulence: Rayleigh/Raman/LIF measurements and modeling*. Dissertation, Vanderbilt University, Nashville, Tennessee.

[169] Nandula, S. P., Pitz, R. W., Barlow, R. S., and Fiechtner, G. J. (1996). Rayleigh/Raman/LIF measurements in a turbulent lean premixed combustor. In *34th Aerospace Sciences Meeting*, number AIAA-96-0937, Reno, Nevada, USA.

[170] Nguyen, P., Vervisch, L., Subramanian, V., and Domingo, P. (2010). Multidimensional flamelet-generated manifolds for partially premixed combustion. *Combust. Flame*, 157:43–61.

[171] Niceno, B., Dhotre, M. T., and Deen, N. G. (2008). One-equation sub-grid scale (SGS) modelling for Euler-Euler large eddy simulation (EELES) of dispersed bubbly flow. *Chemical Engineering Science*, 63:3923–3931.

[172] Nicoud, F. and Ducros, F. (1999). Subgrid-scale stress modelling based on the square of the velocity gradient tensor. *Flow Turb. Combust.*, 62:183–200.

[173] Nogenmyr, K.-J., Fureby, C., Bai, X. S., Petersson, P., Collin, R., and Linne, M. (2009). Large eddy simulation and laser diagnostic studies on a low swirl stratified premixed flame. *Combust. Flame*, 156:25–36.

[174] Nomura, K. and Elghobashi, S. (1992). Mixing characteristics of an inhomogeneous scalar in isotropic and homogeneous sheared turbulence. *Phys. Fluids A*, 4:606.

[175] O'Young, F. and Bilger, R. W. (1997). Scalar gradient and related quantities in turbulent premixed flames. *Combust. Flame*, 109:682–700.

[176] Pan, J. C., Vangsness, M. D., and Ballal, D. R. (1992). Aerodynamics of bluff-body stabilized confined turbulent premixed flames. *J. Eng. Gas Turb. and Power*, 114:783–789.

[177] Pan, J. C., Vangsness, M. D., Heneghan, S. P., and Ballal, D. R. (1991a). Laser diagnostic studies of bluff-body stabilized confined turbulent premixed flames. In *Combustion fundamentals and applications: spring technical meeting*, volume 1991, pages 379–384. Combustion Institute, Central States Section.

[178] Pan, J. C., Vangsness, M. D., Heneghan, S. P., and Ballal, D. R. (1991b). Scalar measurements in bluff body stabilized flames using cars diagnostics. In *36th International gas turbine and aeroengine congress: Separate papers*, volume 1991. ASME.

[179] Pasquier, N., Lecordier, B., Trinite, M., and Cessou, A. (2007). An experimental investigation of flame propagation through a turbulent stratified mixture. *Proc. Combust. Inst.*, 31(1):1567–1574.

[180] Peters, N. (2000). *Turbulent Combustion*. Cambridge University Press.

[181] Pfadler, S., Leipertz, A., and Dinkelacker, F. (2008). Systematic experiments on turbulent premixed Bunsen flames including turbulent flux measurements. *Combust. Flame*, 152:616–631.

[182] Pierce, C. D. and Moin, P. (1998). A dynamic model for subgrid-scale variance and dissipation rate of a conserved scalar. *Phys. Fluids.*, 10(12):3041–3044.

[183] Piomelli, U. (1993). High Reynolds number calculations using the dynamic subgrid scale stress model. *Phys. Fluids A*, 5:1484.

[184] Pitsch, H. (2005). A consistent level set formulation for large-eddy simulation of premixed turbulent combustion. *Combust. Flame*, 143(4):587–598.

[185] Pitsch, H. (2006). Large-eddy simulation of turbulent combustion. *Annu. Rev. Fluid Mech.*, 38:453–482.

[186] Pitsch, H. and de Lagneste, L. D. (2002). Large-eddy simulation of a premixed turbulent combustion using level-set approach. *Proc. Combust. Inst.*, 29:2001–2208.

[187] Poinsot, T., Candel, S., and Trouvé, A. (1995). Application of direct numerical simulation to premixed turbulent combustion. *Prog. Energy Combust. Sci.*, 21:531–576.

[188] Poinsot, T., Echecchi, T., and Mungal, M. G. (1992). A study of the laminar flame tip and implications for premixed turbulent combustion. *Combust. Sci. Technol.*, 81:45–73.

[189] Poinsot, T., Veynante, D., and Candel, S. (1991). Quenching processes and premixed turbulent combustion diagrams. *J. Fluid Mech.*, 228:561–606.

[190] Poinsot, T., Veynante, D., Trouvé, A., and Ruetsch, G. (1996). Turbulent flame propagation in a partially premixed flame. In *Proc. CTR Summer Program*.

[191] Poinsot, T. J. and Veynante, D. (2005). *Theoretical and numerical combustion*. Edwards, second edition.

[192] Pope, S. B. (1985). PDF methods for turbulent reactive flows. *Prog. Energy Combust. Sci.*, 11:119–192.

[193] Pope, S. B. (1988). The evolution of surfaces in turbulence. *Int. J. Engng. Sci.*, 26(5):445–469.

[194] Pope, S. B. (1990). Computations of turbulent combustion: Progress and challenges. *Proc. Combust. Inst.*, 23:591–612.

[195] Pope, S. B. (1997). Computationally efficient implementation of combustion chemistry using in situ adaptive tabulation. *Combust. Theory Model.*, 1:41–63.

[196] Pope, S. B. (2000). *Turbulent Flows*. Cambridge University Press.

[197] Pope, S. B. (2013). Small scales, many species and the manifold challenges of turbulent combustion. *Proc. Combust. Inst.*, 34(1):1–31.

[198] Prasad, R. O. S. and Gore, J. P. (1999). An evaluation of flame surface density models for turbulent premixed jet flames. *Combust. Flame*, 116:1–14.

[199] Radhakrishnan, S. and Bellan, J. (2012). Explicit filtering to obtain grid-spacing-independent and discretization-order-independent large-eddy simulation of compressible single-phase flow. *J. Fluid Mech.*, 697:399–435.

[200] Ribault, C. L., Sarkar, S., and Stanley, S. (1999). Large eddy simulation of a plane jet. *Phys. Fluids*, 11:3069.

[201] Richardson, E., Granet, V., Eyssartier, A., and Chen, J. (2010). Effects of equivalence ratio variation on lean, stratified methane–air laminar counterflow flames. *Combust. Theory Model.*, 14(6):775.

[202] Roberts, W. L., Driscoll, J. F., Drake, M. C., and Goss, L. P. (1993). Images of the quenching of a flame by a vortex—to quantify regimes of turbulent combustion. *Combust. Flame*, 94:58–69.

[203] Robin, V., Mura, A., Champion, M., Degardin, O. ., Renou, B., and Boukhalfa, M. (2008). Experimental and numerical analysis of stratified turbulent V-shaped flames. *Combust. Flame*, 153:288–315.

[204] Rowinski, D. H. and Pope, S. B. (2013). Computational study of lean premixed turbulent flames using RANS PDF and LES PDF methods. *Combust. Theory Modelling*, 17(4):610–656.

[205] Ruan, S., Swaminathan, N., Bray, K. N. C., Mizobuchi, Y., and Takeno, T. (2012). Scalar and its dissipation in the near field of turbulent lifted jet flame. *Combust. Flame*, 159:591–608.

[206] Ruan, S., Swaminathan, N., and Darbyshire, O. (2014). Modelling of turbulent lifted jet flames using flamelets: a priori assessment and a posteriori validation. *Combust. Theory Modelling*, 18(2):295–329.

[207] Rutland, C. J. and Trouvé, A. (1993). Direct simulations of premixed turbulent flames with nonunity Lewis numbers. *Combust. Flame*, 94:41–57.

[208] Salehi, M. M. and Bushe, W. (2010). Presumed PDF modelling for RANS simulation of turbulent premixed flames. *Combust. Theory Model.*, 14(3):381–403.

[209] Salehi, M. M., Bushe, W., and Daun, K. (2012). Application of the conditional source term estimation for turbulence chemistry interactions in a premixed flame. *Combust. Theory Model.*, 16(2):301–320.

[210] Salehi, M. M., Bushe, W. K., Shahbazian, N., and Groth, C. P. T. (2013). Modified laminar flamelet presumed probability density function for LES of premixed turbulent combustion. *Proc. Combust. Inst*, 34(1203-1211).

[211] Sankaran, V. and Menon, S. (2005). Subgrid combustion modeling of 3-D premixed flames in the thin-reaction-zone regime. *Proc. Combust. Inst.*, 30:575–582.

[212] Sarghini, F., Piomelli, U., and Balaras, E. (1999). Scale-similarity models for large-eddy simulations. *Phys. Fluids*, 11:6.

[213] Savre, J., Carlsson, H., and Bai, X. S. (2013). Tubulent methane/air premixed flame structure at high Karlovitz numbers. *Flow Turb. Combust.*, 90:325–341.

[214] Schefer, R. W. (1998). Data base for a turbulent, nonpremixed, nonreacting porpane-jet flow. Sandia Report http://www.sandia.gov/TNF/DataArch/ProJet.html, Sandia National Labortories, Livermore, CA.

[215] Schrödinger, C., Paschereit, C. O., and Oevermann, M. (2014). Numerical studies on the impact of equivalence ratio oscillations on lean premixed flame characteristics and emissions. *Combust. Sci. Technol.*, 186:1392–1409.

[216] Schumann, U. (1975). Subgrid scale model for finite difference simulations of turbulent flows in plane channels and annuli. *J. Comput. Physics*, 18:374–404.

[217] Smagorinsky, J. (1963). General circulation experiments with the primitive equations I. the basic experiment. *Mon. Weather Rev.*, 91(3):99–164.

[218] Smiljanovski, V., Moser, V., and Klein, R. (1997). A capturing-tracking hybrid scheme for deflagration discontinuities. *Combust. Theory Model.*, 1:183–215.

[219] Spalding, D. B. (1971). Mixing and chemical reaction in steady confined turbulent flames. In *Symp. (Int.) on Combustion*, volume 13, pages 649–657. The Combustion Institute.

[220] Srinivasan, S. and Menon, S. (2014). Linear eddy mixing model studies of high Karlovitz number turbulent premixed flames. *Flow Turb. Combust.*, 93:189–219.

[221] Steinberg, A. M., Driscoll, J. F., and Swaminathan, N. (2012). Statistics and dynamics of turbulence-flame alignment in premixed combustion. *Combust. Flame*, 159(8):2576–2588.

[222] Stöllinger, M. and Heinz, S. (2008). PDF modelling and simulation of premixed turbulent combustion. *Monte Carlo Methods Appl.*, 14(4):343–377.

[223] Stöllinger, M. and Heinz, S. (2010). Evaluation of scalar mixing and time scale models in PDF simulations of a turbulent premixed flame. *Combust. Flame*, 157(9):1671–1685.

[224] Sung, C. J., Li, B., Wang, H., and Law, C. K. (1998). Structure of sooting limits in counterflow methane/air and propane/air diffusion flames from 1 to 5 atmospheres. *Proc. Combust. Inst.*, 27(1):1523–1529.

[225] Swaminathan, N. and Bray, K. N. C. (2005). Effect of dilatiation on scalar dissipation in turbulent premixed flames. *Combust. Flame*, 143:549–565.

[226] Swaminathan, N. and Bray, K. N. C. (2011). Fundamentals and challenges. In Swaminathan, N. and Bray, K. N. C., editors, *Turbulent Premixed Flames*, chapter 1, pages 1–40. Cambridge University Press, Cambridge, UK.

[227] Swaminathan, N. and Grout, R. W. (2006). Interaction of turbulence and scalar fields in premixed flames. *Physics of Fluids*, 18(4):045102.

[228] Swaminathan, N., Xu, G., Dowling, A. P., and Balachandran, R. (2012). Heat release rate correlation and combustion noise in premixed flames. *J. Fluid Mech.*, 681:80–115.

[229] Sweeney, M. S., Hochgreb, S., and Barlow, R. S. (2011). The structure of premixed and stratified low turbulence flames. *Combust. Flame*, 158:935–948.

[230] Thornber, B., Masri, A., Bilger, R. W., and Hawkes, E. R. (2011). Conditional moment closure for les of compressible premixed combustion. *J. Comp. Phys.*, 230:7687–7705.

[231] Tsui, H. P. and Bushe, W. K. (2014). Linear-eddy model formulated probability density function and scalar dissipation rate models for premixed combustion. *Flow Turb. Combust.*, 93:487–503.

[232] Undapalli, S., Srinivasan, S., and Menon, S. (2009). LES of premixed and non-premixed combustion in a stagnation point reverse flow combustor. *Proc. Combust. Inst.*, 32:1537–1544.

[233] Urata, Y. and Taylor, M. K. P. (2011). Application of lean flames in internal combustion engines. In Swaminathan, N. and Bray, K. N. C., editors, *Turbulent Premixed Flames*, chapter 4, pages 244–309. Cambridge University Press, Cambridge, UK.

[234] van Oijen, J. A. and de Goey, L. P. H. (2000). Modelling of premixed laminar flames using flamelet-generated manifold. *Combust. Sci. Technol.*, 161:113–137.

[235] Vanella, M., Piomelli, U., and Balaras, E. (2008). Effect of grid discontinuities on large-eddy simulation statistics and flow fields. *J. Turbul.*, 9:1–23.

[236] Veynante, D., Trouvé, A., Bray, K. N. C., and Mantel, T. (1997). Gradient and counter-gradient transport in turbulent premixed flames. *J. Fluid Mech.*, 332:263–293.

[237] Veynante, D. and Vervisch, L. (2002). Turbulent combustion modeling. *Prog. Energy Combust. Sci.*, 28(3):193–266.

[238] Viswanathan, S., Wang, H., and Pope, S. B. (2011). Numerical implementation of mixing and molecular transport in LES/PDF studies of turbulent reacting flows. *J. Comp. Phys.*, 230:6916–6957.

[239] Vreman, A. W., van Oijen, J. A., de Goey, L. P. H., and Bastiaans, R. J. M. (2009). Subgrid scale modelling in large-eddy simulation of turbulent combustion using premixed flamelet chemistry. *Flow Turb. Combust.*, 82:511–535.

[240] Wang, G., Boileau, M., and Veynante, D. (2011). Implementation of a dynamic thickened flame model for large eddy simulations of turbulent premixed combustion. *Combust. Flame*, 158:2199–2213.

[241] Wang, G., Boileau, M., Veynante, D., and Truffin, K. (2012). Large eddy simulation of a growing turbulent premixed flame kernel using a dynamic flame surface density model. *Combust. Flame*, 159(8):2742–2754.

[242] Williams, F. A. (1985). *Combustion Theory*. The Benjamin/Cummings Publishing Company, Inc., second edition edition.

[243] Yilmaz, S. L., Nik, M. B., Givi, P., and Strakey, P. A. (2010). Scalar filtered density function for large eddy simulation of a Bunsen burner. *J. Propul. Power*, 26(1):84–93.

[244] Yoshikawa, I., Shim, Y.-S., Nada, Y., Tanahashi, M., and Miyauchi, T. (2013). A dynamic SGS combustion model based on fractal characteristics of turbulent premixed flames. *Proc. Combust. Inst*, 34:1373–1381.

Appendix A

Database

The most relevant simulations are listed here for each of the cases investigated in this thesis. This data is freely accessible on-line and available for interested researchers. For information about how to get access, please contact the author of this thesis at il246@cam.ac.uk or ivanlang87@gmail.com.

Table A.1 Simulations list for the piloted flames case from Chen *et al.* [46] - algebraic model (AM).

Name	β_c	u'_Δ	Sc	Grid size	τ	T_{pilot}	Description	Remark
CA1	7.5	Eq. (3.50)	dyn	4.2M	6.48	1950K	Sensitivity to SGS-velocity	See §5.3
CA2	"	Eq. (3.51)	"	"	"	"	"	"
CA3	"	Eq. (3.52)	"	"	"	"	"	"
CA4	"	Eq. (3.55)	"	"	"	"	"	"
CA5-8	"	Eqs. (3.50-3.55)	"	1.5M	"	"	Sensitivity to grid size	"
CA9-13	2.4 -12.1	Eq. (3.51)	"	1.5M	"	"	Sensitivity to β_c	"
CA14	7.5	"	"	"	"	"	Look-up table unfiltered	Over-prediction of heat release rate
CA15	7.5	"	"	"	"	"	Filter size in look-up table three times larger	Insensitive
CA16	"	"	"	"	"	1810	Sensitivity to pilot temperature	Sensitive close to jet exit
CA17	"	"	"	"	"	2100	"	"
CA18-20	"	$\sqrt{2k_{\text{sgs}}/3}$	"	"	"	1950	Models of Table 5.1	See §5.3.4
CA21	"	$\sqrt{2k_{\text{sgs}}/3}$	"	4.2M	"	1950	Model K3 of Table 5.1, sensitivity to grid size	Same as in §5.3
CA22	"	Eq. (3.51)	"	1.5M	"	"	Enlarged domain	Insensitive
CA23	"	Eq. (3.51)	"	1.5M	"	"	Longer simulation time	"
CA24	"	"	"	"	$1+\frac{\rho_u}{\bar{\rho}}$	"	Dynamic computation of heat release parameter	"
CA25	"	"	"	"	6.48	"	Using $\overline{\rho\phi}$ instead of $\widetilde{\phi}$ in look-up table	Large inaccuracies
CA26-27	"	"	0.4/0.7	"	"	"	Sensitivity to Schmidt numbers	Small sensitivity in this range
CA28-30	"	$\sqrt{2k_{\text{sgs}}/3}$	0.7	"	"	"	Sensitivity to Schmidt numbers, models of Table 5.1	"
CA31	dyn	Eq. (3.51)	dyn	"	"	"	dynamic computation of β_c	See §5.4
CA32	dyn	Eq. (3.51)	dyn	4.2M	"	"	dynamic computation of β_c	See §5.4
CA33-34	"	"	"	1.5M	"	"	Increasing/decreasing physical limit for β_c	Inaccuracies
CA34	"	$\sqrt{2k_{\text{sgs}}/3}$	"	"	"	"	Model K2 of Table 5.1	Weakly sensitive

Table A.2 Simulations list for the piloted flames case from Chen *et al.* [46] - unstrained flamelets model (UFM).

Name	β_c	Sc_T	Grid size	T_{pilot}	Description	Remark
CU1	7.5	dyn	1.5M	1950K	See §6.4	See §6.4
CU2	7.5	"	4.2M	"	Sensitivity to grid size	See §6.4
CU3	6.0	"	1.5M	"	Sensitivity to β_c	Almost insensitive up to 20% variation; less sensitive than algebraic model
CU4	6.0	"	4.2M	"	"	"
CU5	6.0	"	4.2M	"	Using $g = \sigma^2_{c,\mathrm{sgs}}/[\widetilde{c}(1-\widetilde{c})]$ instead of $\sigma^2_{c,\mathrm{sgs}}$ to parametrise the look-up table	Numerical issues and inaccuracies
CU6	7.5	"	1.5M	1750	Sensitivity to pilot temperature	Sensitive close to jet exit
CU7	7.5	0.7	1.5M	1950	Sensitivity to Schmidt numbers	Insensitive
CU8	"	dyn	"	1950	Pre-filtering the look-up table before integration	Large inaccuraices
CU9	"	dyn	"	"	Vertical velocity ($1\,\mathrm{m/s}$) assigned on lateral boundaries	Insensitive
CU10	dyn	"	"	"	See §6.4	See §6.4
CU11	dyn	"	4.2M	"	See §6.4	See §6.4

Table A.3 Simulations list for the piloted flames case from Chen *et al.* [46] - strained flamelets model (SFM).

Name	β_c	Grid size	σ_N	$\psi_{\max}$	Description	Remark
CS1	dyn	1.5M	0.3	500	See §6.4	See §6.4
CS2	7.5	"	0.3	500	Sensitivity to β_c	Weakly sensitive
CS3	6.0	"	"	"	Sensitivity to β_c	Weakly sensitive
CS4	dyn	"	0.5	"	Sensitivity to σ_N	Decreasing accuracy
CS5	dyn	"	0.3	700	Sensitivity to $\psi_{\max}$	Insensitive
CS6	"	4.2M	0.3	500	Sensitivity to grid size	Insensitive

$\psi_{\max}$ is the upper bound of the integration domain in Eq.(3.40).

σ_N is the standard deviation of $\ln(\psi|c)$ in Eq. (3.41).

Table A.4 Simulations list for the bluff body case [168, 169].

Name	Model	β_c	Grid size	S.T.	W.R.	W.F.	Description	Remark
N1-2	A/U	dyn	1.8M	No	No	Yes	See §7.2.1	See §7.2.1
N3-4	A/U	"	2.2M	"	Yes	No	See §7.2.1	See §7.2.1
N5-6	A/U	"	2.2M	"	Yes	Yes	Sensitivity to wall functions	Decreasing performance because grid is within subviscous layer
N7-8	A/U	"	7.6M	"	No	Yes	Grid sensitivity	Similar to 1.8M grid
N9	U	"	11.2M	"	Yes	No	Grid and W.R. sensitivity	Similar to 2.2 M grid
N10	A	"	1.8M	"	No	No	Sensitivity to wall functions	Decreased accuracy
N11-12	A	"	1.8M	"	No	Yes	U_{air} varied from 0.02 to 2.2 m/s	Insensitive
N13	A	"	"	"	No	Yes	Sensitivity to inlet velocity ($U_0 = 10.5\,\text{m/s}$)	Weakly sensitive
N14-15	A	"	"	"	No	Yes	Coflow temperature 1000/1600K	Insensitive
N16-17	A/U	"	"	"	No	Yes	Using H_2O as progress variable	Weakly sensitive
N18-19	A/U	"	2.2M	"	Yes	No	"	Weakly sensitive
N20	A	2.4	1.8M	"	No	Yes	Sensitivity to β_c	Over-prediction of reaction rate
N21	U	2.4	2.2M	"	Yes	No	"	"
N22	A	dyn	1.8M	"	No	Yes	Increased combustor length	Weakly sensitive at $x/D = 6$
N23	U	dyn	2.2M	Yes	Yes	No	See §7.2.2	See §7.2.2
N24	A	dyn	1.8M	Yes	No	Yes	See §7.2.2	See §7.2.2
N25	A	4.0	1.8M	"	No	Yes	Static β_c from dynamic analysis	Similar to dynamic evaluation
N26	U	4.0	2.2M	"	Yes	No	"	"
N27	A	12.0	1.8M	"	No	Yes	Sensitivity to β_c	Under-prediction of reaction rate
N28	U	12.0	2.2M	"	Yes	No	"	"
N29	U	dyn	2.2M	"	Yes	No	Sc = 0.7 instead of dynamic formulation	Insensitive
N30	A	dyn	7.6M	"	No	Yes	Sensitivity to grid size	Small differences
N31	U	dyn	11.2M	"	Yes	No	"	"
N32	U	dyn	2.2M	"	Yes	No	Using H_2O as progress variable	See §7.5.1
N33	U	dyn	2.2M	"	Yes	No	Using $CO_2 + CO$ as progress variable	See §7.5.1

A = algebraic; U = Unstrained; S.T. = Synthetic turbulence; W.R. = Wall refinement; W.F. = Wall functions.

Table A.5 Simulations list for the low-turbulence flame case from Furukawa *et al.* [76].

Name	Model	β_c	Grid size	u'_Δ	u' [m/s]	Description	Remark
W1-2	A/U	dyn	5.4M	Eq. (3.51)	0	Testing dynamic β_c	β_c largely over-predicted; inadequate because of low-tubulence
W3-4	A/U	"	"	"	0.22	"	"
W5-6	A/U	"	"	"	0.37	Sensitivity to higher turbulence	"
W7	U	6.0	"	"	0.22	See Chapter 8	See Chapter 8
W8	U	6.0	"	Eq. (3.56)	"	See Chapter 8	See Chapter 8
W9	U	10.0	"	Eq. (3.50)	"	See Chapter 8	See Chapter 8
W10-12	A	7.5/15	"	Eq. (3.51)	0	Testing algebraic model	Flame too short
W13-14	A	12.5/15	"	"	0.37	"	"
W15-17	U	7.5	"	Eqs. (3.50,3.51,3.56)	0.22	Sensitivity to β_c	Very sensitive
W18-19	U	7.5	"	Eq. (3.50)	0/0.15	Sensitivity to inlet turbulence	Very sensitive
W20	U	4.5	23M	Eq. (3.51)	0.22	Grid sensitivity	See §8.3.4

A = algebraic; U = Unstrained.